TECHNICAL REPORT STANDARD PAGE

1. Report No.	2. Government Accession No.	3. Recipient's Catalog No.
FHWA/LA.10/472		

4. Title and Subtitle	5. Report Date
Development and Performance Evaluation of Fiber Reinforced Polymer Bridge	**March 2014**
	6. Performing Organization Code

7. Author(s)	8. Performing Organization Report No.
C.S. Cai, Ph.D., P.E., Archana Nair, Shuang Hou, Ph.D., Miao Xia	

9. Performing Organization Name and Address	10. Work Unit No.
Department of Civil and Environmental Engineering Louisiana State University Baton Rouge, LA 70803	11. Contract or Grant No. **LTRC Project Number: 05-5ST State Project Number: 736-99-1370**

12. Sponsoring Agency Name and Address	13. Type of Report and Period Covered
Louisiana Department of Transportation and Development P.O. Box 94245 Baton Rouge, LA 70804-9245	**Final Report Nov. 2005-Nov. 2010**
	14. Sponsoring Agency Code

15. Supplementary Notes

Conducted in Cooperation with the U.S. Department of Transportation, Federal Highway Administration

16. Abstract

Fiber reinforced polymers (FRP) have become more popular construction materials in the last decade due to the reduction of material costs. The installation and performance evaluation of the first FRP-wrapped balsa wood bridge in Louisiana is described in this document. A comprehensive instrumentation and loading test scheme is discussed and details are illustrated. The selected bridge structure in this demonstration project will potentially provide a new approach to enhancing the transportation infrastructure in Louisiana. The test bridge is the Pierre Part Bridge located on route LA 70 in Assumption Parish, LADOTD District 61.

The instrumentation consisted of regular strain gauges, fiber optic strain and temperature sensors, accelerometers, and acoustic emission sensors. The measured results from each of the gauges are summarized, and comparisons are made between the finite element models of the bridge structure and the field test results. Before placing the instrumentation on the field bridge, extensive laboratory explorations and numerical analysis were conducted and the research results have been documented in this report.

Several years after the bridge had been opened to traffic, a delamination in one of the panels was observed. The deck was removed and replaced with a new deck grating. After a visual inspection and discussion with the fabricator, it turned out that a shifting on the top FRP surface in one of the panels occurred while the panel was being infused with epoxy. There is a good reason that less epoxy was infused after the rearranging of the FRP stop surface was carried out, and this could have led to the delamination problem.

17. Key Words	18. Distribution Statement
Balsawood, FRP, bridge deck, instrumentation, live load testing	**Unrestricted. This document is available through the National Technical Information Service, Springfield, VA 21161.**

19. Security Classif. (of this report)	20. Security Classif. (of this page)	21. No. of Pages	22. Price
N/A	N/A	217	N/A

Project Review Committee

Each research project will have an advisory committee appointed by the LTRC Director. The Project Review Committee is responsible for assisting the LTRC Administrator or Manager in the development of acceptable research problem statements, requests for proposals, review of research proposals, oversight of approved research projects, and implementation of findings.

LTRC appreciates the dedication of the following Project Review Committee Members in guiding this research study to fruition.

LTRC Manager

Walid Alaywan, Ph.D., P.E.
Structures Research Manager

Members

Paul Fossier, P.E.
Gill Gautreau, P.E.
Michael Boudreaux, P.E.
Art Aguirre, P.E.

Directorate Implementation Sponsor

Richard Savoie, P.E.
DOTD Chief Engineer

Development and Performance Evaluation of Fiber Reinforced Polymer Bridge

by

C.S.Cai, Ph.D., P.E.
Archana Nair
Shuang Hou, Ph.D.
Miao Xia

Department of Civil Engineering
Louisiana State University
Baton Rouge, Louisiana 70803

LTRC Project No. 05-5ST
State Project No. 736-99-1370

conducted for

Louisiana Department of Transportation and Development
Louisiana Transportation Research Center

March 2014

ABSTRACT

Fiber reinforced polymers (FRP) have become more popular construction materials in the last decade due to the reduction of material costs. The installation and performance evaluation of the first FRP-wrapped balsa wood bridge in Louisiana is described in this document. A comprehensive instrumentation and loading test scheme is discussed and details are illustrated. The selected bridge structure in this demonstration project will potentially provide a new approach to enhancing the transportation infrastructure in Louisiana. The test bridge is the Pierre Part Bridge located on route LA 70 in Assumption Parish, LADOTD District 61.

The instrumentation consisted of regular strain gauges, fiber optic strain and temperature sensors, accelerometers, and acoustic emission sensors. The measured results from each of the gauges are summarized, and comparisons are made between the finite element models of the bridge structure and the field test results. Before placing the instrumentation on the field bridge, extensive laboratory explorations and numerical analysis were conducted and the research results have been documented in this report.

Several years after the bridge had been opened to traffic, a delamination in one of the panels was observed. The deck was removed and replaced with a new deck grating. After a visual inspection and discussion with the fabricator, it turned out that a shifting on the top FRP surface in one of the panels occurred while the panel was being infused with epoxy. There is a good reason that less epoxy was infused after the rearranging of the FRP stop surface was carried out, and this could have led to the delamination problem.

ACKNOWLEDGMENTS

This research project was the second Innovative Bridge Research and Construction (IBRC) award that Louisiana has received. The investigators are thankful to the Federal Highway Administration (FHWA) and the Louisiana Transportation Research Center (LTRC) for funding this project. The contents of this report reflect only the views of the writers who are responsible for the facts and the accuracy of the data presented herein. The authors would like to thank those who provided help during the development of the initial tasks of this research program. Special thanks goes to the project manager Dr. Walid Alaywan, the Louisiana Department of Transportation and Development (LADOTD) crew, and graduate students at Louisiana State University (LSU) for their hard work during the installation and bridge testing process. The bridge deck was manufactured by Dr. Kurt Feichtinger from Alcan Baltek Corporation and John Parker from Crescent City Composites. Their efforts for this project are greatly appreciated.

IMPLEMENTATION STATEMENT

Though other states have been using FRP decks to replace deteriorating ones, Louisiana was the first state to incorporate balsawood in its FRP deck, making this product second to none worldwide. As such, extensive research had to be performed to design and understand the behavior of this FRP-balsawood deck before placing it on any of its bridges.

Though the cost of purchasing the FRP-balsawood deck is higher than that of a grid metal deck, the FRP-balsawood deck offers many advantages when it comes to corrosion resistance, cost and speed of installation, low maintenance, and durability.

Several years after the deck had been placed and opened to traffic, local residents began complaining about loud noises at night when trucks crossed the bridge. An LADOTD team went to the bridge site to investigate the complaint. Trucks crossed the bridge and no loud noises could be heard. As complaints continued, the LADOTD bridge maintenance forces noticed a delamination in one of the six panels. As a result, LADOTD District decided to remove the deck and replace it with a new steel grating.

In November 2013, an inspection of the six bridge panels stored at the bridge maintenance yard revealed that five of the six did not show any sign of delamination. The manufacturer of the bridge panel indicated that he experienced a problem during the infusion of the epoxy in the system. The top FRP surface shifted during fabrication. The fabrication process had to be stopped to rearrange that surface. That led to a delay in completing the infusion and could have resulted in too little epoxy at the top of that one panel.

In summary, this project has demonstrated the practical potential of FRP-wrapped balsawood decks as viable counterparts to conventional deck grating and concrete decks provided QC/QA are carried out to avoid similar problem during fabrication.

TABLE OF CONTENTS

LIST OF TABLES

LIST OF FIGURES

INTRODUCTION

Conventionally, highway bridge decks in the US are predominantly made of steel-reinforced concrete. However, repair and maintenance costs of these bridges incurred at the federal and state levels are overwhelming. As a result, for many years, there has been pressure on transportation agencies to find new cost-effective and reliable construction materials [*1*]. A very promising alternative is the Fiber Reinforced Polymer (FRP) bridge deck system. FRP composites have found increasing applications in bridge design and construction.

Lightweight, high strength and stiffness, durability, and ease of construction are major advantages of this material that makes its application in civil infrastructures viable *[2], [3]*. Meanwhile issues such as high initial construction costs, lack of design guidelines or standards, and the material's sensitivity to ultraviolet radiation stand against its widespread application *[1],[4],[5],[6]*.

Some of the first applications of FRP for complete bridge structures were in China. A number of pedestrian bridges have been built, but the first entire composite bridge deck was the Miyun Bridge completed in September 1982 near Beijing, which carries full highway traffic. The Ulenbergstrasse Bridge in Germany was the world's first in the use of high tensile strength glass fiber prestressing tendons. Since then, many bridges have been constructed in various parts of the world using FRP. These include both pedestrian and vehicular bridges. One example is the Aberfeldy Footbridge that crosses the River Tay in Scotland and was erected in 1992. It is the world's first and longest advanced composite footbridge. Another example is the Bonds Mill lift bridge (completed in 1994), which is an electrically operated lift bridge. It was the first bridge in England to be constructed from plastic. The Tech 21 (Smith Road) Bridge is Ohio's first all-composite bridge. Other important projects involving composites in the US were the No-Name Creek Bridge, Kansas (1996); Bridge 1-351, Delaware (1998); Bennet's Bridge, New York (1998), etc., *[7]*.

Similar to the condition in any other state of the United States, a large number of existing bridges in Louisiana are weight restricted. There is an urgent need to repair and upgrade the state's bridge system. Applications of new materials such as FRP are new explorations in dealing with the state's infrastructure problems. A FRP-wrapped balsa wood bridge deck system has been developed and installed in Louisiana. In this study, the bridge performance has been evaluated by using live load testing, and its long-term performance will be monitored using fiber optic sensors throughout its service life. Fiber optic sensors have the advantages of small dimensions, good resolution and accuracy, as well as an excellent ability to transmit signals at long distances. They are also immune to electromagnetic, radio

frequency interference, and may incorporate a series of integrated sensors multiplexed along a single fiber. These advantages make fiber optic sensors an ideal tool for structural performance monitoring *[8]*. Preliminary results from acoustic emission, traditional strain sensors, and fiber optic sensors were analyzed to assess the bridge performance. Taking advantage of the new development in FRP materials and fiber optic sensors, this demonstration project will potentially provide a new approach to enhancing the transportation infrastructure in Louisiana and set up long-term FRP bridge monitoring guidelines.

Bridge Description

The bridge selected for this study is the Pierre Part Bridge on Route LA 70 in Assumption Parish. The bridge was built in 1988 with a design load of HS20-44 and an average daily traffic (ADT) of about 6000. The bridge, with a total length of 145 ft. (44.2 m) and a roadway width of 46 ft. (14 m), consists of six 20-ft. (6.1-m) spans and a 25-ft. (7.6-m) span. The 20-ft. (6.1-m) spans are concrete structures and the 25-ft. (7.6-m) span consists of a steel grid deck supported on steel girders. The height of the superstructure from the top of concrete pedestal to the top of roadway is about 20 in. (0.51 m). The 25-ft. (7.6-m) steel span is designed for being lifted for river navigation when needed. Figure 1 shows the damaged grid deck that needs to be replaced in the 25-ft. (7.6-m) span. The requirement of being movable, the appropriate span length 25 ft. (7.6 m), and the existing height of the superstructure 20 in. (0.51 m) make this steel span a good candidate to be replaced with a FRP slab system.

The span to be replaced has eight 299.21-in. x 70.86-in. (7600-mm x 1800-mm) deck panels across the traffic direction, as shown in Figure 2. The FRP deck panels that will be bonded on the I girders have the same dimensions as the steel grid deck panels. Labels A through P in Figure 2 stand for the girder positions, and 2 through 4 are the reference lines where sensors are located. In this project, the issues of interest for the bridge's long-term performance monitoring are: (1) integrity of the FRP-wrapped balsa wood bridge deck system, (2) the strains in the transverse direction of the deck and the longitudinal direction of the individual girders, and (3) bridge deck–girder interface bond integrity.

Figure 1
Pierre Part bridge

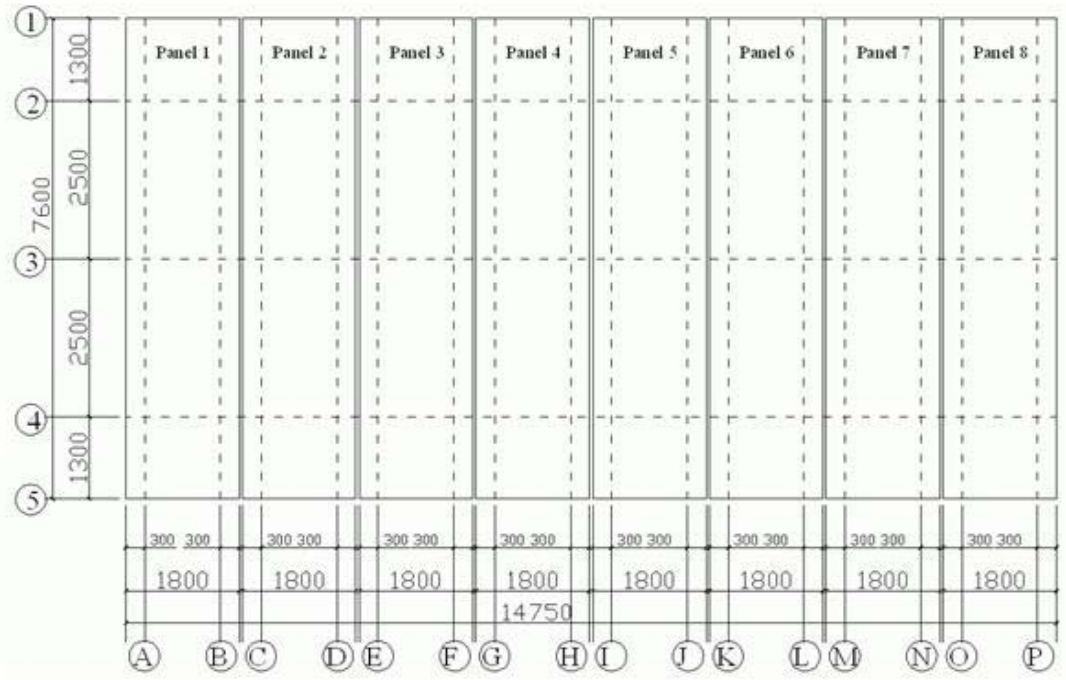

Figure 2
Bridge deck plan view

OBJECTIVE

The objectives of this research were to develop a FRP-wrapped balsa wood bridge deck system suitable for replacing a damaged steel grid deck in the bridge chosen for this project, assess the options for long term monitoring, and develop long-term monitoring guidelines.

These objectives were achieved by focusing on a detailed literature review, planning, and design leading to opt for the best FRP deck configuration and developing comprehensive plans to provide performance evaluation and continuous monitoring of the new structural system developed in this project. The ultimate objective was to take advantage of the promising characteristics of FRP materials to develop a more durable, less maintenance intensive bridge system to save the limited budget for more urgent needs in the transportation infrastructure system.

SCOPE

The scope of this work included finite element prediction, performance evaluation, and quality assurance through laboratory and field bridge testing, along with the development of long-term monitoring strategies. The FRP-wrapped balsa wood deck system was selected and provided by LADOTD to the research team. The scope of this research was achieved through:

3-D Finite Element Analysis and FRP System Design — 3-D finite element models were developed to simulate the structural behavior of selected FRP bridge deck system.

Laboratory Test — An instrumentation plan was developed based on finite element analysis results. Before onsite application of the instrumentation system, laboratory tests were carried out to verify the system and methodology.

Installation and Field Test — The selected bridge was instrumented for both short- and long-term monitoring. After the installation of the deck, a field test was conducted to verify the bridge performance under known loads. Another purpose of the test under given loads was to establish the performance baseline with which the future measured performance could be compared for long-term monitoring purposes.

Long-term Monitoring — Many issues associated with the long-term fatigue, thermal effects, and other environmental loads of this composite bridge system may not be revealed during short-term testing. By periodically collecting relevant environmental information at the bridge site and the monitoring of the bridge performance, a reliable evaluation of the actual bridge performance, prediction of bridge residual life, and development of the most economical approach to upgrading the bridge capacity can be achieved. A long-term monitoring strategy was thus developed for this specific FRP bridge system.

METHODOLOGY

To achieve the research objective stated earlier, the research work was classified into four parts. The first part developed a numerical prediction procedure whose results will be compared to available laboratory or field-testing results to calibrate the finite element models. The second part was to use the predicted bridge performance to design instrumentation and monitoring systems. The third part involved field installation and testing, and the final part developed a long-term monitoring strategy detailed in Appendix G and H.

Analytical Modeling for Instrumentation Scheme Design

Initially, finite element models were developed for both the FRP deck and deck-girder assembly and their performance assessed to identify critical locations of interest for monitoring. Available bridge component laboratory test results were used to calibrate the model. Model dimensions and applied loads adopted for this purpose are illustrated in Figure 3. Nodal strain contour plots are generated in Figures 4 and 5 after girder and deck systems were analyzed using roughly a factored HS 20 truck wheel load. The maximum stress at the bottom of the composite deck from the model was determined to be 26,613 psi, which lies well below 66,173 psi, the ultimate strength of the hardwire component in the deck. From the finite element analysis, the FRP deck was identified as the member more sensitive to the load than the girders. From all this preliminary information, strategic locations for monitoring were selected for both deck and girder performance evaluation using appropriate sensors.

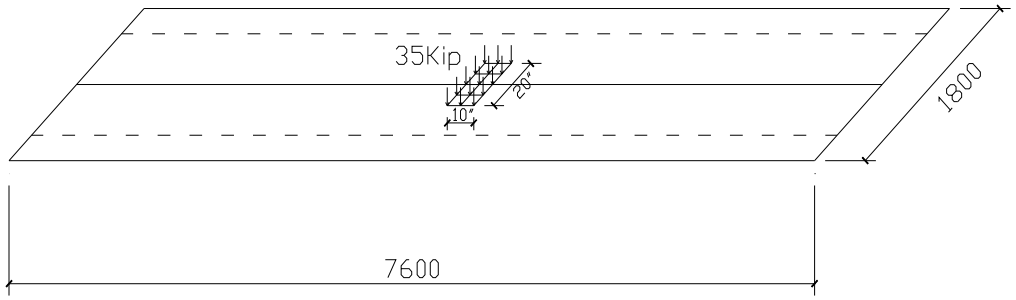

(a)

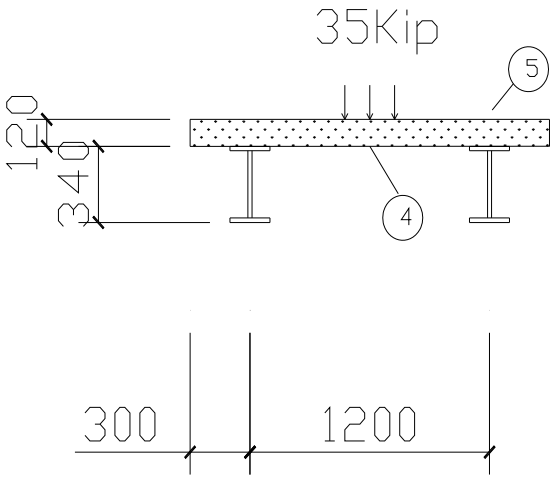

(b) (all dimensions in mm)

Figure 3
(a) Isometric view of deck and (b) transverse view of deck-girder assembly model with applied loads

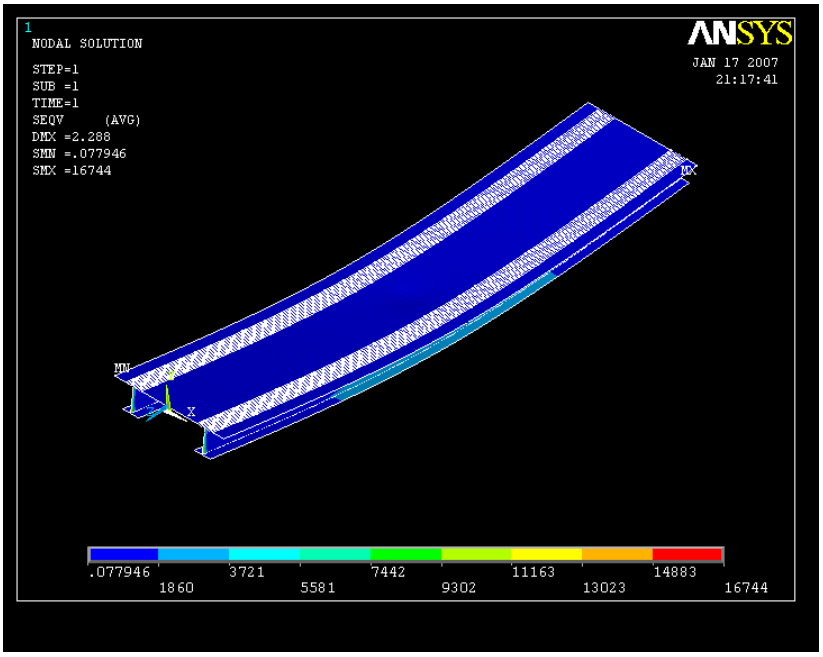

Figure 4
Strain contour plot for deck-girder assembly

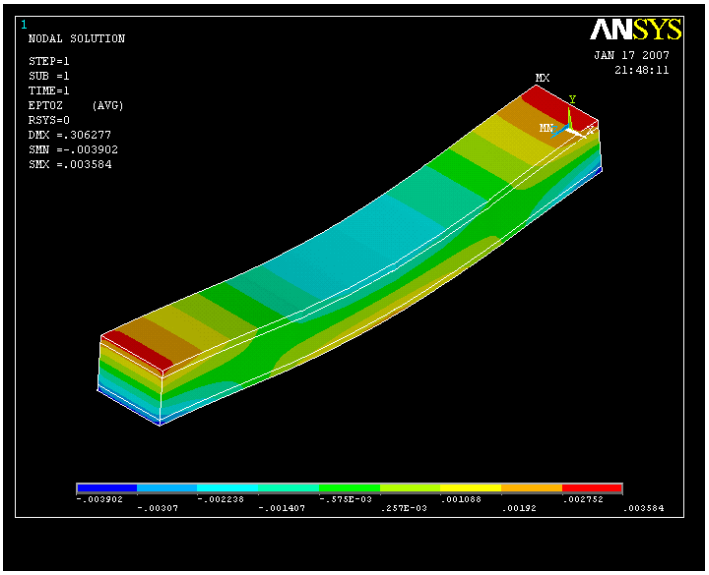

Figure 5
Strain contour plot for composite deck

Design of Monitoring System

The analytical results from FE modeling provided important information, such as stress distribution, of the FRP-wrapped bridge system. This information was used to guide the design of the instrumentation and monitoring system for this bridge. A brief summary of the overall instrumentation plan adopted will be discussed in this section.

The instrumentation plan was designed to measure the live load response behavior of the superstructure. The central four composite panels and supporting girders were instrumented with sensors. Both internally and externally attached fiber optic fiber bragg grating (FBG) and optical time domain reflectometer (OTDR) sensors were used in this project. These sensors enable both short-term and long-term monitoring of strains, slips, and temperature in both deck and girder members. Sixteen traditional strain transducers, six accelerometers, and eight acoustic emission (AE) sensors were also mounted during the live load testing conducted immediately after construction, working as a reference for cross checking the fiber optic sensor (FOS) instrumentation system.

FBG Sensors

Although FBG sensors are available commercially, using them as gauges requires customization. The type of application, material surfaces on which the sensors need to be attached, etc. play a vital role in deciding the appropriate gauge packaging. In this project since the deck was made of FRP-wrapped balsa wood and the girders were of steel, the

sensors were assembled as shown in Figures 6 and 7. To attain realistic strain values, the gauges attached on the deck were packaged with a strip of carbon fiber (Figure 7) while steel shims with shallow grooves (Figure 6) were chosen for the steel girder gauges. All packaged gauges were tested in the laboratory before installation to ensure their functionality.

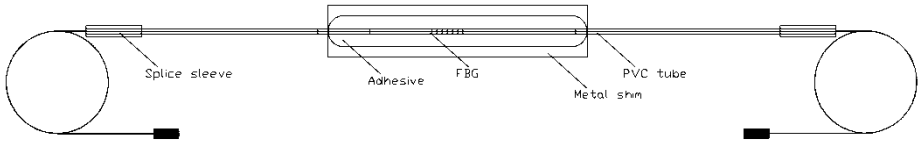

Figure 6
Steel girder mountable-packaged sensor

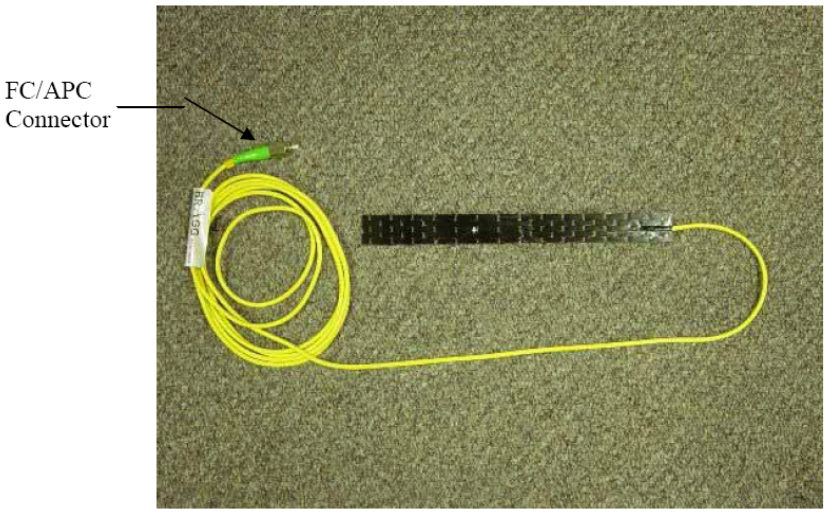

Figure 7
Composite deck mountable packaged sensor

Deck Instrumentation

In general, from the configuration of the FRP deck and the finite element analysis results, it was understood that the strains along the transverse direction of the deck (perpendicular to traffic direction) were the critical parameters to be monitored. This fact led to aligning both the FBG strain sensors and traditional strain gauges attached to the deck to positions about 3 ft. 3 in. (1 m) away from the end of the deck. The array of sensors attached to the four central decks is clearly illustrated in Figure 8.

Girder Instrumentation

Along with instrumenting the four central panels, the supporting girders were also instrumented. FBG sensors were attached at the bottom of all eight-I girders as shown in Figures 8 and 9. Three positions of the I girder were chosen for monitoring, which was the mid-span and the other two positions about 4 ft. (1.219 m) away from either end of the girder. Sensors were denoted as a combination of the cable number and an increased sensor number. For example, the four sensors in cable 9 were numbered as 9-1, 9-2, 9-3, and 9-4. Sensors 9-4 and 16-4 were dummy sensors placed for temperature monitoring.

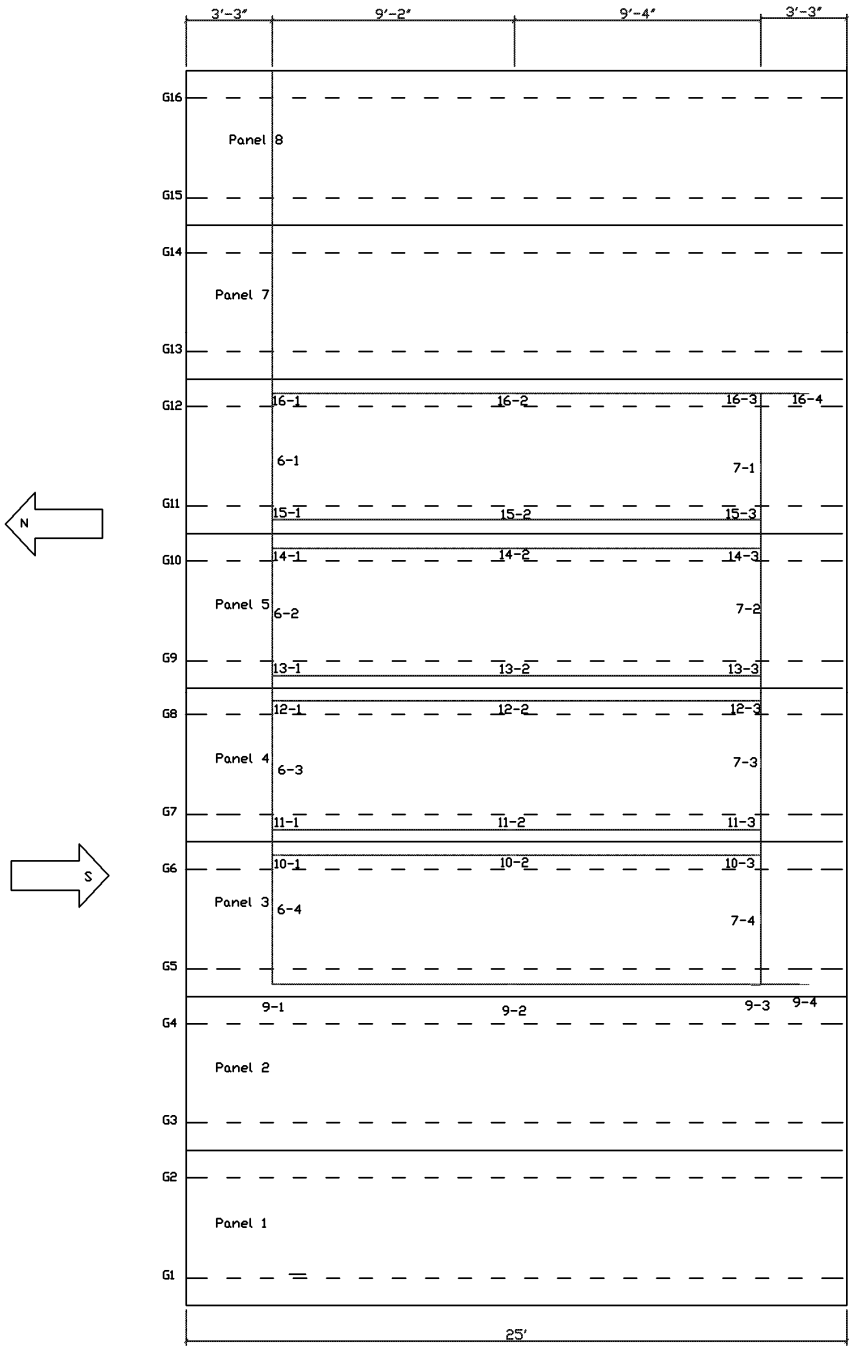

Figure 8
Plan view of all installed FBG sensors at the bottom of I girder and deck panels

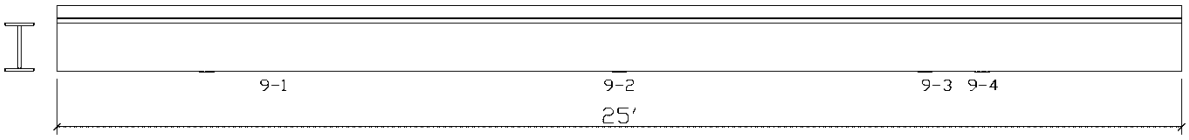

Figure 9
Cross section detail of typical FBG sensor array along girder 5

OTDR Sensors

The non-mechanical glue-bond between the deck and girder components adopted in this bridge system needs assessment as the structure's integrity and long-term performance can be influenced by this bonding method. Monitoring the slip at the deck-girder interface was identified as one such parameter that may help assess the bond integrity. For this, an OTDR based debonding monitoring system with the bare optic fibers placed at the interface between the I girder and FRP-wrapped balsa wood deck as shown in Figures 10 and 11 was used.

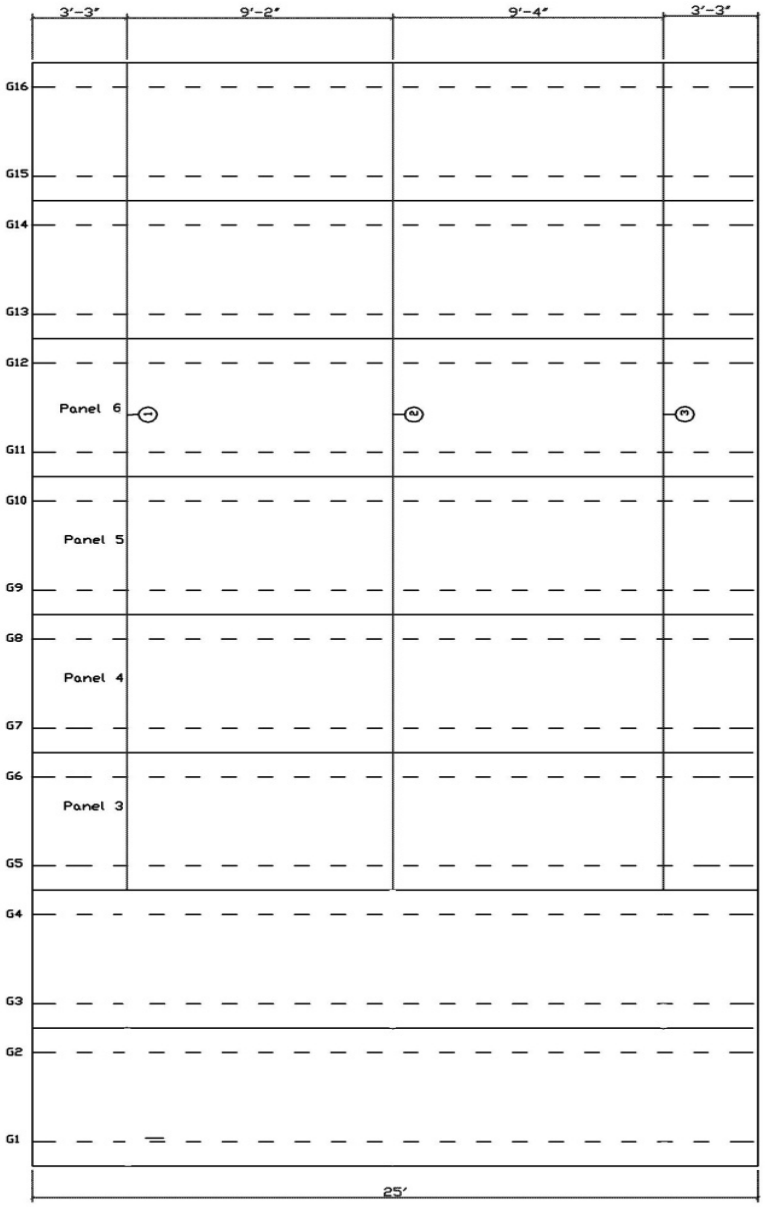

Figure 10
Plan view of all installed OTDR sensors at the deck-girder interface

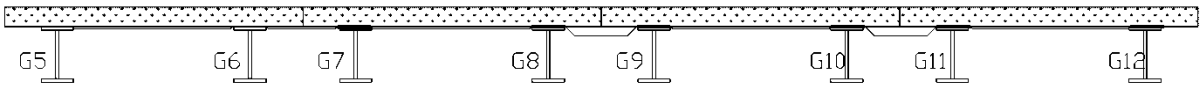

Figure 11
Cross sectional detail of typical OTDR sensor layout at the deck-girder interface

Traditional Strain Gauges, AE Sensors, and Accelerometers

To supplement and cross-check the strain information collected from the FBG sensors, a few traditional strain gauge transducers were also placed at coincident locations on both deck panel and girder surfaces. The traditional transducer chosen for this project was a Bridge Diagnostics, Inc. (BDI) intelliducer (shown later in Figure 20).

From Figure 12, it is clear that strain sensors (SG1- SG16) were attached to the bottom of the FRP deck assembly along the centerline between two girders, while sensors attached to the steel girders were located at the mid-span. Sensors on the girders were attached to both the bottom flange and top flange to identify extent of composite action between the deck and girder.

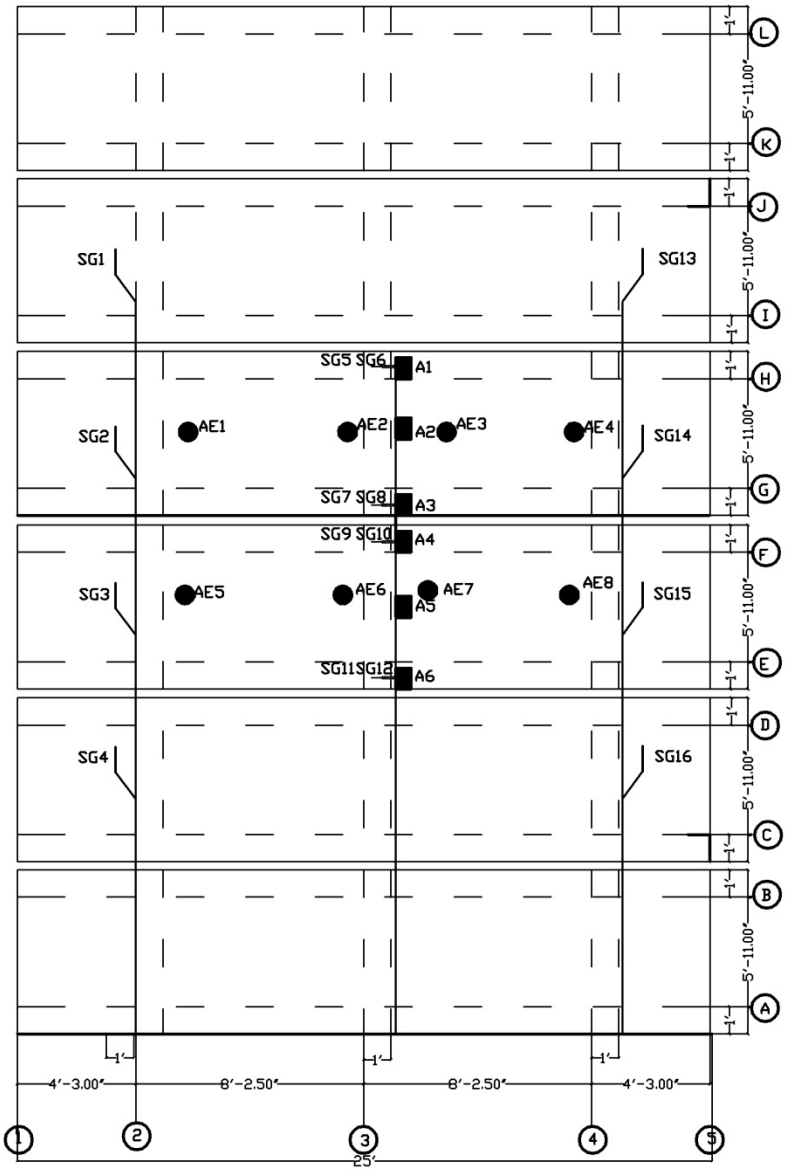

Figure 12
Traditional strain gauge, accelerometer, and AE sensor layout on bridge

The AE sensors (Figure 13) used in this project were the resonant type R15I manufactured by Physical Acoustics Corporation (PAC). Eight AE sensors (AE 1-8) were included in the instrumentation plan as shown in the sensor layout in Figure 12. These are located on the two central panels of the bridge along the centerline of the deck between two supporting girders. Since the deck is glued to the girder in this span of the bridge, the interface cannot be inspected visually to confirm bond integrity. The AE sensors used in this test plan were

intended to be used as a tool to help assess the integrity of this interface.

Figure 13
R15I AE sensor

Additionally, six accelerometers (A1-6) were also affixed to the decks and girders during live load testing to capture the modal characteristics of the bridge during dynamic loading.

FRP Deck Manufacture and Final Installation

The new bridge deck consists of pre-fabricated FRP-wrapped balsa wood units. The fabrication sequence of the bridge deck units and final installation are illustrated in Figure 14(a) that shows the balsa wood beam being wrapped with glass fiber reinforced polymer (GFRP) sheets. In Figure 14(b), a single panel is being assembled using several of the wrapped balsa wood beams and hardwire layers. The deck was adhesively bonded to the steel girder using customized epoxy [Figure 14(c)] and a bonded panel is shown in Figure 14(d). The panels were transported and placed on site as seen in Figure 14(e) and finally all sensors required for performance evaluation of the newly constructed bridge were installed as shown in [Figure 14(f)].

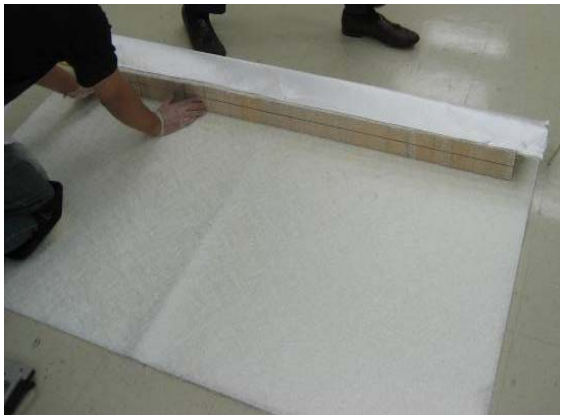
(a)
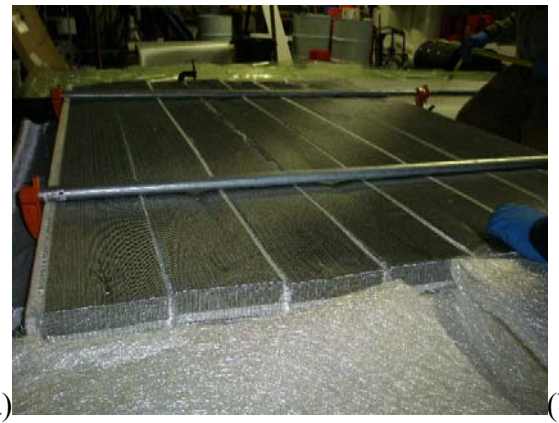
(b)
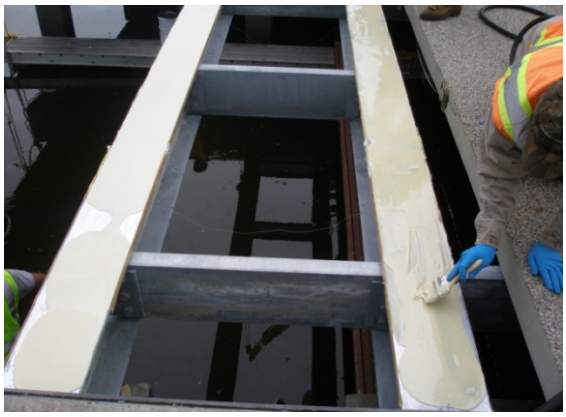
(c)

(d)

(e)

(f)

Figure 14
FRP-wrapped balsa wood bridge deck installation: (a) balsa wood beam wrapped with FRP material; (b) FRP deck assembly; (c) application of bonding agent on girder; (d) finished FRP deck attached to steel girder; (e) bridge deck placement; (f) sensors installed after bridge construction

After the construction phase, live load tests were conducted in October 2009 to evaluate the performance of the newly installed deck system. Six loading tests were performed, which comprised of four static and two dynamic load cases (Figures 16 and 17) for each traffic lane. The static tests involved both static stopping and static rolling tests while dynamic tests involved varied speed levels. The vehicle configuration used for all bridge tests is

represented in Figure 15. Prior to the testing, the vehicles were weighed and measured. The vehicle was loaded with bags of crushed asphalt. Only one truck was used to test both lanes. Axle and gross vehicle weights are summarized in Table 1.

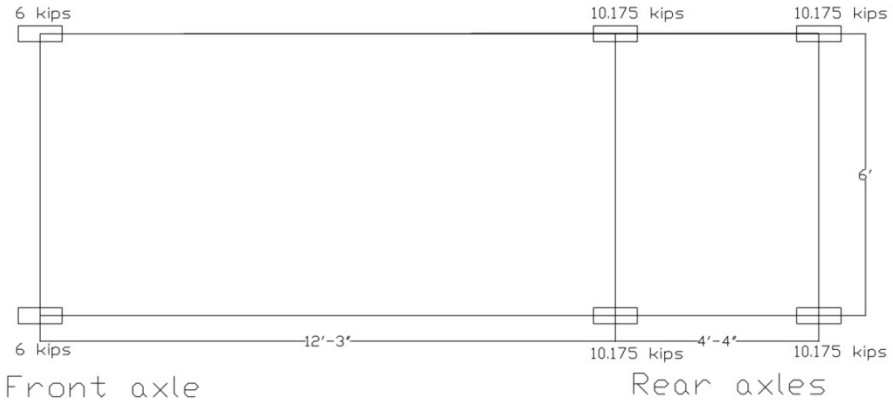

Figure 15
Test truck axle configuration

Table 1
Test truck axle weight details

Test Vehicle	Front Axle Wt. (kips)	Rear Axle Wt. (kips)	Gross Vehicle Wt. (kips)
Truck 1	12.000	40.700	52.7

For the static stopping tests, the trucks were stopped for a few seconds at three locations on the bridge (Figure 16). While in all static rolling tests, the test truck travelled at a constant speed of about 3-5 mph. For the dynamic tests, the trucks passed by each traffic lane twice at an approximate speed of 30 mph followed by the permitted lane speed of 55 mph.

Static Loading

The static load tests comprised of static stopping and static rolling tests. During the static stopping tests, the trucks were stopped at marked locations shown in Figure 16 to coincide with sensor positions beneath the bridge. Except for the first truck stopping location at the bridge entrance where the rear axle was aligned at the marked location, the mid axle of the truck for all the other static tests was aligned at midspan and exit end stopping locations. For these load cases, data acquisition in all acquisition systems was carried out for approximately 30 seconds. The static rolling test involved the test truck to be driven at a constant crawling speed of about 3-5 mph. Each pass was repeated once and for each traffic lane as shown in

Figures 16 and 17.

Dynamic Loading

Dynamic loading tests were performed twice through the same traffic lane with the same truck at higher speeds (30-55 mph). Continuous data acquisition was enabled in all acquisition systems during these live load tests.

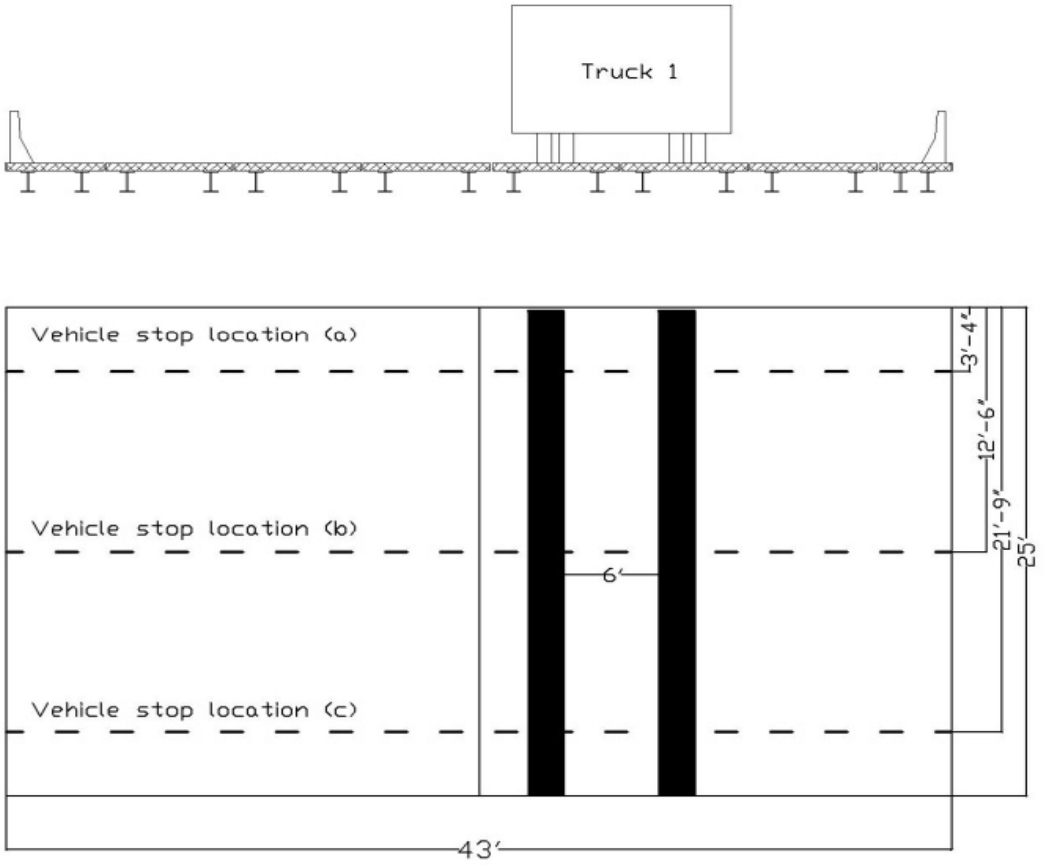

Figure 16
Static and dynamic truck loading path for south bound traffic lane

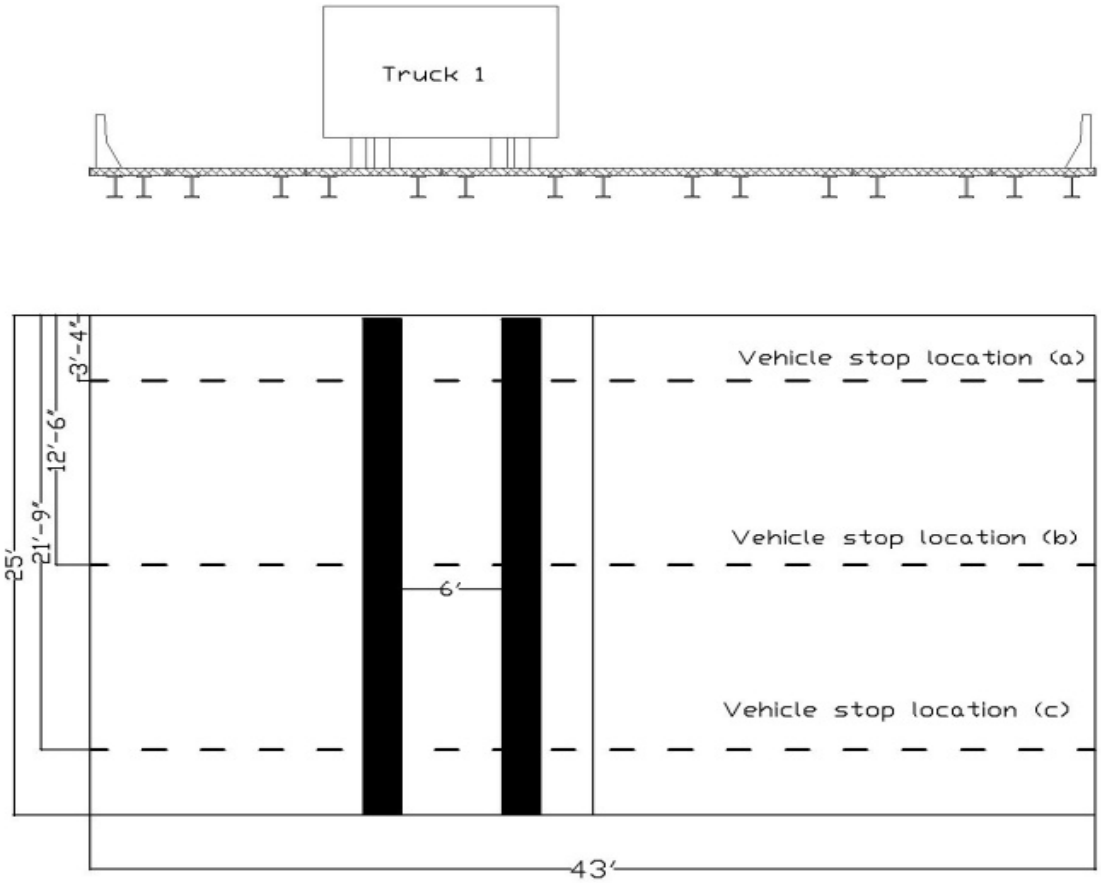

Figure 17
Static and dynamic truck loading path for north bound traffic lane

To facilitate easy identification of data collected for the same load case in different acquisition systems, a typical naming convention was developed and is detailed in Table 2. The traffic lane is identified as North and South bound using letters "N" and "S." Static stopping load case is identified as "SS" and static rolling is "SR." Each load pass is identified with numerals 1, 2, etc. Since the static stopping load case has three data collection points, these are named sequentially as a, b, c, etc. The numbers 30/55 after the dynamic load case name signify the speed of the truck adopted for that load case.

To acquire data from the live load tests, from all the sensors mentioned in the instrumentation plan, several acquisition systems were used. The following section briefly summarizes the acquisition systems used in this project.

Table 2
Test data file naming convention

Load case	Test name	
	North bound lane	South Bound lane
Static stopping – pass1	N_SS1_a, N_SS1_b, N_SS 1_c	S_SS1_a, S_SS1_b, S_SS 1_c
Static stopping – pass2	N_SS2_a, N_SS2_b, N_SS 2_c	S_SS2_a, S_SS2_b, S_SS 2_c
Static rolling – pass1	N_SR1	S_SR1
Static rolling – pass2	N_SR2	S_SR2
Dynamic – pass 1	N_D1_30/55	S_D1_30/55
Dynamic – pass 2	N_D2_30/55	S_D2_30/55

Data Acquisition Systems

FBG Interrogator

Strain measurements from the FBG sensors located at critical points on the girder and deck were collected using the si425 Optical Sensing Interrogator from Micron Optics, Inc. (Figure 18). The interrogator provides rapid, accurate measurements of hundreds of optical sensors in real time. This system can be controlled and monitored remotely through a complete set of Ethernet controls. The 16 channel (4 before extension) si425 optical sensing interrogator system allows for quick collection of strain and temperature information from FBG sensors.

Figure 18
si425 optical sensing interrogator

OTDR Acquisition System

The FTB-200 Compact Modular Platform (Figure 19) by EXFO is the acquisition system that measures optical backscatter as a function of linear position in an optical fiber. The fiber characteristics such as attenuation of the link, loss trends, and length of fiber are deduced from the backscattered light. Thus, this principle of the OTDR sensors aids in locating the existence of any debonding in the monitored interface.

Figure 19
EXFO FTB-200

BDI Structural Testing System II

Traditional strain gauges used in this project are manufactured by Bridge Diagnostics, Inc. The 16-channel Structural Testing System II (BDI-STS II) shown in Figure 20 is used in conjunction with the intelliducers/strain gauges to monitor strain profiles during live load tests.

Figure 20
STS II data acquisition system and intelliducer

Acoustic Emission DISP System

The eight channel AE Micro DiSP system (Figure 21) was used with the AE sensors installed on the deck to monitor the deck-girder bond integrity of the new bridge system. Acoustic events generated during loading of the bridge were collected by an array of resonant AE sensors.

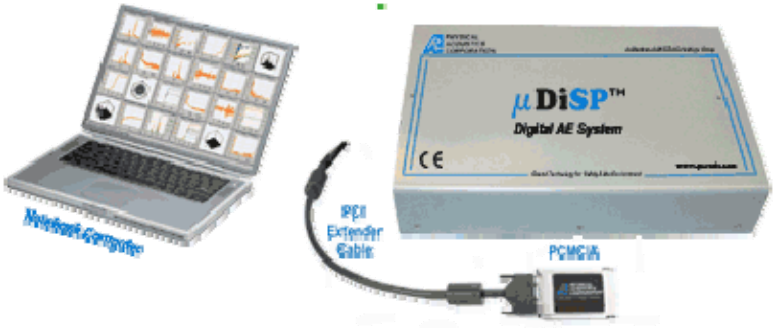

Figure 21
AE micro DiSP system

Gould Data Acquisition

The structures vibration frequency information was traced by mounting six accelerometers and collecting the data using Gould DAStarNet data acquisition system shown in Figure 22.

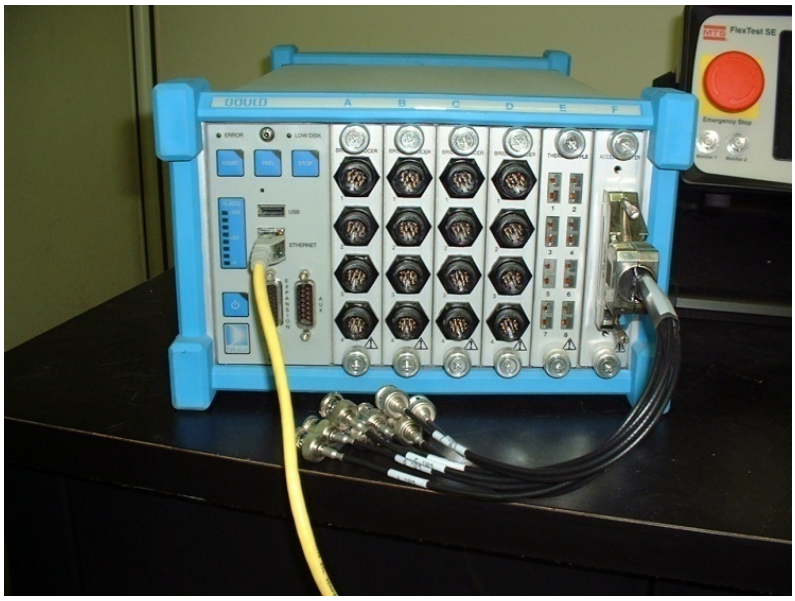

Figure 22
Gould data acquisition system

Data Analysis Scheme

The data collected from FBG Interrogators for each load case were in the form of wavelength shifts and were externally processed using MATLAB and Microsoft Excel to convert the values to meaningful strain/temperature data using appropriate calibration factors. The equation used to convert wavelength shifts in FBG strain and temperature gauges is represented as:

$$\frac{\Delta\lambda_b}{\lambda_b} = G_\varepsilon \Delta\varepsilon + G_T \Delta T \quad \textbf{(1)}$$

where,

G_ε is the strain gauge factor, $G_\varepsilon = 1.2 \times 10\text{-}^{6}\mu\varepsilon$

G_T is the temperature gauge factor, $G_T = 10 \times 10\text{-}^{6}/^{o}C$ *[9]*

Data from the BDI strain transducers did not need any external processing, as they directly provide the real time measured strain values. Post-processing of data to generate meaningful plots to better understand the structural performance under service loads is required for data acquired from all acquisition systems and are presented and discussed in detail in the next section.

DISCUSSION OF RESULTS

Field Data Analysis

Traditional Strain Data Analysis

The measured static live load strain changes in micro strain (με) at each of the 16 gauge locations were plotted versus time/position along the bridge for all load cases. Figure 23 is a sensor layout plan for all functional strain gauges installed on the central four panels of the bridge.

As stated earlier, for the static rolling tests, the trucks were driven at a crawling speed of 3-5 mph, while trucks attained speeds up to 55 mph for the dynamic load test case. The observations made from only the south bound-lane testing will be discussed in this section. Results generated for these gauges from all other load cases conducted are presented in Figures 44 and 45 of Appendix A. The general trends observed from plots in Figure 24 to Figure 25 are:

- Maximum strains of up to 350 με were observed from the gauges located on the deck for most static rolling load cases. Strain peaks were generally seen to decrease under dynamic test cases from sensors attached on the deck.

- The maximum recorded strains on the girders for all load cases fall in the range of 150-200 με. Differences were observed in strain readings at the same location from the top and bottom flanges of the girder implying the presence of composite action between the girder and deck.

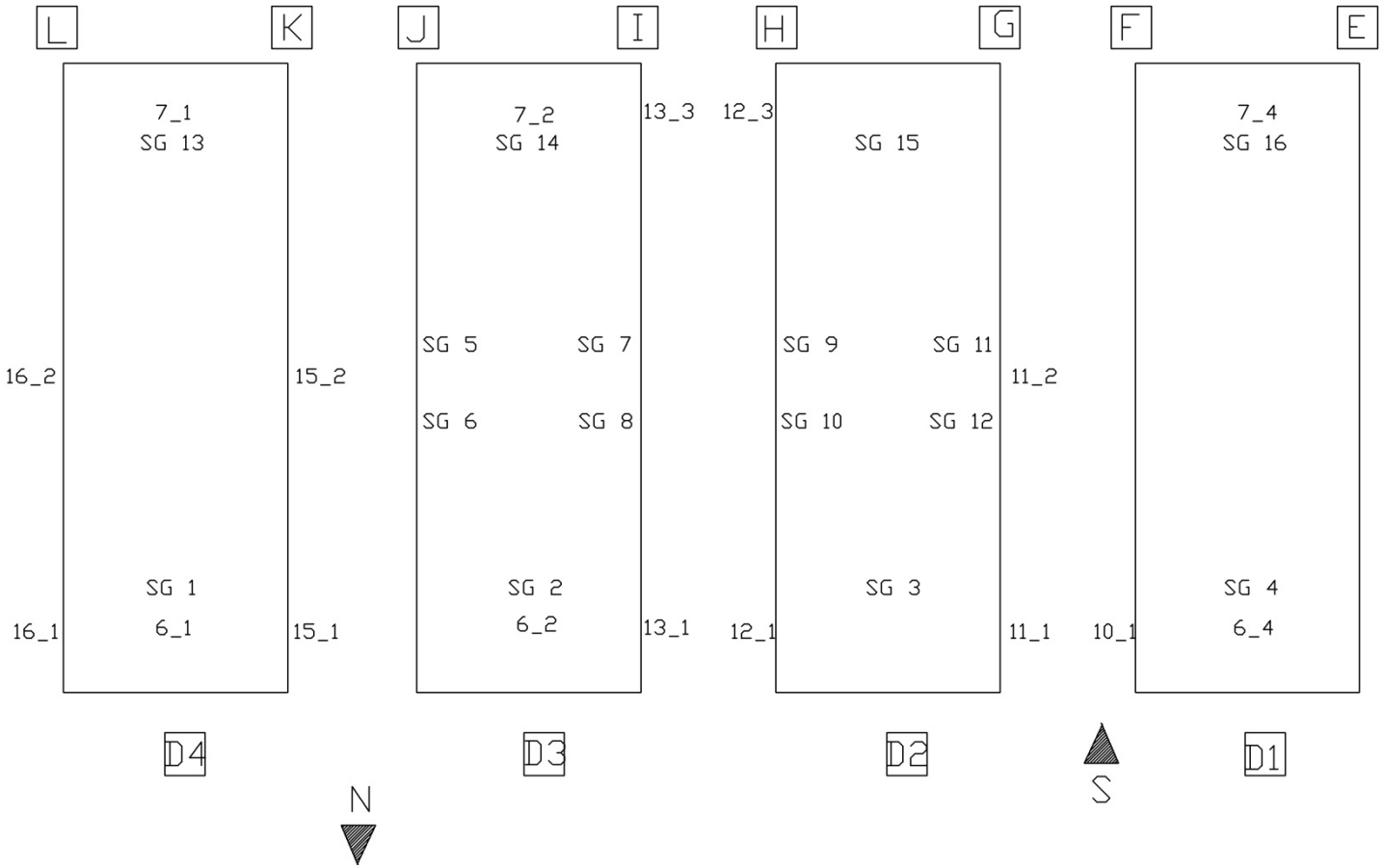

Figure 23
Plan view of all functional strain sensors attached to decks and girders during short-term test

E-L – Girders
D1 – D4 – Deck panels
SG: Traditional Strain Gauge
X-1, 2, 3, 4- FBG sensors

South Bound Lane — Static Load Case Strain Plots.

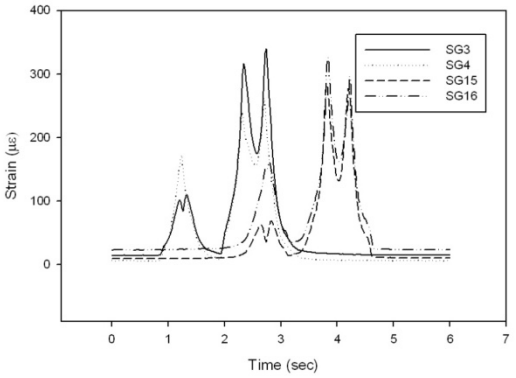

BDI Strain plot for load case S_SR1

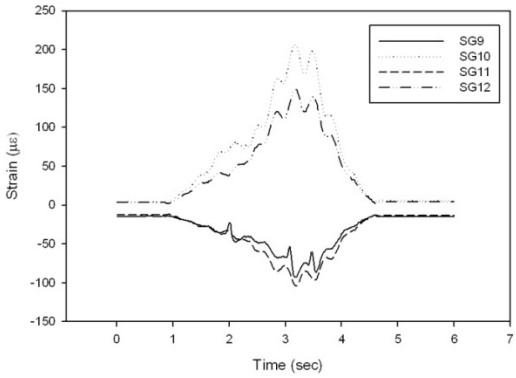

(a) (b) BDI Strain plot for load case S_SR1

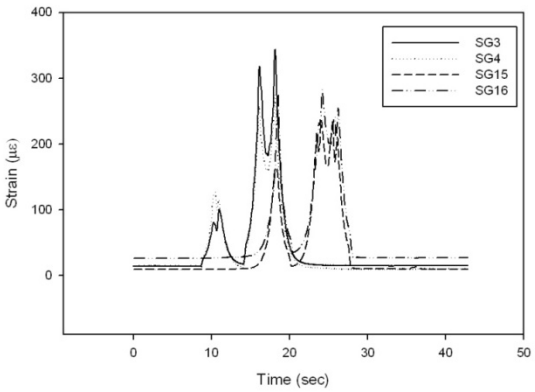

(c) BDI Strain plot for load case S_SR2

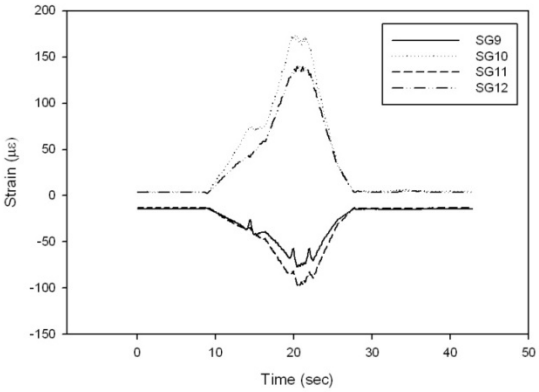

(d) BDI Strain plot for load case S_SR2

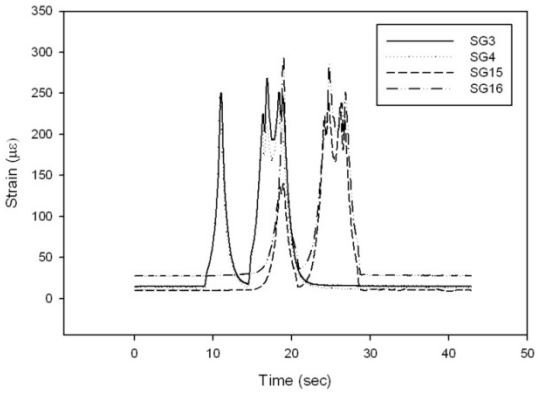

(e) BDI Strain plot for load case S_SR3

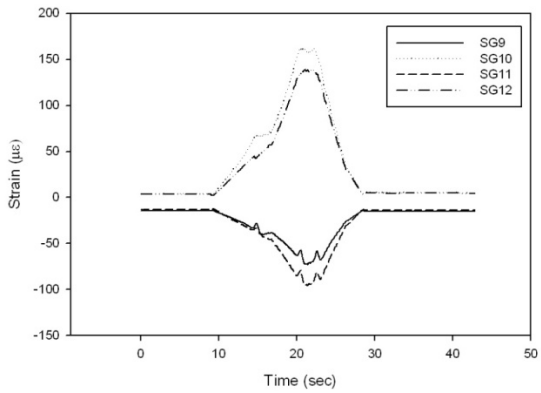

(f) BDI Strain plot for load case S_SR3

(1) Deck (2) Girder

Figure 24
Strain plots of sensors on deck panels (a, c, e) and girders (b, d, f) for all static rolling load cases

South Bound Lane — Dynamic Load Case Strain Plots.

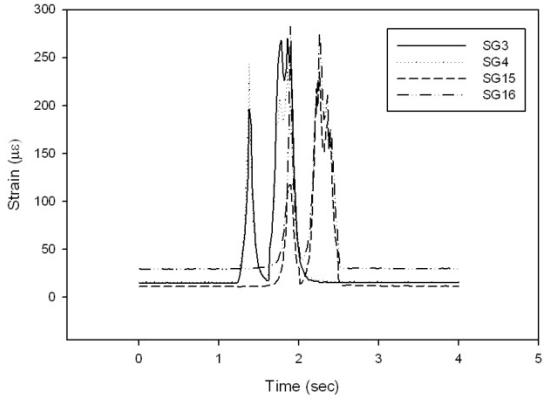

(a) BDI Strain plot for load case S_D1_30

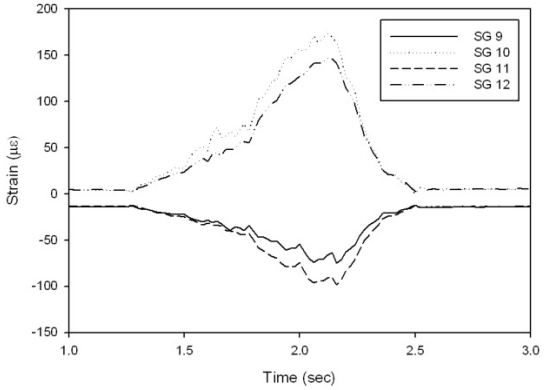

(b) BDI Strain plot for load case S_D1_30

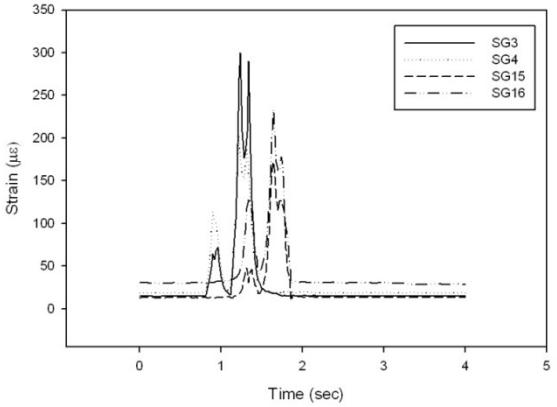

(c)BDI Strain plot for load case S_D2_30

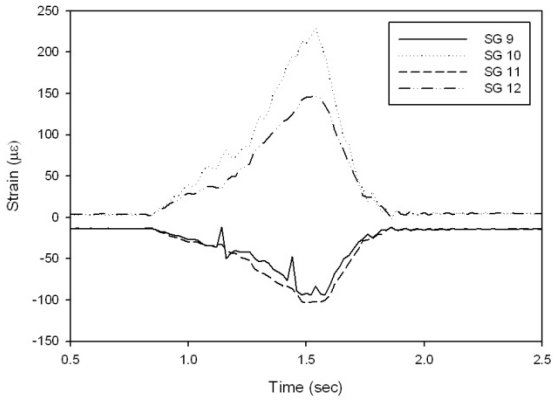

(d) BDI Strain plot for load case S_D2_30

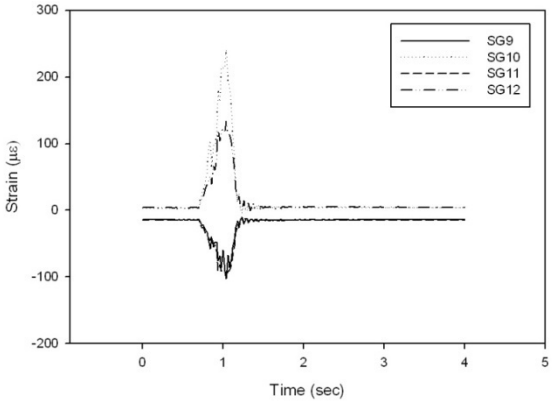

(e) BDI Strain plot for load case S_D1_55

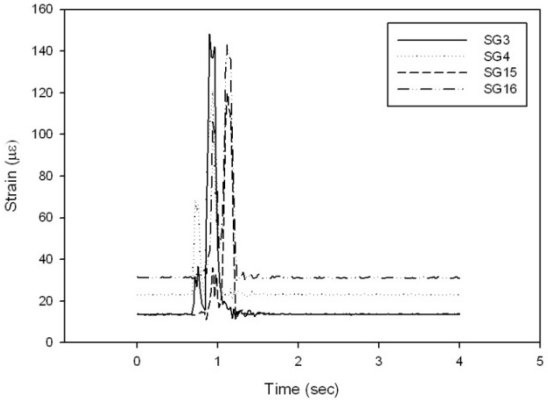

(f) BDI Strain plot for load case S_D1_55

(1) Deck (2) Girder

Figure 25
Strain plots of sensors on deck panels (a, c, e) and girders (b, d, f) for all dynamic load cases

FBG Strain Data Analysis

The strain plots for decks and girders are separately presented here. Again, only south bound lane results are discussed in this section shown in Figure 26. Plots generated for these gauges from all other load cases are shown in Figures 46 and 47 of Appendix A. While collecting the FBG data, some sensors malfunctioned during testing, thus their results are omitted from the discussion. Although maximum girder strains range from 150-200 με and strain profile indicates load sensitivity, they do not match up exactly with strain readings from the traditional gauge. This could be attributed to the lack of direct adhesion of the gauges on the structural surface and thus influence of sensor backing material behavior.

South Bound Lane — Girder Strain Plots.

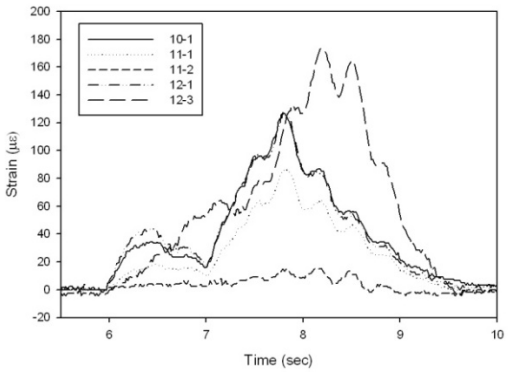

(a) FBG Strain plot for load case S_SR1

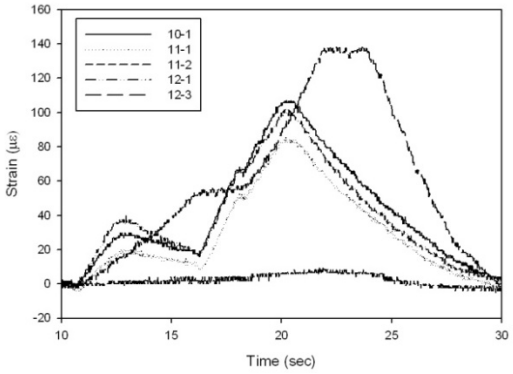

(b) FBG Strain plot for load case S_SR2

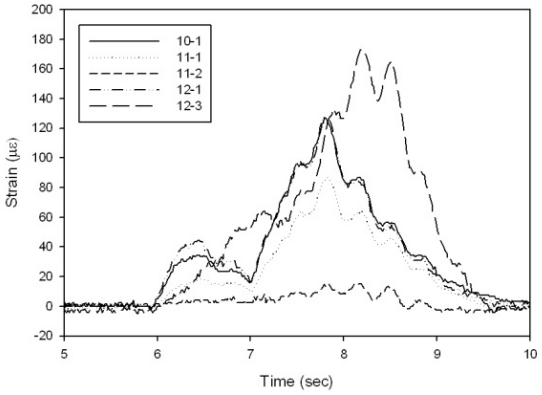

(c) FBG Strain plot for load case S_D1_30

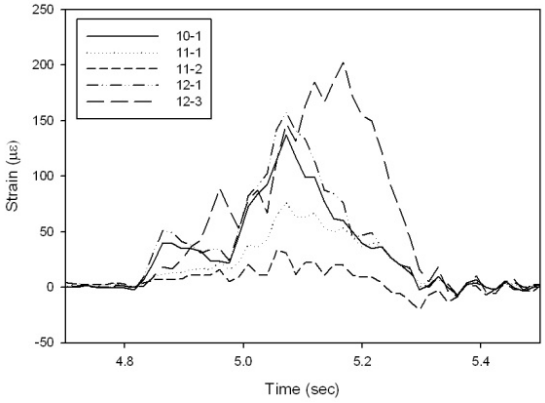

(d) FBG Strain plot for load case S_D2_30

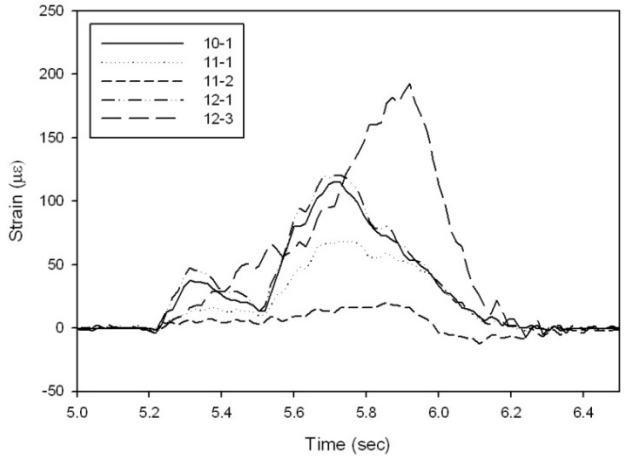

(e) FBG Strain plot for load case S_D1_55

Figure 26
Strain plots of girder sensors for all load cases

South Bound Lane — Deck Strain Plots. Only one sensor attached to the deck was functional for the static rolling load cases, thus the plot represents the strains from one sensor for both load cases. All other plots (Figure 27) are strain plots for each load case from the two sensors on the deck in the south-bound lane. Compared to the traditional strain gauge records, the data peaks collected from the FBG sensors for similar load cases seem to show a 25 percent decrease on average.

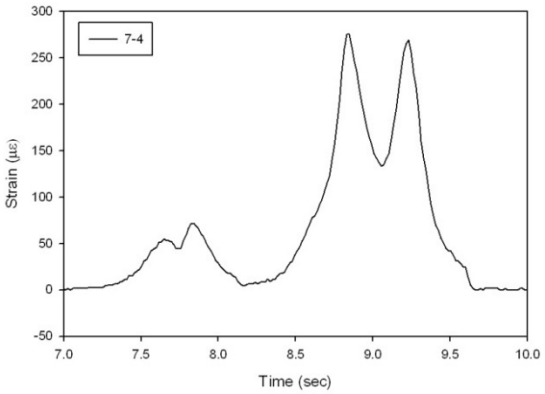

(a) FBG Strain plot for load case S_SR1

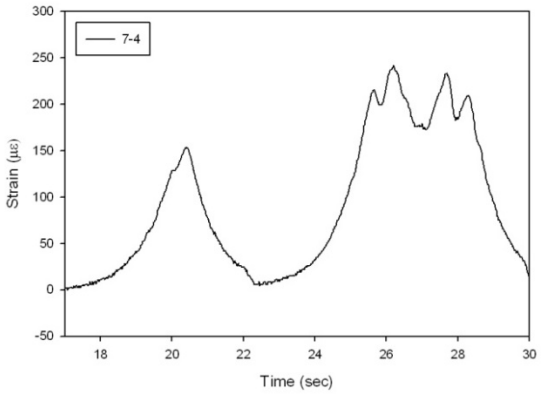

(b) FBG Strain plot for load case S_SR2

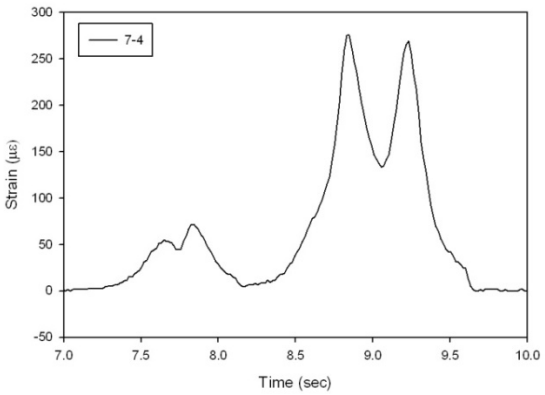

(c) FBG Strain plot for load case S_D1_30

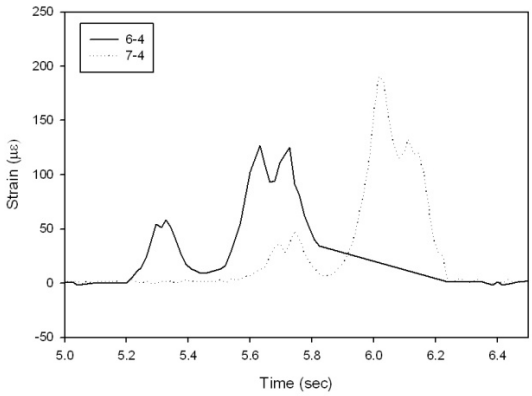

(d) FBG Strain plot for load case S_D2_30

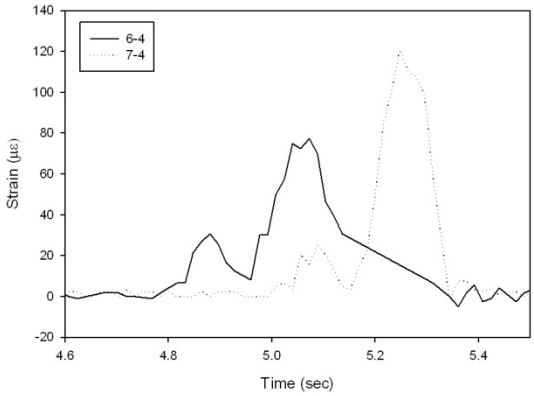

(e) FBG Strain plot for load case S_D1_55

Figure 27
Strain plots of deck panel sensors for all load cases

AE Data Analysis

Each composite deck of this bridge was glued using epoxy to a pair of steel girders. Although this unique configuration speeds up construction, the visual inspection at the deck-girder interface was not possible. Thus to assess the behavior of the structural components under service loads, AE sensors were used. Here, results of AE monitoring at the composite deck are discussed. AE parameters were recorded at a 45dB threshold using an AE 8-channel DiSP system. All eight sensors used in this test were R15I, with a resonant frequency of 150 kHz and 40 dB integral amplifier.

The AE sensors were attached along the centerline of each deck with four sensors placed at 6-ft. (1.828-m) intervals on each deck (Figure 28). The sensors were arranged so for each lane that was tested a set of four sensors will correspond to the travel of the left-side wheels of the truck as detailed in Figure 29.

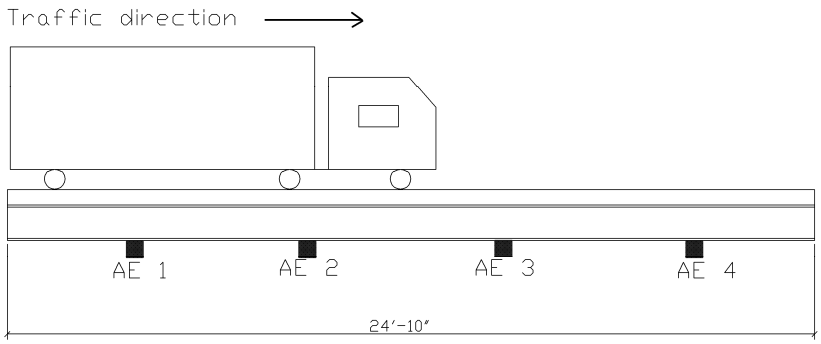

Figure 28
Cross sectional view of AE sensor placement on deck panel with truck load direction

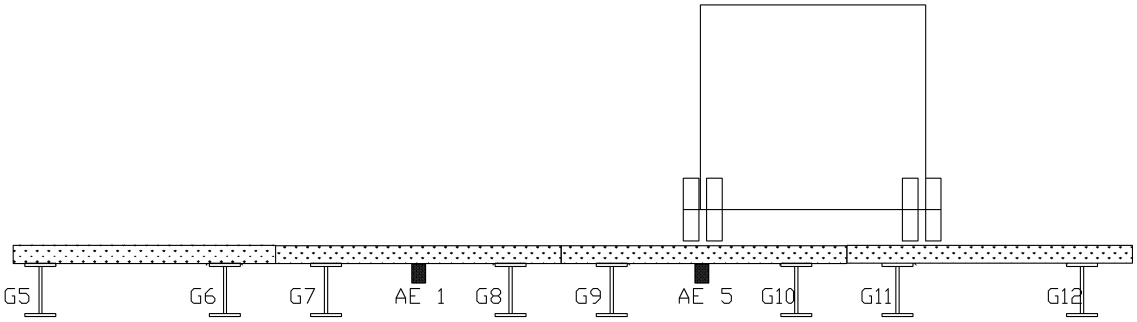

Figure 29
Transverse sectional view of bridge with truck load and AE sensor position detail

The results discussed here are for AE data collected when the south-bound lane was tested. When the vehicles moved at a crawling speed of 3-5 mph, the cumulative AE hits collected by each sensor along the tested lane is shown in Figure 30. It was observed that the most active channel was channel 6 located close to the midspan of the bridge. The same sensors were observed to collect a significantly lower number of AE hits when the static loading case was repeated, implying the structure's stability under the same load. The AE activity was comparatively higher when the truck entered the bridge than when it exited, indicating an impact load induced activity at entry end of the bridge.

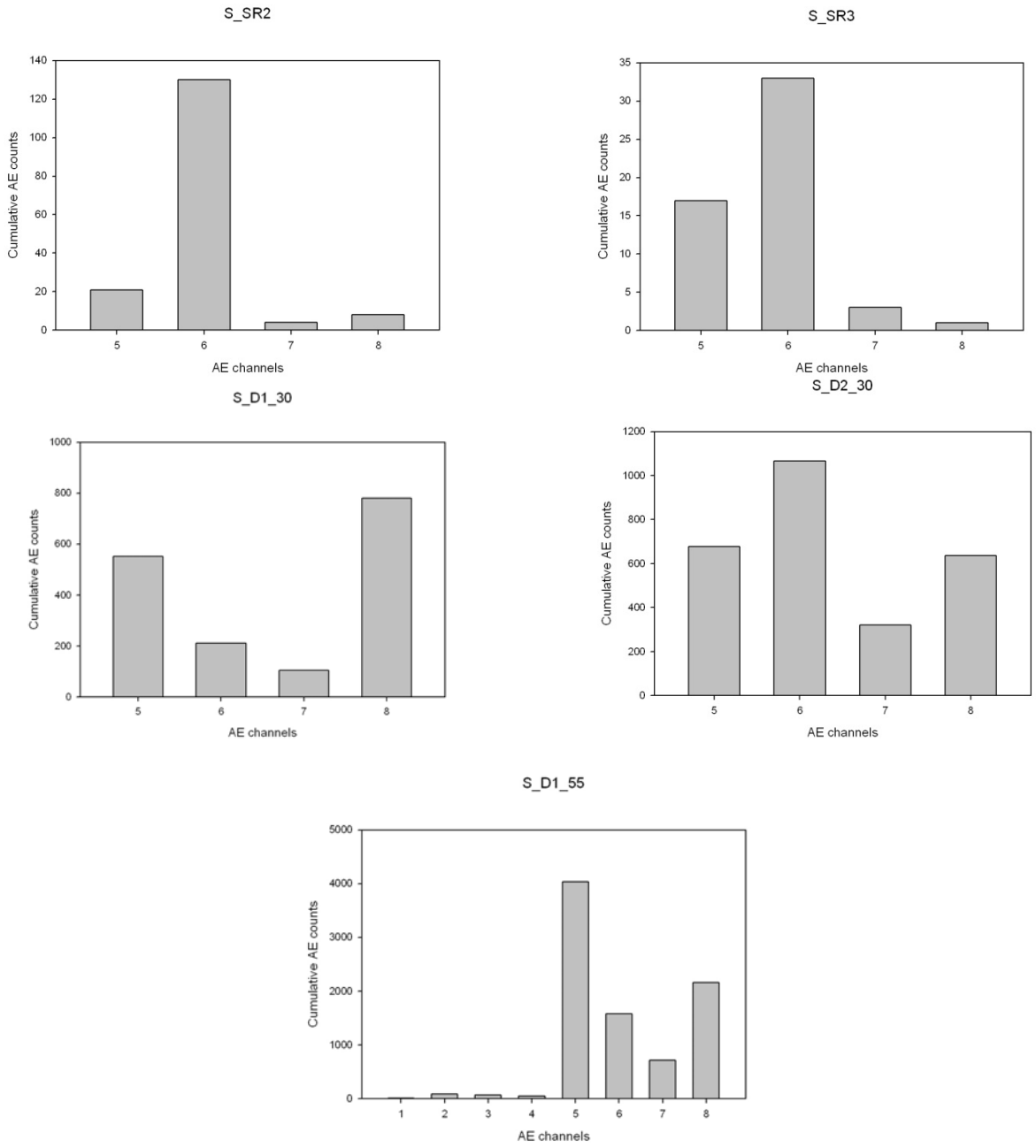

Figure 30
Cumulative AE hits observed by active channels for all live load test cases in south bound lane

Clear trends are not visible in the total AE hits collected from repeated load cases, when the test truck travelled at a speed of 30 mph. Yet, a much larger proportion (85 percent more) of AE hits was generated when compared to the static load case. All AE sensors attached to the deck exhibited activity only when the test truck drove through the south bound lane at a speed of 55 mph. Higher AE activity was definitely picked up by the sensors located under

the tested traffic lane with higher activity at the ends of the bridge, indicating impact loading at the entrance and exit of the monitored span.

To ensure genuity of the AE data collected, the AE signal strength parameter was also assessed and represented in Figure 31 for the same load cases previously mentioned. As is clear from Figure 31, the trends observed are similar to the AE counts distribution discussed in the previous section. The general trend is for signal strengths in all load cases to lie below 105 pVs. Additional AE plots with similar trends have been generated for the north-bound lane as well and can be found in Figures 48 and 49 of Appendix A.

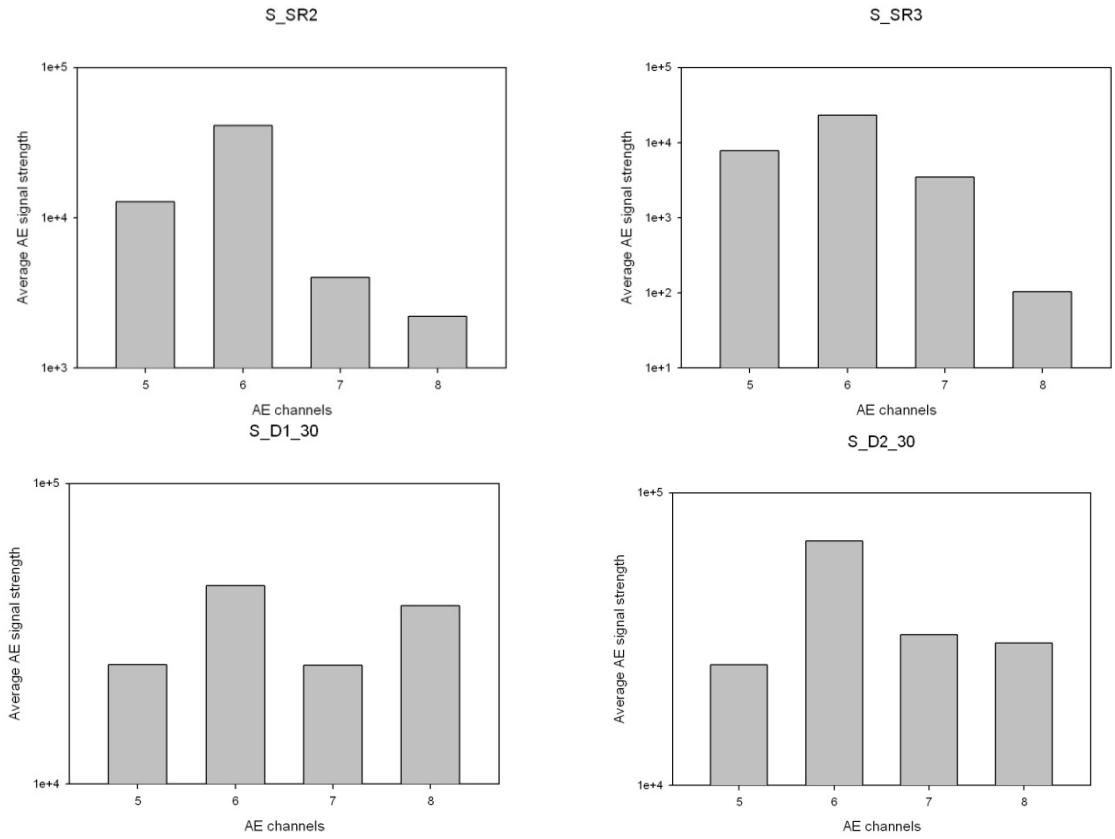

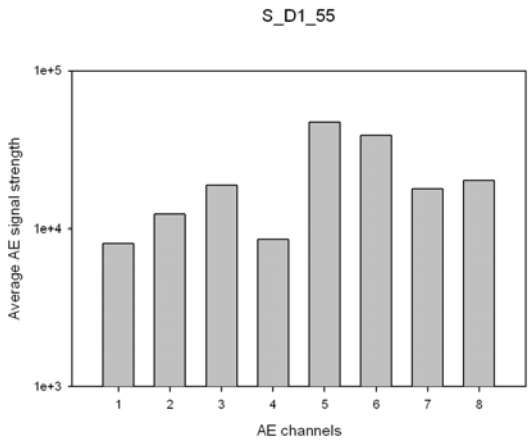

Figure 31
Average AE signal strengths observed by active channels for all live load test cases in south bound lane

Although the source of AE hits generated during this test cannot be individually identified, a baseline AE data activity trend has been collected. Any changes to this activity trend in future testing can reveal the possible changes in the monitored bridge component behavior over time.

Accelerometer Data Analysis

In Figures 32 and 33, the acceleration information obtained from dynamic load test cases for both lanes tested is plotted. Gauges A2 and A5 were located on the midspan of the deck while all other sensors were on the bottom flange girder midspan as seen in Figure 12 earlier. The slightly decreased acceleration recorded by the accelerometers A2 and A5 may be indicative of the existence of partial composite action between deck and girder.

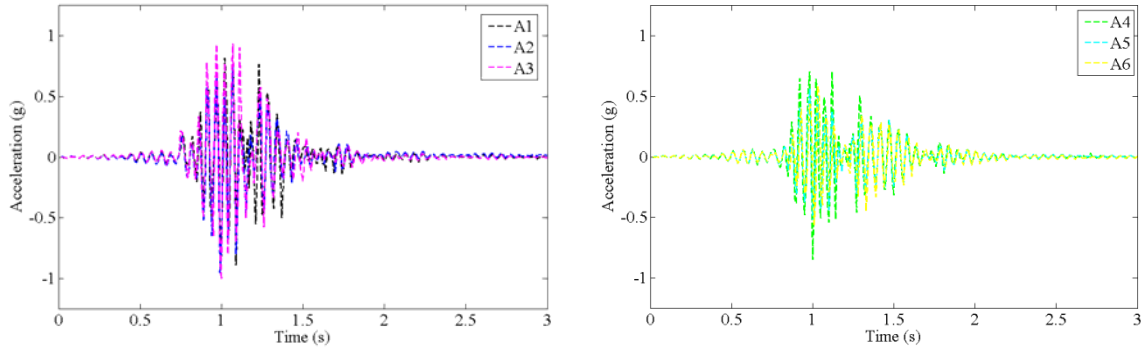

Figure 32
Acceleration from sensors A1-A6 for S_D1_55 load case (south bound)

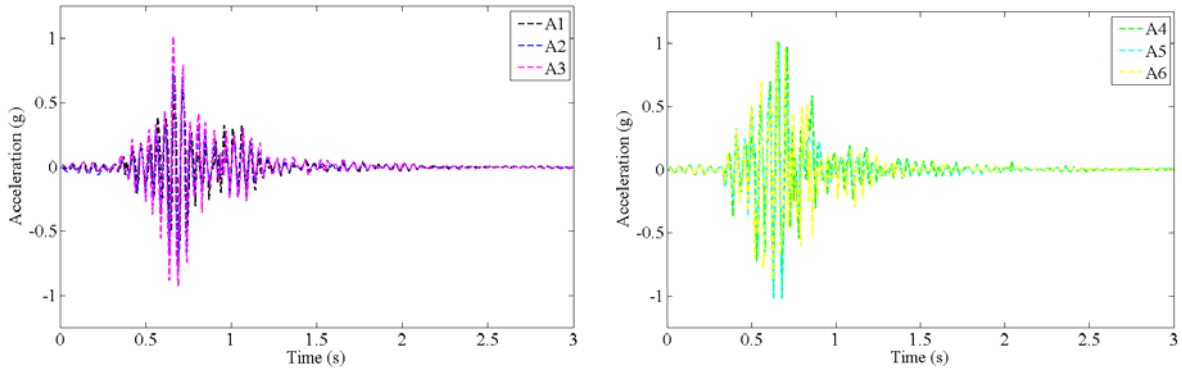

Figure 33
Acceleration from sensors A1-A6 for N_D1_55 load case (north bound)

Strain Data Comparison

The data from functional traditional strain gauges (BDI) and FBG strain sensors in the same location were compared to verify the FBG sensor performance during live load tests and their long-term monitoring capability. A direct comparison with each individual sensor located on the deck and girder of the bridge structure is graphically represented in Figure 34. Figures 34(a) and (b) show deck strain comparisons from the south bound lane and Figures 34(c) to (f) show strain comparison of gauges located on deck and girder of the north bound lane.

From the trends observed in Figures 34(a) and (b), it can be seen that although the live load response of the FBG sensors under the same loading conditions in the south bound lane is similar, their absolute values are considerably lower in comparison with readings obtained from the traditional gauges. No coincident gauge information was available at the girders along this lane. While observing Figures 34(c) to (f) that come from the sensors located on the north bound lane, the FBG strains seem to mostly match or slightly overestimate the strains recorded by the traditional strain gauges.

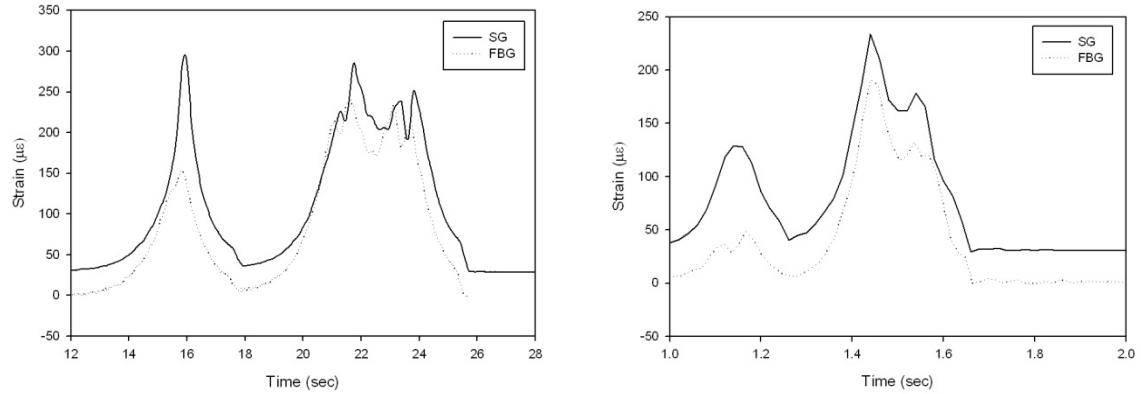

(a) Deck 1 (north end) for load case S_SR3 (b) Deck 1 (north end) for load case S_D2_30

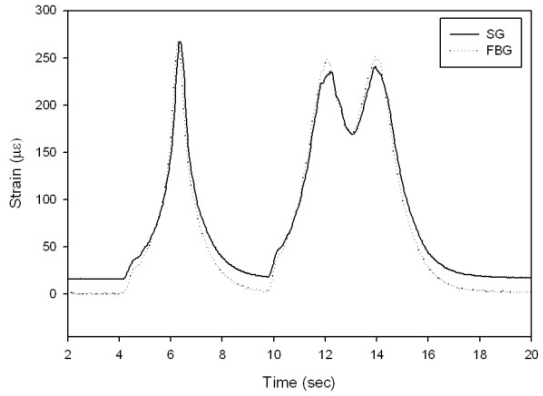

(c) Deck 3 (north end) for load case N_SR1

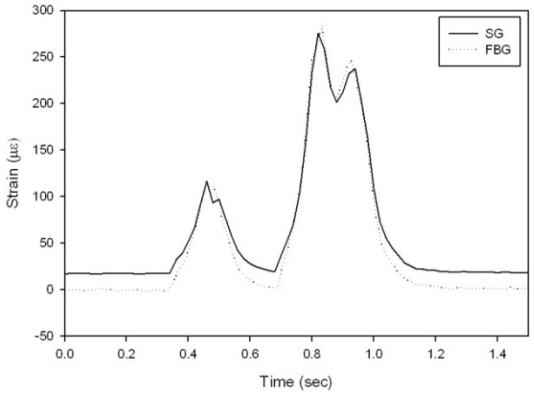

(d) Deck 3 (north end) for load case N_D1_30

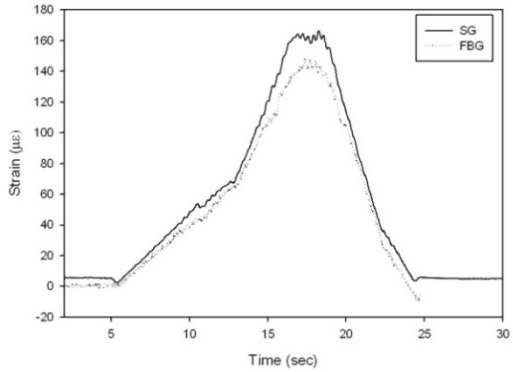

(e) Girder for load case N_SR2

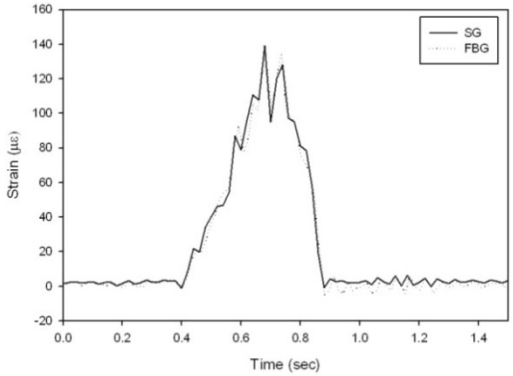

(f) Girder for load case N_D1_55

Figure 34
SG and FBG strain comparison for deck and girder of both lanes

Finite Element Analysis

The slight discrepancies in the strain data collected from FBG and BDI strain transducers required the analytical modeling of the bridge structure to better understand the strain values that actually reflects the structural behavior of the monitored bridge. A finite element model (FEM) was developed for one lane of the tested bridge in Ansys for both fully composite and non-composite conditions. After an initial comparison of the fully composite model [Figure 36(a)] strain values with field data, it was observed that although the girder strains were close, the deck strains were considerably lower than the live load test data. Thus, the non-composite model was generated to inspect if improvements could be achieved in the deck strain values. The measured strains from the static stopping test case were compared to strains calculated from the FE model under comparable loading conditions.

In this model, the components of the bridge were modeled using shell elements. The slab was modeled using eight-node Shell 99 elements that have six degrees of freedom at each node. Beams and diaphragms were modeled using the four-node Shell 63 elements that also have six degrees of freedom. The isometric view of the composite model of the bridge is shown in Figure 35. For the non-composite representation, the deck and girder were separated by a 1 in. (0.0254 m) gap and coupled along the centerline nodes of the girder to the corresponding nodes on the deck [Figure 36(b)].The global coordinate system adopted for this model was with the x axis taken along the transverse direction of the bridge, the y axis along the depth, and the z axis along the length of the bridge. At all the simply supported ends, the moments are released at the end nodes at the location of the supports. Boundary conditions (BC) and material properties used for the bridge model are summarized in Table 3.

Table 3
FEM model input details

Property	Details
Geometry	2-D a) two 3 layer composite deck 70 in. X 300 in. X 0.635 in. b) Four steel girders @ 4 ft. spacing
Material property *Composite deck* a)GFRP layer b)Balsa wood *Girder* Steel	**Ex** **Ey** **Gxy** **μ** (msi) (msi) (msi) 3.12 3.32 1.12 0.25 0.018 0.836 0.04 0.02 29 0.3
Boundary Conditions DOF at z = 0 in. DOF at z = 300 in. DOF at diaphragm ends	 UY =0; UZ = 0 UY = 0; UX = 0 UX = 0; UZ = 0

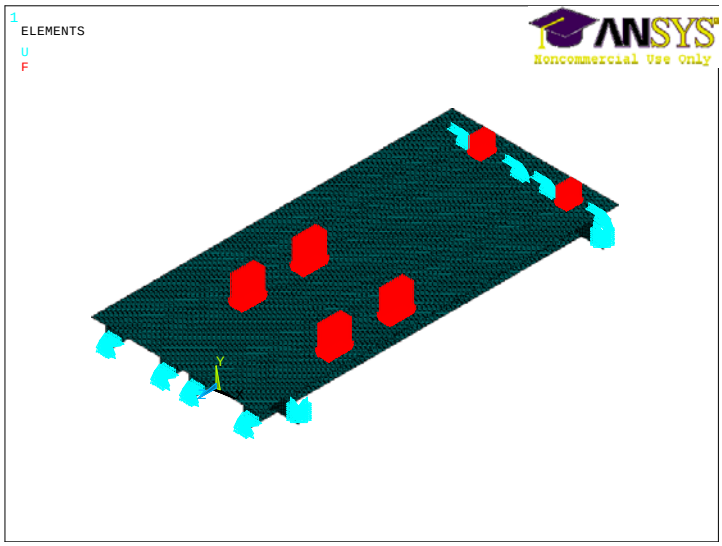

Figure 35
Isometric view of composite bridge

(a) (b)

Figure 36
Composite and non-composite joint detail in FEM model

Loading Data

In this study, the truck loading used in the model was of the actual truck used during live load testing. The truck modeled here consisted of 3 axles with both the wheels of each axle carrying the same load (see Figure 15). The weight of the first axle was 12 kips and the other two axles weighed 20.35 kips each. The spacing between the first axle and the second axle was 12 ft. (3.657 m), and the spacing between the second axle and the third axle was 4 ft. (1.219 m). The truck was 6 ft. (1.828 m) wide.

The truck loads were intended to generate maximum straining action at locations coincident with sensor location in the bridge by placing the middle axle of the truck at these predetermined locations except for the first loading position as discussed earlier. Each axle wheel load was applied as nodal loads in a uniform area of 20 in. X 10 in. (0.5 m X 0.254 m) patch, representing tire pressure. The FE results reported here are only from static stopping load cases.

Results Discussion

To make a close comparison with the field strain data, the strain data from the FE model was collected from nodes that were located approximately at the same location as the field measurement points. Since strain data comparisons includes data collected from both the deck and girder the FE strain results were correspondingly collected in both the transverse direction (x) and longitudinal direction (z).

Composite Model Results

The strains predicted by the FE model and the data collected in the field revealed generally similar behavior in the girders, but there were some noticeable differences in values obtained for the deck. Essentially three load positions were considered for modeling:

Load case (a) Loading vehicle with end axle centered along one-eighth span (S_SS1_a)

Load case (b) Loading vehicle with mid axle centered along mid span and (S_SS1_b)

Load case (c) Loading vehicle with mid axle centered along seven-eighth span. (S_SS1_c)

Generally the measured and FEM strains were observed to be the largest on the members right under the load. Strain values predicted for all girders were almost always higher than the measured value by 10-15 percent in this model as will be further discussed in Table 4. The strains predicted on members away from the load were relatively small in the model, thus not comparable with field measured values at those locations. The lesser strain values predicted by the model along the x-direction (deck) led to the need to construct another model where the deck and girder act as non-composite sections as discussed earlier. Figures 37-39 represent the strain contour plots obtained for all load cases considered.

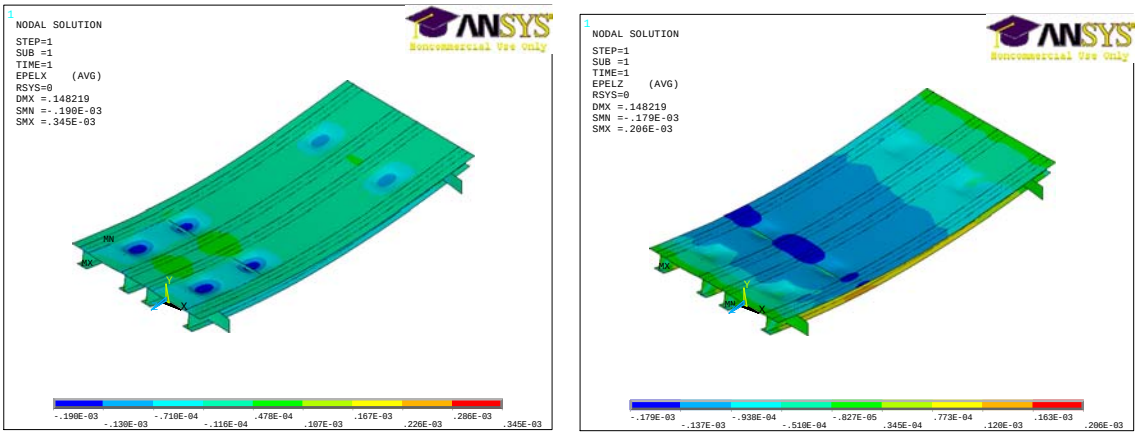

(a) (b)

Figure 37
Strain contour plots for S_SS1_a (a) along x direction (b) along z direction

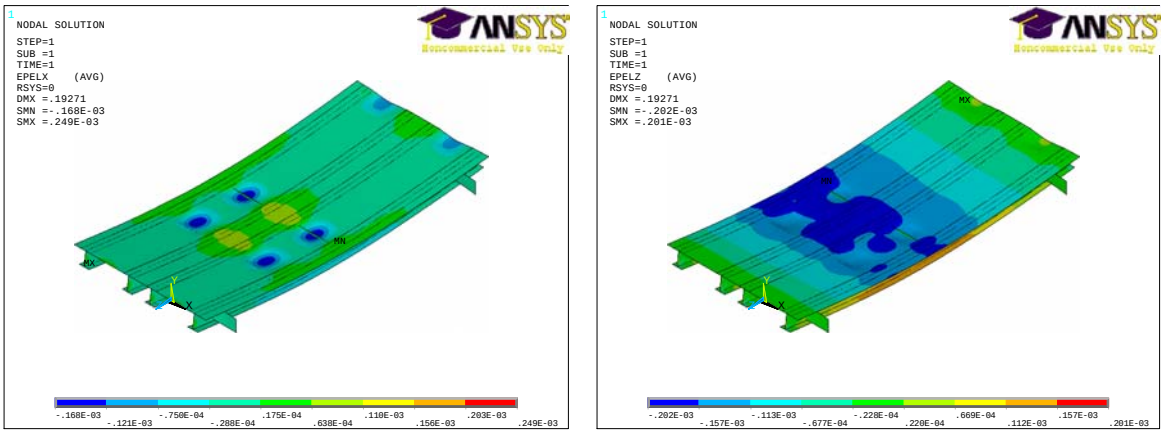

(a) (b)

Figure 38
Strain contour plots for S_SS1_b (a) along x direction (b) along z direction

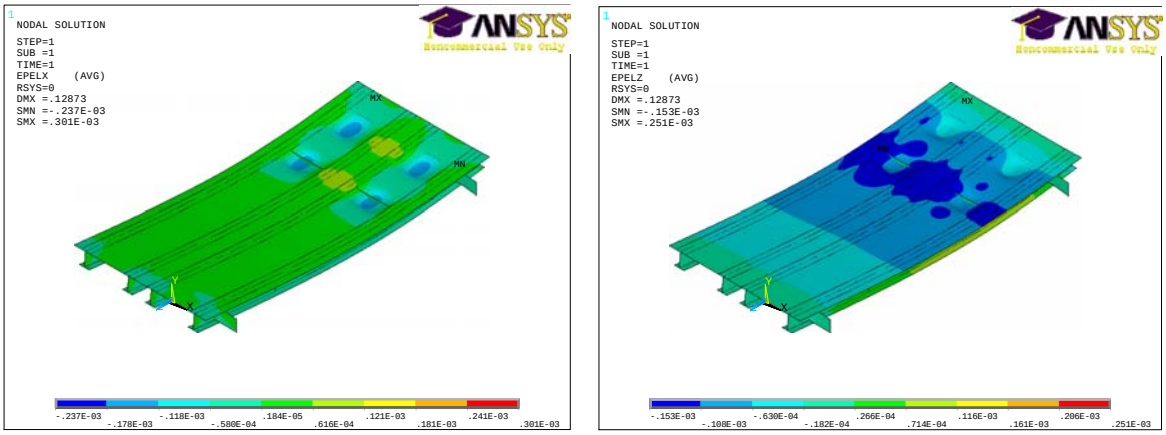

(a) (b)

Figure 39
Strain contour plots for S_SS1_c (a) along x direction (b) along z direction

Non-Composite Model Results

Although comparatively higher strains were observed at the deck from this model than from the composite one, the measured strain values were still higher than the FE estimate. One of the possible explanations for this trend could be that the actual slab is not as stiff as predicted by the FE model. It is noted that the deck consists of balsa wood, high strength wires, and multi-layered FRP materials, which makes the accurate modeling of the deck system very difficult. A direct comparison of all strain values collected from BDI strain gauges and FE models is summarized in Table 4. Figures 40-42 represent the strain contour plots obtained for all load cases considered.

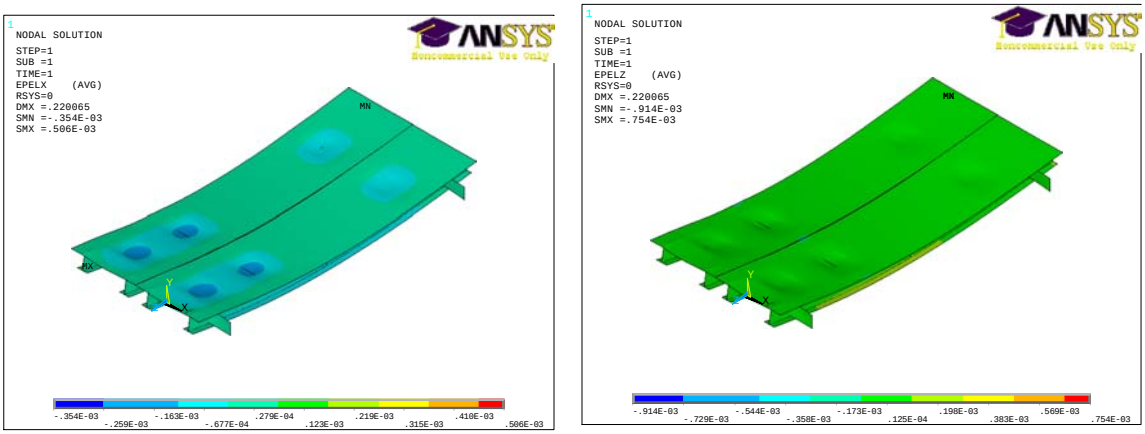

(a) (b)

Figure 40
Strain contour plots for S_SS1_a (a) along x direction (b) along z direction

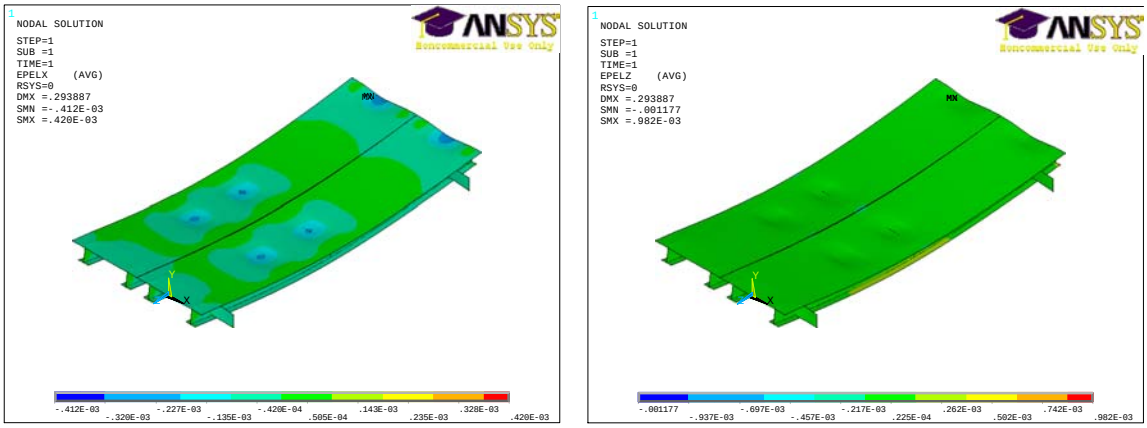

(a) (b)

Figure 41
Strain contour plots for S_SS1_b (a) along x direction (b) along z direction

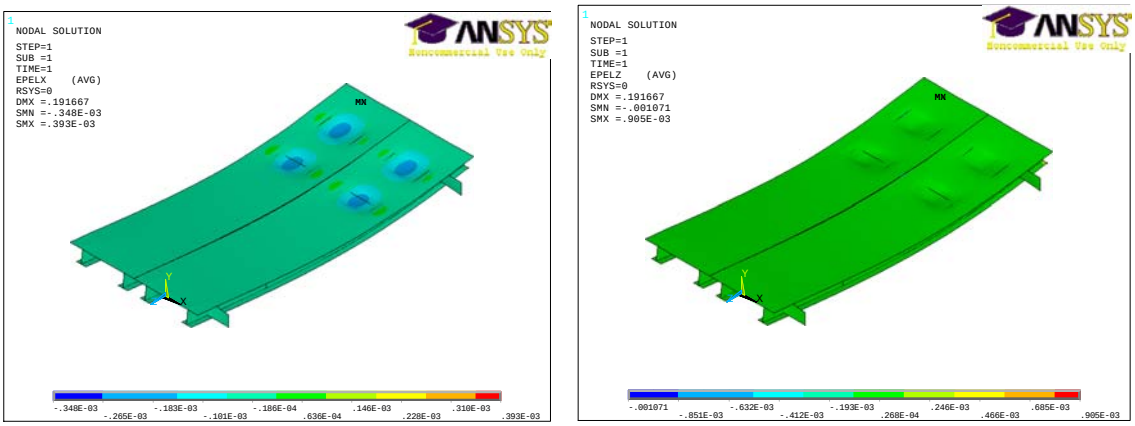

(a) (b)

Figure 42
Strain contour plots for S_SS1_c (a) along x direction (b) along z direction

Table 4
Strain comparisons

	Girder				Deck			
	SG9	SG 10	SG11	SG 12	SG3	SG4	SG15	SG16
S_SS1_a	G1_Top	G1_Bott	G2_Top	G2_Bott	D_1(S)	D_2(S)	D_1(N)	D_2(N)
BDI	-42.45	101.55	-57.5	86.1	241.5	223.5	131.5	91.1
FEM (C)*	-52.2	123.44	-51.36	120.36	172.19	168.92	38.8	31.2
FEM(N_C)**	-144.47	144.5	-125.97	127.6	198.75	201.58	45	43.5
S_SS1_b								
BDI	-55.5	164.5	-76.7	134	50.5	34.65	30.4	47.3
FEM (C)	-91.07	179.6	-66.01	176.55	6.4	7.96	27.8	22.4
FEM N_C)	-227.7	224.87	-185.73	194.16	7.242	7.72	34.5	41.1
S_SS1_c								
BDI	-41.3	83.6	-53.2	69.65	18.25	2.9725	216.5	263.5
FEM (C)	-48.7	96.45	-39.64	93.21	1.78	2.34	163.58	168.5
FEM(N_C)	-118.6	118.6	-104.35	104.6	1.995	2.33	202.12	200.9

Notes: FEM (C) – results from the composite model
FEM (N_C) – results from the non-composite model

Allowable Live Load Strain

The maximum dead load stress at the mid-span from the finite element model is estimated to be 0.914 ksi. Assuming that the allowable stress = 55 percent of ultimate strength = 19.8 ksi and Impact factor = 0.3, then the allowable strain for live load is estimated as (19.8-0.914) / (1.3*29000) = 500 με; that is higher than the strain readings from both short-term live load tests and long-term monitoring.

Benefit Cost Analysis

Costs for deck materials and installation for the purpose of comparison between the grid metal deck and composite deck were collected and are displayed in Table 5 and Figure 43. (Information below was obtained from the deck manufacturer)

Table 5
Different costs for grid metal deck and composite deck ($/FT²)

Deck Type	Cost of Materials	Cost of Installation	Total Cost
Grid-Metal	55.00	40.41	95.00
Composite	109.00	13.65	123.00

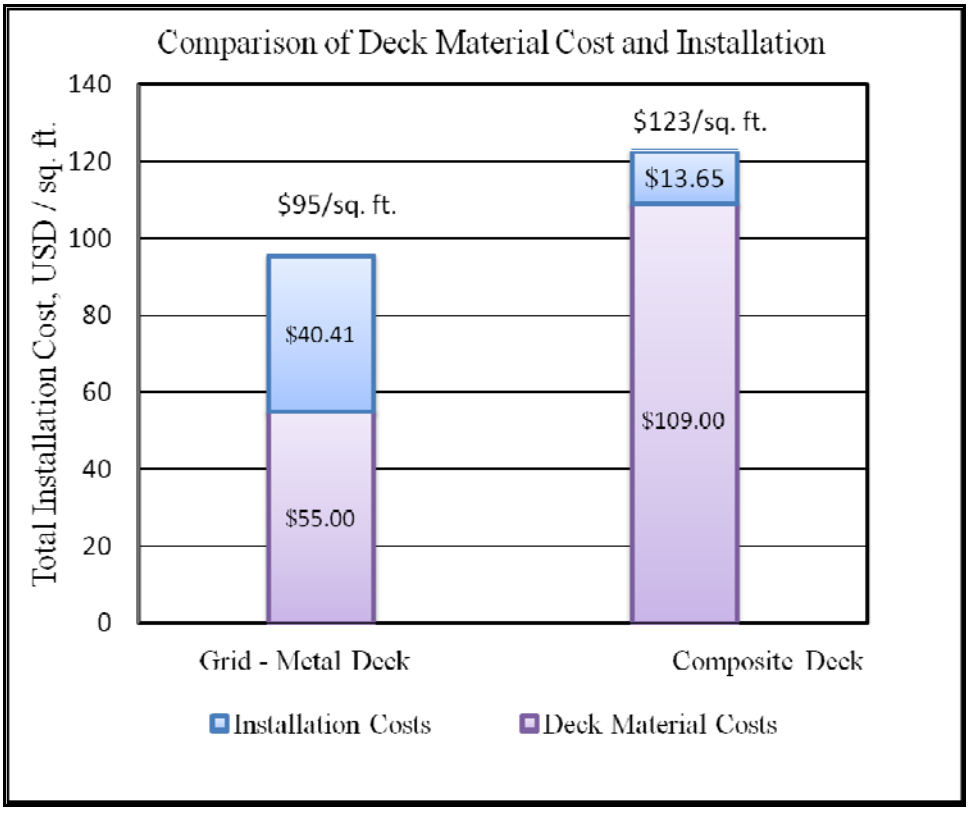

Figure 43
Comparison of deck material cost and installation

The cost per sq. ft. for purchasing the grid metal deck and the composite deck was $55 and $109, respectively, while the cost of installation of the grid metal deck and the composite deck was $40.41 and $13.65, respectively. The total cost for purchasing and installing the grid metal deck and the composite deck was about $95 and $123, respectively. The following observations can be made:

- Though the cost of purchasing the metal deck is half that of the composite deck, the composite deck lasts longer since it is corrosion resistant whereas the metal decks corrode, causing safety issues to the traveling public.

- The cost of installing composite decks is one-third the cost of installing grid metal decks. The grid metal deck requires hundreds of welds to the supporting girders, whereas the composite deck can be glued to the supporting girders with a fast curing compound, thus cutting the time of installation to one-third of that of the grid metal deck.

- The speed of installing composite decks compared to metal grid deck will be realized in cost savings by minimizing traffic control and bridge down-time.

- The low maintenance of the composite deck makes it a more desirable product than the metal grid deck.

- The long-term durability of the composite deck makes it a more desirable product than the metal grid deck.

- The weight per square foot of the composite deck prior to application of an epoxy/Arkansas Flint Rock non-skid overlay is 19 lbs., well within the specified range of grid-metal deck.

CONCLUSIONS

A pilot demonstration project of a FRP-wrapped balsa wood bridge deck system was developed and has been installed in Louisiana. This bridge deck project is the first bridge replacement project in the world that is made of balsawood, hardwire, FRP material, as well as nanotube particles in the resin. Extensive monitoring strategies are implemented to evaluate both the short- and long-term performance of this bridge using conventional gauges along with new generation fiber optic sensors. The small size, light weight, and passive monitoring capabilities of fiber optic sensors make them an optimal choice in continuous long-term applications such as in this bridge.

After installation, a live load test scheme was conducted to study the initial performance of the new bridge system. The analysis of the data collected from various gauges used during this test led researchers to arrive at these preliminary conclusions:

- The maximum tensile strain measured at both deck and girder members remained well below the original design limit, thus assuring the structural integrity of the new deck girder system.
- The strain data collected from both BDI and FBG strain gauges enabled neutral axis estimation and revealed that partial-composite action was pertinent between the epoxy glued FRP deck and steel girder.
- Although the tensile strain profiles of the steel girders from field data were similar to those from the finite-element analysis of the composite model of the bridge superstructure, only a non-composite model could generate strain profiles similar to those collected from the deck. Uncertainties in the overall material property estimations used as inputs in the FEM model may have influenced the discrepancies visible in field and analytical data comparisons.
- The acoustic sensors used during this load test helped to establish a baseline AE data trend to assess the integrity of the glued FRP bridge deck — steel girder bond. Any change in this trend in a future test can help to reveal any discontinuities in this bond line over time.
- The existence of partial composite action between the superstructure components was also ascertained from the accelerometer readings.
- The similarities obtained by comparing strain profiles gathered at the same locations by both BDI and FBG sensors allowed for the continued use of the permanently installed FBG sensors on the bridge for long-term bridge performance monitoring.

RECOMMENDATIONS

Despite the fabrication issue encountered in one of the six panels, this project has demonstrated the practical potentials of both FRP-wrapped balsawood decks as viable counterparts of conventional deck grating and concrete decks.

Based on the initial and ending results obtained from this research program, the following recommendations are made:

- LA DOTD should not implement this product until the delamination problem has been addressed and resolved.
- Since this bridge involves the use of relatively new materials and component assemblies, it is essential to engage in long-term monitoring strategies to fully understand its structural performance under traffic loads. The data acquired in the first phase of monitoring involving several types of sensors helped to setup a baseline activity for the new bridge immediately after construction.
- Should the new product be installed, periodic visual inspection of the bridge along with data acquisition from the permanently installed gauges should be carried out.

ACRONYMS, ABBREVIATIONS & SYMBOLS

μ	Poisson's ratio
με	micro strain
A	Accelerometers
AASHTO	American Association of State Highway and Transportation Officials
ADT	average daily traffic, vehicles/day
AE	Acoustic Emission
ASD	Allowable Stress Design
BC	Boundary Condition
BDI	Bridge Diagnostics Incorporation
cm	centimeter(s)
dB	decibels
DOF	degree of freedom
Ex	Elastic modulus along longitudinal axis
Ey	Elastic modulus along lateral axis
FBG	Fiber Bragg Grating
FEM	Finite Element Model
FHWA	Federal Highway Administration
ft.	foot (feet)
FOS	Fiber Optic Sensor
FRP	Fiber Reinforced Polymer
GFRP	Glass Fiber Reinforced Polymer
G_T	Temperature gauge factor
Gxy	Modulus of rigidity
G_ε	Strain gauge factor
in.	inch (es)
kHz	kilo hertz
kip	kilo Pounds
LADOTD	Louisiana Department of Transportation and Development
lb.	pound (s)
LFD	Load Factor Design
LVDT	Linear variable differential transducer
LTRC	Louisiana Transportation Research Center
m	meter (s)

mm	millimeter
mph	miles per hour
msi	megapounds per square inch
MTS	Material Testing Systems
nm	nanometer
OTDR	Optical Time Domain Reflectometer
PAC	Physical Acoustics Corporation
pm	picometer
pVs	pico-Volt second
SG	Strain Gauge
$\Delta\varepsilon$	Change in strain
λ_b	Original wavelength

REFERENCES

1. Ehlen, M. A. "Life-Cycle Costs of Fiber-Reinforced-Polymer Bridge Decks." *Journal of Material in Civil Engineering*, Vol. 11, No. 3, 1999, pp. 224-230.
2. Murton, M. C. "Commercialization of FRP Bridge Decks: Lessons and Challenges for Ohio's 'Project 100.'" International SAMPE Symposium and Exhibition: Proceedings, Vol. 46, 2001, pp. 943-951.
3. Klaiber, F.; Dunker, K.; Wipt, T.; and Sanders, W. "Methods of Strengthening Highway Bridges," Transportation Research Board, NCHRP Research Report. 293, 1987.
4. Zureick, A.; Shih, B.; and Munley, E. "Fiber-Reinforced Polymeric Bridge Decks." *Structural Engineering Review*, Vol. 7, No. 3, 1995, pp. 257-266.
5. Munley, E. "Federal Highway Administration Research Program: Fiber Reinforced Polymer Composite Materials" 10th ASM/ESD Advanced Composites Conference, Dearborn, MI, 1994.
6. Scott, I. and Wheeler, K. "Application of Fibre Reinforced Polymer Composites in Bridge Construction." The Second IPWEA Conference, October 28, 2001, Port Macquarie, NSW, Australia, 2001.
7. Mertz, D. R.; Chajes M. J.; Gillespie, J. W.; Kukich, D. S.; Sabol, S. A.; Hawkins, N. M.; Aquino, W.; and Deen, T. B. "Application of Fiber Reinforced Polymer Composites to the Highway Infrastructure," National Cooperative Highway Research Program (NCHRP) Report 503, Washington, DC, 2003.
8. Deng, L. and Cai, C.S. "Applications of Fiber Optic Sensors in Civil Engineering." *Structural Engineering and Mechanics*, Vol. 25, No. 5, 2007, pp. 577-596.
9. Measures, M. R. "Structural Monitoring with Fiber Optic Technology." Academic Press, 2001, pp. 257-258.
10. American Association of State Highway and Transportation Officials (AASHTO). AASHTO LRFD Bridge Design Specifications, American Association of State Highway and Transportation Officials, Washington, DC, 2004.
11. Demitz, J. R.; Mertz, D. R.; and Gillespie, J. W. "Deflection Requirements for Bridges Constructed with Advanced Composite Materials." *Journal of Bridge Engineering*, Vol. 8, No. 2, 2003, pp. 73-83.
12. Lesko, J.J. and Davalos, J.F. "Fiber-reinforced Polymer Decks for Bridge Systems." *Journal of Composites for Construction*, ASCE, Special 150th Anniversary, 2001.
13. Liao Y.B. "Fiber Optics," Tsinghua University Press, Beijing, China, 2000, pp. 93–95.

14. Casas, J. R. and Cruz, P. J. S. “Fiber Optic Sensors for Bridge Monitoring.” *Journal of Bridge Engineering*, Vol. 8, No. 6, 2003, pp. 362-373.
15. Li, H.; Li, D.; and Song, G. “Recent Applications of Fiber Optic Sensors to Health Monitoring in Civil Engineering.” *Engineering Structures*, Vol. 26, 2004, pp. 1647-1657.
16. Leung, C. K. Y.; Elvin, N.; Olson, N.; Morse, T. F.; and He, Y.F. “A Novel Distributed Optical Crack Sensor for Concrete Structures.” *Engineering Fracture Mechanics*, Vol. 65, No. 2-3, 2005, pp. 133-148.
17. Ehlen, M. A. “Life-Cycle Costs of Fiber-Reinforced-Polymer Bridge Decks,” *Journal of Material in Civil Engineering*, Vol. 11, No. 3, 1999, pp. 224-230.
18. Zureick, A.; Shih, B; and Munley, E. “Fiber-Reinforced Polymeric Bridge Decks.” *Structural Engineering Review*, Vol. 7, No.3, 1995, pp. 257-266.
19. Klaiber, F.; Dunker, K.; Wipt, T.; and Sanders, W. “Methods of Strengthening Existing Highway Bridges,” Transportation Research Board, NCHRP Research Report. 293, 1987, pp. 1-6.
20. Munley, E. “Federal Highway Administration Research Program: Fiber Reinforced Polymer Composite Materials,” 10th ASM/ESD Advanced Composites Conference, Dearborn, MI, 1994.
21. Nearle, K. W. “Advanced Composites and Integrated Sensing for Rehabilitation,” ISIS Canada Annual Report, 1997, p.6.
22. Scott, I. and Wheeler, K. “Application of Fiber Reinforced Polymer Composites in Bridge Construction” The Second IPWEA Conference, October 28, 2001, Port Macquarie, NSW, Australia, 2001.
23. Bakis, C. E.; Bank, L. C.; Brown, V. L.; Cosenza, E.; Davalos, J. F.; Lesko, J. J.; Machida, A.; Rizkalla, S. H.; and Triantafillou, T. C. “Fiber-Reinforced Polymer Composites for Construction – State-of-the-Art Review,” *Journal of Composites for Construction*, Vol. 6, No. 2, 2002, pp. 73-87.
24. Shekar, V.; Petro, S. H.; and GangaRao, H. V. S. “Construction of Fiber-Reinforced Plastic Modular Decks for Highway Bridges.” Transportation Research Record, No. 1813, 2002, pp. 203-209.
25. GangaRao, H.V.S. and Laosiriphone, K. “Design and Construction of Market Street Bridge – WV,” International SAMPE Symposium and Exhibition: Proceedings, Vol. 46 II, 2001, pp. 1321-1330.
26. Davalos, J.F.; Qiao, P.; Xu, X.F.; Robinson, J.; and Barth, K.E. “Modeling and Characterization of Fiber-Reinforced Plastic Honeycomb Sandwich Panels,” *Composite Structures*, Vol. 52, No. 3-4, 2001, pp. 441-452.

27. Davalos, J.F.; Salim, H. A.; Qiao, P.; and Lopez-Anido, R. “Analysis and Design of Pultruded FRP Shapes under Bending,” Composites. Part B, Engineering, Vol. 27, No. 3-4, 1996, pp. 295-305.
28. Schreiner, J. and Barker, L. “Lateral Distribution in Kansas Dot Steel Girder Bridge with FRP Deck” Report No. Ks-04-4, Final Report to Kansas Department of Transportation, Topeka, Kansas, 2005, pp. 1-26.
29. Coogler, K.; Harries, K. A.; Wan, B.; Rizos, D. C.; and Petrou, M. F. “Critical Evaluation of Strain Measurements in Glass Fiber-Reinforced Polymer Bridge Decks,” *Journal of Bridge Engineering*, Vol. 10, No. 6, 2005, pp. 704-712.
30. Aluri, S.; Jinka, C.; and GangaRao, H. V. S. “Dynamic Response of Three Fiber Reinforced Polymer Composite Bridges,” *Journal of Bridge Engineering*, Vol. 10, No. 6, 2005, pp. 722-730.
31. Ziehl, P., and Bane, W.S. “Nondestructive Evaluation of Fiber Reinforced Polymer Bridges and Decks,“ LTRC Project No. 03-1TUL, Report to Louisiana Department of Transportation and Development, Louisiana Transportation Research Center, 2003, pp. 1-60.
32. Alampalli, S.; Jerome O.; and Arthur P. Y. “Design, Fabrication, Construction, and Testing of an FRP Superstructure.” Special Report 134, Transportation Research and Development Bureau, New York State Department of Transportation, 2000.
33. Khalifa, M.A.; Kaska, S.S.B.; and Krieger, J. “Bridges Constructed using Fiber Reinforced Plastics,” *Concrete International: Design and Construction*, Vol. 15, No. 6, 1993, pp. 43-47.
34. Foster, D.C.; Richards, D.; and Bogner, B.R. “Design and Installation of Fiber Reinforced Polymer Composite Bridge,” *Journal of Composites for Construction*, Vol. 4, 2000, pp. 33- 37.
35. American Society of Nondestructive testing (ASNT): Non Destructive Handbook - Acoustic Emission Testing; Vol. 6, 2005, pp. 31-79.
36. Rens, K.L.; Wipf, T.J.; Klaiber, F.W. “Review of Nondestructive Evaluation Techniques of Civil Infrastructure.” *Journal of Performance of Constructed Facilities*, ASCE, Vol. 11, No. 4, 1997, pp. 152-160.
37. ASTM E1316-07b. Standard Terminology for Nondestructive Examinations. West Conshohocken (PA): ASTM International; 2007.
38. Grosse, C.U. www.ndt.net — “Editorial: Special Issue on Acoustic Emission.” 2002.
39. Grandt. A.F. “Fundamentals of Structural Integrity, Damage Tolerant Design and Nondestructive Evaluation.” 2003, pp. 426-428.
40. Arrington. M. “Acoustic emissions, Non-Destructive Testing of Fiber Reinforced Composites,” edited by Summerscales, J., Elsevier, London, 2003, pp. 25-63.

41. Nakamura, Y. “Acoustic Emission Monitoring System for Detection of Cracks in a Complex Structure,” *Material Evaluation*, Vol. 29, No. 1, 1971, pp. 8-12.
42. Horak, C.R. and Weyhreter, A.F. “Acoustic Emission System for Monitoring Components and Structures in a Severe Fatigue Noise Environment,” *Material Evaluation*, Vol. 35, 2003, pp. 59–68.
43. Watson, J.R.; Cole, P.T.; Holford, K.M.; and Davies, A.W. “Damage Assessment Using Acoustic Emission.” *Key Engineering Materials*, Vol. 204-205, 2001, pp. 309-318.
44. Lozev, M.G.; Clemena, G.G.; Duke, J.C.; Sison, M.F.; and Horne, M.R. “Acoustic Emission Monitoring of Steel Bridge Members.” Final Report, FHWA/VTRC 97-R13, 1997.
45. Yuyuma, S.; Okamoto, T.; Shigeishi, M.; Ohtsu, M. ; and Kishi, T. “A Proposed Standard for Evaluating Structural Integrity of Reinforced Concrete Beams by Acoustic Emission,” Acoustic Emission: Standards and Technology Update, ASTM STP 1353, Edited by Vahaviolos, S.J., American Society for Testing and Materials, West Conshohocken, PA, 1999.
46. Golaski, L.; Gebski, P.; and Ono, K. “Diagnostics of Reinforced Concrete Bridges by Acoustic Emission.” *Journal of Acoustic Emission*, Vol. 20, 2002, pp. 83-98.
47. Landis, E.N. and Baillon, L. “Experiments to Relate Acoustic Emission Energy to Fracture Energy of Concrete.” *Journal of Engineering Mechanics*, ASCE ,Vol. 128, No. 6, 2002, pp. 698-702.
48. Malhotra,V.M. and Carino, N.J. “Handbook on Nondestructive Testing of Concrete.” Second Edition, CRC Press, 2004, pp.16-14.
49. Ziehl, P. and Lamanna, A.J. “Monitoring of the Bonnet Carre Spillway Bridge during Extreme Overload.” LTRC project No. 03-6ST, 2003, pp. 1-65.
50. Ghorbanpoor A. and Benish N. “Non-destructive Testing of Highway Bridges.” Final report No. 0092-00-15. Madison (WI): Wisconsin Department of Transportation, 2003, pp. 1-99.
51. Watson, J.R.; Yuyuma, S.; Pullin, R.; and Ing, M. “Acoustic Emission Monitoring Applications for Civil Structures,” Bridge Management 5, Thomas Telford, London, 2005, pp. 563-570.
52. Weiler, B.; Xu, S.; and Mayer, U. “Acoustic Emission Analysis Applied to Concrete Under Different Loading Conditions.” *Otto-Graf-Journal*, Vol. 8, 1997, pp. 255-269.
53. Yoon, D.J.; Weiss, W.J.; and Shah, S.P. “Assessing Damage in Corroded Reinforced Concrete using Acoustic Emission.” *Journal of Engineering Mechanics*, ASCE, Vol. 126, No. 3, 2000, pp. 273-283.

54. Beck,P.; Bradshaw,T.P.; Lark,R.J.; and Holford,K.M. “A Quantitative Study of the Relationship between Concrete Crack Parameters and Acoustic Emission Energy Released during Failure.” *Key Engineering Materials*, Vols. 245-246, 2003, pp. 461-466.
55. Ohtsu, M.; Uchida, M.; Okamoto, T.; and Yuyama, S. “ Damage Assessment of Reinforced Concrete Beams Qualified by Acoustic Emission.” *ACI Structural Journal*, Vol. 99, No.4, 2002, pp. 411-417.
56. Colombo, I.S.; Forde, M.C.; Main, I.G.; Halliday, J.; and Shigeishi, M. “AE Energy Analysis on Concrete Bridge Beams.” International Symposium (NDT - CE 2003).
57. Morton, T.M.; Harrington, R.M.; and Bjeletich, J.G. “Acoustic Emissions of Fatigue Crack Growth,” *Engineering Fracture Mechanics*, Vol. 5, 1973, pp. 691-697.
58. Carter, D.C. and Holford, K.M. “Strategic Consideration for AE Monitoring of Bridges: A Discussion and Case Study.” *INSIGHT – Journal of British Institute of NDT*, Vol. 40, No. 2, 1998, pp. 112–116.
59. Holford, K.M.; Davies, H.W.; and Sammarco, A. “Analysis of Fatigue Crack Growth in Structural Steels by Classification by Acoustic Emission Signals.” *Engineering Systems Design and Analysis*, Vol. 8, 1994, pp. 349-353.
60. Sharma, R.K.; Prakash, O.; and Pandey, R.K. “Studies on Correlation of Acoustic Emission Parameters and Fatigue Crack Growth Behaviour in Plain Carbon Steel.” Trends in NDE Science & Technology, Proceedings of the 14th World Conference on Non-Destructive Testing, New Delhi, 8-13 December 1996,Vol. 4, pp. 2369 - 2372.
61. Gostautas, R.S.; Ramirez, G.; Peterman, R.J.; and Meggers, D. “Acoustic Emission Monitoring and Analysis of Glass Fiber-Reinforced Composites Bridge Decks.” *Journal of Bridge Engineering*, ASCE, Vol. 10, No. 6, 2005, pp. 713-721.
62. Mirmiran, A. and Philip, S. “Comparison of Acoustic Emission Activity in Steel-Reinforced and FRP-Reinforced Concrete Beams.” *Construction and Building Materials*, Vol. 14, No. 6, 2000, pp. 299-310.
63. Cecchini, A. “Damage Detection and Identification in Sandwich Composites Using Neural Networks,” M.S. Thesis, 2005, pp. 20-21.
64. Prosser,W.H.; Jackson, K.E.; Kellas,S.; Smith, B.T.; McKeon, Z.J.; and Friedman, A. “Advanced, Waveform Based Acoustic Emission Detection of Matrix Cracking in Composites.” Vol. 53, No. 9, 1995, pp. 1052-1058.
65. Kalny, O.; Peterman, R.J.; and Ramirez, G. “Performance Evaluation of Repair Technique for Damaged Fiber-Reinforced Polymer Honeycomb Bridge Deck Panels.” *Journal of Bridge Engineering*, ASCE, Vol. 9, No. 1, 2004, pp. 75 - 86.

66. Stryk. J., and Pospisisl. K. "Rebar Corrosion in Concrete Bridges and its Detection by Acoustic Emission Method." CDV- Transport Research Center, Czech Ministry of Transportation and Communications, 2001, pp. 1–6.
67. Paulson, P.O.; Elliott, J.F.; and Youdan, D.G. " SoundPrint® Acoustic Monitoring to Confirm Integrity of Stressed Wire in Bridges, Structures and Water Pipelines." 2004.
68. Vallen, D.I.H. "AE Testing Fundamentals, Equipment, Applications," www.ndt.net, Vol. 7, No. 9, 2002.
69. Grosse, C.U.; Finck, F.; Kurz, J.H.; and Reinhardt H.W. "Monitoring Techniques Based on Wireless AE Sensors for Large Structures in Civil Engineering," Proceedings of EWGAE 2004 Symposium, 2004. pp. 843–56.
70. Maalej, M.; Ahmed, S. F.U.; Kuang, K. S. C.; and Paramasivam, P. "Fiber Optic Sensing for Monitoring Corrosion-Induced Damage." *Structural Health Monitoring*,Vol. 3, No. 2, 2004, pp.165-176.
71. Tennyson, R.C.; Coroy, T.; Duck, G.; Manuelpillai, G.; Mulvihill, P.; Cooper, David J.F.; Smith, P.W.E.; Mufti, A.A.; and Jalali, S.J. "Fiber Optic Sensors in Civil Engineering Structures." *Canadian Journal of Civil Engineering*, Vol. 27, No. 5, 2000, pp. 880-889.
72. Bonfiglioli, B. and Pascale, G. "Internal Strain Measurements in Concrete Elements by Fiber Optic Sensors." *Journal of Materials and Civil Engineering*, Vol. 15, No. 2, 2003, pp. 125-133.
73. Habel, W. R. "Fiber Optic Sensor in Civil Engineering: Experiences and Requirements," Proceedings of Smart Structures: Optical Instrumentation and Sensing Systems, SPIE, Bellingham, WA, 2509, 1999, pp.12-19.
74. Merzbacher, C. I.; Kersey, A. D.; and Friebele, E. J. "Fiber Optic Sensor in Concrete Structures: A Review." *Smart Materials and Structures*, Vol. 5, 1996, pp. 196-208.
75. Tennyson, R. C.; Mufti, A. A.; Rizkalla, S.; Tadros, G.; and Benmokrane, B. "Structural Health Monitoring of Innovative Bridges in Canada with Fiber Optic Sensors." *Smart Materials and Structures*, Vol. 10, 2001, pp. 560-573.
76. Wanser, K. H. and Voss, K. H. "Crack Detection Using Multimode Fiber Optical Time Domain Reflectometry." Proceedings of Distributed and Multiplexed Fiber Optic Sensors, SPIE, Bellingham, WA, 2294, 1994, pp. 43-52.
77. Liu, H. and Yang, Z. "Distributed Optical Fiber Sensing of Cracks in Concrete." Proceedings of Optical and Fiber Optic Sensor Systems, SPIE, Bellingham, WA, 3555, 1998, pp. 291-299.
78. Lee, D. C.; Lee, J. J.; and Kwon, I. B. "Monitoring of Fatigue Crack Growth in Steel Structures Using Intensity-Based Optical Fiber Sensors." *Journal of Intelligent Material Systems and Structures*, Vol. 11, 2000, pp. 100-107.

79. Ansari, F. and Navalurkar, R. K. “Kinematics of Crack Formation in Cementitious Composites by Fiber Optics.” *Journal of Engineering Mechanics*, Vol. 119, No. 5, 1993, pp. 1048-1061.
80. Wolff, R. and Miesseler, H. J. “Monitoring of Prestressed Concrete Structures with Optic Fiber Sensors.” Proceedings of the first European Conference on Smart Structures and Materials, Glasgow, 1992, pp. 23-29.
81. Grossmann, B.G. and Huang, L. “Fiber Optic Sensor Array for Multi-Dimensional Strain Measurement.” *Smart Materials and Structure*, Vol. 7, 1998, pp. 159-165.
82. Kenel, A.; Nellen, P.; Frank, A.; and Marti, P. “Reinforcing Steel Strains Measured by Bragg Grating Sensors.” *Journal of Materials in Civil Engineering*, ASCE, Vol. 17, No. 4, 2005, pp. 423-431.
83. Fuhr, P. L.; Ambrose, T. P.; Huston, D. R.; and Mcpadden, A. P. “Fiber Optic Corrosion Sensing for Bridges and Roadway Surfaces.” Proceedings of Smart Structures and Materials 1995: Smart Systems for Bridges, Structures, and Highways, SPIE, Bellingham, WA, 2446, 1995, pp. 2-8.
84. Fuhr, P. L. and Huston, D. R. “Corrosion Detection in Reinforced Concrete Roadways and Bridges via Embedded Fiber Optic Sensor.” *Smart Materials and Structures*, Vol. 7, 1998, pp. 217-228.
85. Casas, J. R. and Frangopol, D. M. “Monitoring and Reliability Management of Deteriorating Concrete Bridges.” Proceedings of Second International Workshop on Life-cycle Cost Analysis and Design of Civil Infrastructure Systems, Editors A. Miyamoto and D. M. Frangopol, Yamaguchi University, Ube, Japan, 2001, pp. 127-141.
86. Fuhr, P. L.; Huston, D. K.; Kajenski, P. J.; and Ambrose, T. P. “Performance and Health Monitoring of the Stafford Medical Building Using Embedded Sensors.” *Smart Materials and Structures*, Vol. 1, 1992, pp. 63-68.
87. Iwaki, H.; Yamakawa, H.; and Mita, A. “Health Monitoring System using FBG-Based Sensors for a 12-Story Building with Column Dampers.” Proceedings of Smart Structures and Materials: Smart systems for Bridges, Structures, and Highways, SPIE, Bellingham, WA, 4330, 2001, pp. 471-477.
88. Whelan, M. P.; Albrecht, D.; and Capsoni, A. “Remote Structural Monitoring of the Cathedral of Como using an Optical Fiber Bragg Sensor System.” Proceedings of Smart Structures and Materials and Non-destructive Evaluation for Health Monitoring and Diagnostics, SPIE, Bellingham, WA, 4330, 2002, pp. 471-477.
89. Bastianini, F.; Corradi, M.; Borri, A.; and Tommaso, A. D. “Retrofit and Monitoring of an Historical Building using ‘Smart’ CFRP With Embedded Fiber Optic Brillouin Sensors.” *Construction and Building Materials*, Vol. 19, No. 7, 2005, pp. 525-535.

90. Habel, W. R. and Hofmann, D. “Determination of Structural Parameters Concerning Load Capacity Based on Fiber-Fabry-Pérot-Interferometers.” Proceedings of SPIE, 2361, 1994, pp. 176-179.
91. Inaudi, D.; Rufenacht, A.; Von Arx, B.; Noher, H.P.; Vurpillot, S.; and Glisic, B. “Monitoring of a Concrete Arch Bridge during Construction.” Proceedings of Smart Structures and Materials 2002: Smart Systems for Bridges, Structures, and Highways SPIE, 4696, 2002, pp. 89-103.
92. Idriss, R. L.; Kodindouma, M. B.; Kersey, A. D.; and Davis, M. A. “Multiplexed Bragg Grating Optical Fiber Sensors for Damage Evaluation in Highway Bridges.” *Smart Materials and Structures,* Vol. 7, 1998, pp. 209-216.
93. Ou, J. P.; Zhao, X. F.; Li, H.; Zhou, Z.; Zhang, Z.; and Wang, C. “Health Monitoring of Binzhou Yellow River Highway Bridge using Fiber Bragg Gratings.” Proceedings of Smart Structures and Materials 2005: Sensors and Smart Structures Technologies for Civil, Mechanical, and Aerospace Systems, SPIE, Bellingham, WA, 5765, 2005, pp. 576-583.
94. Wang, C.; Zhou, Z.; Hu, Q. L.; and Ou, J. P. “Construction Control of Mass Concrete of Nanjing 3rd Yangtze Bridge using FRP-Packaged FBG Sensors.” Proceedings of 17th International Conference on Optical Fiber Sensors, SPIE, Bellingham, WA, 5855,2005, pp. 1012-1015.
95. Grossman, B.G.; Cosentino, P.J.; Kalajian, E.H.; Kumar, G.; Doi, S.; Verghese, J.; and Lai, P. “Fiber Optic Pore Pressure Sensor Development.” Transportation Research Record 1432, Transportation Research Board, Washington, DC, 1994, pp. 76-85.
96. Body, J.; Teral, S.; Caussignac, J.M.; and Siffert, M. “Vehicle Weighing in Motion with Fiber Optic Sensors.” *Measurement and Control*, Vol. 26, No. 2, 1993, pp. 45-47.
97. Eckroth, W. V. “Development and Modeling of Embedded Fiber-Optic Traffic Sensors.” PhD Dissertation, Florida Institute of Technology, Melbourne, FL, 1999.
98. Cosentino, P. J.; Eckroth, W. V.; and Grossman, B. G. “Analysis of Fiber Optic Traffic Sensors in Flexible Pavements.” *Journal of Transportation Engineering*, Vol. 129, No. 5, pp. 549-557.
99. Bergmeister, K. and Santa, U. “Global Monitoring Concepts for Bridges.” *Structural Concrete Journal*, Vol. 2, No. 1, 2003, pp. 29-39.
100. Udd, E.; Kunzler, M.; Laylor, M.; Schulz, W.; Kreger, S.; Corones, J.; McMahon, R.; Soltesz, S.; and Edgar, R. “Fiber Grating Systems for Traffic Monitoring.” Proceedings of Health Monitoring and Management of Civil Infrastructure Systems. SPIE, Bellingham, WA, 4337, 2001, pp. 510-516.

101. Fuhr, P. L. and Huston, D. “Multiplexed Fiber Optic Pressure and Vibration Sensors for Hydroelectric Dam Monitoring.” *Smart Materials and Structures*, Vol. 2, 1993, pp. 260-263.
102. Fuhr, P. L.; Huston, D. R.; Ambrose, T. P.; and Barker, D. A. “Embedded Sensor Results from the Winooski One Hydroelectric Dam.” Proceedings of Smart Structures and Materials, SPIE, Bellingham, WA, 2191, 1994, pp. 446-456.
103. Nellen, P. M.; Frank, A.; Bronnimann, R.; and Sennhauser, U. “Optical Fiber Bragg Gratings for Tunnel Surveillance.” Proceedings of SPIE, 3986, 2000, pp. 263-270.
104. Inaudi, D.; Del Grosso, A.; and Lanata, F. “Analysis of Long-term Deformation Data from the San Giorgio Harbor Pier In Genoa.” Proceedings of Health Monitoring and Management of Civil Infrastructure Systems SPIE, Bellingham, WA, 4337, 2001, pp. 459-465.
105. Fernandez, M. L.; Tapanes, E. E.; and Zelitskaya, P. V. “Pipeline Hydrocarbon Transportation: Some Operating Concerns and RD Trends.” Proceedings of the first International Pipeline Conference, ASME OMAE, Vol. 1, 1996, pp. 95-102.
106. Tennyson, R. C.; Morison, W. D.; and Manuelpillai, G. “Intelligent Pipelines using Fiber Optic Sensors.” Proceedings of Smart Structures and Materials: Smart Sensor Technology and Measurement System, SPIE, Bellingham, WA, 5050, 2003, pp. 295-304
107. Glisic, B.; Inaudi, D.; and Nan, C. “Pile Monitoring with Fiber Optic Sensors during Axial Compression, Pullout, and Flexure Tests.” Transportation Research Record, 1808, 2002, pp. 11-20.
108. Lee, W.; Lee, W. J.; Lee, S. B.; and Salgado, R. “Measurement of Pile Load Transfer Using the Fiber Bragg Grating Sensor System.” *Canadian Geotechnical Journal*, Vol. 41, No. 6, 2004, pp. 1222-1232.
109. Ansari, F. and Yuan, L. “Mechanics of Bond and Interface Shear Transfer in Optical Fiber Sensors.” *Journal of Engineering Mechanics*, Vol. 124, No. 4, 1998, pp. 385-394.
110. Li, Q.; Li, G.; Wang, G.; Ansari, F.; and Liu, Q. “Elasto-Plastic Bonding of Embedded Optical Fiber Sensors in Concrete.” *Journal of Engineering Mechanics*, Vol. 128, 2002, pp. 471-478.
111. Lee, D. C.; Lee, J. J.; and Kwon, I. B. “Monitoring of Fatigue Crack Growth in Steel Structures using Intensity-Based Optical Fiber Sensors.” *Journal of Intelligent Material Systems and Structures*, Vol. 11, 2000, pp. 100-107.
112. Gheorghiu, G.; Labossiere, P.; and Proulx, J. “Fiber Optic Sensors for Strain Measurement of CFRP-Strengthened RC Beams.” *Structural Health Monitoring*, Vol. 4, No. 1, 2005, pp. 67-80.

113. Kuang, K. S. C. and Cantwell, W. J. “Use of Conventional Optical Fibers and Fiber Bragg Gratings for Damage Detection in Advanced Composite Structures: A Review.” *Applied Mechanics Reviews*, Vol. 56, No. 5, 2003, pp. 493-513.
114. Roberts, S. S. and Davidson, R. “Mechanical Properties of Composite Materials Containing Embedded Fiber Optic Sensors.” Proceedings of Fiber Optic Smart Structures and Skins, SPIE, Bellingham, WA, 1588, 1991, pp. 326-341.
115. Holl, M. W. and Boyd, S. “Effect of Embedded Fiber Optics on the Mechanical Properties of a Composite Host Material.” Proceedings of Smart Structures and Materials 1993: Smart Materials, SPIE, Bellingham, WA, 1916, 1993, pp. 109-117.
116. Mall, S.; Dosedel, S. B.; and Holl, M. W. “The Performance of Graphite-Epoxy Composite with Embedded Optical Fibers under Compression.” *Smart Materials and Structures*, Vol. 5, 1996, pp. 209-215.

APPENDIX

Appendix A North Bound Lane Results
Appendix B Strain Data Comparison
Appendix C Experimental Study to Examine Deck Relative Deflection
Appendix D Load Rating Using FEM of Steel Grid Deck
Appendix E Laboratory Work for Moisture Monitoring of Balsa Wood with FBG Sensors and Slip Monitoring using OTDR
Appendix F Installation Procedure for Fiber Optic FBG and OTDR Sensors
Appendix G Long Term Monitoring Procedural Guidelines
Appendix H Long Term Monitoring Results
Appendix I Literature Review and Background Information

APPENDIX A

North Bound Lane Results

Part 1: BDI Strain Gauge Plots

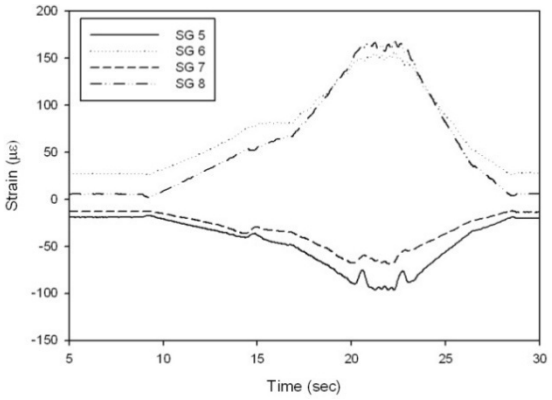

(a) BDI strain plot for load case N_SR1

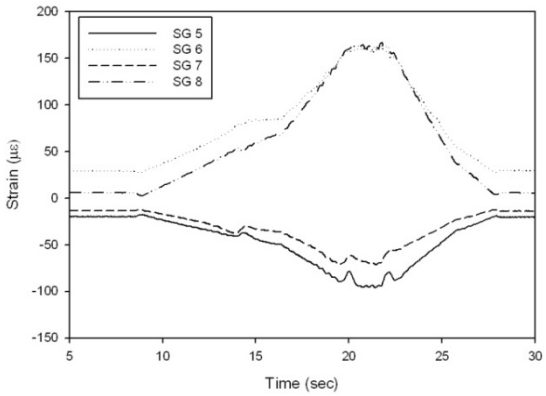

(b) BDI strain plot for load case N_SR2

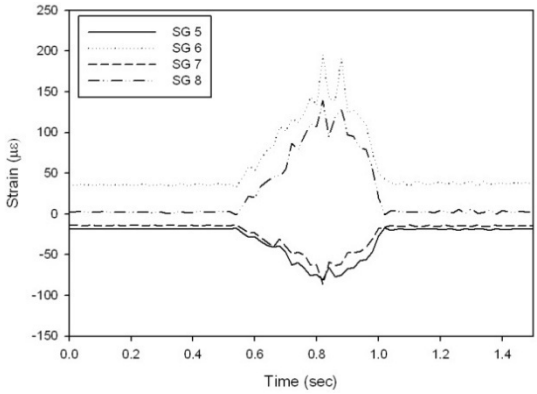

(c) BDI strain plot for load case N_D1_30

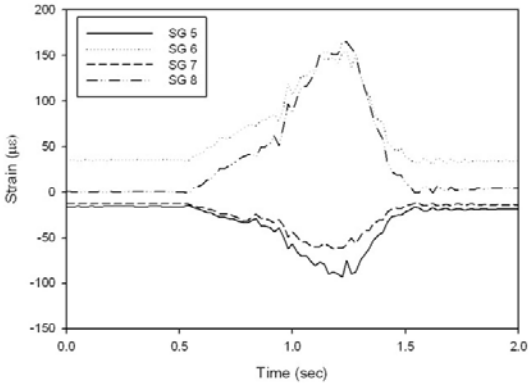

(d) BDI strain plot for load case N_D2_30

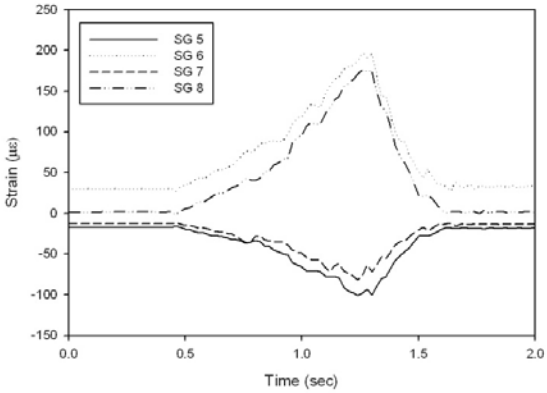

(e) BDI strain plot for load case N_D1_55

Figure 44
Strain plots from BDI sensors on girders for all static rolling and dynamic load cases – girder strains

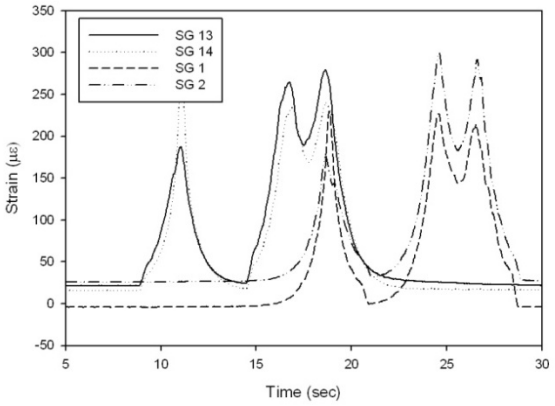

(a) BDI strain plot for load case N_SR1

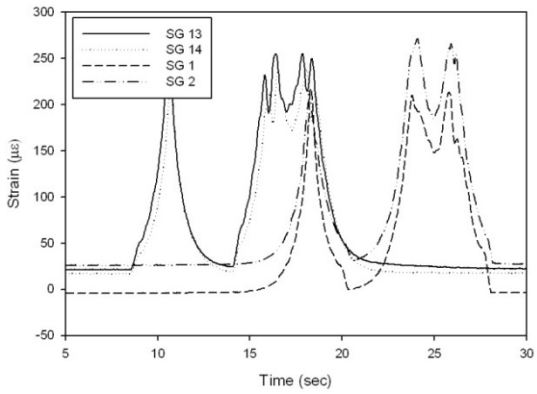

(b) BDI strain plot for load case N_SR2

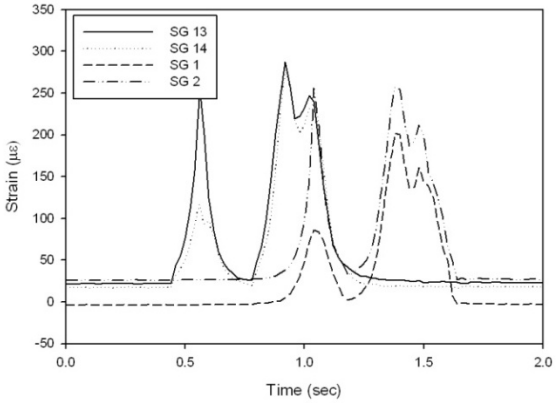

(c) BDI strain plot for load case N_D1_30

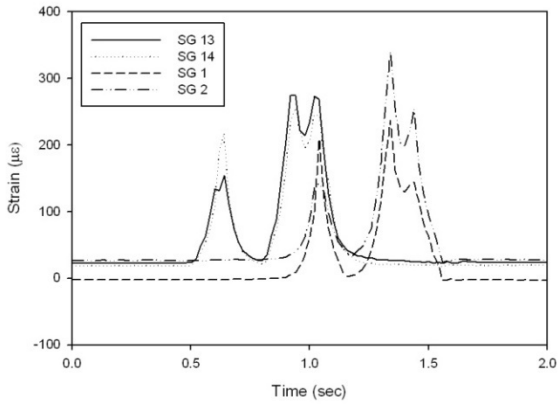

(d) BDI strain plot for load case N_D2_30

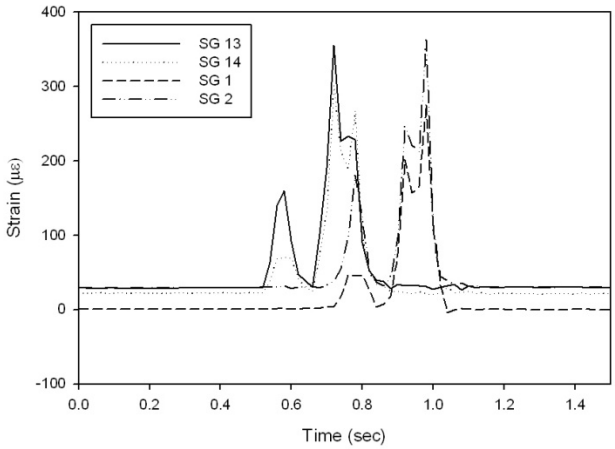

(e) BDI strain plot for load case N_D1_55

Figure 45
Strain plots from BDI sensors on deck for all static rolling and dynamic load cases – deck strains

Part 2: FBG Strain Plots

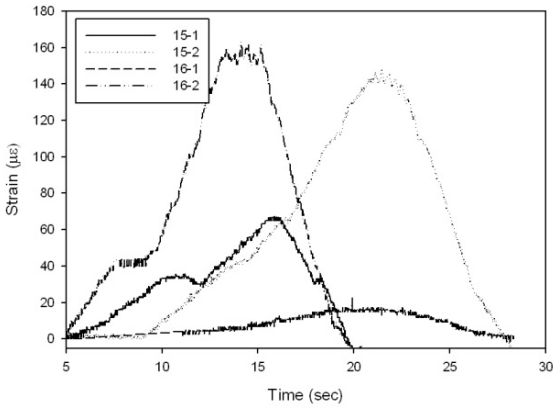

(a) FBG strain plot for load case N_SR1

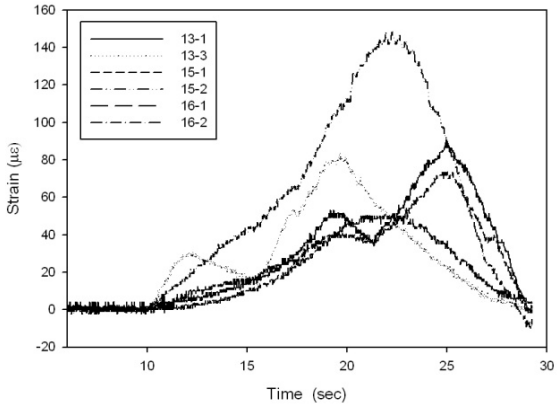

(b) FBG strain plot for load case N_SR2

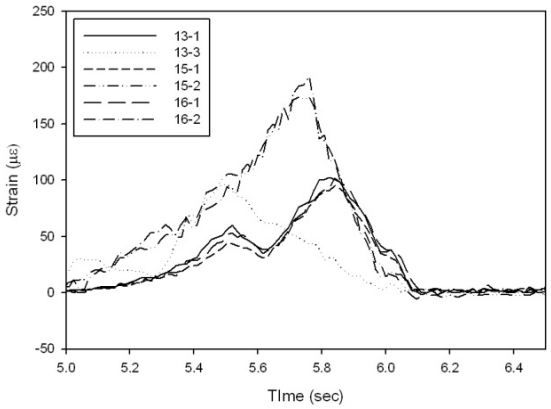

(c) FBG strain plot for load case N_D1_30

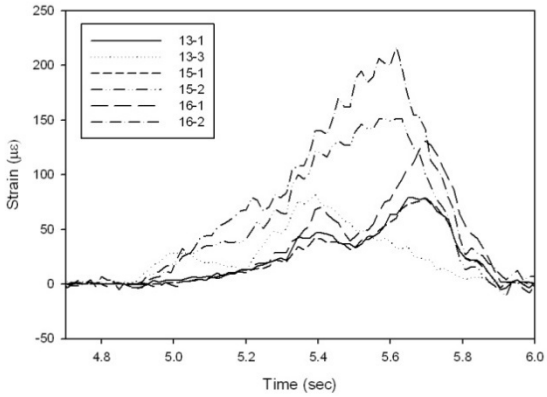

(d) FBG strain plot for load case N_D2_30

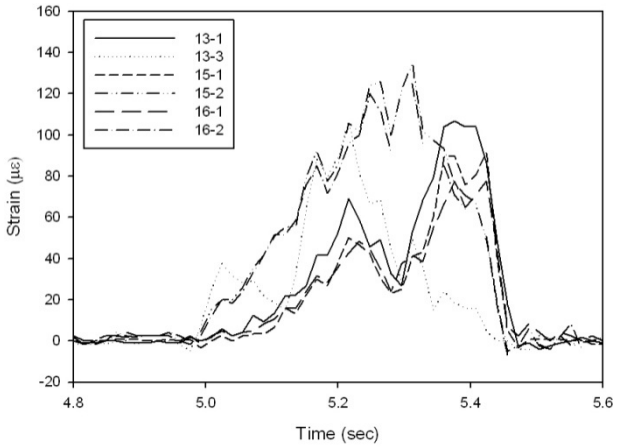

(e) FBG strain plot for load case N_D1_55

Figure 46
Strain plots from FBG sensors on girder for all static rolling and dynamic load cases – girder strains

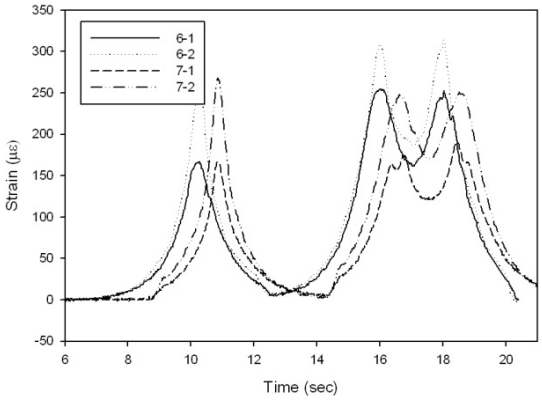

(a) FBG strain plot for load case N_SR1

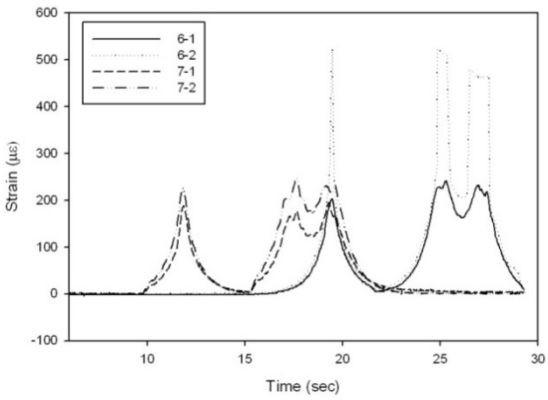

(b) FBG strain plot for load case N_SR2

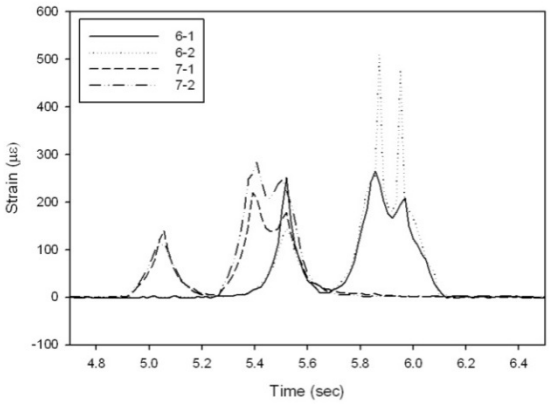

(c) FBG strain plot for load case N_D1_30

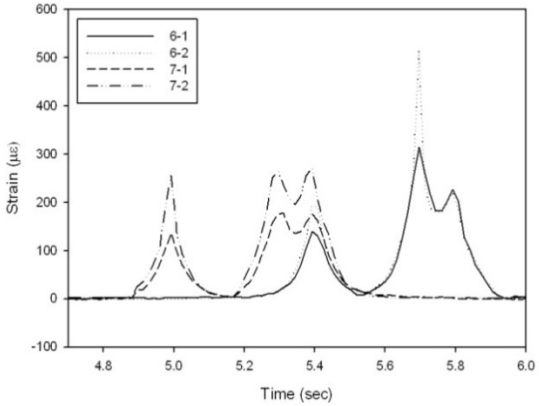

(d) FBG strain plot for load case N_D2_30

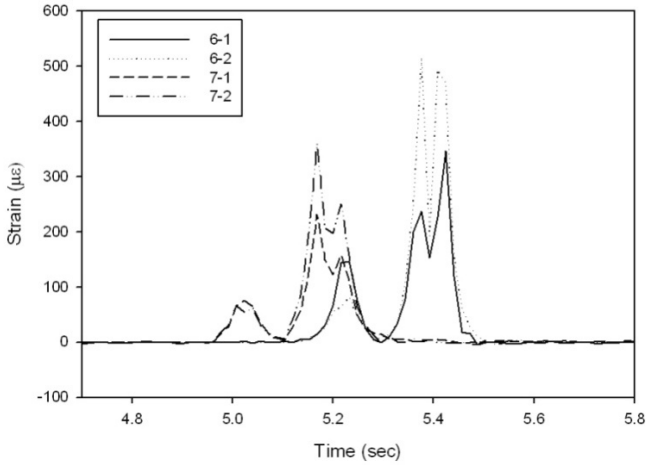

(e) FBG strain plot for load case N_D1_55

Figure 47
Strain plots from FBG sensors on girder for all static rolling and dynamic load cases – deck strains

Part 3: AE Plots

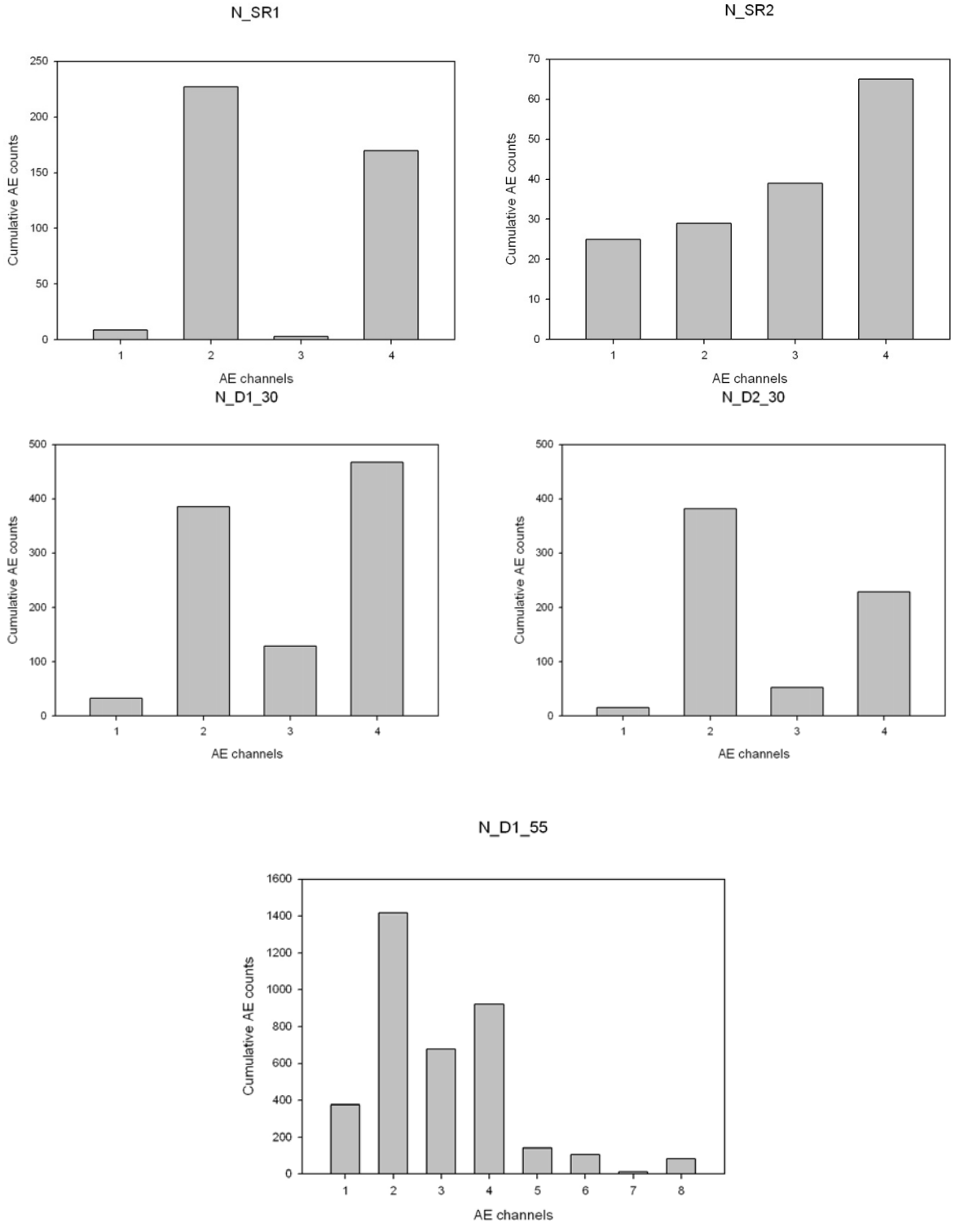

Figure 48
Cumulative AE hits observed by active channels for all live load test cases in north bound lane

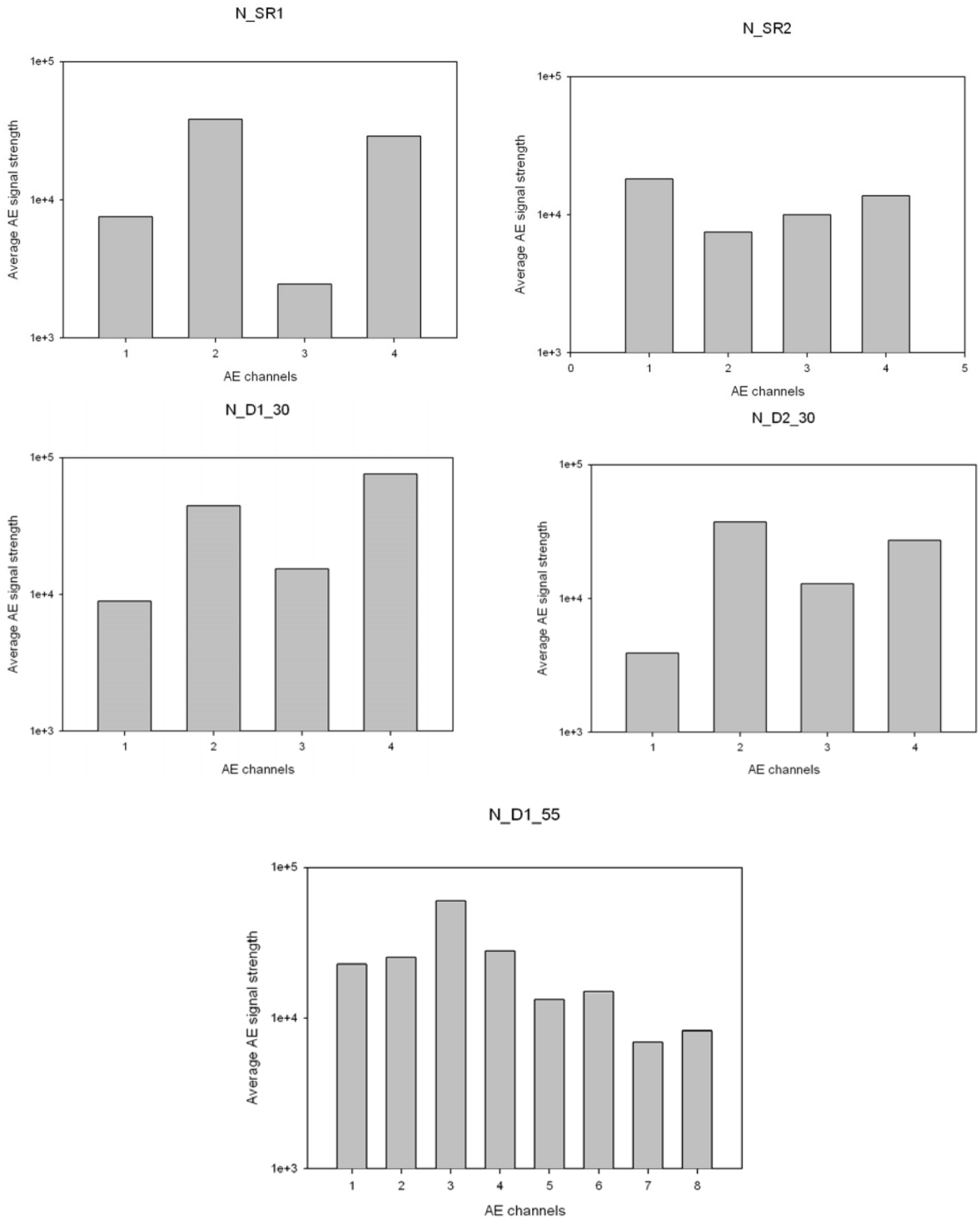

Figure 49

Average AE signal strengths observed by active channels for all live load test cases in north bound lane

APPENDIX B

Strain Data Comparison

The point-to-point data comparison from all functional traditional strain gauges (BDI) and FBG strain sensors in the same location are presented in this section. A direct comparison with each individual sensor located on the deck and girder of the bridge structure is graphically represented in Figures 50 to 63. Figures 50 to 62 show deck strain comparisons from both lanes and Figure 63 shows strain comparison for all load cases of gauges located on girder of the north bound lane.

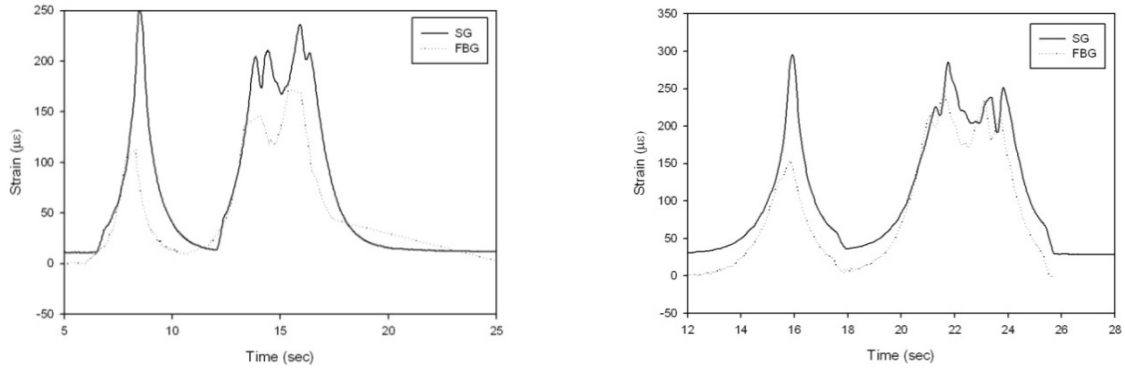

(a) south end (b) north end

Figure 50
SG and FBG strain comparison on deck 1 for load case S_SR3

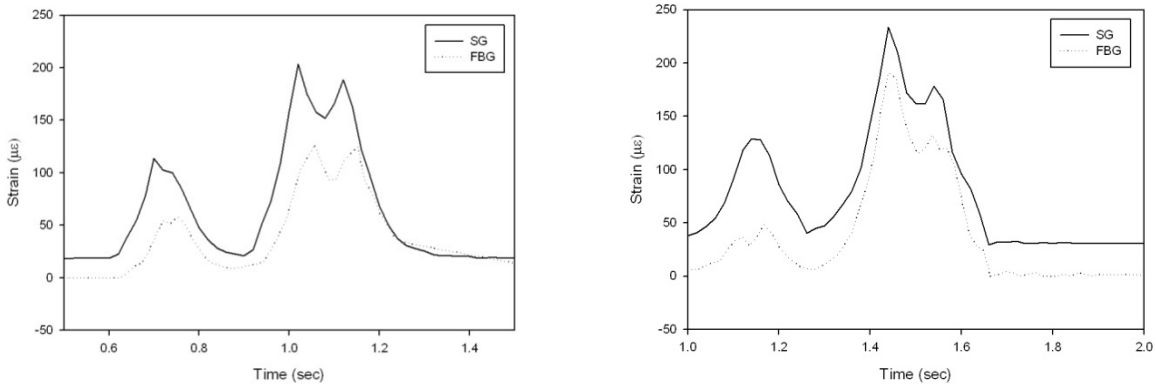

(a) south end (b) north end

Figure 51
SG and FBG strain comparison on deck 1 for load case S_D2_30

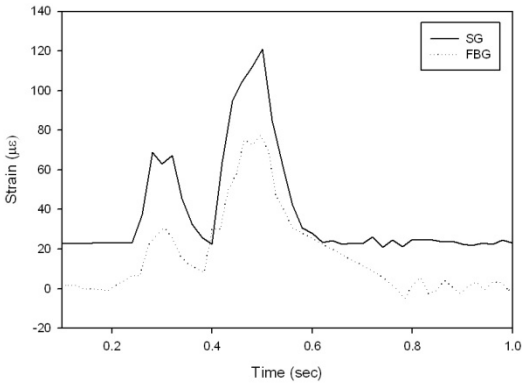

(a) south end

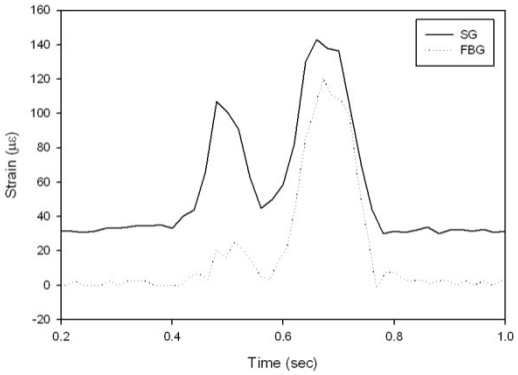

(b) north end

Figure 52
SG and FBG strain comparison on deck 1 for load case S_D1_55

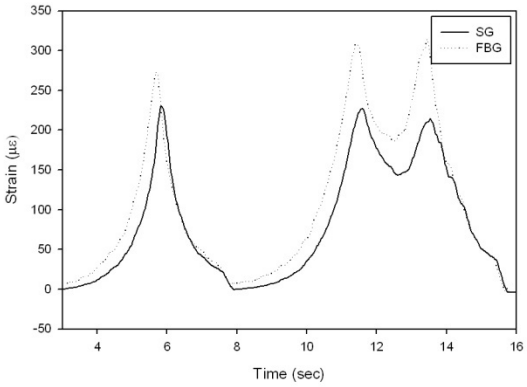

(a) south end

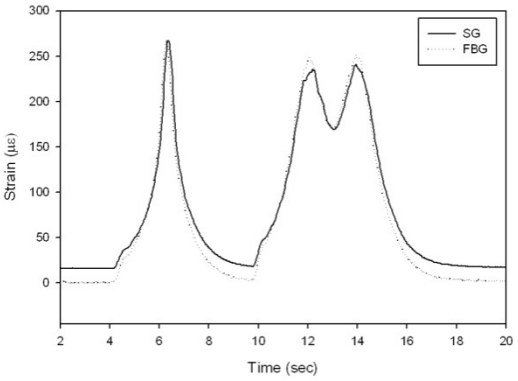

(b) north end

Figure 53
SG and FBG strain comparison on deck 3 for load case N_SR1

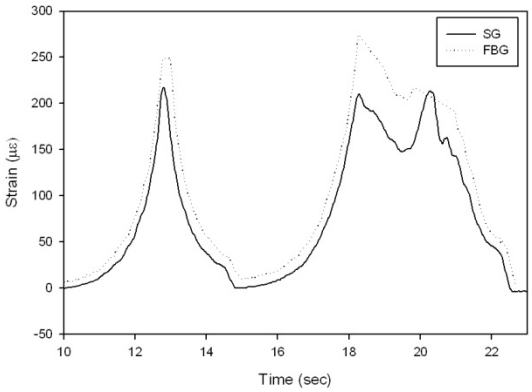

(a) south end

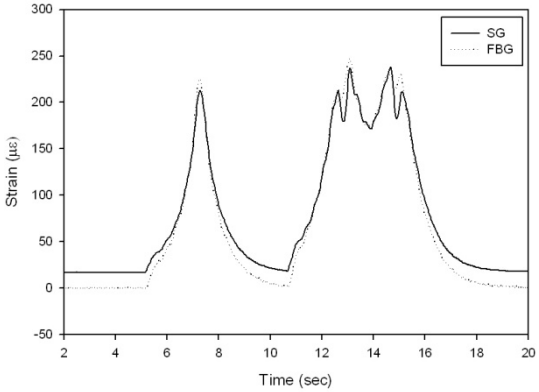

(b) north end

Figure 54
SG and FBG strain comparison on deck 3 for load case N_SR2

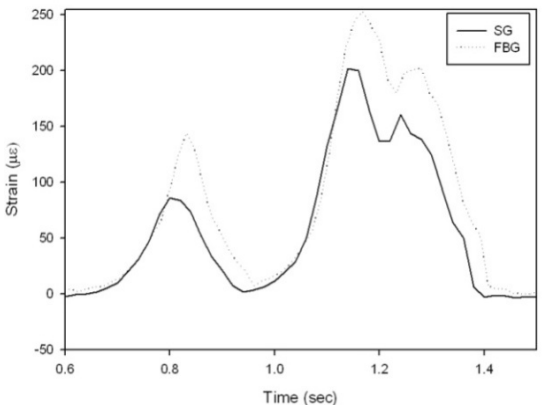

(a) south end

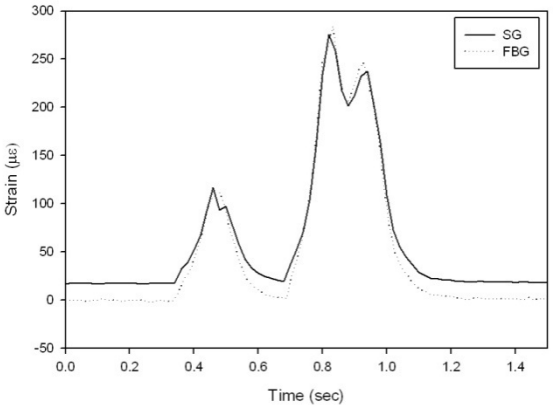

(b) north end

Figure 55
SG and FBG strain comparison on deck 3 for load case N_D1_30

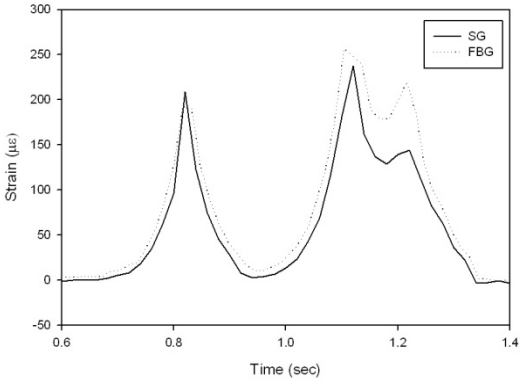

(a) south end

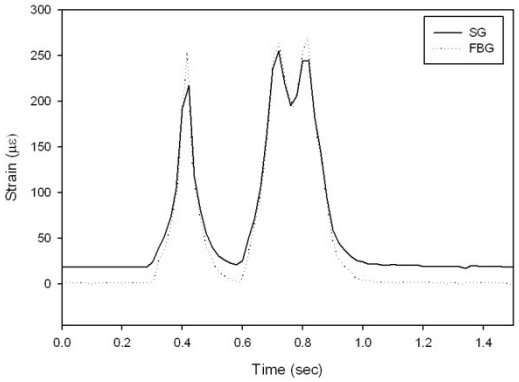

(b) north end

Figure 56
SG and FBG strain comparison on deck 3 for load case N_D2_30

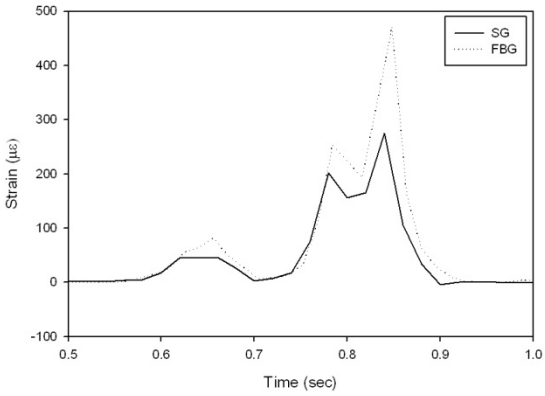

(a) south end

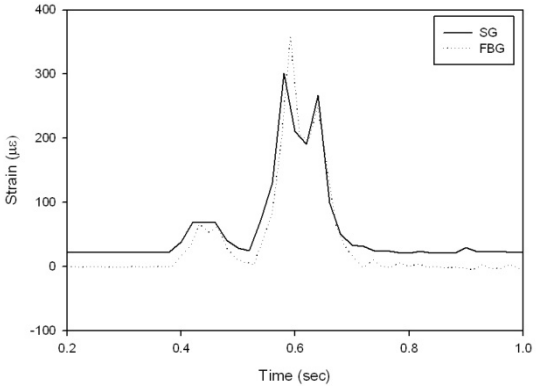

(b) north end

Figure 57
SG and FBG strain comparison on deck 3 for load case N_D1_55

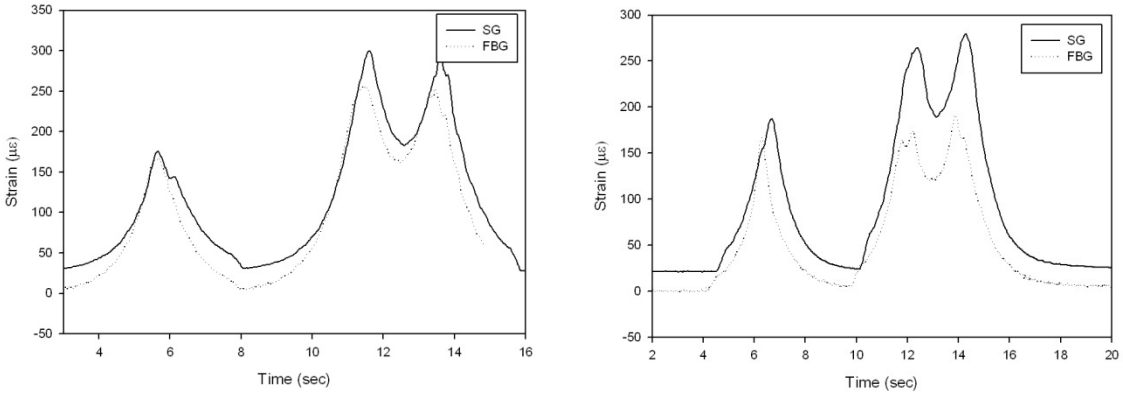

(a) south end (b) north end

Figure 58
SG and FBG strain comparison on deck 4 for load case N_SR1

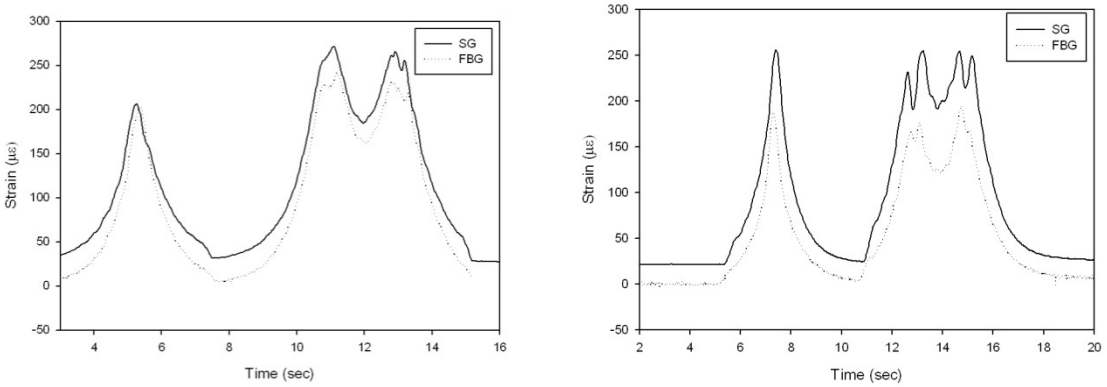

(a) south end (b) north end

Figure 59
SG and FBG strain comparison on deck 4 for load case N_SR2

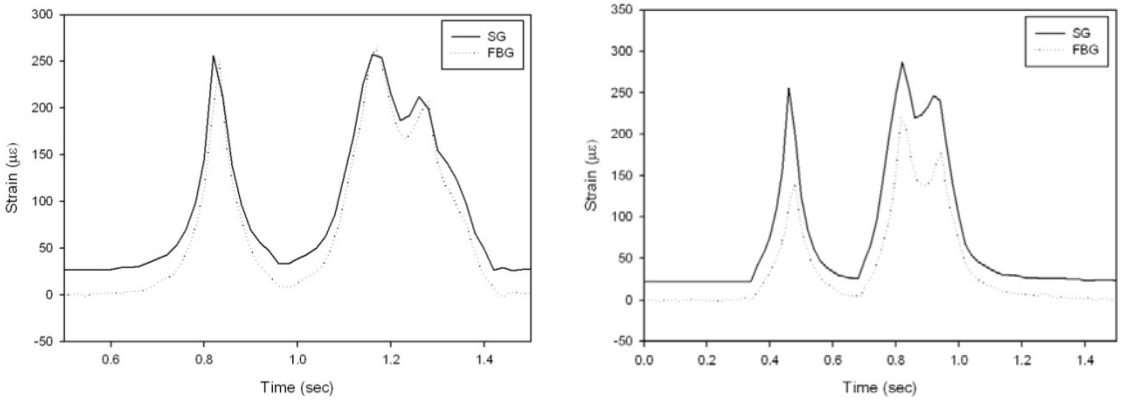

(a) south end (b) north end

Figure 60
SG and FBG strain comparison on deck 4 for load case N_D1_30

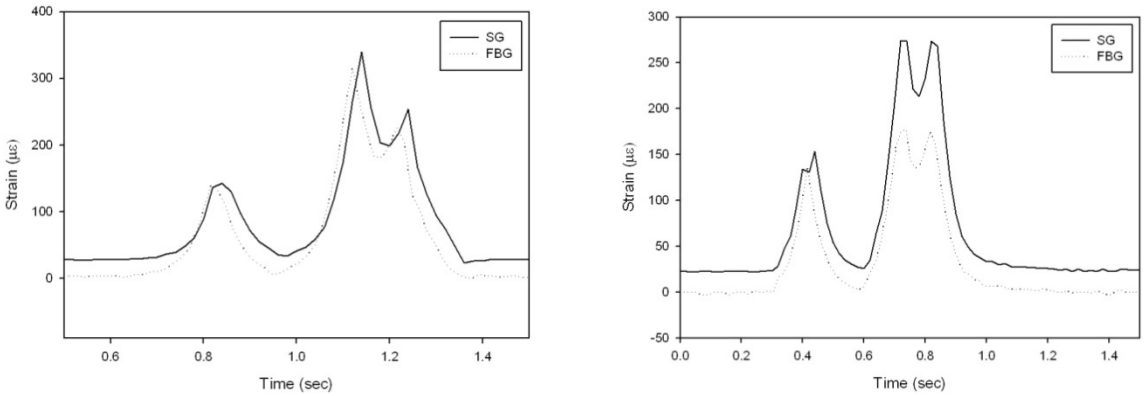

(a) south end (b) north end

Figure 61
SG and FBG strain comparison on deck 4 for load case N_D2_30

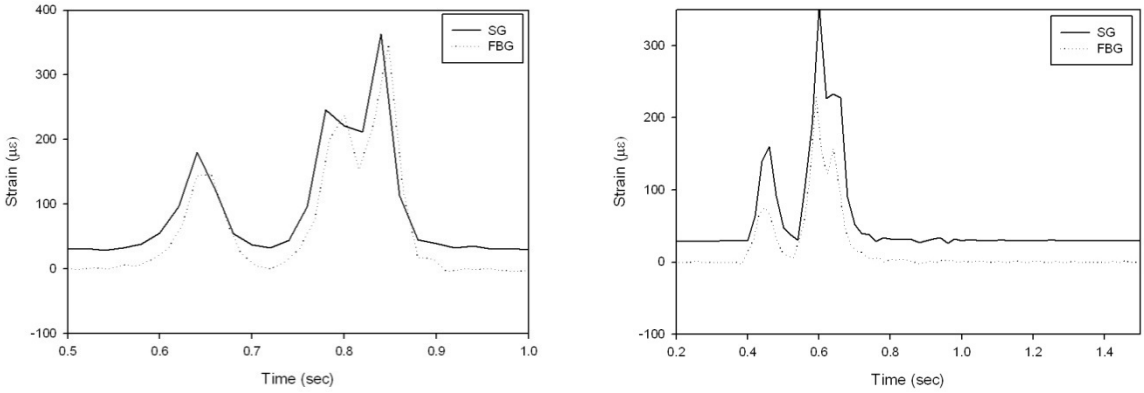

(a) south end (b) north end

Figure 62
SG and FBG strain comparison on deck 4 for load case N_D1_55

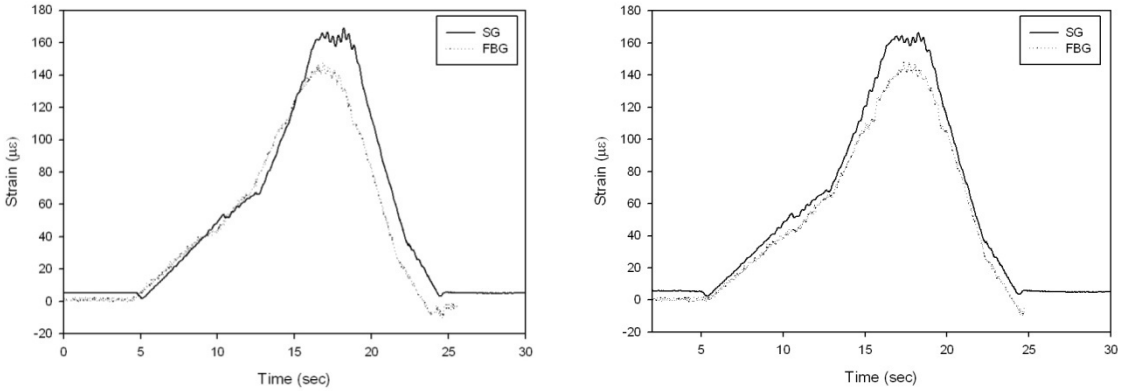

(a) Load case N_SR1 (b) Load case N_SR2

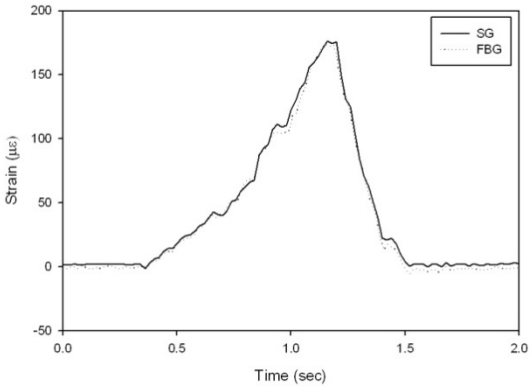

(c) Load case N_D1_30

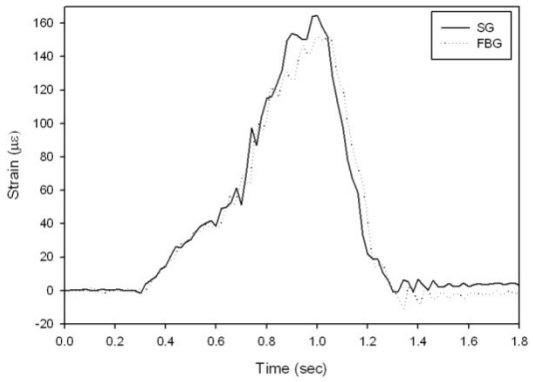

(d) Load case N_D2_30

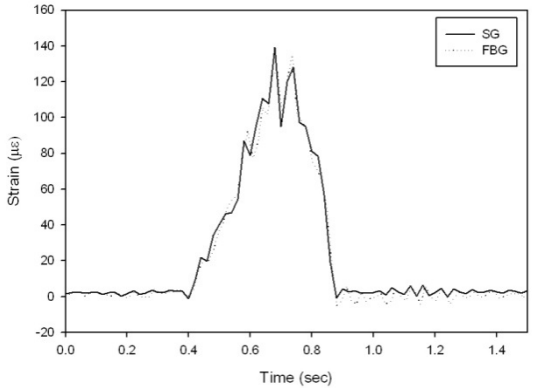

(e) Load case N_D1_55

Figure 63
SG and FBG strain comparison for sensors on girder

APPENDIX C

Experimental Study to Examine Deck Relative Deflection

The American Association of State Highway and Transportation Officials (AASHTO) load and resistance factor design (LRFD) bridge design specifications has recommended limits of live load deflection for concrete, steel, and wood construction, as shown in Table 5 *[10]*. However, no limits have been established for FRP decks. From literature, it is clear that composite bridges constructed for demonstration projects have been designed for allowable deflections from a range of L/425 to L/1,300 where L represents the support span *[11], [12]*. Since no current standard exists on the deflection limit in the design of these systems, an experiment was carried out on small section of the actual bridge deck. The FRP bridge panel specimen was evaluated by monitoring acoustic emission, load, and displacement.

Table 6
Allowable live load deflection limits in AASHTO LRFD bridge design specifications

Material	Allowable deflection at service load
Steel, Concrete and Aluminum	L/800
Wood	L/425

Description of the Test Specimen

The test specimen was provided by Alcan Baltek Corporation. Except for dimensions, the configuration and manufacture of the specimen was carried out in the same manner as the Pierre Part Bridge panel constructed in Assumption Parish, Louisiana. The overall depth of the specimen was 5 in. (0.127 m) and the thickness of the face sheets were 0.5 in. (0.0127 m). The specimen is representative of an approximately 19-in. (0.4826-m) wide strip of the original panel used during bridge construction. The dimensions and support setup of the test specimen have been detailed in Figure 64.

On arrival at LSU, it was noted that the provided test specimen had a few dimensional irregularities at certain ends. These irregularities were a result of an improper setup during the initial trial resin vacuum-infusion process.

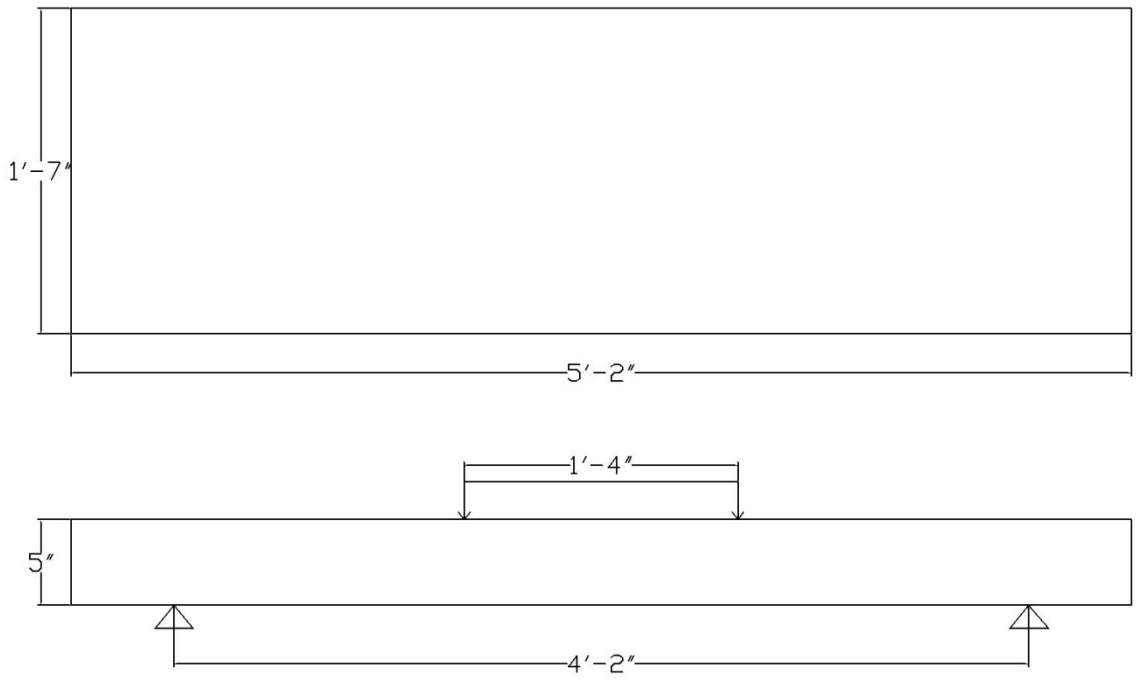

Figure 64
Test panel dimensions

Test Setup and Instrumentation

Bending tests were conducted using 4-point loading conditions. The panel was placed on support I beams separated by a distance of 50 in. (1.27 m). Elastomeric bearing pads were inserted between the contact surface of the support beam and composite panel to reduce noise due to friction. A bearing pad was also inserted below the loading arm of the loading machine.

A load was applied to the specimen by means of a material testing system (MTS) 550 kip testing machine with a 6-in. (0.1524-m) stroke length. Since the MTS did not have a load cell, the load was measured indirectly from the displacement measures of the cross-head. The loading procedure adopted comprised of a stepped incremental load, hold, and reload pattern shown in Figure 64 to enable non-destructive structural integrity assessment. A single LVDT sensor was placed at midspan of the panel to measure deflection. The LVDT was attached with a data acquisition unit (Cooper data chart 2000), which gives the instantaneous displacement of the beam. Both load and deflection measurements were collected at a 1 Hz sampling rate. Final test setup adopted for the test panel is shown in Figure 66.

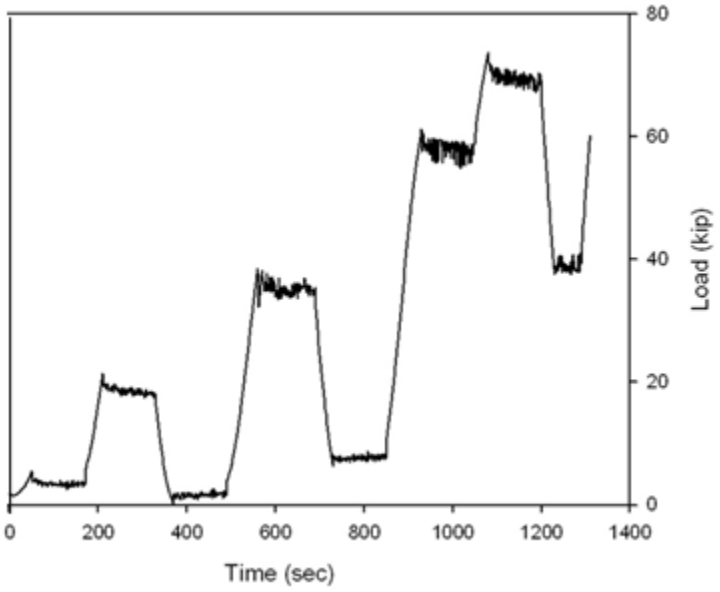

Figure 65
Load profile

Figure 66
Experimental setup with instrumentation

Results

The primary result from the experimental four-point bending tests is shown in Figure 66. To assess the deflection of the panel under service load, a HS-20 truck load, i.e., a 16-kip single tire load can be placed on this panel. From Figure 67, a deflection of 0.23 in. (0.584 cm) can be estimated for a 16-kip load.

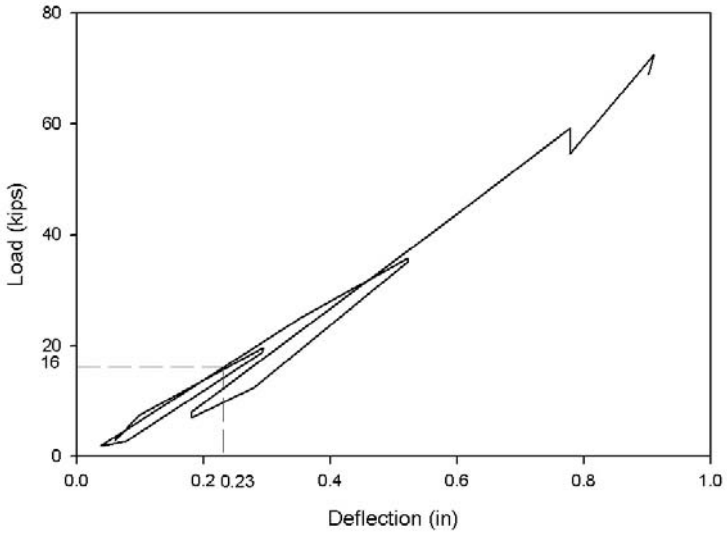

Figure 67
Measured load and displacement

To calculate the actual deflection of deck, an equivalent strip width rather than the specimen width [19 in. (0.4826 m)] should be used. There are no code specifications in this regard available. AASHTO LRFD code specifications for concrete deck and wood deck are used here as a reference:

> Cast-in-place concrete, positive moment, equivalent width = 26 + 6.6S = 26 + 6.6 x 4.17 in. = 53.5 in. (1.3589 m)
> Wood, interconnected, equivalent width = 4.0h + 30 = 4 x 5 in. + 30 = 50 in. (1.27 m)

If the equivalent width is assumed to be 50 in. (1.27 m) (same as wood deck), then the actual deflection under a HS20 wheel load considering a dynamic allowance of 0.33 = 19 in. /50 in. x 0.23 in. x (1 + 0.33) = 0.1162 in. (0.29 cm). Thus the span/deflection ratio = 50 in. /0.23 in. = 430. Hence, a 50 in. (1.27 m) beam support span approximately generates an L/430 response at the design service load. It does not meet the desired deflection index of less than L/800, which is the recommended limit of live load deflection for steel, aluminum, and concrete construction by AASHTO. However, it does seem to be closer to the recommended deflection limits for wood construction (L/425).

APPENDIX D

Load Rating using FEM of Steel Grid Deck

The bridge selected for this study is the Pierre Part Bridge on route LA 70 in District 61, Assumption Parish, Louisiana. The bridge was built in 1988 with a design load of HS20-44 and ADT about 6000. The bridge, with a total length of 145 ft. (44.2 m) and a roadway width of 46 ft. (14 m), consists of six 20-ft. (6.1-m) spans and a 25-ft. (7.6-m) span. The 20-ft. (6.1-m) spans are concrete structures and the 25-ft. (7.6-m) span consisted of a steel grid deck supported on steel girders. Figures 67 and 68 show the damaged grid deck that needs to be replaced in the 25-ft. (7.6-m) span. Under these conditions, the bridge's load rating was carried out using FEM, and the reduction in its load rating was assessed and replacement with an FRP deck was justified.

Figure 68
Repaired sections of the damaged grid deck

Figure 69
Lost sections in the steel bridge deck

Description of Girders and Deck
Span = 25 ft. (7.6 m)

Beam spacing = 4 ft. (1.21 m)

Depth of beam section = 13.89 in. (0.3528 m)

Width of top and bottom flange = 9.995 in. (0.2538 m)
Thickness of flange= 0.645 in. (0.016 m)
Thickness of web= 0.375 in. (0.0095 m)
Fy = 36 ksi (248 MPa)
Metal deck thickness = 5 in. (0.127 m)
Deck material unit weight = 0.49 kcf (15.7 k/m^3)

a) Girder with deck

Finite Element Model Details. To determine the moments required for a bridge rating, a single steel grid deck (69.38in. X 298 in. (1.76 m X 7.56 m)) supported on two W14X61 girders was modeled in Ansys using the Shell 63 element. The deck was modeled to act compositely with the girder. Details of the model are shown in Table 7. FEM models used for analysis for both intact and damaged decks supported on steel girders are represented in Figures 70 and 71.

Table 7
FEM model details

Property	Details
Geometry	2-D a)Steel grid deck 70 in. X 300 in. X 0.5 in. b)Two steel girders @ 4 ft. spacing
Material property *Deck and Girder* Steel	**Ex** **μ** (msi) 29 0.3
BC DOF at z = 0 in. DOF at z = 300 in.	 UX = 0;UY =0; UZ = 0 UY = 0; UX = 0

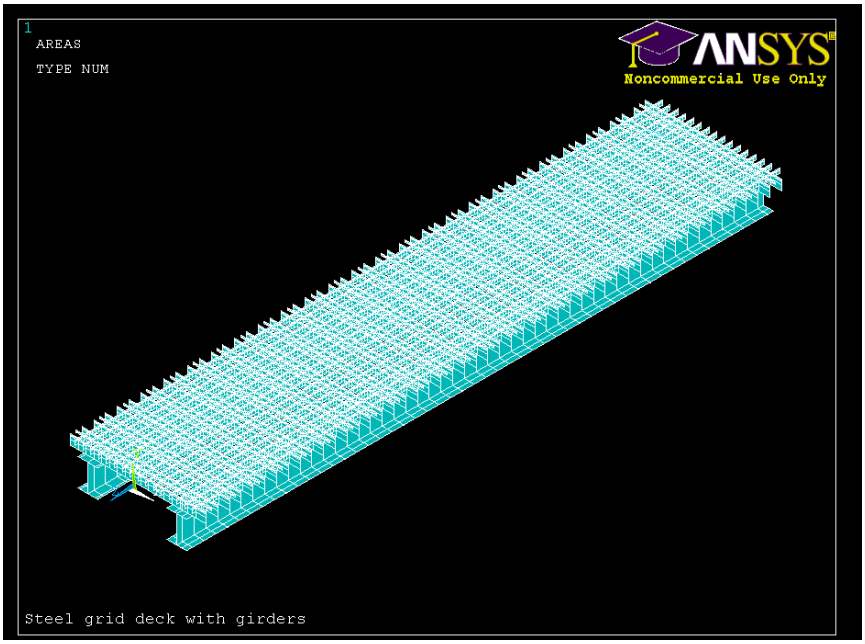

Figure 70
FEM model for intact steel deck on steel girders (one panel)

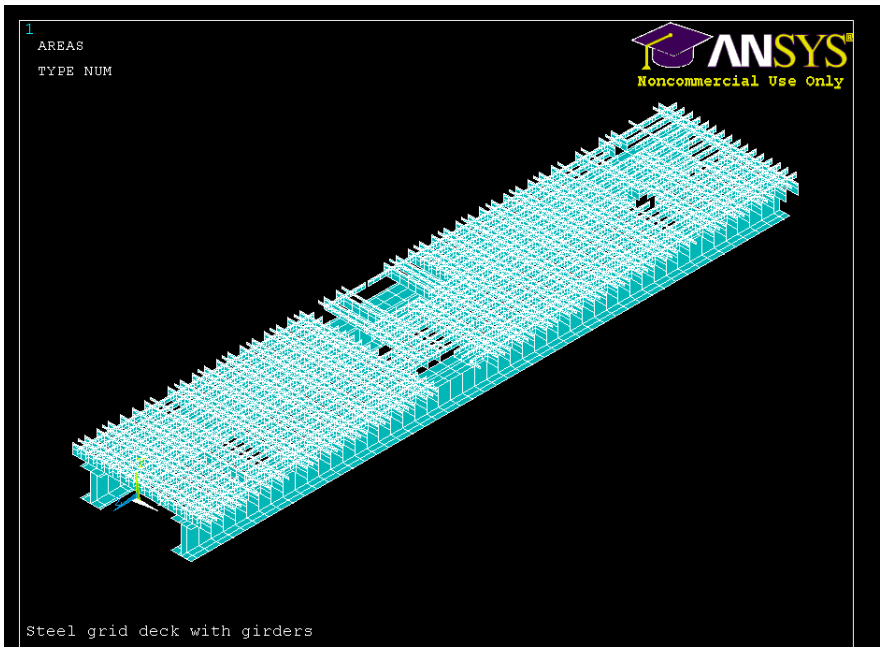

Figure 71
FEM model for damaged steel deck on steel girders (one panel)

Load Rating Analysis

Since LADOTD had used the H 20 truck model to determine the rating using the LFD method, the same was followed in all calculations shown below. Being a short span bridge, the live load moments were determined by applying a single 32-kip point load on the midspan of the bridge. The results are summarized in Table 8.

To determine rating, the following sets of formulas based on moment capacity were used:

a) Allowable Stress Design (ASD)

$$RF_{INV} = \frac{M_{INV} - M_{DL}}{M_{LL}(1 + I)}$$

$$RF_{OPR} = \frac{M_{OPR} - M_{DL}}{M_{LL}(1 + I)}$$

b) Load Factor Design (LFD)

$$RF_{INV} = \frac{3/5\ M_U/1.3 - M_{DL}}{M_{LL}(1 + I)}$$

$$RF_{OPR} = \frac{M_U/1.3 - M_{DL}}{M_{LL}(1 + I)}$$

Moments

Intact Deck

M_{DL}(FEM) =144.6 k-in. (16.3 kNm)

M_{LL} (FEM) = 671.232 k-in. (75.83 kNm)

Damaged Deck

M_{DL}(FEM) =130.03 k-in. (14.69 kNm)

M_{LL} (FEM) = 674.27 k-in. (76.18 kNm)

M_{allow} (Inv) = 1825.56 k-in. (206.25 kNm)

M_{allow} (Opr) = 2489.4 k-in. (281.25 kNm)

Mu = 2987.28 k-in. (337.5 kNm)

Table 8
Result summary of steel girders

	Load	**R.F** (ASD)	**R.F** (LDF)	**Rating (Tons)**	**Rating (DOTD)**
Intact deck					
Inventory	H 20	1.88	1.38	20*1.88 = 37.6	36
Operating	H 20	2.62	2.41	20*2.62 = 52.4	60
Damaged deck					
Inventory	H 20	1.8	1.3	20*1.8 = 36	
Operating	H 20	2.6	2.4	20*2.6 = 52	

b) Deck

Finite Element Model Details. A single simply supported steel grid deck [69.38 in. X 300 in. (1.76 m X 7.56 m)] was modeled in Ansys using the Shell 63 element. The details of the model are shown in Table 9. The stresses required for the rating were determined from FEM models for both intact and damaged decks as represented in Figures 72 and 73.

Table 9
FEM model details

Property	Details
Geometry	2-D a)Steel grid deck 69.38 in. X 300 in. X 5 in. (1.76 m X 7.56 m X 0.127 m)
Material property Deck and Girder Steel	Ex μ (msi) 9 0.3
BC DOF at x = 22.69 in. (0.57 m) DOF at x = -22.69 in. (-0.57 m)	 UX = 0;UY =0; UZ = 0 UY = 0; UX = 0

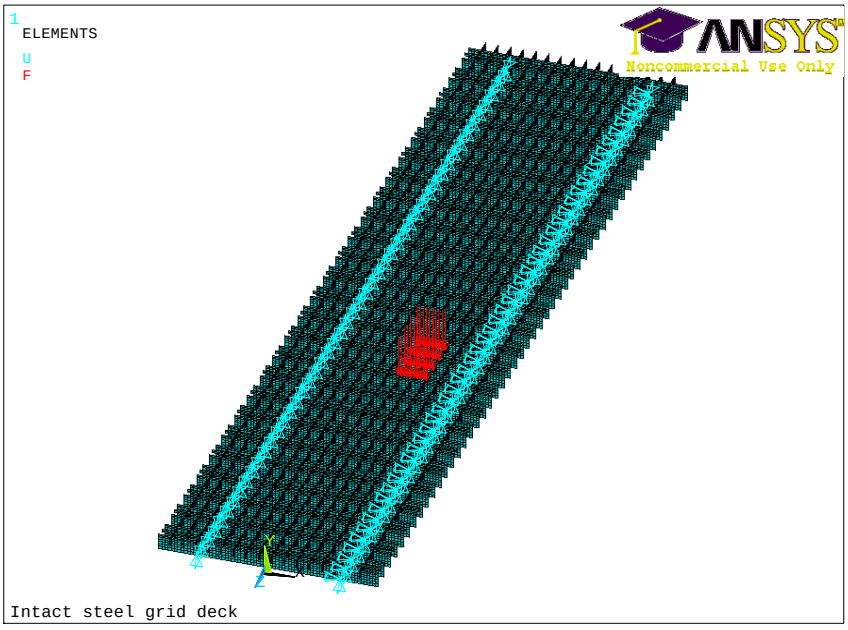

Figure 72
FEM model for intact steel deck (one panel)

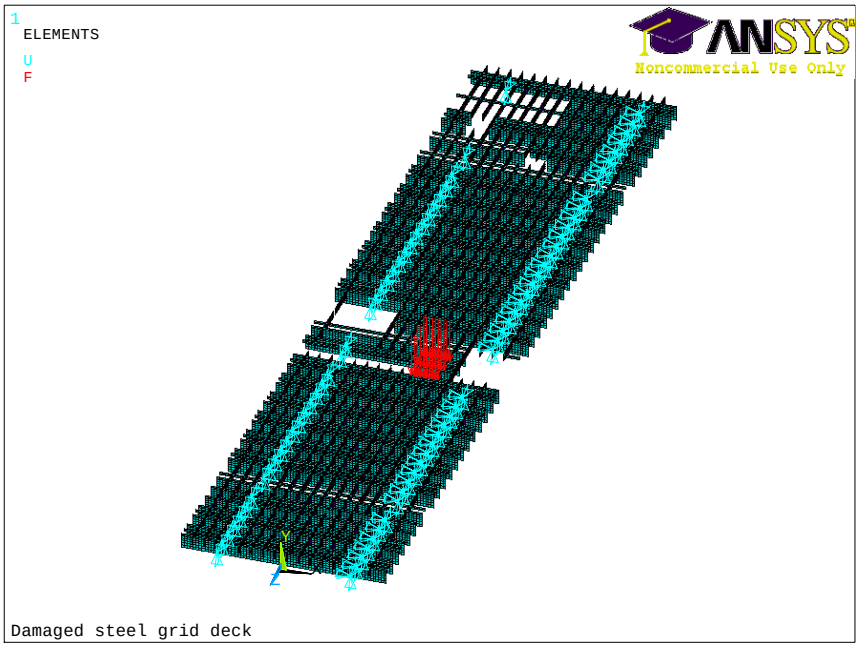

Figure 73
FEM model for damaged steel deck

Load Rating Analysis

An HS 20 truck model was used to determine the rating using the ASD method. Being a short span bridge, the live load moments were determined by applying a 16-kip pressure load on the midspan of the bridge. To determine rating, the following sets of formulas based on stresses were used. The results are summarized in Table 10:

a) ASD

$$RF_{INV} = \frac{F_{INV} - F_{DL}}{F_{LL}\,(1 + I)}$$

$$RF_{OPR} = \frac{F_{OPR} - F_{DL}}{F_{LL}\,(1 + I)}$$

Stresses

Intact Deck	Damaged Deck
FDL (FEM) = 0.075322 ksi (0.519 MPa)	FDL (FEM) = 0.141044 ksi (0.972 MPa)
FLL (FEM) = 6.762 ksi (46.62 MPa)	FLL (FEM) = 15.499 ksi (106.86 MPa)
Fallow (INV) = 19.8 ksi (136.5 MPa)	
Fallow (OPR) = 27 ksi (186.15 MPa)	

Table 10
Result summary of steel deck

	Load	**R.F** (ASD)	**Rating (Tons)**
Intact deck			
Inventory	HS 20	2.24	20*2.24 = 44.8
Operating	HS 20	3.06	20*3.06 = 61.2
Damaged deck			
Inventory	HS 20	0.97	20*0.97= 19.4
Operating	HS 20	1.3	20*1.3 = 26.6

APPENDIX E

Laboratory Work for Moisture Monitoring of Balsa Wood with FBG Sensors and Slip Monitoring using OTDR

Part I: Moisture Monitoring

Specimen Description. The specimen used in this work was a small section of a FRP-wrapped balsa wood beam. The specimen cross section was 6.3 in. X 4.72 in. (160 mm X 120 mm). The sensor layout is depicted in Figure 74. The optic fiber embedded with two FBG sensors passed through two closely aligned PVC flexible tubes with each of the FBG sensors positioned in the middle of the tubes. The optic fiber terminated in the second tube. The length of the PVC tube matched the perimeter of the balsa wood cross section and the distance between the two tubes was about 1.18 in. (30 mm). Before installation, the optic fiber ends were temporarily fixed to the PVC tubes to prevent slipping. The optic fiber was then helically wrapped and bonded around the balsa wood with a winding pitch being the tube outer diameter. When winding the optic fiber, a certain force was applied to ensure firm contact between the PVC tube and balsa wood, leaving a tensile force in the fiber. Two parts of the optic fiber (A and B as shown in Figure 74) were bonded on the balsa surface, forming two fiber loops. In such a configuration, the FBG senor in the first loop will be used to measure the specimen hoop expansion, while the other FBG sensor in the back loop, staying loosely in the PVC tube thus immune to external force influence, will be used to measure the temperature. For convenience, the first FBG sensor is referred as FRP moisture sensor, and the second one is referred as FBG reference sensor. The ends of the PVC tube were sealed with silicon gel to avoid water ingress.

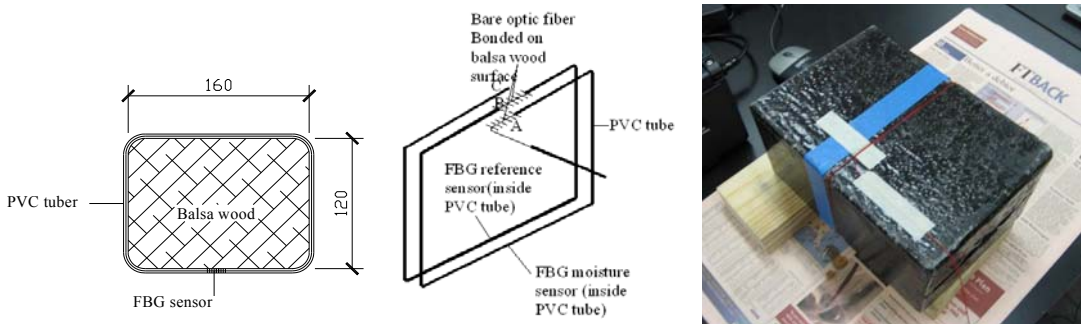

Figure 74
Moisture sensor configuration

The specimen was fully soaked in water as shown in Figure 75. A steel object was placed above the specimen to hold the specimen in the water bath. Moisture can only penetrate the wood through the exposed wooden cross section.

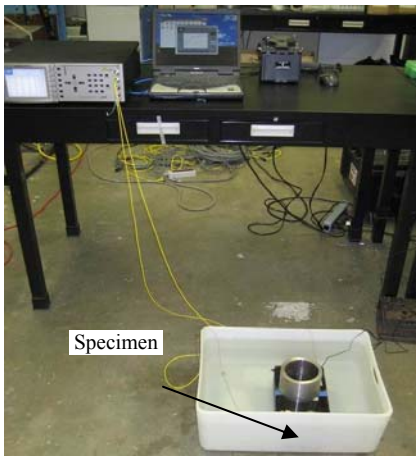

Figure 75
Test configuration

Test Result Analysis and Discussion

In Figure 76, the wavelength shift of the FBG moisture sensor and its reference sensor is plotted. During the first five hours, the wavelength of the FBG moisture sensor kept dropping by 50 pm. The trend changed in the subsequent three hours indicating a 17 pm rise and then maintaining a constant level. The wavelength shift of the FBG moisture sensor was caused due to both moisture expansion and temperature change. Since the temperature kept decreasing in the whole process as shown by the reference sensor, the rising fraction in the curve can only be attributed to moisture expansion.

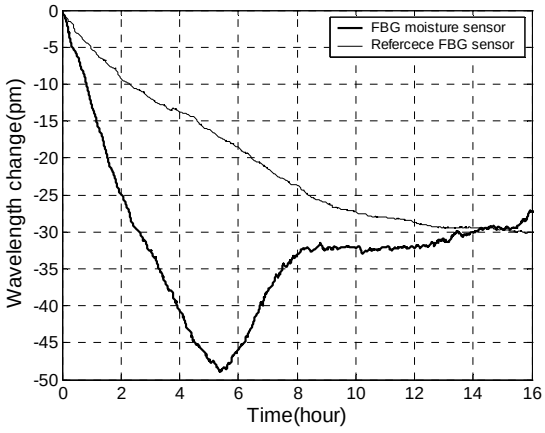

Figure 76
Wavelength shift of FBG moisture sensor and the reference FBG sensor

To identify the moisture expansion part of the curve, thermal expansion influence should be eliminated. The thermal expansion coefficient of the specimen was calibrated in an adjustable temperature chamber as shown in Figure 77. The calibrated factor in terms of wavelength shift was deduced to be 38.8pm/°C as shown in Figure 78.

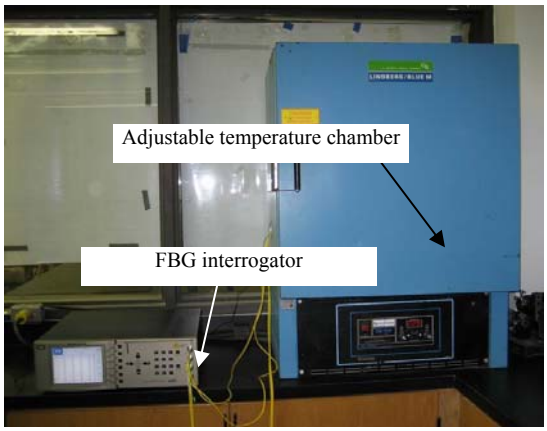

Figure 77
Measurement of the thermal expansion factor of the specimen

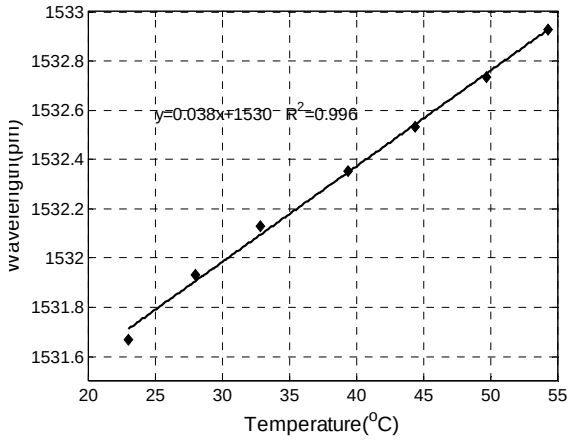

Figure 78
Calibration of round thermal expansion factor of specimen

Subtracting the thermal expansion from the curve, the hoop moisture expansion is plotted as shown in Figure 79. From this plot, it can be observed that, in the first five hours, the moisture expansion changed, only slightly, in the range less than 7με. In the next five hours, the moisture expansion climbed at a faster rate, by an increment of 50με, which implies that in five hours time the moisture had reached the monitored cross section where the FBG moisture sensor was located. The decreasing trend observed after 10 hours indicated that the moisture in the considered cross section had reached the saturation state.

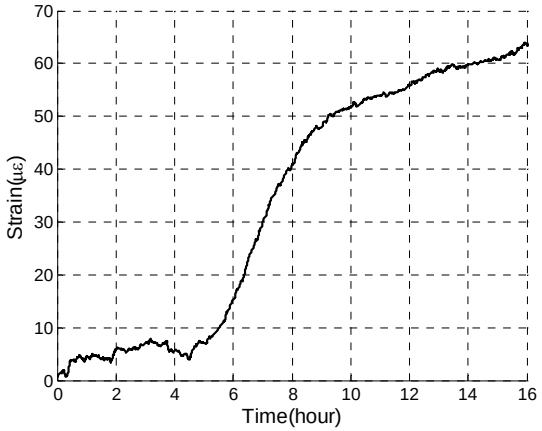

Figure 79
Hoop moisture expansion of the specimen

Summary

A novel moisture monitoring technique using FBG sensors was investigated, by which volume change was measured to indicate the moisture. It was found that the expansion of the FRP-wrapped balsa wood assembly due to moisture action is evident and can be used to indicate the moisture change.

Further research should be pursued to establish the relationship between moisture content and expansion ratio. More factors such as temperature and wood fiber direction should be taken into account.

Part II: Slip Monitoring Using OTDR

Debonding Monitoring Principle

A measurement of optical backscatter as a function of linear position, OTDR (optic time domain reflectometer), is a well established method for examining fiber-optic cables. For example, areas of high loss (excessive bends) or points of fiber fracture and fiber ends are shown in Figure 80. The technology is well developed and a wide range of instruments able to resolve changes in the backscatter signal of less than 0.001dB in magnitude with a spatial resolution of centimeter magnitude is commercially available.

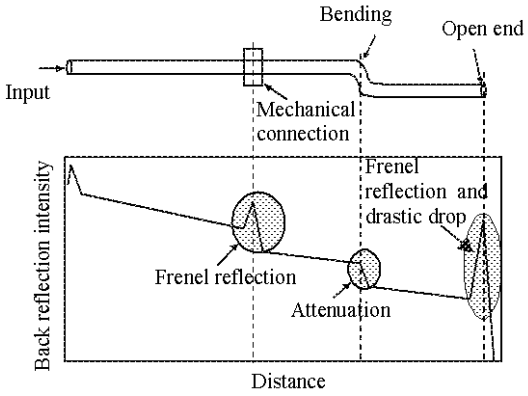

Figure 80
Typical reflection chart of OTDR

Figure 81 demonstrates the application concept of the distributed fiber optic technology in bridge deck slip monitoring. A tiny V-shaped notch with a depth of 0.01968 in. (0.5 mm) was made on the upper web of the steel girder. However, the depth of the notch was so small that it didn't influence the performance of the girder. A sensing optic fiber was put inside the notch and the notch was filled with epoxy. The bridge deck was placed on the girder after the

cure of the epoxy in the notch. Then the sensing optic fiber was fixed on the bridge deck with epoxy at the place close to the upper web edge of the girder, leaving the fiber in between free of epoxy. During the application, the optic fiber was slightly stressed with the tensile load. Ideally, when the bridge deck slips, the optic fiber in interface will stay together with girder and the part of the optic fiber fixed on the deck will go together with deck. The optic fiber will bend at the two points of the girder edge and the epoxy edge. This will introduce loss in the optic fiber, which can be identified by OTDR when debonding occurs. In general, the optic power loss resulted from bending is related to the curvature radius R of the bent optical fiber as:

$$\alpha = AR^{-1/2} \exp(-UR) \tag{2}$$

where, R is the bending radius of the optical fiber, and A and U are the coefficients independent of R *[13]*. When R is less than 0.787 in. (20 mm), the bending loss is obvious. Theoretically, the curvature R is likely to be decided by the crack width. However, in practice, because of the complexity of stress condition of optic fibers, this relationship is normally obtained by calibration test.

By one optic fiber cable, multiple places on the bridge deck can be monitored as shown in Figure 82. This distributed sensor configuration can greatly reduce the work in the sensor application compared with other traditional "pointed" sensors.

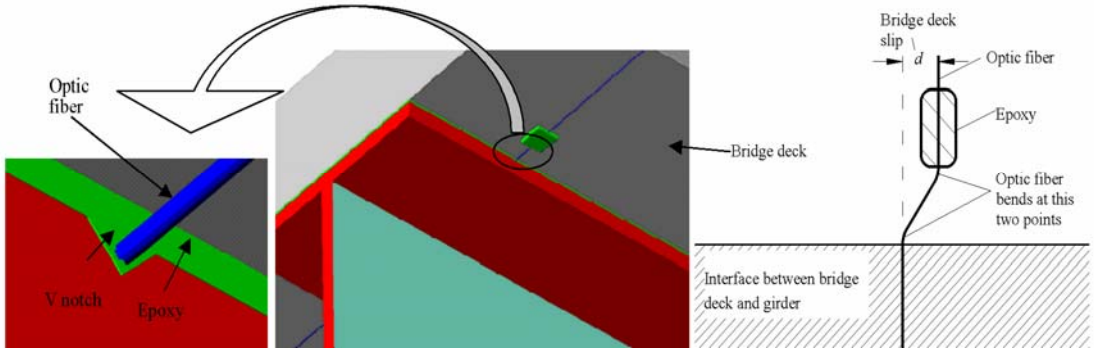

Figure 81
Monitoring principle

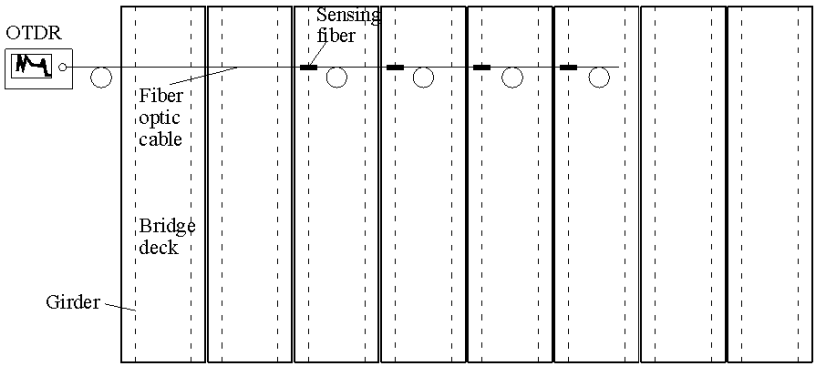

Figure 82
Sensor instrumentation plan

Experiments and Results

To validate the proposed monitoring method, a steel specimen, which was composed of two parts, was made to simulate the slip situation between the bridge deck and the girder. The specimen's dimension is shown in Figure 83. The two parts of the specimen form an interface between them. Part 1, which represents the bridge deck, is wider than Part 2, which represents the girder. The sensor installation is schematically depicted in Figure 84. A v-shaped notch was cut on Part 2 for holding the optic fiber. The epoxy used here was M-bond AE10 (produced by Vishay Company). The optic fiber used was the standard graded-index fiber with the 62.5/125μm core/cladding diameter and a layer of 250μm acrylate cladding. The OTDR [EXFO FTB200 with module 7200D, resolving backscatter signal of 0.001dB in magnitude with a spatial resolution of 0.131 in. (0.04 m)] was linked to the sensing optic fiber with a spool of fiber between the OTDR bulkhead and the sensing optic fiber, so the very weak backscattered signals from the fiber bending would not be overwhelmed by the strong pulse created at the bulkhead connection.

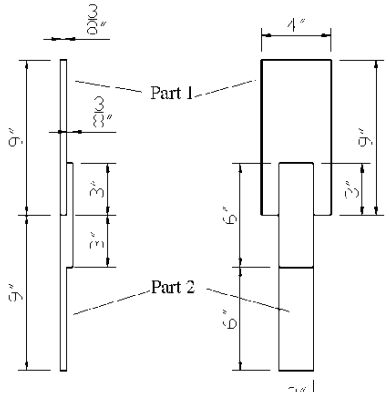

Figure 83
Specimen dimension

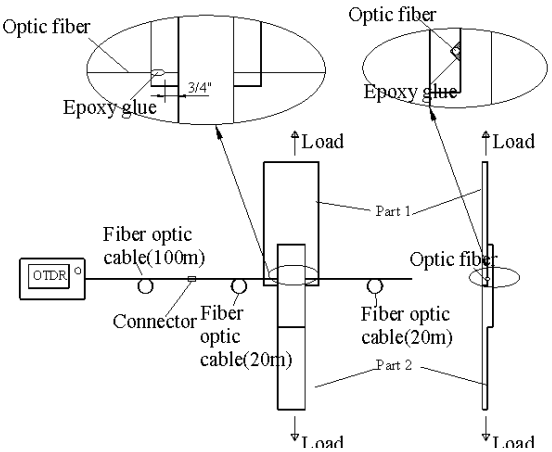

Figure 84
Fiber optic sensor instrumentation

Two identical tests, namely test 1 and test 2, were conducted to validate the proposed method. The test configuration is shown in Figure 85. The two parts of the steel specimen were bonded together with the sensing optic fiber instrumented as described in Figure 83. The specimen was loaded monotonically by the MTS machine from its two ends. A displacement transducer with a resolution of 1.64 in. (0.5 m) was used to measure the slip between the two parts. During the loading process, the optic fiber was interrogated through OTDR. Before the interface failure, no signal change on the optic fiber was observed. Once the interface fails, the optic power loss was identified by OTDR.

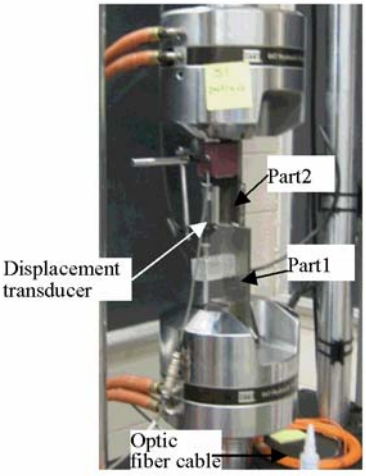

Figure 85
Test configuration

Figure 86 compares the two OTDR traces in the states before the loading and after interface failure for test 1. When the interface failed, a significant power loss was observed. The interface failed at 0.0137 in. (0.348 mm), inducing the optic power loss of 0.416 dB in the sensing optic fiber. Figure 87 shows the typical OTDR traces during the loading process, indicating the continuously increased power loss against the increasing slip. Figures 88 and 89 show the cases for test 2. The interface failed at 0.0066 in. (0.17 mm), causing an optic power loss of 0.24 dB. After the interface debonding, the inner part of the optic fiber, including the fiber core and the cladding in the polymer coating, remained undamaged. With the increase of the interface slip, the optic power loss in the optic fiber kept increasing. The relationship between the slip and the optic power loss and slip is shown in Figure 90. The two curves show a similar trend. Thus the event of the debonding can be detected by the proposed method and the extent of slip can also be evaluated.

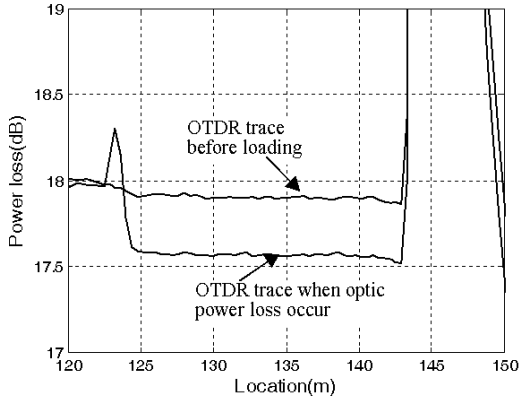

Figure 86
Comparison of OTDR traces between the state before loading and the state after interface failed for test 1

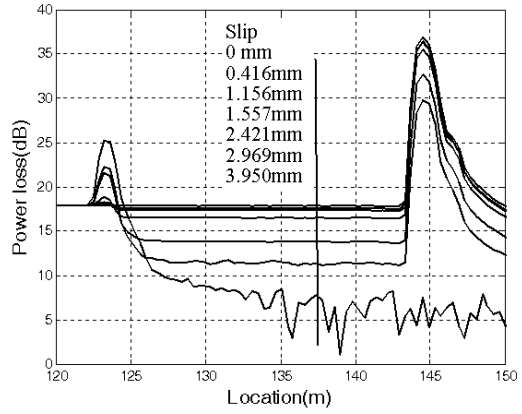

Figure 87
Typical OTDR reflection traces of test 1

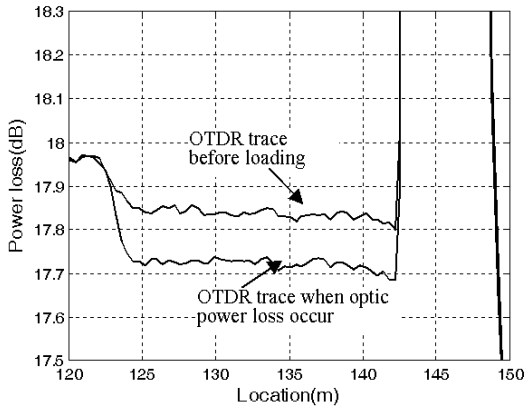

Figure 88

Comparison of OTDR traces between the state before loading and the state after interface failed for test 2

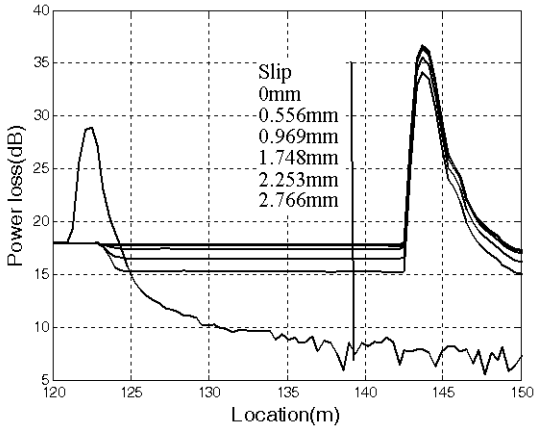

Figure 89

Typical OTDR reflection traces of test 2

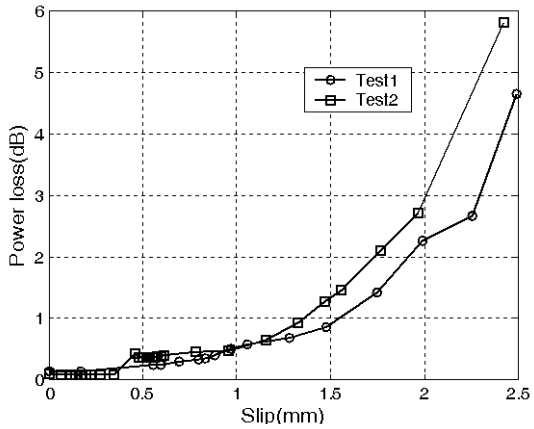

Figure 90

Relationship between the power loss and the interface slip

Summary

A monitoring system for the interface debonding based on common commercial OTDR was proposed. Experiments were conducted in the laboratory to validate this method. From the research conducted, the following conclusions can be drawn:

1) The proposed method is sensitive to the occurrence of the interface debonding. Once the debonding occurs, an obvious power loss induced from optic fiber bending can be observed.
2) The sensing optic fiber can slide within its polymer coating, leaving the cladding and the fiber core undamaged during the debonding. Thus, by the distributed arrangement, multiple places can be monitored through a piece of optic fiber.
3) The slip extent of the interface can be evaluated after the debonding. The optic power loss will keep increasing against the increasing interface slip.

APPENDIX F

Installation Procedure for Fiber Optic FBG and OTDR Sensors

Among the six FRP-balsa wood composite panels that were to replace the steel panels, one panel was chosen to include FBG sensors internally to monitor the strain in the transverse direction and moisture ingress (internal meaning sensor placement at the balsa wood core surface of the composite deck). Unique characteristics such as small size, immunity to electromagnetic/radio frequency interference, etc. enable convenient embedding of fiber optic sensors within the panel core without influencing final panel form or properties. Once installed, sufficient care in fabrication, placing, handling, and transportation of the panels are necessary to ensure functionality of the internally mounted sensors.

A typical bridge panel includes 50 individually wrapped balsa wood core FRP beams with a length of 5 ft. 10 in. (1.778 m) and cross-section 6 in. X 4 in. (0.1524 m X 0.1016 m), giving the panel an approximate dimension 300 in. X 70 in. (7.62 m X 1.778 m). Six balsa wood core beams were chosen for instrumentation of FBG sensors for strain, moisture, and temperature monitoring. Based on the instrumentation plan, the following components and tools were required:

FOS components:

- 9 FBG sensors for strain monitoring (3/instrumented beam)
- 6 FBG sensors for moisture and temperature monitoring (2/instrumented beam)
- PVC tube material (sufficient length)
- Hot melt glue/super glue
- Protection sleeves
- Optic fiber cables/connectors

Tools required:

- Marker pen
- Hand saw
- Cleaver and splicer unit
- Stripper, isopropyl wipes
- Standard measuring tape
- FBG data acquisition system

The general installation layout plan for the internal FBG sensors is detailed in the instrumentation plan document. Since the FBG sensors are to be installed internally, this step

has to be done prior to the deck fabrication process. Thus the following section is split into four parts:

(a) Strain sensor installation
(b) Moisture and temperature installation
(c) Composite panel fabrication process
(d) Slip sensor installation

Before discussing the installation procedure, some basics of fiber optic sensors and installations are first introduced below.

Fundamentals of FOS (Fiber Optic Sensing)

Optical Fiber. An optical fiber basically consists of a flexible dielectric waveguide that traps optical radiation at one end and guides it to the other. An optic fiber usually consists of at least two optically dissimilar materials. A typical fiber is packaged as shown in Figure 91. It is clear that besides the core and cladding mostly made of glass, a few additional layers made of different materials are added to enhance mechanical strength and flexibility properties of the fiber. The core is the main component that carries the light waves and defines two available modes of fiber configurations: single mode (core size < 10 μm) and multi-mode (core size 50 ~ 100 μm) *[8], [14]*.

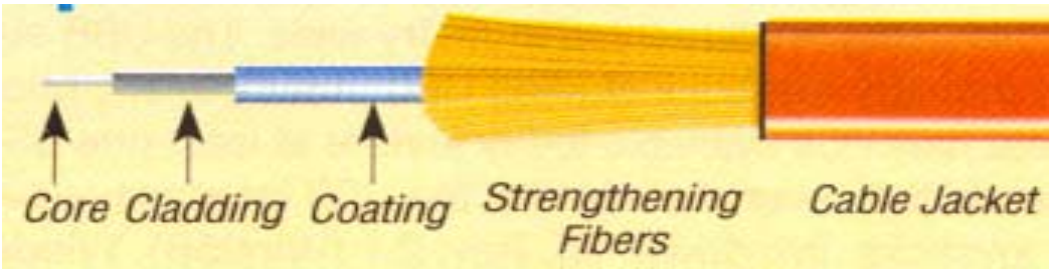

Figure 91
Basic structure of optical fiber

FOS is based on measuring changes in the physical properties such as phase, polarization state, intensity, and wavelength of the guided light. Based on the varied transduction methods of the guided light, FOS can be classified into: intensiometric, interferometric, and spectrometric. The sensing ability of the fiber can yet again categorize FOS into point/local, distributed, or multiplexed sensors. Optical fibers come in two configurations, multi-mode (core size 50 ~ 100 μm) and single mode (core size < 10 μm) *[8]*.

Unique characteristics of the FBG and OTDR type FOS sensors have led to favor the application of these sensors in structural health monitoring applications.

FOS Technology. The technology involves the installation of optical fiber sensors that measure strain and temperature in various civil engineering materials such as concrete, steel, composites, etc. Light waves transmitted down a thin optical cable measure change in signal properties that are correlated to elongation and contraction, measured in microstrains. When fiber optic sensors are used, strain is detected by a special demodulation unit and processed to yield a digital signal. Converting these signals to strains/temperatures is then performed by a data acquisition system. A number of different fiber optic sensors have been developed in recent years, from simple sensors that only measure an on/off state to multiplexed sensors that measure a range of wavelengths.

Monitoring with FBG Optic Fibers

FBG (Fiber Bragg Gratings) forms the integral sensing unit of this FOS. The FBG are intrinsic spectrometric sensors with local and multiplexing sensing abilities. An FBG is generated by engraving a periodic modulation of the refractive index of about 0.393 in. (1 cm) in the core of an optical fiber. The basic principle involved in the functioning of a FBG sensor is shown in Figure 92. Usually, the FBG sensor measures strain but can be modulated to measure displacement, acceleration, etc. The achievable resolution for these sensors is 1μ strain and they can have a working range of over 5000 μ strains
[15].

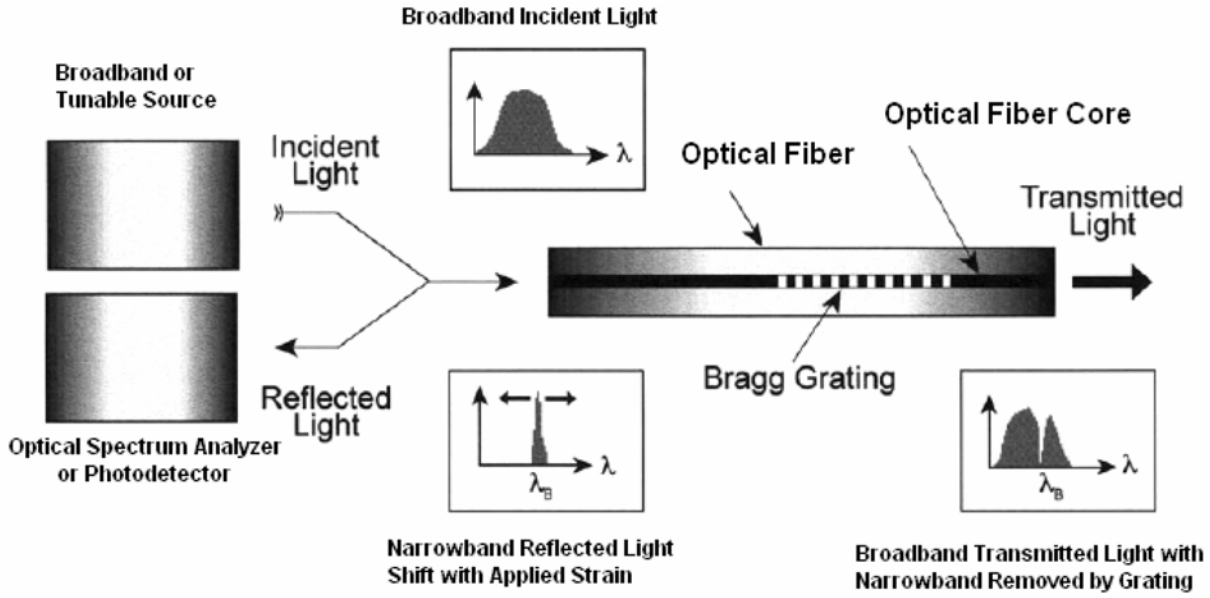

Figure 92
Principle of FBG

The spacing of the grating, called the "pitch," reflects the incident light with a narrow band centered about the "Bragg" wavelength, defined by:

$$\lambda_0 = 2n\Lambda \quad (3)$$

where, λ_0 is the Bragg wavelength, n is the average effective index of refraction of the grating, and Λ is the pitch spacing.

The FBG also provides a linear response based on the measurement of wavelength shift ($\Delta\lambda$) due to the straining of the gauge. Once temperature effects are accounted for in the wavelength shift, $\Delta\lambda$ provides a means of determining the strain according to the equation:

$$\Delta \lambda/\lambda_0 = (GF)\, \varepsilon + \beta\Delta T \quad (4)$$

where, $\Delta\lambda = \lambda - \lambda 0$; GF is the FBG gauge factor, typically about 0.75 − 0.82, ε is the strain; β is the thermal coefficient; and ΔT is the temperature change relative to the temperature at installation.

FBG sensors have a unique property over other FOS in that they encode the wavelength that does not suffer from disturbances of the light paths. FBG sensors could be particularly useful when gratings with different periods are arranged along an optical fiber. Each of the reflected signals will have a unique wavelength and can be easily monitored, thus achieving multiplexing of the outputs of multiple sensors using a single fiber. FBG sensors are preferred in many civil engineering applications and have been successfully employed in several structures requiring multi-point sensing distributed over a long range *[15]*.

A major advantage of FBG sensors is that they can be embedded in structures to measure strain. A lot of research has been conducted on the measurement of strain on reinforcement bars. A FBG strain sensor bonded to a piece of rebar (Figure 93) with the jacket of the fiber removed only in the sensing zone is bonded to the polished surface of the rebar by means of special glue. The sensing part is protected by several layers of rubber, and the input/output lead is protected by the fiber jackets *[14]*.

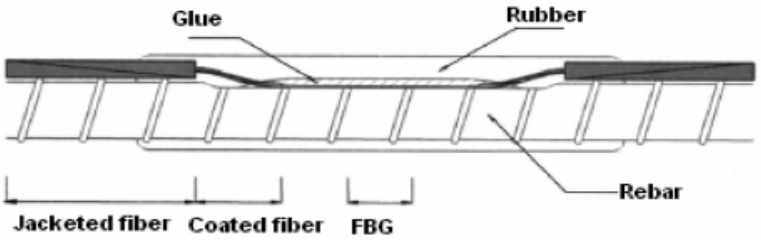

Figure 93
FBG sensors for strain measurement in rebar *[14]*

Monitoring with OTDR Based Optic Fibers

In simple terms, an OTDR (optical time domain reflectometer) based optic fiber is an

intensiometric sensor that carries and modulates the light within the fiber and has a sensing capability throughout the length of the fiber. These sensors can be used to measure either temperature or strain and give a resolution of 19.68 in. (0.5 m) or every 1°C for up to 6561 ft. (2 km) distance *[15]*.

The principle by which these sensors function is illustrated in Figure 94. These sensors are efficient for use in large structures like bridges as all portions of the fiber acts as a sensor, thus enabling monitoring changes along its length. Cracks or local strain changes can lead to a light intensity variation within the fiber that reflects as a power loss *[15]*.

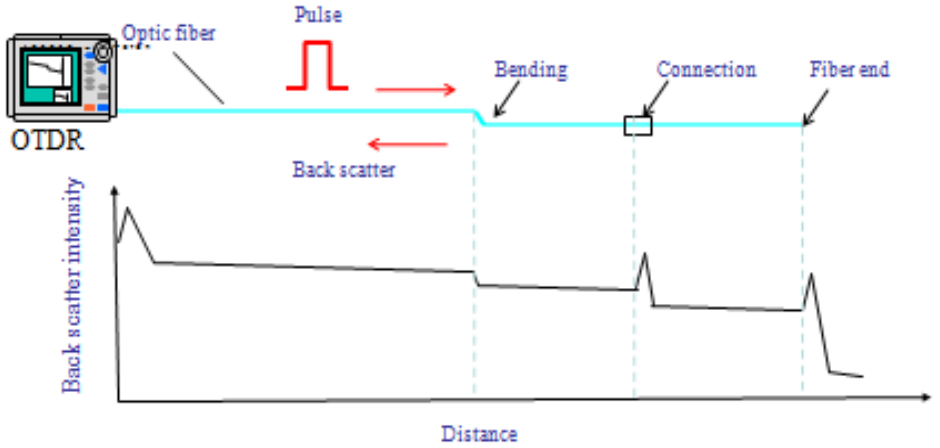

Figure 94
Principle of OTDR based optic fiber

The pulsed laser input signal sent from the OTDR equipment is reflected at each of the perturbations along the length of sensor as a power loss. This power loss is considered to be the outcome of mainly two effects in the optic fiber: bending/curvature or breaking. This intensity change can directly relate to the damage state when appropriately calibrated.

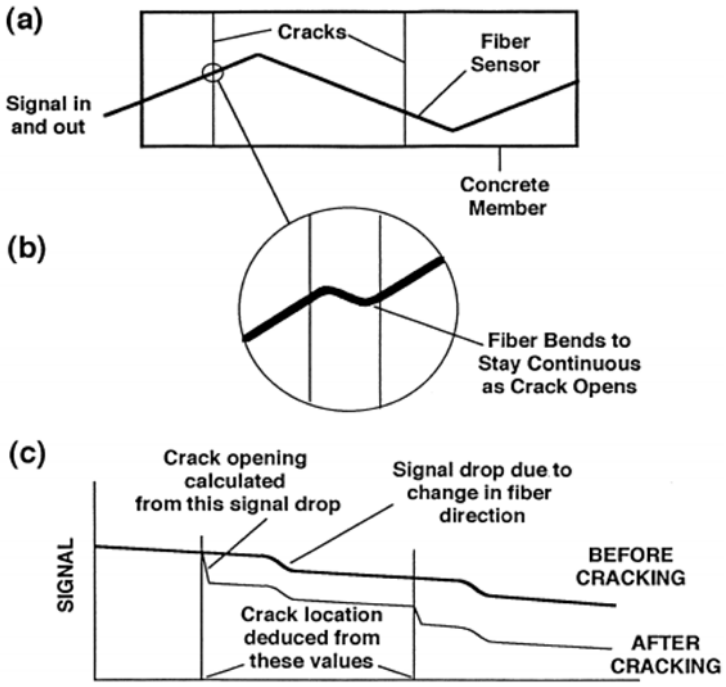

Figure 95
OTDR based optic fiber crack sensor *[16]*

To overcome limitations of conventional FOS such as local sensing and a lack of differentiation in the extent of damage, the zigzag sensor was introduced *[16]*. The working principle of this sensor is shown in Figure 95. The sensor was affixed to the bottom of a bridge deck to illustrate its applicability. A backscattered signal versus time data is collected before crack formation to establish a datum for comparison once the cracks are formed along the sensor length. There exist signal losses in the datum line as well, probably due to the absorption of light by the cladding of the fiber. When a crack opens in a structure, a fiber intersecting the crack at an angle other than 90^{o} has to bend to stay continuous [Figure 94 (b)]. This sudden bending of the fiber at the crack results in a sharp drop in the optical signal [Figure 95(c)]. From the time history data collected by the OTDR system, cracks can be located from the sharp signal drops. This data can be made quantitative by carefully calibrating the data to correspond to the crack opening length *[16]*.

Preparing the Fiber Optic Cables

Prior to using the FOS cables, they need to get prepared for use with the optical systems. Although, when coated with polymer cladding, the sensors are pretty tough once they are stripped of this layer before installation; care must be given to protect them from any damage. At times, the fiber might break or a specific end point for the fiber may be desired. To facilitate this, two devices are used, namely:

1. Fiber Cleaver - Fujikura CT-30 and
2. Fusion Splicer - Fujikura FSM-50S splicer

Fujikura CT-30

The CT-30 (Figure 96) provides a clean, straight fiber cut on both ends, making it suitable for splicing later. The 16-position blade yields 48,000 single-fiber cleaves and the built-in scrap collector stores fiber shards until they can be safely discarded.

Figure 96
The Fiber Cleaver unit - Fujikura CT-30

Procedure for cleaving is as follows:

- Remove at least 2 in. (0.0508 m) of the coating on the fiber from the section to be cleaved using a stripping tool.
- Clean the stripped end with lint free tissue soaked in iso-propyl alcohol.
- Open the cleaver cover and blade assembly.
- Place the fiber across the cleaving area, ensuring sufficient material crosses the cleaving section.
- Adjust the position of the non-stripped portion of fiber at the appropriate marking provided at the blade assembly. Lock the fiber in this position.
- Press down on the cleaver cover until a click is heard.
- Remove fiber from the cleaver apparatus and directly place into fusion splicer.

Fujikura FSM-50S Splicer

The FSM-50S Fusion Splicer uses a high temperature welding process to provide a better optical connection. The unit, shown in Figure 97, has both a splicing section and shrinking tube/protective sleeve heating section, which provides further protection to the newly spliced components. The unit also includes user friendly features such as calibration-free arc adjustments (with auto splice mode), automatic fiber type identification, and reduced operational steps. The device is operated by an easy-to-use touch screen menu.

Figure 97
Fiber splicing unit - Fujikura FSM-50S

Procedure for splicing is as follows:

- Power up the system (press on green icon) until it shows it's ready for fusion splicing.
- Open the middle compartment wherein the cleaved fiber ends have to be properly placed.
- If a protection sleeve is desired to protect the connection, make sure this has already been inserted through one of the cable ends before splicing.
- Place fiber ends into the fiber holder and ensure fibers are properly aligned before clamping them in position by looking at the touch screen.
- Press the "SET" button, located close to the heating device to begin splicing.
- Once the machine begins to splice the two ends, messages as to the progress of the splicing are displayed on the touch screen. Once splicing is completed the Optical power loss will be reported on the monitor and the fiber is ready for use. Typically an optical loss of up to 0.01dB is acceptable. It is possible that at times error messages will be obtained, stating misalignment and presence of dust. In such situations, remove the fiber ends, and prepare them again as explained in the procedure above.
- After splicing, remove the spliced fiber from the clamps. Slide the protection sleeve over the connection and place it directly into the heating section at the rear end of the apparatus.
- Once the fiber has been placed appropriately, close the top cover of the heating tube and press the "SET" button.
- Once heating and cooling operations are carried out, the system will beep to inform that the process has been completed.

Strain Sensor Installation

Three balsa wood core beams (S1, S2, and S3) were chosen for strain sensor installation. The general layout plan for the FOS sensors on the wooden beam is shown in Figure 98.

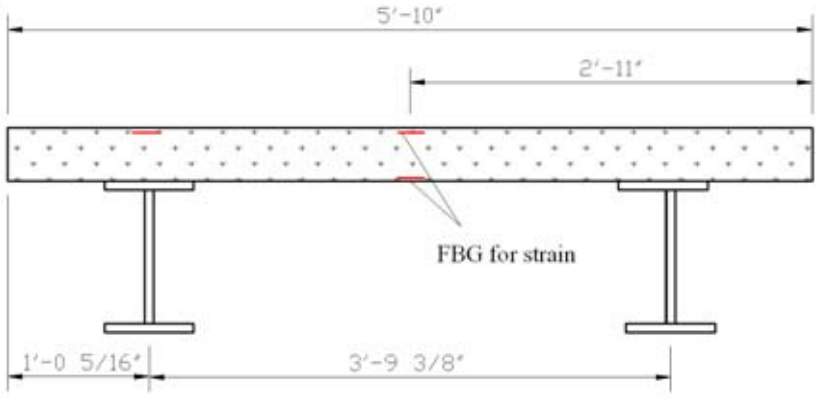

Figure 98
Instrumentation plan for strain sensors

The sensor installation basically is carried out in two steps:

(a) Preparation: This step involves identification of top and bottom surfaces of the wooden beam, all sensor locations from the sensor layout plan and marking these using a permanent marker as shown in Figure 99. Using a hand saw, shallow grooves are created from the edge of the beam to about 10 in. (0.254 m) into the beam to enable housing two cable jacket widths (Figure 9100). Shallow grooves are made across the cross-section where protected fibers have to be routed from one surface to the other to avoid sharp bends in the optic fiber cable and thus evade optical power loss. Cable lengths, PVC tube lengths for fiber protection, and connections that need to be spliced before fixing them onto the beam surface have to be decided.

(b) Installation: Ensure the sensing part of the optic cable is bare and carefully fixed at their previously marked positions using superglue. Spliced optic fiber connections need to be protected with resilient protection sleeves. The entire optic fiber layout is intermittently glued to the beam surface using either hot melt/super glue. While routing the FOS leads for all sensors, care must be taken to bring all of them through the bottom of the beam to ease cable aligning during the rest of the panel assembly process.

Figure 99
Strain sensor location marking

Figure 100
Optic fiber cable leads at beam edge

Moisture and Temperature Sensor Installation

Three of the balsa wood beams (M1, M2, and M3) were instrumented with FBG sensors for moisture ingress and temperature monitoring. The proposed layout for this monitoring is slightly different from the previous arrangement and is shown in Figure 101.

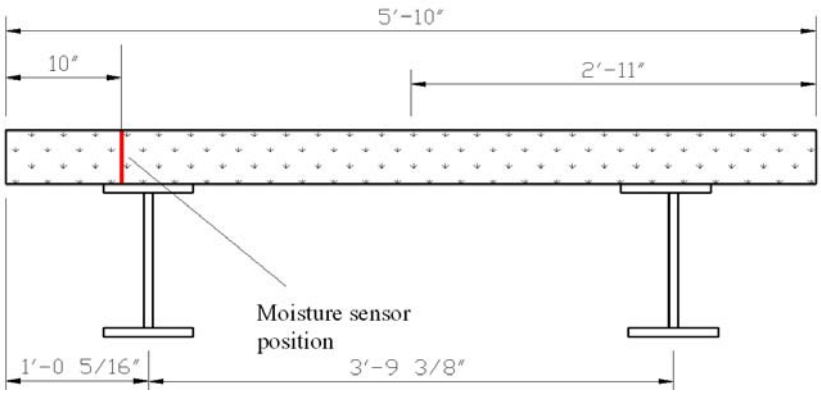

Figure 101
Instrumentation plan for moisture and temperature sensors

Again, the installation procedure involves two steps:

(a) Preparation: As mentioned previously, sensor layout is clearly marked and appropriate grooves have to be made along the circumference and edge of the beam as shown in Figure 102.

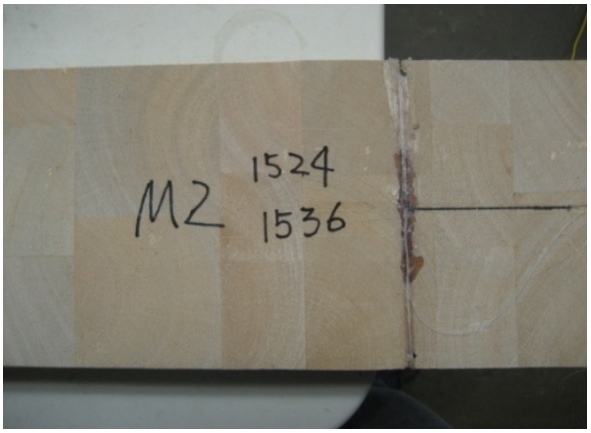

Figure 102
FBG sensor location marking

(b) Installation: Two FBG sensors have to be specially packaged in PVC tubes and placed circumferentially in the groove to enable moisture and temperature monitoring. This arrangement involves two loops as shown in Figure 103. The first loop with an FBG sensor attached to the beam surface senses the moisture contents of the wood by measuring the perimeter variation of the wood cross section, and the second loop housing the reference FBG, which is free of external force sensitivity, enables temperature measurement.

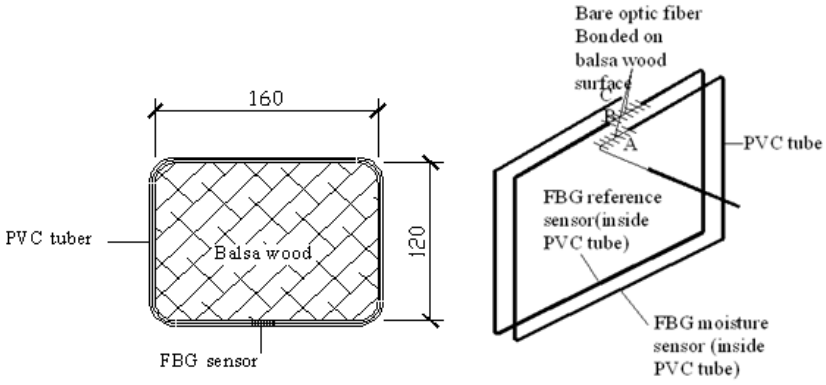

Figure 103
FBG loop moisture and temperature sensor

Before fixing the FBG sensor that monitors moisture in its position, the optical fiber has to be connected to the acquisition system to check both the wavelength of the FBG sensors used and exert an external tension force (approximately $\approx$ 1nm wavelength increase) as shown in Figure 104. Fix all optic fiber cables at marked locations using either hot melt/super glue.

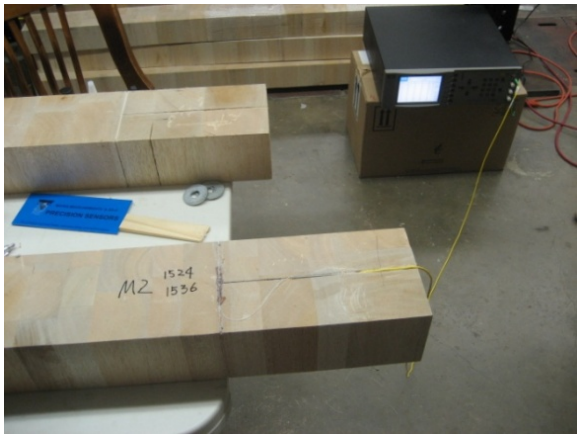

Figure 104
Optic cable connected to acquisition system

Composite Bridge Deck Panel Fabrication

Once all sensors were installed and functionality verified, the balsa wood beams were ready to be used in the bridge panel fabrication process. First, each of the beams were individually wrapped in a piece of balanced E glass fabric with a piece of continuous filament mat (CFM) underneath, secured to the wood by staples. Subsequent layers of E glass and CFM were assembled according to design specifications and wrapped around the beam and held firmly together using staples as seen here in Figure 105.

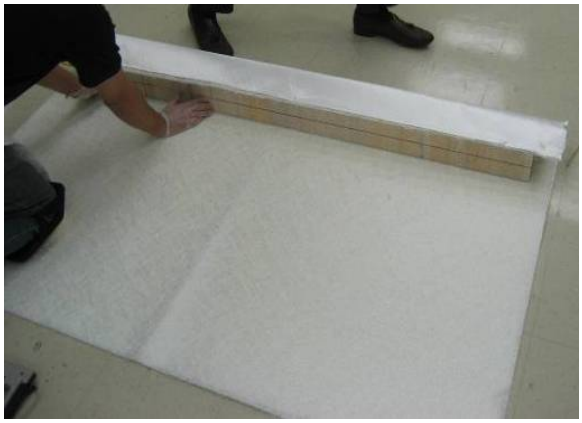

Figure 105
Wrapping of balsa wood beam with Eglass

Figure 106
Hardwire wrapped individual beams

The next step involved the laying of 3SX-21-12 hardwire cut to length of 75 in. (1.905 m) along both top and bottom surfaces of the balsa wood beam core. Once each beam was individually wrapped with hardwire (Figure 106), they were assembled onto a platform that held all 50 beams that constituted the actual bridge deck. The bottom of the platform was lined with sufficient E-glass fabric and CFM. The beams were then placed on this arrangement and held tightly together using a jack (Figure 107). Transverse and longitudinal pieces of hardwire were laid along the entire deck as shown in Figure 108.

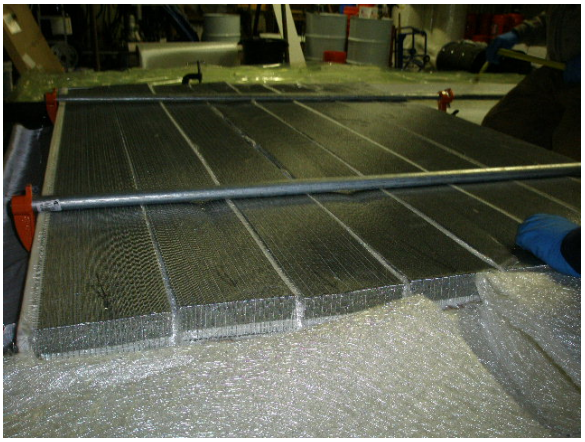

Figure 107
Beams being assembled on platform

Figure 108
Deck covered with longitudinal pieces of hardwire

As is clear from Figure 109, the optic fiber cables routed through the bottom of the wooden beams were let outside by providing slits in the wrapping material both during the wrapping and beam layup processes. Extra E-glass fiber mat pieces were provided at the optic cable outlets to further protect the cables.

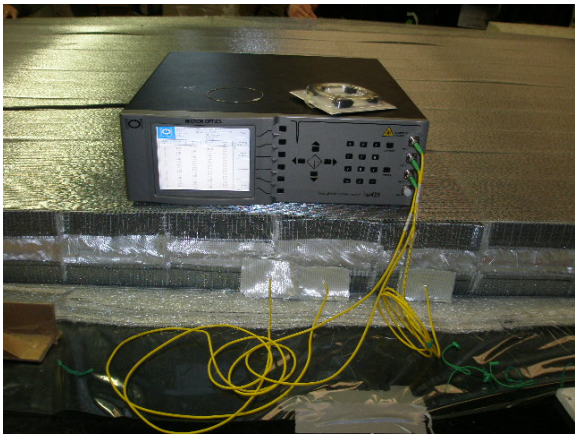

Figure 109
FBG sensors sensitivity check after layup of instrumented beams in panel

The final layup consisted of the CFM on the top surface of the deck (Figure 110). Since the entire panel was intended to be vacuum infused in a single step, the vacuum bag was customized accordingly. Thus, polythene sheets and peel ply fabric were inserted both at the top and bottom surface of the panel across the entire panel length.

Figure 110
Final layer of CFM placed over deck panel

To secure the optic fiber cables during the vacuum infusion process, customized packaging was adopted. Each pair of connector ends were inserted in PVC pipes open at one end and sealed with epoxy that allows for easy removal after infusion. The rest of the cable lengths were placed into polythene bags as shown in Figure 111 secured with butyl rubber sealant tape. The final step was to set the polythene bags with optic fiber cables to the sides of the panel along with the removable peel ply fabric (Figure 112). All sides of the panel were finally secured with 4 in. (0.1016 m) wide plastic plates after appropriate vacuum and resin inputs were placed.

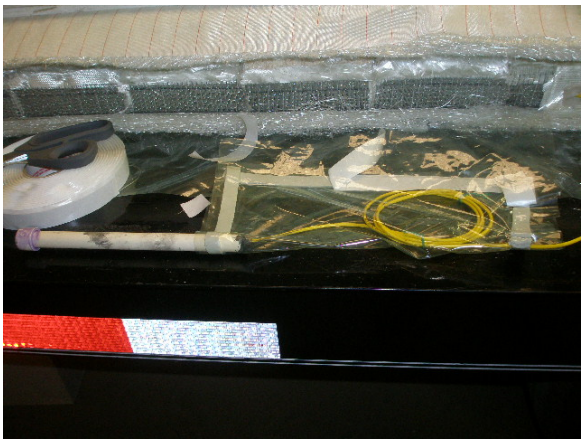

Figure 111
Optic fiber cables in customized packaging

Figure 112
Fiber cables in packaging secured to the panel edge with ply peel fabric

The entire assembly was vacuum-infused with vinyl ester resin and allowed to cure for a day in a similar setup as seen in Figure 113. A non-skid surface was applied after the deck was cured (Figure 114).

Figure 113
Vacuum infusion process

Figure 114
Finished bridge deck with non-skid surface

Slip Sensor Instrumentation in the Field

The proposed monitoring system was applied on the FRP-wrapped balsa wood bridge deck as shown in Figure 115. Before the instrumentation, a 0.0393 in. (1 mm) deep v-shape notch was cut on the surface of the steel bridge girder. The sensing optic fiber was then embedded into the v-shape notch, and the epoxy was evenly poured upon the surface of the bridge girder for bonding the bridge deck. Figure 116 shows one of the typical OTDR trace after the instrumentation of the monitoring system. The first reflection peak is induced from the mechanical connector and second one is from the optic fiber end. The sensing fiber position is at the position of 393.7 ft. (120 m) away from OTDR device. From this plot, no significant optic power loss is found at the sensing fiber position, indicating the integrity of the interface.

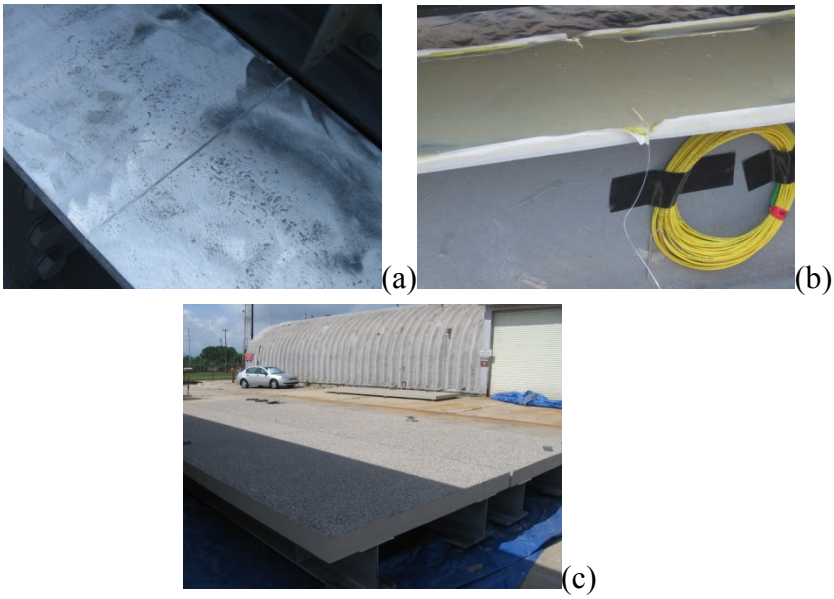

Figure 115
Instrumentation process of the monitoring system, (a) cut a v-notch in the bridge girder, (b) embedded the sensor (c) bond the deck on the girder

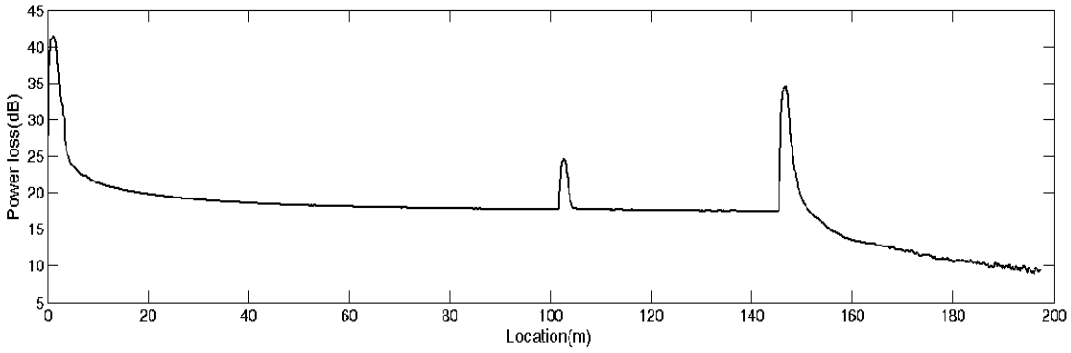

Figure 116
OTDR trace after the instrumentation of the monitoring system

APPENDIX G

Long Term Monitoring Procedural Guidelines

FBG INSTRUMENTATION

The new bridge girder-deck system can be continuously/periodically monitored with the FBG sensors permanently attached to the structure. For this, all cable leads from the FBG sensor cable arrangement are stored in a safe place along one edge of the bridge. Figure 117 shows a typical setup where the FBG interrogator is placed conveniently on the banks of the river under the bridge and collecting information from the attached sensor array.

Figure 117
FBG interogattor setup for periodic inspection at bridge site

A routine periodic inspection involves careful planning before and during testing. The following is a comprehensive list of all items required on-site for any such routine inspection:

a) For data acquisition

i) si425 Interoggator
ii) Channel Coupler extension
iii) Laptop with Micron Optics software installed
iv) Connector cables
v) Connectors
vi) Connector head cleaner
vii) Cable ties

b) For power supply

i) Portable Generator
ii) Extension cord
ii) Fuel for generator
iii) Lubricant Oil

c) For setup and safety

i) Hard hats
ii) Vests
iii) Ladders
iv)Table

System Concepts

FBG (Fiber Bragg Gratings) form the integral sensing unit of this FOS system. They are intrinsic spectrometric sensors with local and multiplexing sensing abilities. FBG are generated by engraving a periodic modulation of the refractive index of about 0.393 in. (1 cm) in the core of an optical fiber.

Strain indicated by expansion or contraction of the optical fiber can be caused by loading or temperature changes. The spacing of the grating in a sensor, called the "pitch," reflects the incident light with a narrow band centered about the "Bragg" wavelength, defined by

$$\lambda_0 = 2n\Lambda \tag{5}$$

where, λ_0 is the Bragg wavelength, n is the average effective index of refraction of the grating, and Λ is the pitch spacing.

FBG also provides a linear response based on the measurement of wavelength shift ($\Delta\lambda$) due to the straining of the gauge. Once temperature effects are accounted for in the wavelength shift, $\Delta\lambda$ provides a means of determining the strain according to the equation:

$$\Delta \lambda/\lambda_0 = (GF)\varepsilon + \beta\Delta T \tag{6}$$

where, $\Delta\lambda = \lambda - \lambda_0$; GF is the FBG gauge factor, typically about 0.75 − 0.82;

ε is the strain; β is the thermal coefficient; and ΔT is the temperature change relative to the temperature at installation.

The change in the length of an optical fiber with Bragg gratings indicate strain induced by either loading, temperature, or both. The fiber optic Bragg grating sensor response is a function of axial strain and temperature change on the grating as clear from equation (6). The GF and β are manufacture provided values.

Appropriate calibration tests have revealed that 1.2 pm/με is the average strain gauge factor. Wavelength shift due to a combination of strain and temperature can be isolated with certain sensors being strategically installed as dummy sensors.

Monitoring Procedure

Before beginning data acquisition, all instruments should be conveniently setup at the proximity of the bridge. The generator should be primed and started to supply power to all instrumentation used. Once both the interrogator and laptop is ready for operation, all sensor cable leads from the stored location have to be brought out to the data acquisition system. Connect the appropriate cables to the interrogator outlet and check their functionality by shifting through the various views available in the si425 front panel graphical interface. A brief introduction to the si425 system along with step-by-step operation instructions is detailed in the following section.

SI425 Optical Sensing Interrogator

The si425 Optical Sensing Interrogator from Micron Optics, Inc., provides rapid, accurate measurements of hundreds of optical sensors in real time. It is a multi-FBG sensor system that can support up to 512 sensors on four fibers, powered by a high output power swept laser source. The current si425- 500 system has four functional channels on the main unit, which has a working wavelength range of 1510-1590 nm. The scan rate is 250 Hz for less than 100 sensors used simultaneously. An additional coupler extension module can increase the number of available channels further. This system can be controlled and monitored remotely through a complete set of ethernet controls.

The si425 optical sensing interrogator system allows for a quick collection of wavelength shift information from fiber optic sensors. Their applications include strain measurements for civil structure such as bridges and roads, force monitoring in prestressed tendons, performance monitoring of web-flange interface in composite decks, and long-term performance monitoring of rehabilitated structures.

System Description

The front control panel of the si425 mainly consists of an LCD display screen that allows real time data viewing, menu keys for navigation through options menus, arrow keys for

incrementing integer data inputs, number keys for numeric data entry, and FC/APC connectors for connecting the optical sensors as seen in Figure 118(a). The alternating action power switch of the system is located at the rear of the unit, as shown in Figure 118(b).

(a) Front panel view

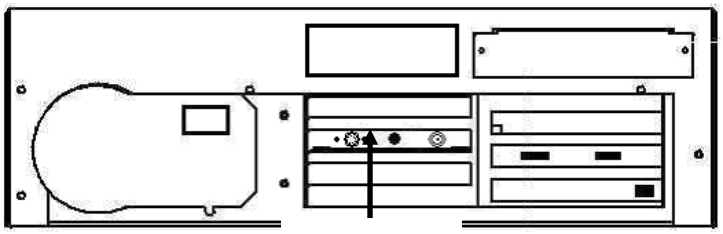

(b) Rear panel view

Figure 118
Front and rear panel view of si425

SM040-016 (16-ch. Coupler Extension)

This 1U chassis contains four 1 x 4 couplers to accommodate connections of up to four fibers to each si425-500 optical channel. All fibers are scanned simultaneously. It is solely intended to provide more fiber connection options. When structural strain monitoring requires several fiber optic sensors and more than just four optical fibers, the expansion module sm040-016 facilitates this (Figure 119).

Figure 119
sm040-016 (16-ch. coupler extension)

SI425 Acquisition System Interface

The front panel graphical interface provides four standard screen views either through the built-in LCD or via Ethernet on a remote PC; they are:

1. Sensor Wavelength View: shows wavelength vs. time for selected sensors. In this view, the user can select both the data acquisition rate of the si425 as well as the time base over which data are displayed to the screen as seen in Figure 120.

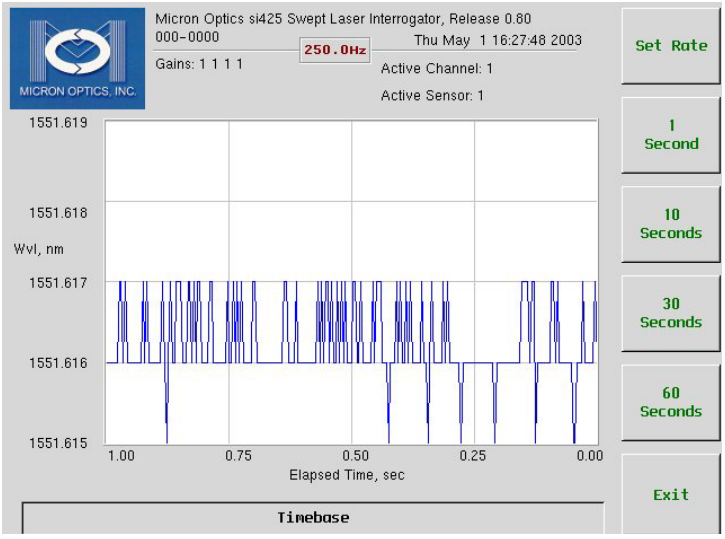

Figure 120
Sensor wavelength view screenshot

2. Table View: simultaneously displays wavelengths for all sensors on all channels as shown in Figure 121.

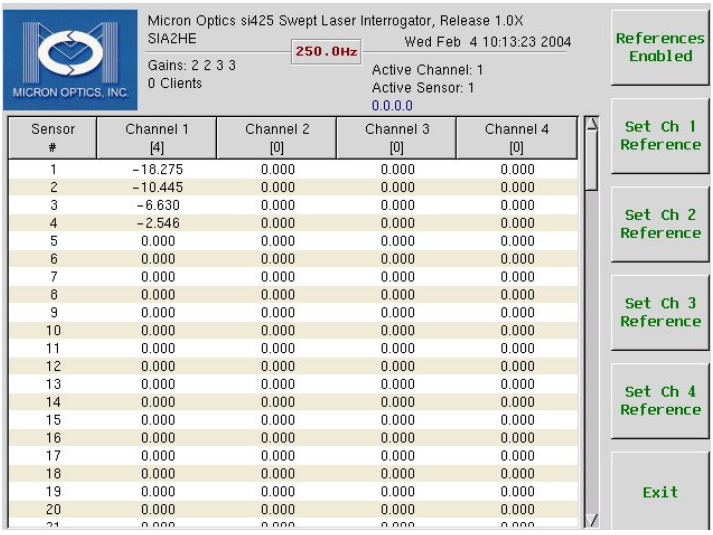

Sensor #	Channel 1 [4]	Channel 2 [0]	Channel 3 [0]	Channel 4 [0]
1	-18.275	0.000	0.000	0.000
2	-10.445	0.000	0.000	0.000
3	-6.630	0.000	0.000	0.000
4	-2.546	0.000	0.000	0.000
5	0.000	0.000	0.000	0.000
6	0.000	0.000	0.000	0.000
7	0.000	0.000	0.000	0.000
8	0.000	0.000	0.000	0.000
9	0.000	0.000	0.000	0.000
10	0.000	0.000	0.000	0.000
11	0.000	0.000	0.000	0.000
12	0.000	0.000	0.000	0.000
13	0.000	0.000	0.000	0.000
14	0.000	0.000	0.000	0.000
15	0.000	0.000	0.000	0.000
16	0.000	0.000	0.000	0.000
17	0.000	0.000	0.000	0.000
18	0.000	0.000	0.000	0.000
19	0.000	0.000	0.000	0.000
20	0.000	0.000	0.000	0.000

Figure 121
Table view screenshot

3. Channel Power View: gain level for each channel can be set here ensuring that the sensors are in the proper power band for optimal measurements, as shown in Figure 122.

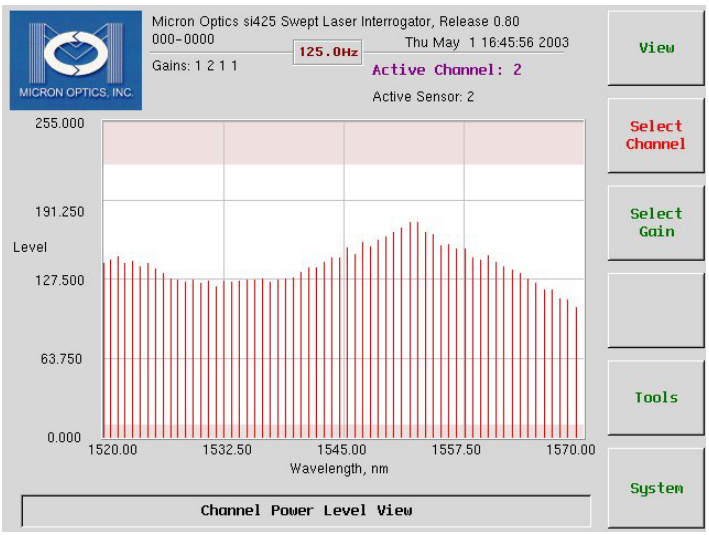

Figure 122
Channel power view screenshot

4. FFT View: this view shown in Figure 123, accurately identifies the fundamental frequency of oscillations.

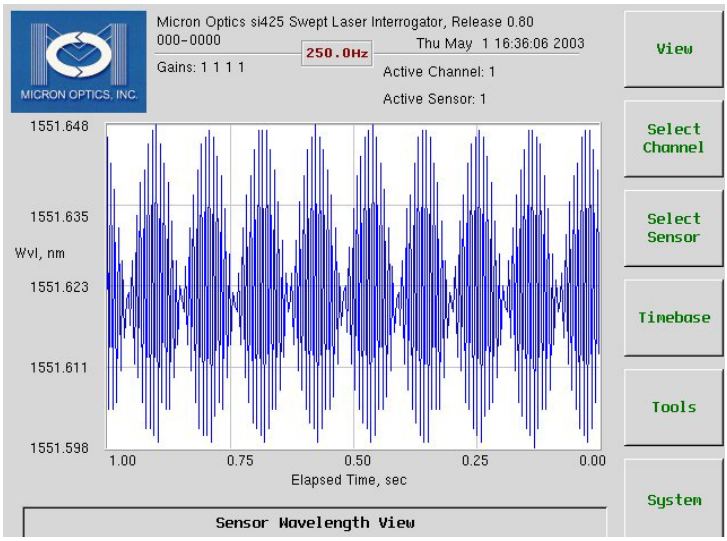

Figure 123
FFT view screenshot

Operation Procedure for the si425 Labview Utility

Step 1: Press the power switch at the rear of the system that leads to an initialization mode of the si425. Connect the crossover Ethernet cable to the host PC with si425 software installed and power up the remote host PC.

Step 2: Once the system has finished initializing, the user is mostly able to see the sensor wavelength view first. The other alternate views such as the sensor FFT view can be accessed from the menu at the right end of the display monitor by clicking on "View." The menus on the right hand side of the display screen are the options available at the beginning shown in Figure 124.

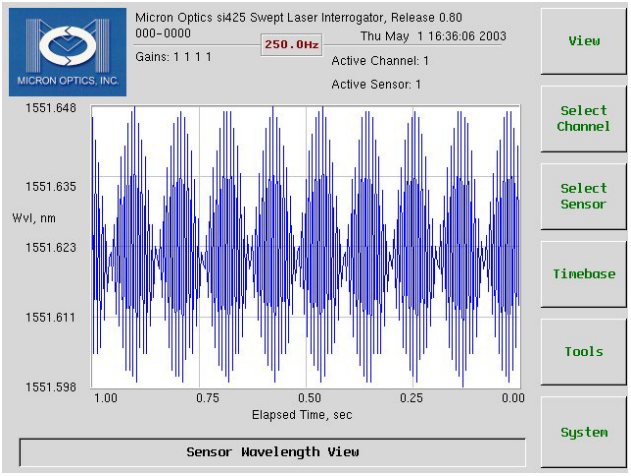

Figure 124
Sensor FFT view with basic menu options

Step 3: The next step to be taken is to establish communication between the si425 and the host PC. To be able to collect and store data while using the interrogator, the si425 system must be connected to a host PC via a provided crossover Ethernet cable. Data transfer to and from the si425 is through a 100Mbit/S Ethernet port on the back of the unit. To setup remote control interface, one should first detect the IP address and network mask of the si425 system. For this, a button labeled "System" placed at the bottom right corner of any view has to be clicked (Figure 123). Clicking on the system button reveals the system menu as seen in Figure 125.

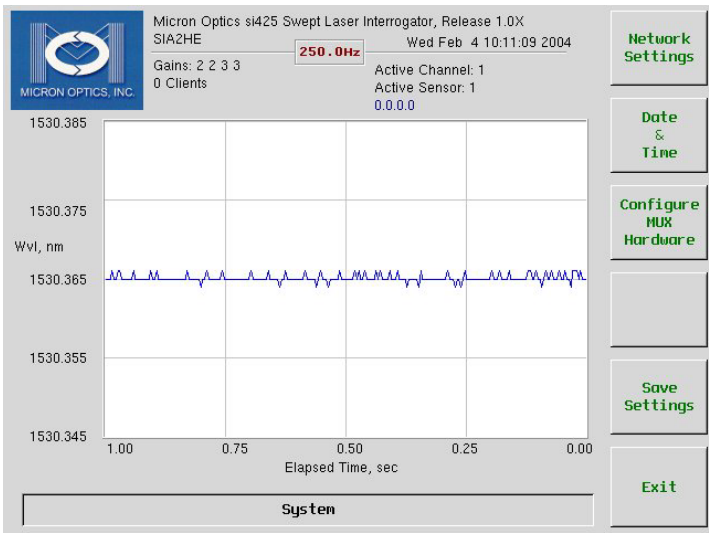

Figure 125
Sensor wavelength view with system menu options

When not connected to a remote client (host PC), the display beside the Micron Optics, Inc., symbol will read "0 Clients." To ensure data transfer, this message has to change to reflect the recognition of a remote client. First, collect the default IP address and Network Mask ID from the si425 system. This information can be accessed by clicking on the "Network Settings" button, giving rise to the button labeled "IP Addr & Netmask" (Figure 126). The default values of IP address and network mask for the si425 are 10.0.0.129 and 255.255.255.0, respectively. For proper communication, the host PC and the si425 must be set for the same network mask and different, but compatible, IP addresses. A typical correct setting is shown in Table 11.

Table 11
Typical correct network settings

	Host PC	si425
IP Address	10.0.0.121	10.0.0.129
Netmask	255.255.255.0	255.255.255.0

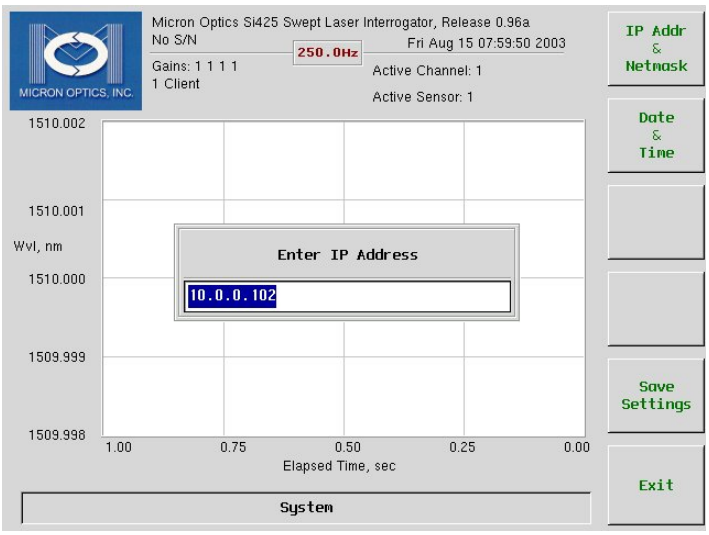

Figure 126
System IP address query screen shot

To begin setting the network mask and IP address on host PC either of the two methods explained below can be adopted.

Method 1. For a personal Windows XP system, i.e., when you are the administrator of the machine being used, go to "Control Panel." Click on the icon "Network Connections," highlight the "Local Area Network" selection, right click, and choose "Properties." The window shown in Figure 127 will appear. Highlight the "TCP/IP" entry and click "Properties." You will then have access to change the IP address and subnet mask. Click "OK" to save settings.

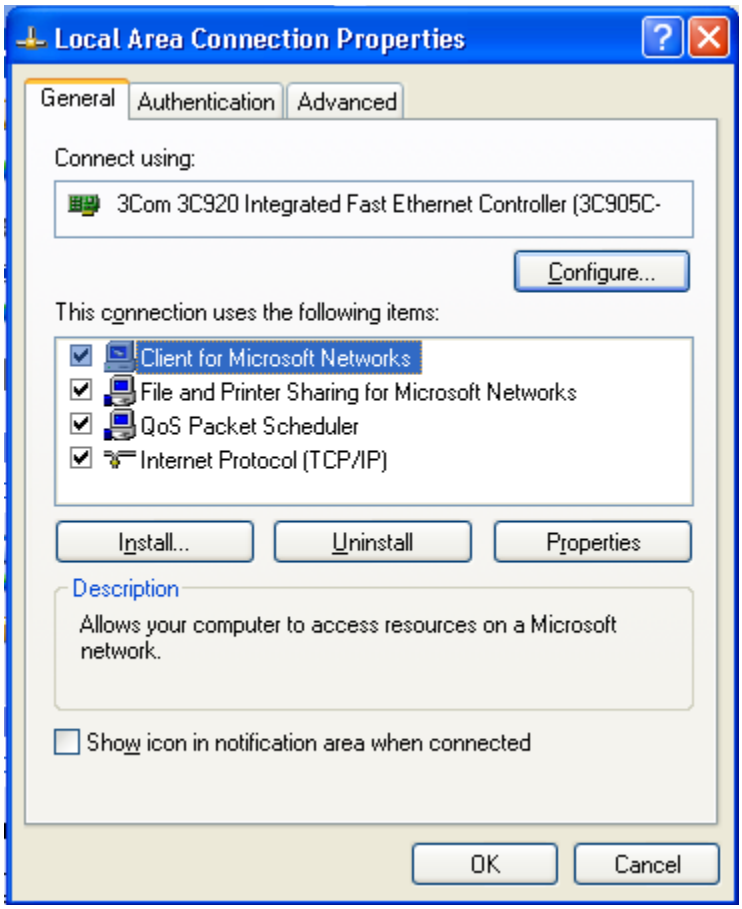

Figure 127
Local area connection property window

Method 2. Get to the command prompt in your system and type in IPCONFIGURE; one can update the IP address as required from there. Once the link is established, the system will recognize the remote client and notice the change in message from "0 Client "to "1 Client" in Figure 128.

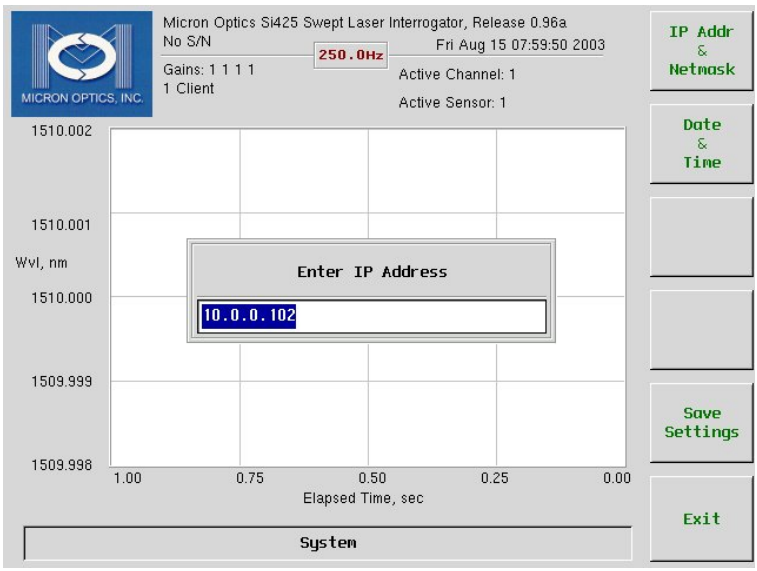

Figure 128
Screen shot when remote client identified

Step 4: The last and final step is to save and retrieve data that are collected from the sensors during testing. Open the si425 utility software in the host PC and the user is typically prompted to enter the IP address and network mask of the interrogator as shown in Figure 129.

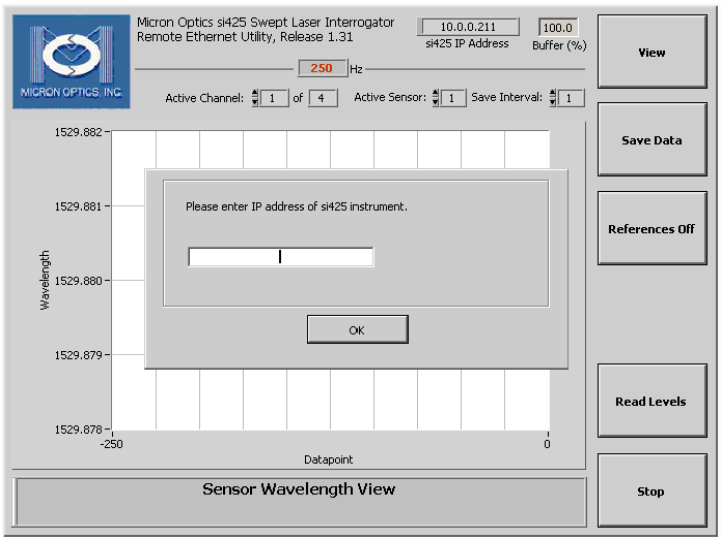

Figure 129
Typical host PC software interface

Enter the appropriate IDs as mentioned in Table 10 and the host PC is ready to collect information from the si425 system. The menu items on the right hand corner of the graphical

user interface (GUI) though similar to the system display menu, have other options such as "Read Levels" and "Save Data."

Clicking on the "Read Levels" button takes the user to a Channel Power Level View shown in Figure 130, which collects both wavelength and level information. The remote Channel Power Level View is intended for setup and diagnostic use, not for full-speed data transfer.

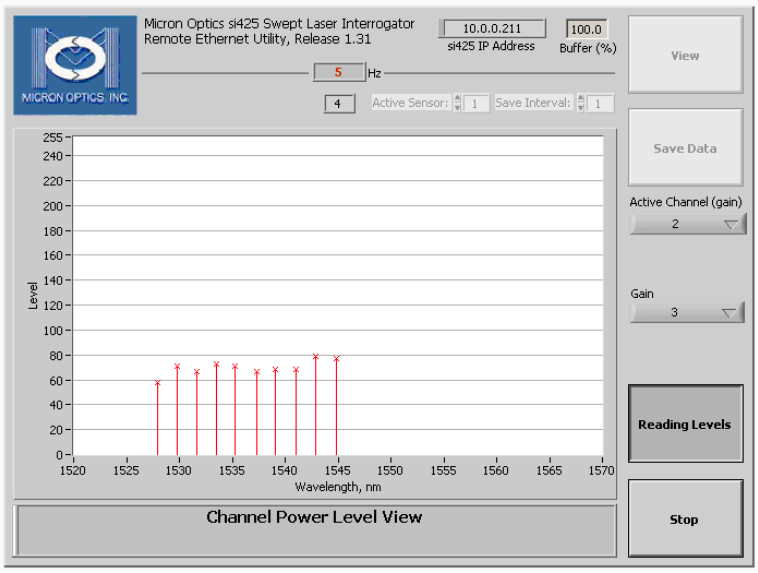

Figure 130
Screen shot of channel power level view in LABVIEW

To initialize data saving, click on the button "Save Data." The program then prompts the user for a file path for the saved data (Figure 131). A customized file name of "###@.txt" can be assigned and accepted by clicking "OK." Once a file path is selected, data saving begins until the "Saving…" button is clicked again, which turns off the data save function. The stored data typically appear as shown in Table 12.

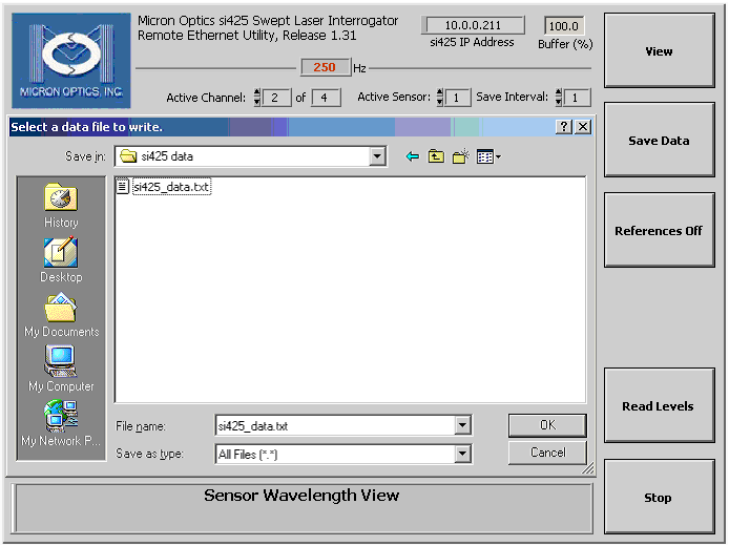

Figure 131
Save data mode screen shot

Table 12
Sample data format

TIMEBASE	CH1_SN	CH2_SN	CH3_SN	CH4_SN	DATA
1052737738.68036	0	0	3	0	1530.973 1538.781 1546.617
1052737738.68446	0	0	3	0	1530.972 1538.781 1546.612
1052737738.68856	0	0	3	0	1530.972 1538.781 1546.615
1052737738.69265	0	0	3	0	1530.972 1538.782 1546.613
1052737738.69675	0	0	3	0	1530.972 1538.781 1546.615
1052737738.70085	0	0	3	0	1530.972 1538.781 1546.614
1052737738.70494	0	0	3	0	1530.973 1538.782 1546.613
1052737738.70905	0	0	3	0	1530.972 1538.781 1546.615
1052737738.71314	0	0	3	0	1530.973 1538.783 1546.613
1052737738.71723	0	0	3	0	1530.971 1538.782 1546.619
1052737738.72133	0	0	3	0	1530.972 1538.783 1546.619

Step 5: As seen in Table 12, only wavelength values are recorded by the si425. Post-processing of this data is done using MATLAB to reveal strain and temperature values.The system concept involved is that strain indicated by expansion or contraction of the optical fiber can be caused by loading or temperature changes. The spacing of the grating in a sensor, called the “pitch” reflects the incident light with a narrow band centered about the “Bragg” wavelength, defined by:

$$\lambda_0 = 2n\Lambda \tag{7}$$

where, λ_0 is the Bragg wavelength, n is the average effective index of refraction of the grating, and Λ is the pitch spacing.

FBG also provide a linear response based on the measurement of wavelength shift ($\Delta\lambda$) due to the straining of the gauge. Once temperature effects are accounted for in the wavelength shift, $\Delta\lambda$ provides a means of determining the strain according to the equation:

$$\Delta \lambda/\lambda_0 = (GF)\ \varepsilon + \beta\Delta T \qquad (8)$$

where, $\Delta\lambda = \lambda - \lambda 0$; GF is the FBG gauge factor, typically about 0.75 − 0.82; ε is the strain;

β is the thermal coefficient; and ΔT is the temperature change relative to the temperature at installation.

OTDR Instrumentation

System Concept

In simple terms, an OTDR (optical time domain reflectometer) based optic fiber is an intensiometric sensor that carries and modulates the light within the fiber and has sensing capability throughout the length of the fiber. The principle by which these sensors function is illustrated in Figure 132. These sensors are efficient for use in large structures like bridges as all portions of the fiber acts as a sensor and thus enable monitoring changes along its length. Cracks or local strain changes can lead to a light intensity variation within the fiber that reflects as a power loss *[15]*.

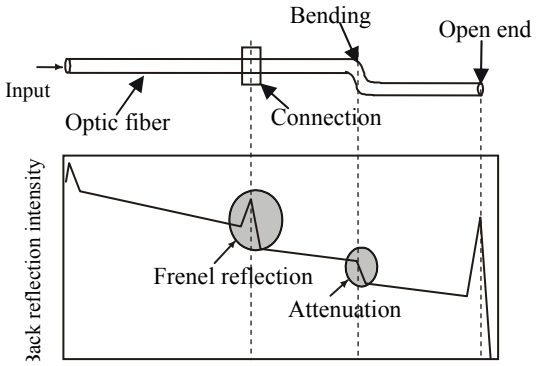

Figure 132
Typical OTDR reflection chart

A typical reflection chart shown in Figure 131 represents a bending in the optic fiber, connection of two fiber ends and open end corresponds to optic power losses and a Frenel reflection peak. In civil engineering applications, by embedding optic fibers in the structure, two types of OTDR-based optic fiber monitoring methods can be achieved: fiber bending-based monitoring method and fiber breaking-based monitoring method.

It has been established that the optic power loss resulted from bending is related to the

curvature radius R of a bent optical fiber as seen in equation (9):

$$\alpha = AR^{-1/2} \exp(-UR) \tag{9}$$

where, R is the bending radius of the optical fiber and A and U are independent coefficients *[13]*. From the measured power loss in the optic fiber, the slip can be quantified. However, in practice, because of the complex stress conditions in an optic fiber, the relationship between the power loss and interface slip has to be obtained through calibration.

FTB-200

The FTB-200 Compact Modular platform is manufactured by EXFO. OTDR is a well established method for examining fiber-optic cables where measurement of optical backscatter is a function of a linear position. The technology is well developed and able to resolve changes in the backscatter signal. EXFO's FTB-200 Compact Modular Platform offers impressive dynamic range with short dead zones. The wavelength range of the system is between 850+/- 20 nm – 1300+/- 20 nm. The system has both the single mode and the multimode option OTDR module, with the single mode being used for distance ranges between 1.3 – 260 kms while multimode is effective for distance ranges from 0.1 – 40 kms.

The system includes a light source that is sent through a glass fiber link. The fiber characteristics such as attenuation of the link, loss trends, and length of fiber are deduced from the backscattered light. The OTDR software displays obvious faults and connections on a generated graph, known as a trace, and provides the loss value in dB as a function of distance. The faults, called events, are listed in a table of events below the OTDR main window. Figure 133 illustrates a typical OTDR acquisition, displaying a trace and its corresponding table of events.

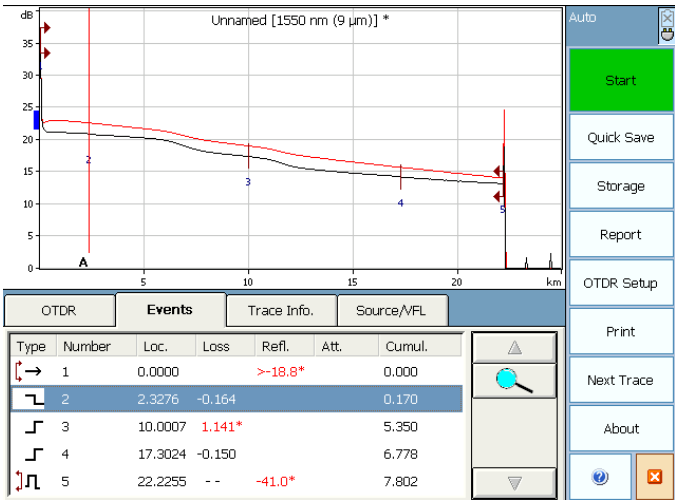

Figure 133
OTDR acquisition trace

OTDR Acquisition System Interface

The front panel of FTB 200 (Figure 134) consists of an LCD touch screen, keypads that give access to various functions such as switching on the unit, saving files, etc. Pressing on the on/off button turns the system on. Holding down the on/off button for a few seconds until the unit beeps twice shuts down the unit.

Figure 134
FTB-200 front panel view

Modes of Operation

The OTDR application provides the following trace acquisition modes:

- Auto: Automatically calculates fiber length, sets acquisition parameters, acquires traces, and displays event tables and acquired traces (Figure 135).

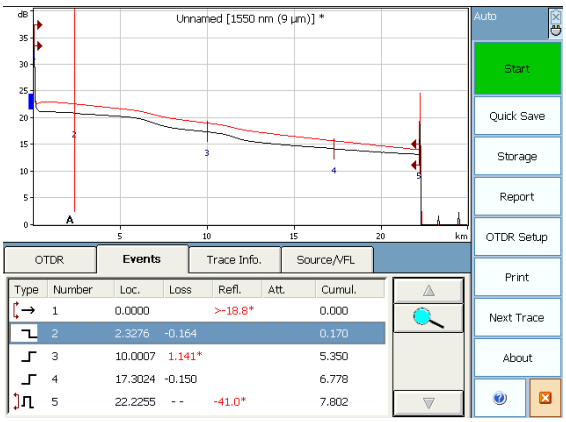

Figure 135
Screen view in auto mode of operation

- Advanced: Offers all the tools needed to perform integral OTDR tests and measurements and gives control over all test parameters.
- Template: Tests fibers and compares the results to a reference trace that was previously acquired and analyzed. This allows time savings when testing a large number of fibers. Reference trace documentation is also automatically copied to new acquisitions

Operation Procedure of FTB-200

Both auto and advanced modes are operated in the same manner except that all parameters are customizable in the auto mode.

Step 1: Clean the connectors properly.
Step 2: Connect a fiber to the OTDR port. Also, based on choice of wavelength, one should use the appropriate connector for single and multimode.
Step 3: Set the autorange acquisition time by choosing the acquisition tab in the OTDR setup menu as shown in Figure 136.

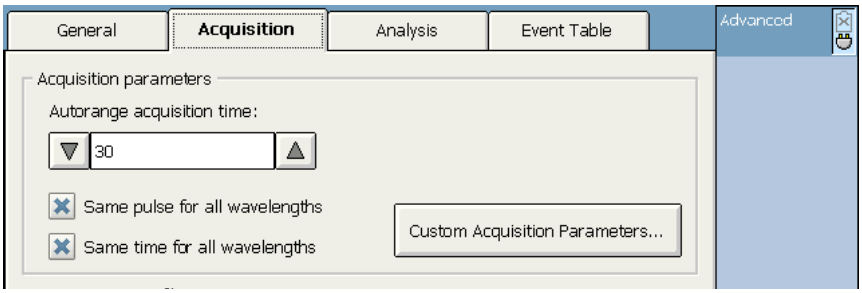

Figure 136
Screen view of acquisition menu

Step 4: Go to the OTDR tab (Figure 137). If the OTDR supports single mode and multimode wavelengths, specify the desired fiber type (for C fiber, select 50 µm, and for D fiber, select 62.5 µm).

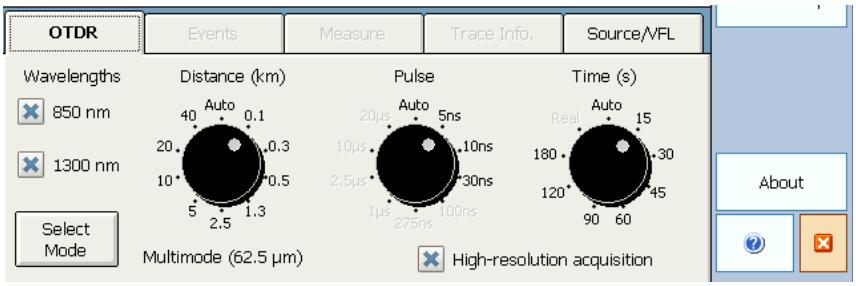

Figure 137
Screen view of OTDR parametric settings menu

Step 5: Select the boxes corresponding to the desired test wavelength(s).

Step 6: Press Start.

Step 7: Once the analysis is complete, save the trace by pressing Quick Save in the button bar or from the keypad.

For template mode, a few different steps need to be followed:

Step 1: Acquire a reference trace before starting, obtained from previous modes.

Step 2: Open the reference trace in the application.

Step 3: When the application prompts you, select the trace as the reference trace.

Step 4: Press Start. Events from all traces will automatically be analyzed and measured. The application will prompt you when new events are found.

Step 5: Once the analysis is complete, save the trace by pressing Quick Save.

Data Processing

The traces in the system are usually in .trc or .sor format (Figure 138). This can be saved into other formats by using EXFO toolbox software installed in any standard computer. To copy, move, rename, or delete trace files, the user have to process the files manually via File Manager available from EXFO ToolBox.

Figure 138
A typical trace obtained from EXFO FTB 200

APPENDIX H

Long Term Monitoring Results

After the short-term monitoring test carried out in October 2009, periodic monitoring of the bridge was carried out in December 2009, February 2010, April 2010, and July 2010. At the time this report was submitted, although four visits were made to the bridge site to collect both strain data due to regular traffic loads and temperature information, only results from the first three visits are summarized here.

Strain Monitoring Results

Although the exact weights and configurations of vehicles that caused the strain in the material were unknown during these periodic visits, the sensor response was comparable with the range of data collected from the static load tests. Generally, south-bound lanes seemed to show higher strain values in both girder and deck components of the bridge in conformance with the trend of heavier trucks often moving towards the south. Figures 139 and 140 represent strain plots for the same sensor over approximately a half-hour period of monitoring for all three days of visit.

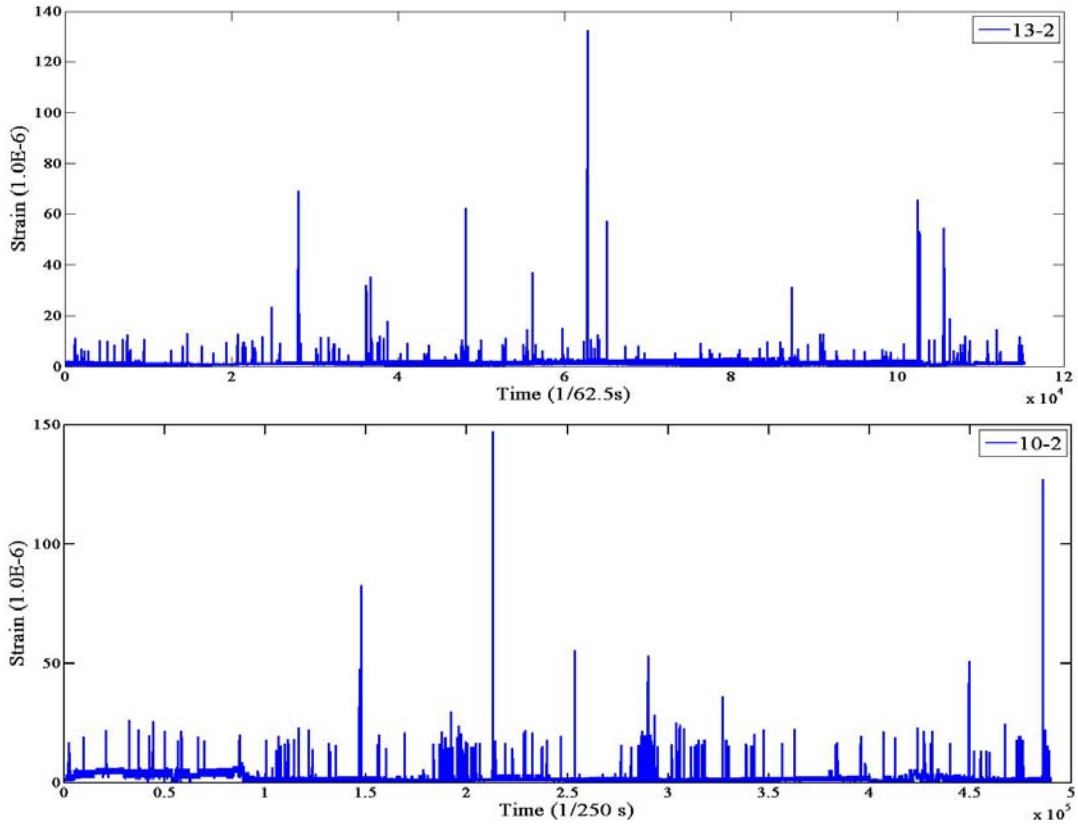

(a) Day 1

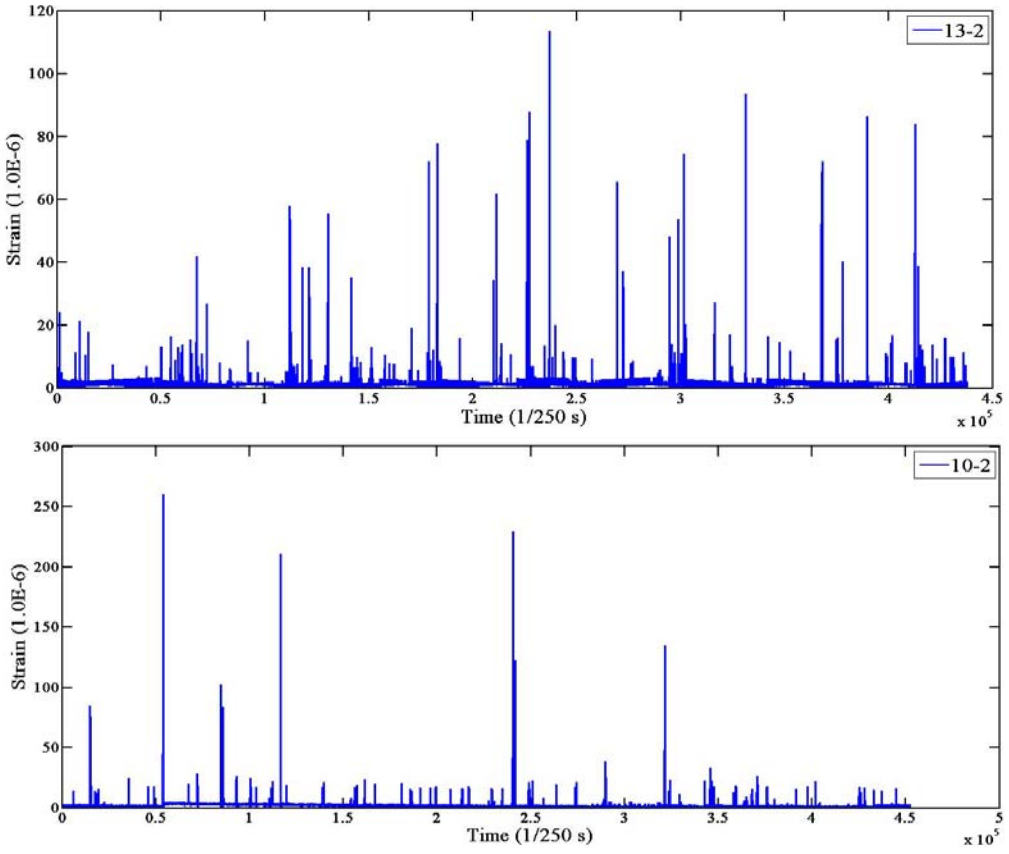
13-2
Strain (1.0E-6)
Time (1/250 s)
x 10^5
10-2
Strain (1.0E-6)
Time (1/250 s)
x 10^5

(b) Day 2

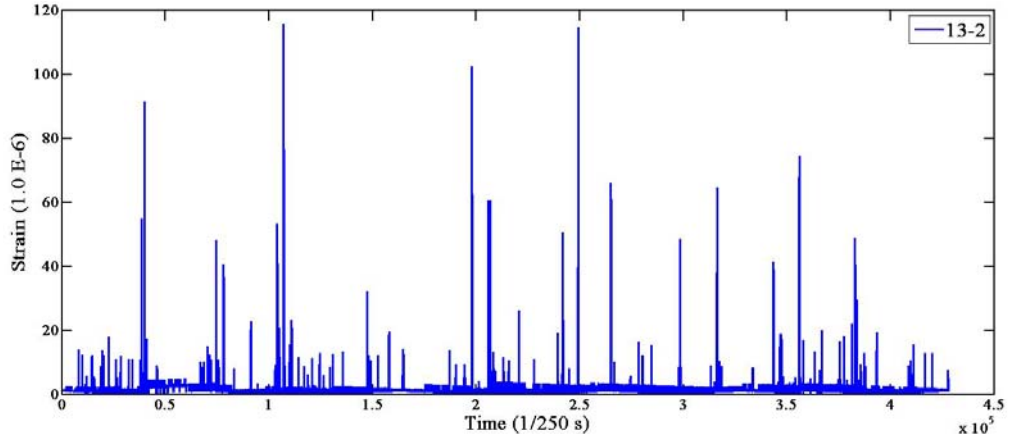
13-2
Strain (1.0 E-6)
Time (1/250 s)
x 10^5

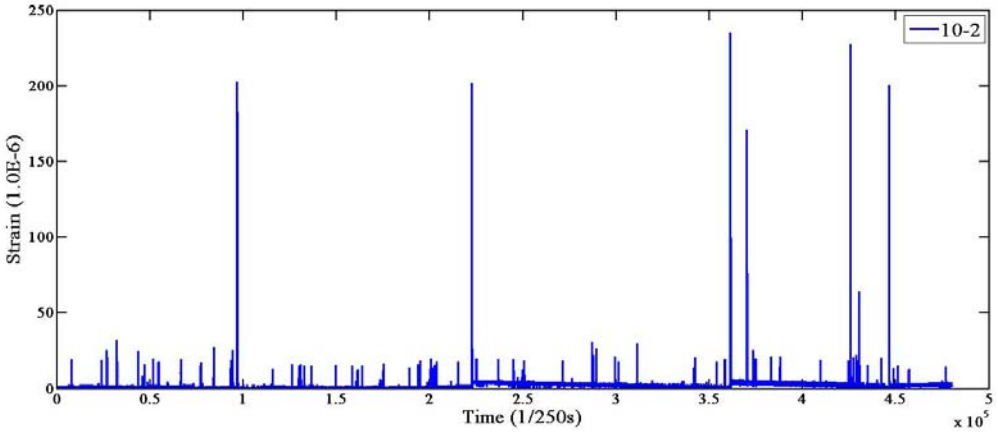

North-bound lane South-bound lane

(c) Day 3

Figure 139

FBG sensor strain data for steel girder at mid-span on all three test days (13-2 north bound lane, 10-2 south bound lane)

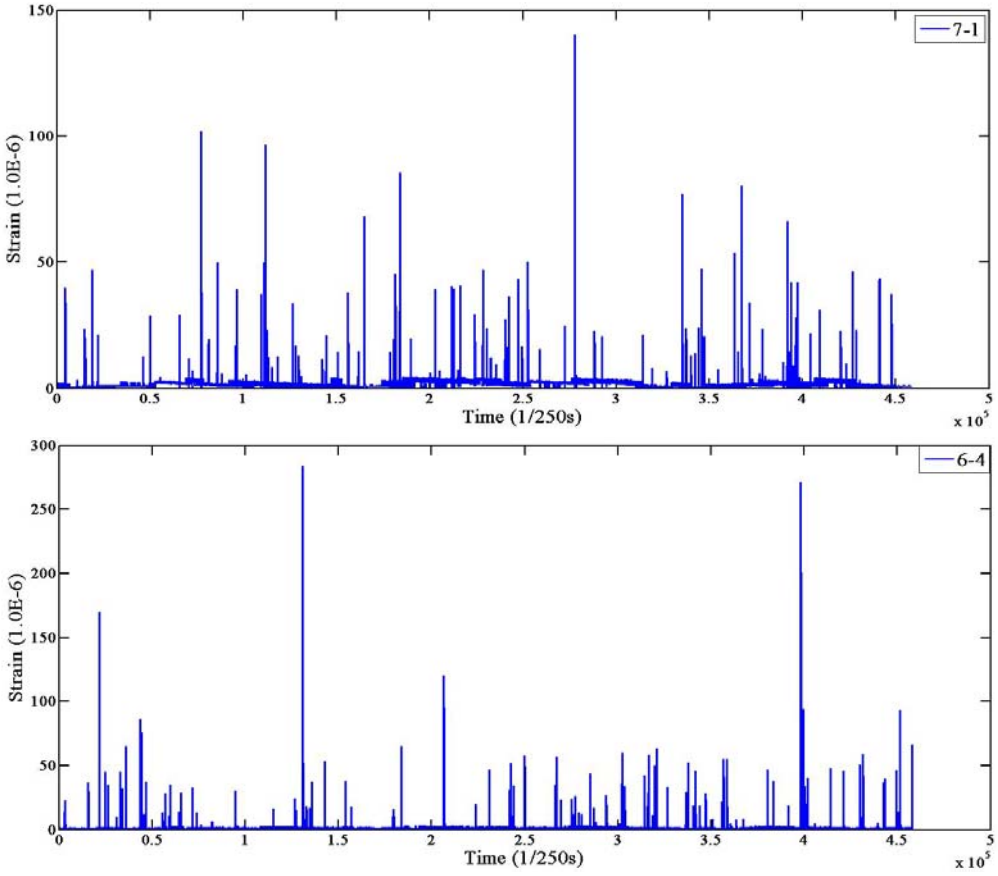

(a) Day 1

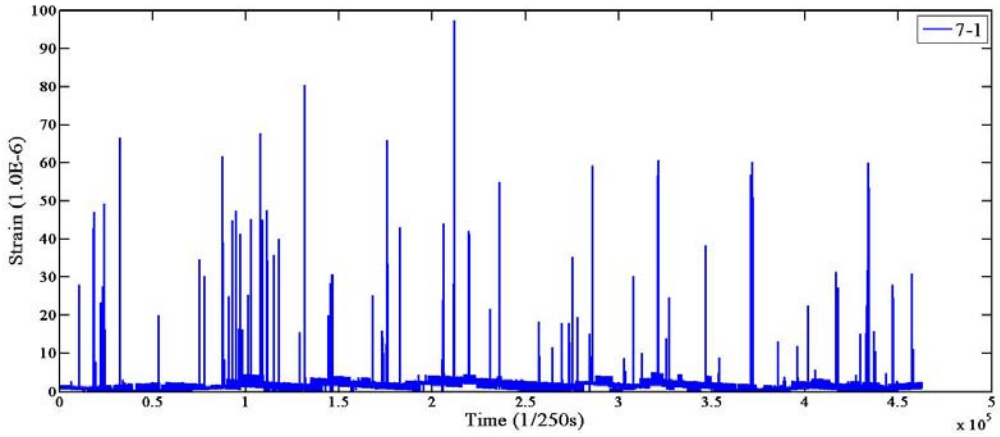

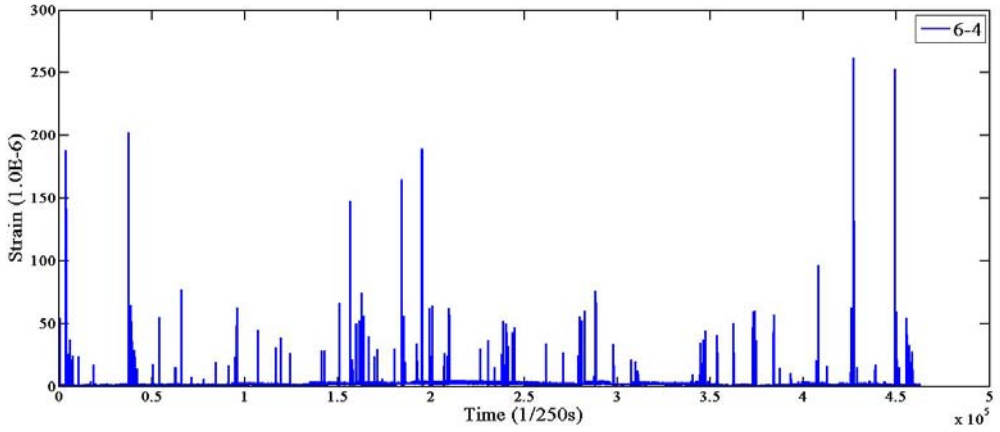

(b) Day 2

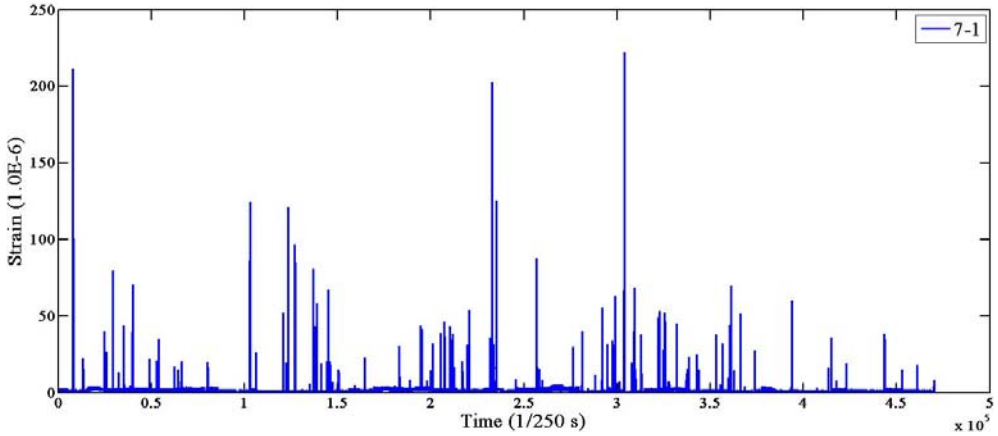

(c) Day 3

Figure 140
FBG sensor strain data for the composite deck on all three test days (7-1 north bound lane, 6-4 south bound lane)

Temperature Monitoring Results

The periodic monitoring led to the collection of data from the temperature sensors installed on the bridge. Figures 141 and 142 are typical temperature profiles collected from FBG sensors (9-4 on south_bound and 16-4 on north_bound lane) over a half-hour duration on different days. The actual temperature measured on-site was close to those measured by the FBG strain gauges.

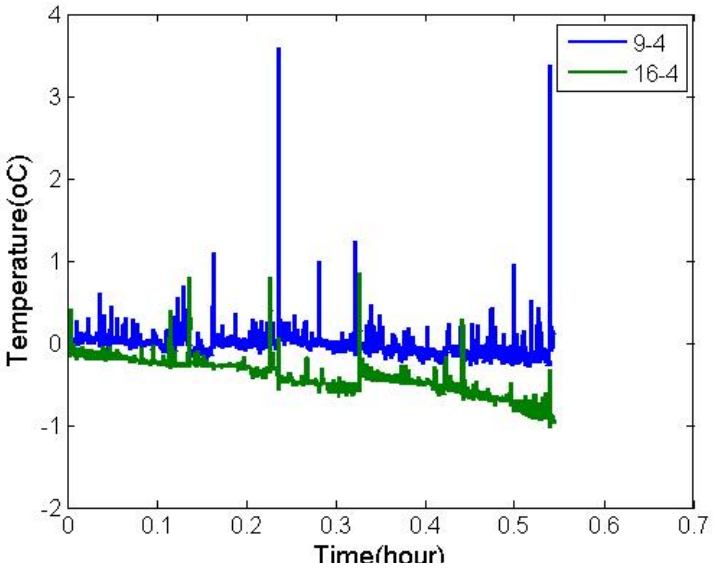

Figure 141

Temperature data for test day 1

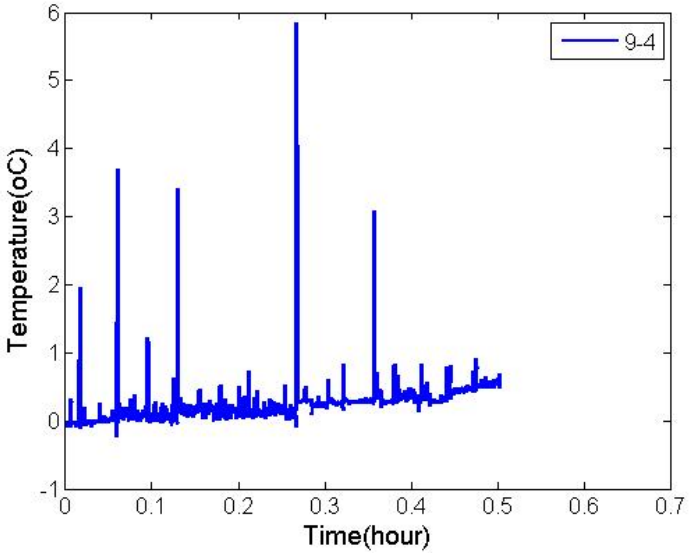

Figure 142

Temperature data for test day 2

APPENDIX I

Literature Review and Background Information

Part 1: Review of Fiber Reinforced Polymer Composites in Bridge Deck Construction

General Background. Highway bridge decks in the US are constructed predominantly with steel-reinforced concrete. However, costs of repair and maintenance of these bridges incurred at the federal and state levels are overwhelming. As a result, for many years, there has been pressure on transportation agencies to find new cost-effective and reliable construction materials *[17]*. A very promising alternative is the fully-composite FRP bridge deck system. FRP composites have found increasing applications in bridge design and construction.

Advantages of FRPS. It is well known that FRP possesses significant advantages, which may present a very good challenge to the more ubiquitous steel, reinforced concrete, and others in the construction field. One main driving force in the use of FRP has been its high strength and stiffness when determined on a weight basis. One source shows that an FRP bridge deck weighs about 20 percent as much as a structurally equivalent reinforced concrete deck *[2]*. The light weight of FRP makes it possible for smaller scale foundations and other supports to be used. Since many bridges in the US are categorized as deficient because of substructure problems or inadequate live load capacity, FRP bridge decks may be a good substitute *[18]*. Among FRP's high strength properties, the most relevant include durability and corrosion resistance. It is also resistant to a chemical attack; hence, it has been suggested that little maintenance may be needed other than periodic wearing surface renewal.

Because deck panels are manufactured in the factory and transported to the construction site, the production process can be closely monitored under a controlled environment. This leads to higher quality products. Potential weather delays can also be greatly reduced as is sometimes a problem with cast-in-place structures. There is also the merit of ease of manufacturing, fabrication, handling, and erection with the project delivery and installation time being greatly reduced.

Disadvantages of FRPs. Like most structural materials, however, FRP has a few drawbacks. One noteworthy disadvantage is the high initial cost. It is interesting though that this high cost can be economically justified as the life cycle cost may be reduced over the life time of the bridge *[17]*. This is because, as was noted above, maintenance cost of an FRP bridge could be relatively low due to high durability of the structure. This is of interest because rehabilitation and maintenance of reinforced concrete bridges has been an issue in

the US in recent years. More than 200,000 bridges worth $78 billion are in need of repair *[19], [20]*. Over $5 billion per year in maintenance would merely maintain the status quo. A similar condition exists in Canada where, according to one report, over 40 percent of the bridges were built in the fifties and sixties, and most of these are in urgent need of rehabilitation *[21]*.

Another disadvantage is the very little or nonexistent design guidance and/or standards. There are also insufficient proven connection details. Additionally, the design and manufacturer require highly trained specialists from many engineering and material science disciplines, and some manufacturing processes do not produce consistent material or structural properties. Without a design code or guide, a structural designer is often limited to his personal judgment based on experience or general practice. For a new material like FRP, this design approach could lead to drastic consequences such as serviceability or strength failures, without a basis to hold someone responsible. In other words, structural members could be poorly or under-designed. On the other hand, an engineer can be held responsible for failure to abide by certain details in a specification once something goes wrong with the structure. This can only be done if such a code or design guide exists. Hence the unavailability of at least a design guide for FRP bridges could result in adverse consequences. Additionally, designing without a guide could lead to a waste of resources such as valuable funds. In an age when budgets are tight, over-design is not the norm.

To solve the problem of a design code of practice, a Load and Resistance Factor Design (LRFD) code for structures using FRP is being developed in the US. It will be based on a probability-based limit state design criteria. In addition, the American Society of Civil Engineers (ASCE) is currently engaged in a research work for the purpose of developing a standard for the design of pultruded FRP composite structures. It is expected that when completed, this document will serve as the basis for the American Association of State Highway and Transportation Officials (AASHTO) design code for FRP *[22]*. The results from this research work would no doubt provide valuable contributions to these developments.

Still discussing some drawbacks, although FRP structures have the advantage of being light in weight, this could render the structure aerodynamically unstable. Other demerits include ultraviolet radiation degradation, photo-degradation, and a lack of awareness. It is reassuring, though, that researchers over the last decade are addressing these issues, and the information is being disseminated in the wider engineering community.

History of FRP Applications

Fiber reinforced polymers have been in use since the 1940s. Due to the incurring of very heavy financial costs, however, the application of FRP was limited to the aerospace and defense industries. To meet the higher performance challenges of space exploration and air travel in the 60s and 70s, fiber materials with higher strength, higher stiffness, and lower density (such as boron, aramid, and carbon) were commercialized. During the 1970s, research was channeled to developing ways to improve the cost of high performance FRPs. By the late 1980s and early 1990s, the defense industry waned and emphasis was placed on cost reduction and the continued growth of the FRP industry *[23]*.

Although fiber reinforced polymers have had a long history, it is only in recent times that it has won the attention of civil engineers as a potential alternative to more conventional structural materials. Throughout the 1990s, various industries have financed demonstration projects and sponsored research programs on this burgeoning field. As research continues, FRP materials are now finding wider acceptance in the construction industry.

Prior to the 1970s, pultruded FRP structural shapes were developed but limited to small sized commodity products for non-structural applications. In the 1970s and 1980s, larger pultruded shapes for structural purposes and load-bearing elements were produced largely as a result of the advancement in pultrusion technology. Pultrusion companies in the United States began to produce “standard” I-shaped beams for construction purposes. A customized building system of pultruded components for the construction of industrial cooling towers was developed in the late 1980s and 1990s. Small pultruded FRP structural shapes for the construction of walkways and short-span pedestrian bridges have increased in use since the early 1990s *[23]*.

Some of the first applications of fiber-reinforced plastics for complete bridge structures were in China. A number of pedestrian bridges have been built, but the first all-composite bridge deck was the Miyun Bridge completed in September 1982 near Beijing, which carries full highway traffic. The Ulenbergstrasse Bridge in Germany was the world’s first in the use of high tensile strength glass fiber prestressing tendons. Since then many bridges have been constructed in various parts of the world using FRP. These include both pedestrian and vehicular bridges. One example is Aberfeldy Footbridge which crosses the River Tay in Scotland erected in 1992 and is the world’s first and longest advanced composite footbridge. Another example is the Bonds Mill lift bridge (completed in 1994), which is an electrically operated lift bridge. It was the first bridge in England to be constructed from plastic. Tech 21 (Smith Road) Bridge is Ohio’s first all-composite bridge. The Butler County Engineer's

Office installed this structure built entirely of advanced composite materials.

Types of FRP Panels

FRP decks can be grouped into two categories based on the type of construction – sandwich and adhesively bonded pultruded shapes. In this research work, focus is directed on a honeycomb core sandwich deck. However, an overview of both types is first given.

Sandwich Construction

This type of construction meets the requirement of high strength and stiffness at a minimum unit weight. Use is made of bonded core materials, separating strong, stiff, and low density face sheets. The entire deck is made to act compositely. A great advantage this type of construction has is its flexibility in designing structures for varied depths and deflection requirements. This is so the manufacturing of face and core components can be controlled by the producer. The most efficient core materials are cellular materials *[23]*.

The connection between sandwich deck panels is usually by tongue and groove ends. A clamp mechanism is used to join the panels with the underlying structure. A major problem experienced by this mode of construction is delamination, and this may be due to some manufacturing defects. Hence, special focus must be given to the connection details during the design and production stages.

One example of this panel type is the sinusoidal wave core configuration in the plane extending vertically between face laminates. The geometry of this panel can be seen in Figure 142. Another example is the web core geometry with a two-way vertical interior core. It has transverse and longitudinal web configuration making it look like a box, as can be seen from Figure 143.

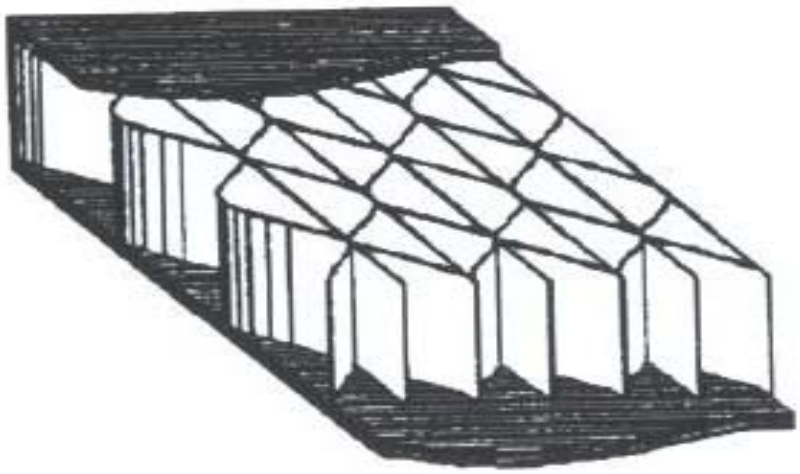

Figure 143
Fiber reinforced polymer honeycomb (FRPH) sandwich panel

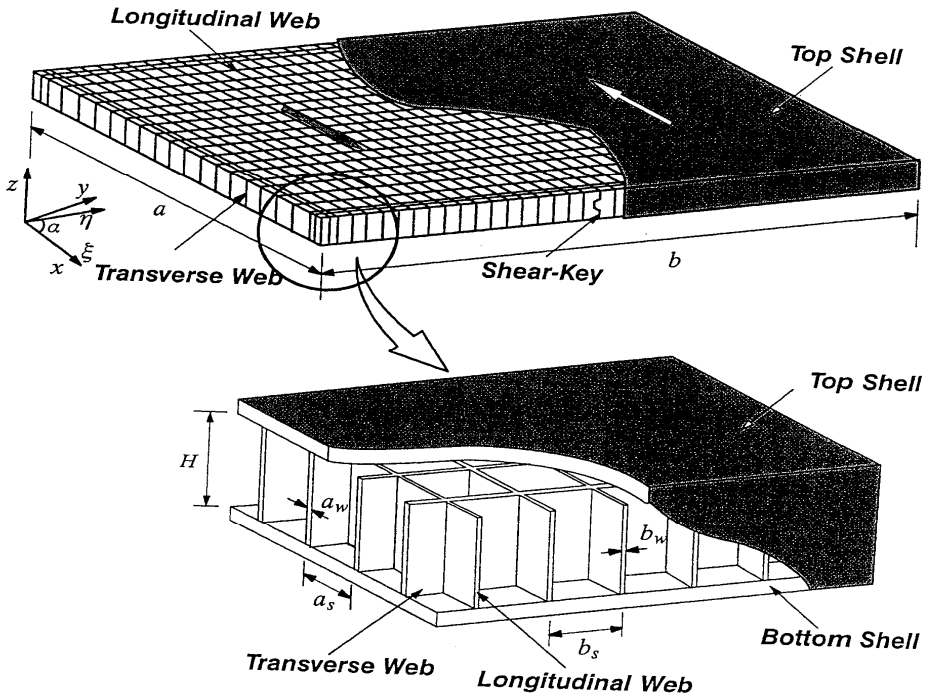

Figure 144
Web core sandwich bridge deck system

Adhesively Bonded Pultruded Shapes

Pultruded shapes are produced by manufacturers using well-established processing techniques. These shapes can be grouped into two–standard and custom. The term "standard" implies that the FRP part is produced on a regular basis by the company, is usually available off-the-shelf, have published dimensions, and meets minimum manufacturing-provided property values *[23]*. Examples include "standard" angles, tubes, channels, and I-shaped sections. Nonstandard shapes are called "custom" shapes.

FRP decks produced by adhesively bonded pultruded shapes include EZSpan (Atlantic Research), Superdeck (Creative Pultrusions), DuraSpan (Martin Marietta Materials), and Strongwell. The pultruded shapes are typically aligned transverse to the direction of traffic flow. Figure 145 below shows a schematic diagram of the DuraSpan pultruded deck system.

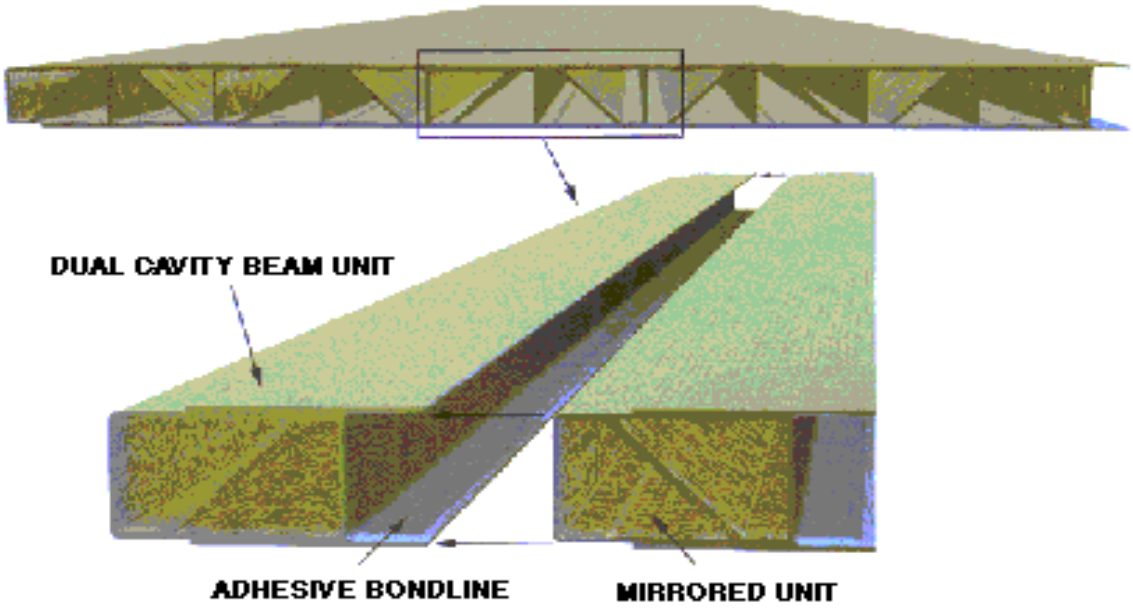

Figure 145
DuraSpan® deck system by Martin Marietta Composites, Inc.

Construction Details

The construction of four different FRP bridges is discussed in connection with details in construction issues. The four bridges are the Laurel Lick, Laurel Hill Creek, Wickwire Run and Market Street bridges. These bridges were among the 20 highway bridges that the Constructed Facilities Center at West Virginia University, in cooperation with FHWA and the West Virginia DOT-DOH, were chose to rehabilitate *[24], [25]*.

Deck Details

The decks for the four bridges were fabricated by Creative Pultrusion Inc. under the trade name of Superdeck. They were all designed to the AASHTO HS25-44 standard for live loading. The weight of the decks was about 20 percent of that of a reinforced concrete deck. The cross sections were made of hexagon and double trapezoids. The fibers used were E-glass multiaxial stitched fabrics with a chopped strand mat and continuous rovings. Vinyl ester resin was used as the matrix phase.

Shipping and Handling

Special hooks were provided by the manufacturer for the purpose of lifting up the deck modules. Much care was taken to prevent any damage of the flanges. To accomplish this, nylon straps were utilized, and the lifting was done in such a way as to transfer the lifting load across the width of the module. To erect the superstructure, a crane was used, whose capacity depended on the size of the deck module.

Surface Preparation

The surfaces of the stringers and the modules were prepared prior to connecting both members. This preparation included sandblasting to remove dirt and grease from the surfaces. According to the Market Development Alliance of the FRP Composite Industry, the edges of the modules have to be wiped clean with a cloth dipped in methyl ethyl ketone *[24]*. As a precautionary measure, the surfaces of the modules and stringers were then covered with blankets until it was time for the bonding operation.

Assembly and Connections

The assembled structure of all four bridges composed of the FRP deck modules aligned transversely to traffic flow and were supported by girders. For three of the bridges (Laurel Lick, Laurel Hill Creek, and Wickwire Run bridges), the connections of deck-to-deck and deck-to-stringer included both adhesive bonding and mechanical fasteners. The mechanical fasteners were in the form of shear keys that provided adequate shear transfer between modules. In the Market Street Bridge, the interconnection of deck-to-deck was done using adhesive bonding only. The modules were connected to steel plate girders by field welding. A steel washer plate was then used to tie the deck down to the girder.

Wearing Surface

For all four bridges, thin polymer concrete (PC) was used as the overlay material. First, surface preparation was carried out. This included sandblasting the deck to get rid of impurities on the surface and improve the bonding. Vacuum cleaning was done to eliminate polymer powder produced during surface preparation. A urethane-based primer was applied. Care was taken to deal with effects in temperature variations during the curing phase of the overlay. The laying of the wearing surface was done when the temperature was above 50^{o}F and below 80^{o}F. This was done to prevent the PC from curing faster or slower than needed *[24]*.

Manufacturing Processes

There are different manufacturing methods used in the production of structural composites. Examples include hand lay-up, vacuum-assisted resin transfer molding (VARTM), pultrusion, vacuum bag molding, press molding, and autoclave molding *[18]*.

Hand Lay-Up

This is a manual approach in which layers of fabric and resin are successively applied onto a mold. The mold is first designed to the shape of the final composite structure. This method is perhaps the simplest, oldest, and least complicated. The fiber layers are oriented in such a way as to develop the desired strength and stiffness. After each layer of fabric is placed, a

roller is used on the composite so that a strong bond results and excess resin is squeezed out. The stacking of fabric materials and resin is done until the required thickness is achieved.

This method is labor intensive and only suitable for production in low volume. It also has a disadvantage of low quality control and inconsistency in properties of various parts of the finished product. However, with this method, complicated shaped composites can be manufactured, such as the complex core configuration of the sinusoidal honeycomb panel. In recent years, the advances in manufacturing technology have resulted in some improvement in this manual process. Today, the hand lay-up has become automated in several applications.

VARTM (Vacuum-Assisted Resin Transfer Molding)

In this process, dry fabrics that needed to produce the structural component are stacked together successively. The fabric is placed in an open mold surface without a top. When the lay-up operation is completed, the mold is covered, and a vacuum is applied to consolidate the material. Resin is then allowed to flow and disperse through the entire structural network, with the mold kept under vacuum. The resin is cured under ambient conditions.

This process has a great advantage of comparatively low cost of production, since the materials, molds, and equipment are inexpensive. It is also advantageous over many other methods because of minimized environmental hazards from toxins associated with the process. The mold is sealed during the resin application, thus controlling environmental threats and reducing health risks of workers.

Pultrusion

This method is used primarily to produce prismatic structural members. Fibers are passed through a resin bath to coat them. The coated fibers are then formed into the desired shapes and passed through a die that helps to consolidate the fibers and produce a composite with a high fiber volume fraction. Then the full section emerges. The resulting shape of the final section depends on the way the die is fabricated.

Vacuum Bag Molding

The purpose of this process is to create a very good bond for the individual plies. The entire composite is placed into a flexible bag and a vacuum is applied. This helps to push together the plies, thus developing a good bond. Volatiles that form during the curing process are also removed.

Press Molding

Here, high pressure and temperature are the catalysts to developing strong chemical bonds between layers. The composite material is placed into the press, where external pressure and elevated temperature are applied. Components of simple shape configurations are usually produced by this method.

Autoclave Molding

The autoclave molding process allows for more complex shapes to be manufactured than does the press molding. A furnace is used to cure the composite at very high temperatures and pressure. The high pressures can force voids and excess resin out of the composite and increase the fiber volume fraction. Also, because the resin is cured at elevated temperatures, properties superior to those resulting from curing at ambient temperatures are developed.

Research

Feasibility studies reveal that FRP honeycomb structures are very efficient in providing high mechanical performance with minimum unit weight. The geometry of this sandwich structure is designed to improve stiffness and buckling response by the continuous support of core elements with the face laminates.

A study by Davalos et al. went further in design modeling and experimental characterization, and obtained an approximate analytical solution through a homogenization process *[26]*. To verify the results, experiments were performed and a finite element analysis (numeric verification) was carried out. The goal of that study was to develop equivalent elastic properties for the core structure. To obtain the equivalent properties of the face laminates, a micro/macro mechanics approach was used, while an energy method combined with mechanics of materials approach was used for the core.

FRP panels used in that study were developed by Kansas Structural Composites, Inc. The production of the panel involves sequentially bonding a flat sheet to a corrugated sheet to form the flat and waved FRP cells. It is then assembled and co-cured with the upper and lower face laminates. The representative volume element of the honeycomb core manufactured by KSCI had a flute width of 2 in. (0.0508 m) and half-sine wavelength of 4 in. (0.1016 m). The constituent materials were E-glass fibers and polyester resin. Verification of the results obtained was done by carrying out experimental testing and finite element modeling of FRP honeycomb beams. These were then correlated with analytical solutions based on first-order shear deformation theory. It was observed that the analytical solution correlated well with both the finite element modeling and experimental results.

In another work, the bending response of pultruded shapes predicted analytically were correlated with results obtained experimentally *[27]*. The pultruded FRP shapes were modeled as a layered system, the fiber volume fractions were then computed and the ply stiffnesses were evaluated using the micromechanics approach. It was shown that the results agreed closely with experiments and was further verified using the finite element analysis. The study proved that ply stiffnesses of the constituent materials of FRP laminates can be accurately predicted using selected micromechanics formulae, as long as the volume fiber fractions are correctly evaluated using the information provided by the manufacturer.

The lateral load distribution characteristics of a 14-girder bridge with corrugated metal decking with asphalt wearing surfaces was compared to the same bridge after the original deck was replaced with a FRP deck with polymer concrete wearing surface *[28]*. These comparisons were developed by field testing the Crawford County Bridge 031 prior to and after the deck rehabilitation. Simple dynamic allowance tests were also conducted. The bridge 031 used in this experiment is located near Pittsburg Kansas on K-126. The data was evaluated to determine when the bridge was experiencing maximum global stress. Lateral distribution of stress was computed, and a summary of maximum values has been provided. The results of the study indicated that the simple dynamic tests are not to be used for decisions or conclusions for dynamic allowance. Testing also indicated very little change in the load distribution between the original deck system and the FRP deck system.

An experimental study was conducted to measure principal strains and deflections of glass fiber-reinforced polymer (GFRP) composite bridge deck systems. The experimental results are shown to correlate well with those of an analytical model. While transverse strains and vertical deflections are observed to be consistent, repeatable, and predictable, longitudinal strains exhibit exceptional sensitivity to both strain sensor and applied load location. Large, reversing strain gradients are observed in the longitudinal direction of the bridge deck. The GFRP deck system's geometry, connectivity, material properties, and manufacturing imperfections coupled with the observed strains suggest that the performance of these structures should be assessed under fatigue loading conditions. Recommendations for accurately assessing longitudinal strain in GFRP bridge decks are made *[29]*.

Aluri et al. conducted dynamic tests on three FRP deck bridges, namely, the Katy Truss Bridge, Market Street Bridge, and Laurel Lick Bridge, in the state of West Virginia. The dynamic response parameters evaluated for the three bridges include dynamic load allowance DLA factors, natural frequencies, damping ratios, and deck accelerations caused by moving test trucks. It was found that the DLA factors for the Katy Truss and Market Street bridges

are within the AASHTO LRFD specifications, but the deck accelerations were found to be high for both these bridges. DLA factors for the Laurel Lick Bridge were found to be as high as 93 percent against the typical design value of 33 percent; however absolute deck stress induced by vehicle loads is less than 10 percent of the deck ultimate stress *[30]*.

The New York State Department of Transportation (NYSDOT) has installed several FRP bridge decks. Several of these decks have deteriorated to various degrees, and the wearing surface on some of the decks has been replaced. There is limited information on the durability of these wearing surfaces.

Ziehl and Bane conducted acoustic emission evaluation of an FRP panel. Strain, load, displacement, and acoustic emission were monitored. A finite element model of the specimen was developed and this model was compared to the measured displacement data. Finally, one area that has not been adequately addressed is inspection methods for these FRP bridges (or any other FRP applications). Bridge management engineers who conduct biennial inspections are not aware of what needs to be done to inspect the FRP composite components. NCHRP Project 10-64 ("Field Inspection of In-Service FRP Bridge Decks") is currently addressing this issue *[31]*.

Bridge Applications of FRPs

The applications of FRPs in civil engineering can be classified into three broad areas. Firstly, new structures such as bridges and columns built exclusively out of FRPs have proved durable and very resistant to environmental hazards. Secondly, and a more common application, is the repair and rehabilitation of damaged or deteriorating structures. Third, FRPs have been used in architectural or aesthetic applications such as in cladding, roofing, flooring, and partitions. FRPs can be used for barriers, docks, marinas, covers, blast shields, vehicle platforms for unstable ground, rapid construction, bridges, bridge decks, etc.

Allampalli et al. discussed the design, fabrication and construction process of the Bennetts Greek Bridge. Structures Division of NYSDOT also documented the seven bridges they had built up to year 2003 and summarized the design suggestions *[32]*.

Most of the bridges have a thin polymer concrete wearing surface although sometimes asphalt is used. Various amounts of testing have been performed in order to design each of these bridges; many of them have been load tested in the field, and/or they are being evaluated using long term monitoring systems. One issue that has yet to be addressed involves guardrails. No crash-test-approved guardrail attachment system or full FRP composite guardrail system exists. Studies have been initiated through ongoing innovative bridge research and construction (IBRC) projects to investigate connections that will enable

traditional guardrails to be safely attached to FRP decks.

Miyun Bridge, Beijing (1982)
Some of the first applications of fiber-reinforced plastics for complete bridge structures were in China. A number of pedestrian bridges have been built, but the first all-composite bridge deck was the Miyun Bridge completed in September 1982 near Beijing, which carries full highway traffic *[22], [33]*.

Ulenbergstrasse Bridge, Düsseldorf (1986)
The Ulenbergstrasse Bridge in Düsseldorf, Germany was the world's first in the use of high tensile strength glass fiber prestressing tendons *[33]*. The bridge cross section has been monitored since its completion in July 1986 with four fiber optic sensors. The results obtained show the effects of temperature variation on strain and also detect any cracking of the concrete structure. This type of monitoring program has thereby proved a cost effective way of introducing a new structural material without lengthy proving trials. Any degradation in structural performance will be indicated by the sensors and the exact location of the defect will be known. Any remedial steps that must be taken will therefore be directed to solving problems as they arise.

Aberfeldy Footbridge (1992)
The Aberfeldy Footbridge, which crosses the River Tay in Scotland, was erected in 1992. It is the world's first and also longest advanced composite footbridge *[22], [33]*. The bridge is a cable-stayed structure with a main span of 207 ft. (63 m) and two back spans of 82 ft. (25 m). The two pylons, each made of Glass FRP, are "A" shaped and have a height of 59 ft. (18 m). The cables are Parafil (Kevlar aramid fibers sheathed in a protective low density polyethylene). The fabrication of the bridge deck was from the Advanced Composite Construction System (ACCS).

Glass reinforced polyester (GRP) hand railing and a wear-resistant deck finish were used to complete the bridge. Minimal foundations and rapid site assembly made this solution very cost-effective. It was originally designed with a live load capacity of 0.5 psi (3.5 kN/m^2), but it has been strengthened since then to accommodate golf carts and had ballast added to improve its performance.

Bonds Mill Lift Bridge (1994)
The Bonds Mill Bridge is an electrically operated lift bridge. It was the first bridge in England to be constructed from plastic. Its construction was completed in 1994. It is also the world's first advanced composite road bridge. It is 27 ft. (8.23 m) long, 14 ft. (4.267 m) wide and 2.8 ft. (0.853 m) deep and was manufactured from Maunsell Structural Plastics'

Advanced Composites Construction System (ACCS). It was constructed utilizing a series of pultruded GRP sections running longitudinally and are bonded together using an epoxy resin to form a cellular box girder with six main cells that are filled with epoxy foam. The deck is a "double ply" of ACCS skins with cells running in two orthogonal directions. The total weight of the entire system is 10 kip (4.5 tons) for 377 ft^2 (35 m^2) of deck area, which gives a live to dead load ratio of 13.5. Composite materials were used because lighter weight structure made it possible to use a smaller lift mechanism.

No-Name Creek Bridge, Kansas (1996)

On November 8, 1996, the nation's first all-composite FRP bridge on a public road was installed over No-Name Creek, just three miles west of Russell, Kansas, and this was done by Kansas Structural Composites, Inc. (KSCI) of Russell, Kansas *[26]*. It is a short-span, self-supporting bridge of 23 ft. (7 m) in length and 27 ft. (8.22 m) in width and demonstrates the viability of the structural panel concept. It was built with the capability of supporting an AASHTO HS-25 load in both lanes. The bridge was constructed of three adjoining longitudinal sandwich panels with a depth of 22.5 in. (0.57 m). The sandwich structure composed of a 20.5 in. (0.52 m) thick core with a 0.75 in. (0.019 m) lower face and a 0.5 in. (0.0127 m) upper face. The core has a sinusoidal wave configuration in the plane extending vertically between the faces as seen in Figure 142. Demonstrating the simplicity of the project, the whole installation process required just one and a half days. Part of the construction is shown in Figure 146.

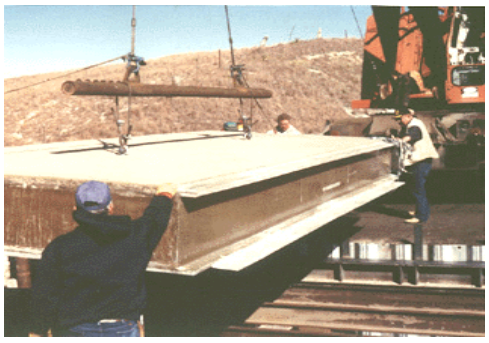

Figure 146
Installation of No-Name Creek Bridge, Russell, Kansas

Laurel Lick Bridge (1997)

The construction of this short-span bridge was completed in May 1997 in Lewis County, West Virginia *[24]*. It spans 20 ft. (6.10 m) and has a width of 16 ft. (4.88 m) . It consists of a modular FRP composite deck supported by pultruded FRP piles and I-beams. Hollow glass fabric shapes were pultruded and combined to obtain an H-deck. This is composed of E-glass fibers in the form of triaxial stitched fabrics, continuous rovings and chopped strand mats.

Sandstone foundation supported the piles for the bridge and was also filled with polymer concrete. The wide-flange pultruded I-beams were attached to the reinforced concrete cap pilings with steel clip plates. These I-beams were spaced at 2.5 ft. (0.76 m) centers. The FRP deck modules were connected to these I-beams with 0.5 in. (1.27 cm) blind fasteners. A polyester polymer concrete overlay of 0.4 in. (1.0 cm) thick was used as the wearing surface. The kerbs were made of FRP square tubes, and a live loading based on AASHTO HS25-44 was the design standard.

Tom's Creek Bridge (1997)

A partnership formed by Virginia Tech, the Virginia transportation research council (VTRC), the Virginia department of transportation (VDOT), the Town of Blacksburg, Virginia, and Strongwell (formerly Morrison Molded Fiber Glass) completed the rehabilitation of a small bridge over Tom's Creek in 1997. The Tom's Creek Bridge is located 1.5 miles from the Virginia Tech on a rural road with a traffic count averaging 1000 vehicles a day during the school year–95 percent of which are commuter vehicles. The original Tom's Creek Bridge was built in 1932 and then repaired in 1964. This original structure was composed of a steel superstructure composed of 12 20 ft. (6.09 m) long W10 x 21 I-beams, a deck composed of 4 in. X 8 in. (10.16 cm X 20.32 cm) wood beams, and a 3 in. (7.62 cm) asphalt surface. The bridge had a span of about 20 ft. (6.09 m) and is 24 ft. (7.31 m), wide at a skew angle of 12.5°. An inspection of the bridge had identified significant corrosion on a number of the steel stringers, and the bridge had been posted at 10 tons (down from its original 20-ton classification). This structure is owned by the Town of Blacksburg, and they were looking for an inexpensive and temporary solution to the problem.

The Town of Blacksburg was interested in trying new technologies and agreed to the replacement of the steel beams utilizing Strongwell's FRP hybrid 8 in. X 6 in. (20.32 m X 15.24 m) double-web beam with carbon fiber reinforcement in the flanges. VDOT supplied an engineer of record for the project and developed the design plans for the rehabilitation. The composite beams to be used in the replacement were tested in the fall of 1996 and the spring of 1997 for modulus and strength. A mock-up of the new bridge was then constructed and tested in the civil engineering structures at Virginia Tech in May 1997. Construction of the new bridge was completed in June 1997 after only one week. This upgrade resulted in increased beam stiffness and an improvement in the bridge capacity from 10-ton to 20-ton after the rusted, severely deteriorated steel beams were replaced.

Tech 21 (Smith Road) Bridge (1997)

This is Ohio's first all-composite bridge. The Butler County Engineer's Office installed this

structure built entirely of advanced composite materials in 1997 *[34]*. Structural polymer matrix composites (PMC) such as glass fibers in thermosetting resins were used in the construction of the bridge, providing high specific strength, specific stiffness, and corrosion resistance. This bridge (also known as the "smart bridge") is also the nation's first fully instrumented bridge. Health monitoring instrumentation was installed for the purpose of providing information on the performance under field conditions. Special sensors have been embedded and linked to special computers designed for continuous monitoring. The bridge has a span of 33 ft. (10.06 m), a width of 24 ft. (7.3 m), and a depth of about 2.8 ft. (0.85 m). It has a weight of less than 22,000 lb. It consists of a DuraSpan™ deck bonded compositely with three U-shaped FRP girders, which serve as supports, and has a reinforced concrete substructure. The deck is a sandwich FRP construction consisting of pultruded tubes between two face sheets. The tubes run parallel with the traffic direction. The bridge was designed with the AASHTO HS25-44 standard for live loading *[22]*.

Laurel Run Road Bridge (1998)

This bridge was constructed in Somerset County, Pennsylvania, and was open to traffic in October 1998 *[22]*. It is a short span composite deck with steel stringers and has a dimension of 28 ft. (8.66 m) by 33 ft. (10.04 m). It consists of the Superdeck™ (modular FRP composite deck) supported on a W14 x 68 galvanized steel I-girders at a spacing of 3 ft. (0.9 m) centers and a substructure of steel-reinforced concrete. The modular deck design is one featuring trapezoids connected with hexagon-shaped pins. Epoxy polymer concrete was overlayed as the wearing surface. FRP square tubes were used for the kerbs. The bridge has been designed for AASHTO HS25-44 live loading.

Troutville Weigh Station (1999)

This bridge, located in Troutville, Virginia, was constructed in 1999 and is a 10 ft. (3.048 m) by 15 ft. (4.572 m) composite deck section *[22]*. Standard EXTREN® structural shapes and a plate of 15 ft. (4.65 m) width were used in the construction of the bridge deck. EXTREN® is a proprietary combination of fiberglass reinforcements and thermosetting polyester or vinyl ester resin systems. It is produced in more than 100 standard shapes and all shapes have a surface veil to protect against glass fibers penetrating the resin surface in service and to increase corrosion and UV resistance. The deck has as support steel I-girders and experiences traffic of over 13,000 fully loaded trucks per day.

Some other features of the bridge include routine inspection capability installed into the system and flexible foundation for the purpose of future experimental bridge decks. A data acquisition monitoring system to collect and report real data has been installed by Virginia Tech.

Salem Avenue Bridge, Dayton (2000)

Several different FRP composite deck sections were installed on the Salem Avenue Bridge (SR-49) in the City of Dayton. The Salem Avenue Bridge, which crosses the Great Miami River, carries six lanes of traffic with an average of 30,000 vehicles per day in and out of the city. It was originally built in 1951 with steel and consisted of twin structures with a longitudinal joint and a four-foot raised concrete median down the center. After many decades, it was observed that the bridge needed replacement; it had developed numerous potholes and cracks. Therefore, in 1999, Ohio Department of Transportation (ODOT) began an experiment to rebuild the 679 ft. (207 m) bridge with light-weight, high-strength FRP panels as part of a project to test this space-age material for various bridge applications. The construction was done in 2000 and was designed based on AASHTO HS25-44 code for live loading. This project is part of the IBRC program (Project OH-98-05), and the ODOT is conducting studies on the effectiveness of the various FRP deck panels that were used to replace the existing concrete deck.

The design, construction, and long-term observation of this bridge illustrate some difficulties encountered in the use of FRP in bridge construction *[22]*. The new bridge, which is 96 ft. (29.26 m) wide and 684 ft. (208.4 m) long, originally consisted of four different FRP deck material sections manufactured by separate companies. These FRP panels for the span did not fit together smoothly and didn't bond correctly to the bridge's beams. Additionally, after a few months of the completion of the project, some complications with some of the panels were noticed, leading to a closure of the north side of the bridge in September 2000. Composite deck cracking and blistering were observed. Sometime later, two of the panels were observed to have experienced delamination. Because of inadequate performance, two of the deck systems have since been removed and replaced with a concrete deck.

Results of this pilot project are providing very useful information regarding the application of lightweight FRP deck panels for the replacement of deteriorated concrete decks. Investigations revealed that the delaminations were due to defects in manufacturing. It was also found that the haunch of the steel girders did not have a uniform contact bearing area under the FRP decks. The joints between different deck systems were also observed to be open because of the variations in the stiffnesses. Thus, variable deflection could result in damage. This shows the need for more careful procedures in the design of connections and other details, as well as proper material selection. Issues such as appropriate detailing and quality assurance/quality control (QA/QC) of the constructed project have come thus to light. Sharing of information among bridge owners on successes and failures can increase knowledge on the appropriate application of FRP materials.

More recently, Ohio initiated Project 100, a statewide initiative of the National Composite Center to extensively introduce FRP composite material technology as a supplement to conventional concrete-and-steel bridge-deck construction. Martin Marietta Composites is the contractor for the project. As with many large-scale demonstration applications, especially those using rapidly evolving technologies, issues related to specific final designs and details for the I-5 bridge (among other reasons) resulted in delays of its actual deployment. From the results of field load tests, ongoing monitoring, and bridge inspections, it appears that the existing FRP bridges are generally performing well. The one area of concern is the durability of the wearing surface. In several cases, significant reflective cracking has been observed. This may be due to the local flexibility of these decks under concentrated wheel loads.

One bridge that has not yet been built, but that has received much attention is the I-5/Gilman Advanced Technology Bridge in La Jolla, California. This cable-stayed bridge, made entirely of FRP composite, will be 450 ft. (137.16 m) long by 48 ft. (14.63 m) wide, carry two 12 ft. (3.65 m) lanes of vehicular traffic, and have two 8 ft. (2.43 m) bike lanes, a walkway, and utility lines. Among many FRP composite components, the bridge will have girders and pylons made of carbon fiber reinforced polymer (CFRP) composite tubes filled with concrete, an FRP deck, and FRP stay cables. The project is currently funded through the IBRC program (Projects CA-98-01, CA-00-01, and CA-01-01).

In this century, further research on FRP continues. These include concrete repair and reinforcement; bridge deck repair and new installation; composite-hybrid technology (the marriage of composites with concrete, wood, and steel); marine piling, and pier upgrade programs.

Part 2: A Review of Acoustic Emission (AE) Monitoring for Bridges

Introduction

The rapid deterioration of civil structures such as bridges is a cause of major concern all over the world. In the US, as of 2004, it was reported that at least 27 percent of all bridges were rated as “deficient” *[35]*. The rating signifies the condition of the bridges and implies that either closure of the bridge or restriction of only light vehicles to pass is recommended due to the decreased structural integrity. The implications of the rising figures of deteriorated structures have caused engineers to look into the need of reforming inspection methods that have been followed over the years. Engineers were also aware of non-destructive techniques used widely in aerospace and pressure vessel industries that they understood could be adapted to suit the civil infrastructure. Thus the decision was made to incorporate the extensive capabilities of these techniques to monitor bridges and also allow predictions that

may extend the remaining service life of a structure.

Of the many techniques available, AE was found to be the most widely used method for highway structures *[36]*. AE testing is a powerful nondestructive testing tool for examining the behavior of materials deforming under stress. By definition, AE is the class of phenomena whereby transient elastic waves are generated by the rapid release of energy from a localized source or sources within a material, or the transient elastic wave(s) so generated *[37]*. Thus the technique can be used to listen to events that lead to failure of a material, using sensors that act like the material scientists' stethoscope. The AE test technique uses either operational or applied loads to simulate emissions from the material to be tested. A single test system may be used for many different measurement applications by making suitable frequency adjustments. In order to interpret the results obtained from these tests, one should know the underlying physical process involving the propagation of the wave in test materials, techniques and equipment used in measurement, inherent material characteristics, and the possibility of background noises that may interfere in the acquisition of data.

Few of the successful applications of AE have been in the areas like intermittent or continuous monitoring of pressure vessels wherein acquisition systems are employed to detect and locate active defects; detect fatigue failures in aerospace and other structures, characterize variant damage mechanisms; and also monitor stress corrosion cracking *[35]*

For bridges, though many successful inspections have been carried out using the technique, there has not been any definite standard that specifies procedural and other requirements that are needed to carry out an AE test. Bridges are mainly made of concrete, then steel, and more recently FRP materials. It is known that these materials emit energy in the form of elastic waves due to various material-relevant damage mechanisms that are produced due to the loading conditions that exist in bridges, of which they are a part of. These waves are picked up by sensors attached to the surface of the material. And the further evaluation of the discontinuities thus detected gives an overall picture as to the condition of the bridge and also prioritize repair and maintenance. One of the first successful bridge monitoring was carried out in 1972, by the joint effort of the Physical Acoustics Corporation (PAC) along with Dunegan Testing on the Dumbarton Bridge over San Francisco Bay (pacndt.com). The intention was to monitor the main lift cables of the bridge. Once the first step was made, a huge number of inspections on several other bridges were carried out using the same technique by not only PAC but also other corporations like TISEC, Vallen, etc.

Basics of Acoustic Emission

The basic principle of acoustic emission testing is that: a developing flaw emits bursts of energy in the form of high frequency sound waves (Figure 147). By separating background noise from AE, the ongoing condition of a structure can be monitored.

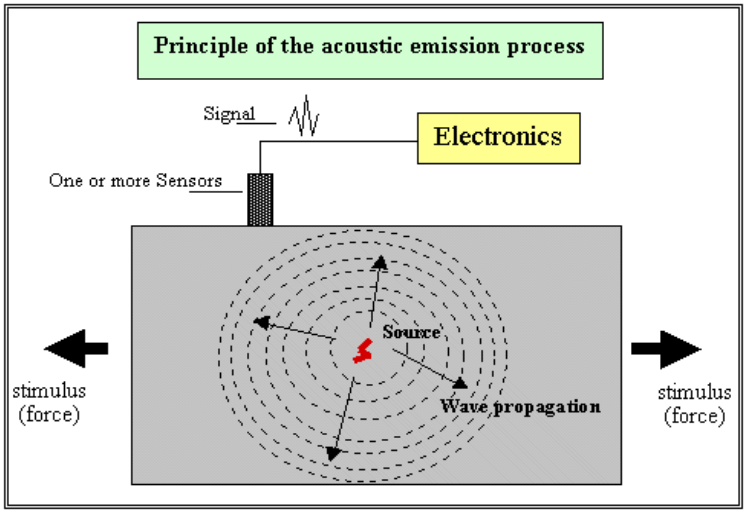

Figure 147
Principle of acoustic emission ***[38]***

Kaiser Effect. This effect was first investigated by Wilhelm Kaiser (1950) who described the phenomenon that a material under load emits acoustic waves only after a primary load level is exceeded. Acoustic activity will be absent in the unloading phase. During reloading, these materials behave elastically before the previous maximum load is reached. If the Kaiser effect is permanent for these materials, little or no acoustic emission will be recorded before the previous maximum stress level is achieved. This is illustrated in Figure 148, which shows the AE rate versus time along with the load for an experiment where a concrete cube subject to compression was tested under a cyclic load. The loading path of 1-2-3 in Figure 148 clearly indicates the absence of emissions up to the previous maximum load.

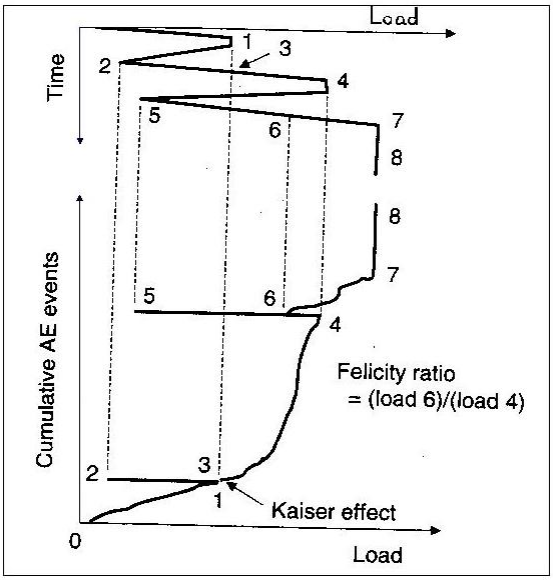

Figure 148
Kaiser and felicity effects *[39]*

Felicity Effect. As the appearance of significant acoustic emission at a load level below the previous maximum applied level, typically observed in composite materials. Clearly from the loading path 4-5-6 in Figure 148, it's seen that at higher levels of stress the material tends to weaken and thus emits acoustic waves a little before the previous maximum load is reached. An understanding of the above effects helps set the loading pattern so as to get sufficient generation of AE detectable by the sensors.

Factors Influencing Dynamics of Acoustic Wave Propagation

There are several important aspects of the dynamics of the wave propagation process that need to be considered, the attainable accuracy is governed by the wave propagation processes such as:

- Attenuation: the process is defined as the loss of signal amplitude due to material damping and also geometry of the material. A quantity that enables determination of sensor configuration.
- Wave velocity: an input parameter in most present day acquisition systems, primarily for source location algorithms.
- Geometry and material properties: crack geometry and material structure are factors that vary the amount of acoustic activity generated.
- Effects of multiple paths and wave modes: during the travel of wave from the source to the sensor, there is no restriction in the path or mode of travel.

- The kind of stress applied to the material may cause display of different acoustic event.
- Even the rate of loading can provide a different AE signature.

Thus detectibility of acoustic emissions may be due to all or a few of the various factors briefed above. High acoustic emissivity may be directly associated with: damage of materials, crack propagation, low-temperature deformation, brittle fracture, etc. *[40]*.

Filtering of Background Noise in AE Signals

The key issue that has held back the progress of the AE technique in bridge monitoring field is the background noise. Though sensitive sensors were designed to pick up all crack related noises, in the early days very minimal success was achieved in reducing the detection of background noise. Fortunately the background noise range is usually in the range of 100 to 300 kHz. This property of noise enables selection of AE monitoring frequency in a range that neglects noise. Researchers like Nakamura, Horak, and Weyhreter, etc. have suggested various solutions to this problem that is implemented in the current day acquisition systems *[41], [42]*. Once this drawback was remedied, the use of AE in bridge sites has become plausible.

Advantages and Disadvantages of AE

Advantages

- Nearly all materials are able to generate acoustic waves on the application of loads.
- Enables both local and global monitoring
- Continuous monitoring possible
- Able to detect and locate defects from a few static sensor locations. Localization made easy by time differential of signals.
- AE signal parameters may be correlated to stress intensity.

Disadvantages

- Though the issue of background noise has been fairly addressed, no material or environmental specific standards are recommended.
- Quantitative results have still not been extended from models to actual structure.

AE Monitoring Procedure for Bridges

Acoustic emission monitoring is an ideal method for bridge monitoring as it enables passive monitoring, and thus avoids the need to hinder traffic on the bridge. The technique can be utilized both in a global and local sense *[43]*. In global monitoring, few sensors are used for coverage of large areas, keeping in mind the maximum allowable spacing between sensors to

enable detection. Whereas, local monitoring is adopted in areas either identified during global monitoring or structural analysis.

To date there is no prescribed standard for bridge monitoring using acoustic emission testing. Based on the experience and proposals developed by various researchers like Lozev et al., Yuyuma et al. and Golaski et al., the general steps to be taken to conduct bridge monitoring using acoustic emission technique can be summarized as detailed below:

- A preliminary step would be to conceive the definite objectives of monitoring the bridge. Based on which the magnitude of monitoring and the duration, i.e., short or long-term may be decided.
- The evaluation technique to be adopted along with equipment suitable for the purpose is decided after the initial assessment is made.
- Generally, the chosen equipment is usually portable and the system is placed in a protected location beneath the bridge.
- While deciding to use resonant sensors for monitoring, it might be necessary to determine the frequency range in which defects are observed in the particular structure. This can be done using wideband sensors. Use of guard sensors may also improve the quality of the signals that are recorded.
- Sensor placement configuration is another important decision that needs to be made before actually attaching the sensors to the structure. This plays a vital role during source location.
- Appropriate couplants and holders should be selected ensuring proper attachment of sensors and preamplifiers.
- Importance should be given to hardware setup in the data acquisition system used. Material and environmental influences are to be considered while setting up hardware.
- Using a Hsu-Neilson (pencil-lead break) source helps to check the entire setup and ensures sensitivity and proper functioning of the system.
- In case of long-term monitoring, monitoring should be done in phases. A period of a week may be considered sufficient for an initial trial. This helps the personnel to make changes in system monitoring configuration that suits the conditions existing for the bridge.
- Due to the advances made in remote monitoring capabilities of systems, data collected over a period of time can be inspected from a remote location. This should be done periodically to take notice of significant emissions. Alarms signaling the advent of an event may be set.

- Over time, when significant emissions begin increasing a bridge inspector should be sent to the site to decide on the necessary action required to be taken to prevent structural failure.

In all, one may conclude that the procedures for AE monitoring of bridges is the same for bridges made of any material. Only minor system setup variations such as threshold settings and sensor spacing may be governed by the material attenuation characteristics. Also extrapolating results seen in laboratory specimens may not always be advisable. On-site loading conditions and background noise presence cannot be imitated in the lab specimens. Discussions of specific bridge types are given below *[44], [45], [46]*.

Concrete Bridges

Concrete is a quasi-brittle material, thus the energy required for crack growth will be greater than that estimated from linear elastic fracture model *[47]*. One of the first studies of AE in concrete specimens under stress was carried out by Rusch (1959). He confirmed the presence of Kaiser effect in concrete at stress levels around 75 to 80 percent of the ultimate strength. L'Hermite (1960) observed that AE activity in concrete increased sharply exactly when the Poisson's ratio increased. With the evolution of the instruments, more refined results were obtained by researchers like Robinson, Wells, and Green, who proposed the use of AE in monitoring of cracks *[48]*.

It has been recognized that for the generation of AE, damage growth is essential and this in turn relies on the load history experienced by the structure *[49]*. The general consensus on the types of damage that forms AE sources in concrete has been listed as: matrix micro cracking, shutting of pores, lack of adhesion between matrix material and filler, physical failure of filler, delamination, corrosion of reinforcing, or prestressing steel, etc. *[45], [50]*. During monitoring the entire superstructure needs to be assessed and the areas to be looked into would be critical sections like shear zones, tension zones, bearing regions, corrosion prone areas, repeated dynamic vehicular loading, etc. *[50]*. The Non-destructive Evaluation Validation Center (NDEVC) in Virginia had conducted acoustic emission tests on concrete bridges during 1996-2000. They used the monitoring technique to detect cracks in bridges, by passing high experimental overloads. These kind of special overloads were required as they could not observe any acoustic activity prior to that.

Parameters affecting AE from concrete

- Kaiser effect – Though its existence at 70 to 85 percent of ultimate strength in concrete is true, other researchers like Spooner confirmed that the effect did not occur beyond the peak of the stress- strain curve.

- Signal attenuation – another major reason of concern is that concrete is a composite material, thus large acoustic even may occur away from the sensor without being detected due to attenuation. It has been observed that matured cements show greater transmission capabilities. As a consequence of the above phenomenon, care must be given while spacing sensors reduce the effects of attenuation as much as possible.

Though most of the initial bridge monitoring capabilities of AE was explored in steel bridges, in the past two decades, there have been numerous efforts made by various universities, highway agencies, etc. to implement the method for concrete bridges as well *[51]*. The exceptional features of this monitoring technique is that there is no issue of traffic interruption during in-service monitoring of the bridges, and the use of sensors with small surface area removes concern for the contact surface profile *[36]*. Reinforcement corrosion and the resulted cracking are considered the main damage mechanisms that have reckoned the need for a long-term condition assessment of concrete bridges.

Numerous studies have been conducted to capture the AE signature in concrete and infer the location of the defect and damage state identification. In 1997, Weiler et al. conducted tests on concrete beams of different configurations acting under varied loading conditions and reported that sensor placement was a crucial factor to get useful information *[52]*. A detailed study of the AE waveforms revealed that signals produced as an outcome of shear and flexural cracking had larger amplitudes and duration than micro cracking phase of damage *[53]*. Figure 149 shows the damage propagation trends in a reinforced concrete (RC) beam.

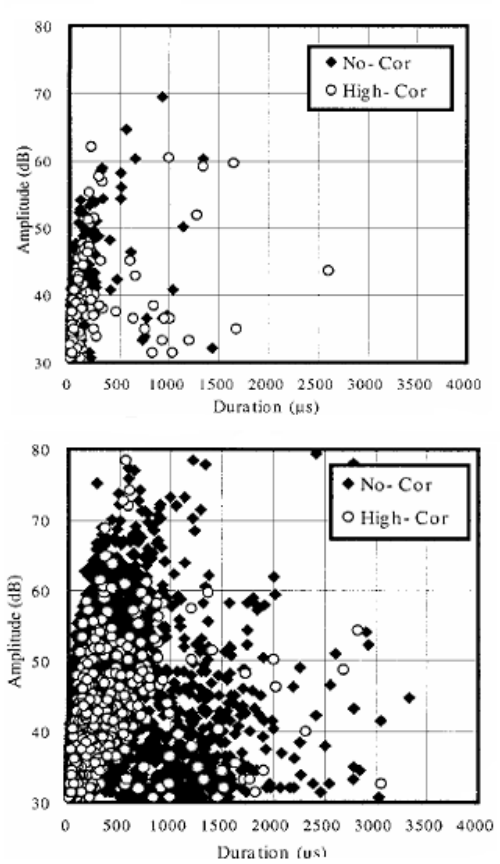

Figure 149
Amplitude-duration plot of AE signals for initial and ultimate stages of damage in an RC specimen *[53]*

AE monitoring is not always used as a primary monitoring method due to the qualitative nature of results. The quantitative approach has been proposed by researchers like Golaski et al., Beck et al., etc. *[46], [54]*. Yet, its field applications have still not been ascertained. Several correlations between AE signal parameters and material characteristics have been attempted. In the following paragraphs, details of the various qualitative and quantitative assessment techniques adopted by various researchers will be discussed.

Yuyuma et al. suggested use of concrete beam integrity (CBI) ratio for evaluating repaired concrete both in lab specimens and field conditions *[45]*. They defined CBI ratio as the ratio of load at onset of AE to maximum prior load. Neither the sensitivity of the sensors nor the attenuation characteristics seemed to influence the CBI value. They concluded that the structure that possesses a value of CBI < 0.8 are considered seriously damaged. Another suggestion was put forward by Ohtsu et al., who introduced the Calm and Load ratios to give a quality assessment of reinforced concrete beams *[55]*. The calm ratio is defined as

cumulative AE activities during the unloading process to last maximum loading. The load ratio is between load at onset of AE to prior loading. The effect of overloads on bridge structures and their corresponding AE signature was the issue that was investigated by Ziehl and Lamanna *[49]*. Though the acquired AE data during overload did not yield complete information, an overall quality assessment of the structures stability could be done. They recommended that a comparison of data obtained prior to overload and post-overload should enhance the significance of the AE data collected.

Though there existed various qualitative assessment techniques to evaluate AE data, the lack of quantification often required the use of other NDT techniques along with AE. Thus gradually attempts were made to quantify the AE data and a few researchers have found reasonable success in doing so. The influence of the micromechanical behavior to bulk material properties was studied by Landis *[47]*. He tried to quantify AE information using moment tensor analysis to characterize the mixed-mode fracturing nature of concrete. One of the important works done on a bridge structure was conducted by *[46]*. They quantified their results from the AE information obtained by the data acquisition system using the terms: historic index and the severity index. The historic index is a measure of the signal strength throughout the test and the severity index is the average signal strength for the 50 events having the largest numerical value of signal strength. Tests were carried out on bridges of different ages, and the results were quantified and represented as shown in Figure 149.

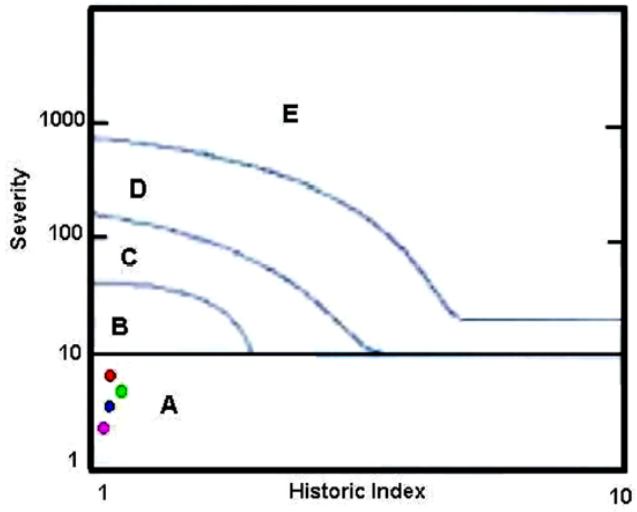

Figure 150
Intensity plot for a whole bridge *[46]*

Figure 149 represents that the bridge structure is sound, as most of the activity lies within the A zone (implying least damage). Over time, AE activity is expected to be visible in zones B

– E, representing the damage progression in the structure. These "b-value" analysis on the AE signal was another proposition that enabled the quantification of results that was mainly developed from its similarities with earthquake wave characteristics. The correlation worked pretty well in tracking the progression of damage but cannot be used on bridges until monitored for a long time and at an early phase of life of the structure *[56]*. Though there exist many unresolved issues of concern with quantification abilities of the method, its qualitative assessment abilities such as source location and damage progression monitoring have been tested in various bridges.

In 2002, Landis et al. looked into another correlation, namely AE energy with concrete fracture energy to enable efficient development of damage models. But the results showed that this was not a good criterion for concrete. Yet another correlation with AE energy to crack parameters revealed that the energy released indicated an association with the crack depth *[54]*. But the test conducted in this case was for mortar specimens, suggesting the results may be extended for concrete. All of the previously mentioned correlations were made mostly on laboratory specimens and the results need much more refinement before it can be applied to a whole bridge.

Steel Bridges

When AE technology was first adopted for bridge monitoring, the initial works were mostly done on steel bridges. In lab conditions, AE was assessed as the best method that can trace the failure modes persistent in metals. But the method was not widely recommended then due to the unresolved issue of background noise elimination, a necessity for on-site bridge monitoring. Today, background noise is no longer a drawback due to the technology update that AE acquisition system has gone through.

Both substructure and superstructure of a steel bridge exhibit typical damage modes like corrosion, cracking, and physical damage due to impact or fire and fatigue cracking *[50]*. Among the different failure modes, fatigue crack monitoring using AE has been investigated by many researchers. Numerous correlations between fatigue crack growth rate and AE data acquired were arrived at by researchers like Morton et al., Holford et al., etc. *[57], [58]*. In Figure 151, a typical waveform pattern of a fatigue crack observed in a steel bridge hanger as acquired from an AE data acquisition system is represented.

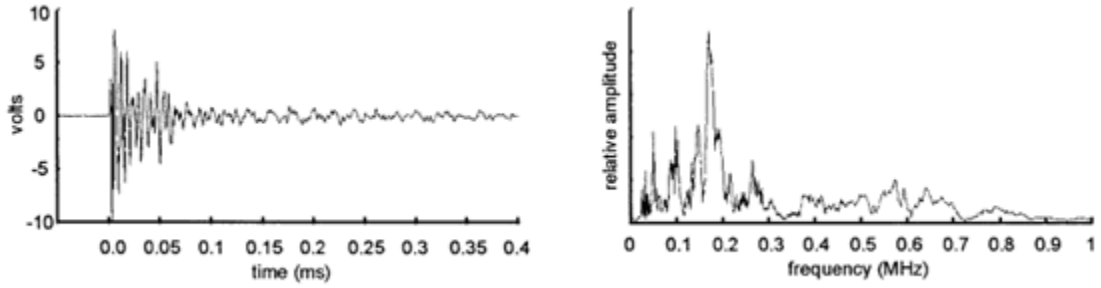

Figure 151
Waveform and frequency spectra from a typical crack in a steel bridge hangar

The VTRC (Virginia Transportation Research Council) has done an appreciable amount of work in studying the nature of AE that is observed from various bridge sites, and they verified the credibility of the AE data collected by them.

Parameters affecting AE from steel

- Attenuation: This property is low in metals like steel compared to composite materials. Yet, they do exist and in turn influence the amplitudes recorded. Higher frequency sensors tend to exhibit greater attenuation with distance *[58]*.
- Secondary emissions: Emissions that are non-crack related are classified as secondary emissions and are usually produced by friction and closing of cracks. As these are observed more frequently than crack-related emissions, they may be exploited to indirectly indicate severity of damage *[59]*.
- Energy: This is another criterion proposed by Sharma et al. that correlates AE energy with fatigue characteristics of carbon-steel *[60]*.

The first long-term monitoring attempt on bridges was made in 1982 by the Dunegan Corporation. They observed the AE generated and tried to distinguish between crack-related events and background noise. They also did a feasibility study for the long-term monitoring possibilities with AE. Researchers at VTRC attempted a qualitative assessment of the acquired AE data from bridge monitoring in field conditions and reported numerous useful insights *[44]*. They noted that progress of a crack may be derived from assessing secondary AE emissions. The use of high-tensioned steel in cable-stayed, suspension, and post-tensioned bridges that are susceptible to corrosion is another area in which AE monitoring proves beneficial. Modern day sensors are well configured to almost accurately detect every event that is associated with wire breaks and aids in preventing major catastrophic failures that may result if such defects are over looked.

Fiber Reinforced Polymer (FRP) Bridge Decks

Though FRP material had been introduced around 1940s, its significant role in civil engineering is fairly recent. Various conventional components of bridges have been replaced with those made of FRP due to its advantageous characteristics such as light-weight, corrosion resistance, etc. Though the use of composites in civil engineering has been limited to mostly strengthening and repair, bridge structures completely made of composites has been around since a decade. Most FRP bridge components and structural projects are doing fairly well, yet various factors like initial cost, lack of complete knowledge with respect to long term performance, and ultimate behavior has slowed the progress of this unique material in civil infrastructure *[61]*.

Typical damage modes observed in FRP bridge decks may be listed as: delamination, matrix cracking, yielding of tensile face sheets, debonding, indentation of the faces and ore at loading points, and fiber breakage *[62], [63]*.

Parameters affecting AE from FRP

- Felicity ratio (FR): This has been recognized as the parameter that can best predict the onset of damage in FRP material *[31], [61]*. The ratio is defined as:
  FR = $\frac{\text{load at which AE events are first generated upon reloading}}{\text{previously applied maximum load.}}$
  A decrease in the value of FR implies damage progression.
- Attenuation: There is severe attenuation losses recurred while waves travel through composites. This causes serious problems when triangulation methods are used for source location, wherein the events may not even be received at a sufficient number of sensors.

The AE signature in composites have been captured and analyzed by various researchers. Though there exist numerous controversies on the general characteristics reported by different agencies, a group of researchers like Shippen, Otsuka, Gostautas (Gostautas et al. 2005), etc., reported that matrix cracking produced low amplitude signals while delamination and fiber breakage showed greater amplitudes *[61], [64]*. Others like Jamison, Valentin, etc. claimed that matrix cracking was the higher amplitude source mechanism. Since attenuation has a great influence on amplitudes recorded yet again, there are researchers who report that amplitude cannot be considered as the sole criterion of composite damage. Correlations between event amplitude and damage growth mechanisms were proposed by Bakuckas et al., and Quispitupa et al. concluded that AE gives accurate results about intensity and location of damages in composites *[63]*.

In 2003, Zeihl and Bane reported their qualitative approach to testing a sinusoidal sandwich FRP bridge deck *[31]*. They devised a cyclic load profile to enable the study of acoustic events generated at load holds and as variations in Felicity ratio as damage progressed. They were successful in tracing the progression of damage and recommended the use of more sensors in future research to refine the results. Another successful qualitative assessment was conducted by Kalny et al. *[65]*. They evaluated the change in AE signature exhibited by a specimen before and after repair, under static loading conditions. They concluded that not only were they able to clearly distinguish the AE activity prior to repair, they noticed increased levels of AE activity implying the possibility of pre-existing damage detection.

On a quantitative outlook, the severity and historic indexes were investigated by Gostautas et al. *[61]*. They did not succeed in formulating intensity zones as done earlier by Golaski et al. in concrete bridges. Yet, they concluded that the intensity analysis was useful to identify onset of damage and calculation of Felicity ratio *[46]*.

In comparison to concrete and steel bridges, the amount of work seen on actual FRP bridge components is limited. Yet there have been efforts both in the direction of qualitative and quantitative assessment of AE data obtained from composites, though there is a definite need to pursue research in understanding the long-term and ultimate load behavior traits.

Remote Monitoring

For actual bridge site applications of AE, the portability of the acquisition system and remote maneuverability are essential. Especially for long-term monitoring, the need for remote monitoring is crucial. Online-monitoring has become one of the key technologies developed by companies like Physical Acoustics Corporation (PAC).

Today, many commercial packages capable of remote monitoring are provided by enterprises such as PAC; Vallen Systems; Pure Technologies, Ltd.; etc. are being used by NDE technicians to evaluate structural integrity of bridges. The Local Area Monitoring (LAM) is an AE monitoring instrument developed by PAC along with the Federal Highway Administration (FHWA). Stryk and Pospisisl proposed to develop a monitoring system that identifies rebar corrosion, a crucial cause of concern in concrete bridges *[66]*. A Canadian company, Pure Technologies, Ltd., developed “SoundPrint” to locate wire breaks in prestressing tendons *[67]*. Vallen systems introduced AMSY4 and AMSY-5 having continuous sampling rate of 10 MHz for the feature extraction required for real-time data processing *[68]*. Using the available technology, though various bridges have been monitored and evaluated, the development of new wireless technologies are greatly influencing the upcoming generation of acquisition systems.

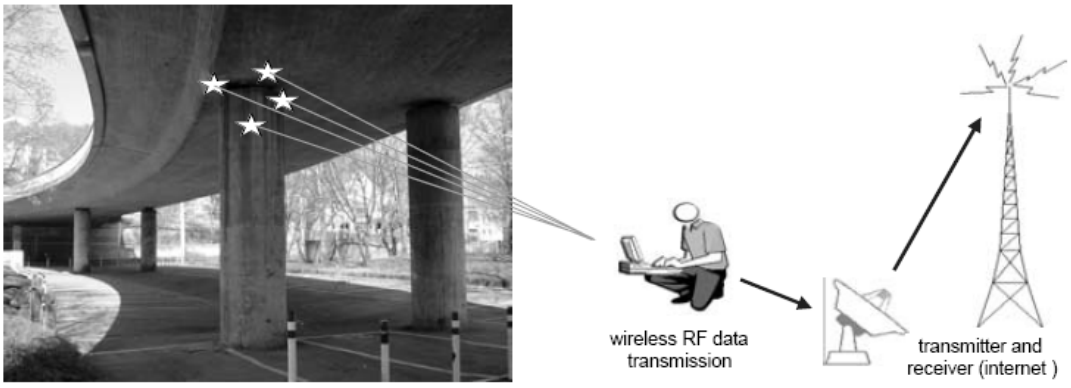

Figure 152
Wireless sensing of bridges using radio frequency transmission *[69]*

Wireless AE sensors are another proposition put forward by Grosse et al. *[69]*. Figure 152provides an idea about the basic concept behind remote monitoring intended with AE using wireless technology. This helps to not only enhance sensor performance by creating sensors based on micro electro mechanical systems (MEMS) but also to make such equipment more economical for use in huge structures like bridges.

Part 3: Review of Application of Fiber Optic Sensors

Introduction

In recent years, researchers have seen increasing attention to the substantial deterioration of civil engineering infrastructures due to the aging and usage beyond the design limits of components. Various non-destructive evaluation (NDE) methods such as ultrasonics, radiography, acoustic emission, eddy current, etc. have been developed to detect damages in civil infrastructures. However, many of these methods suffer from distinct disadvantages such as the lack of portability, susceptibility to electromagnetic interference, and lack of capability for continuous performance monitoring. Electrical strain gauges, on the other hand, are not suitable for monitoring the propagation of internal cracks in concrete since the formation of a crack that intersects across these foil sensors would render them unusable. In addition, electrical strain gauges require smooth bonding surfaces and therefore cannot be readily embedded in the volume of the concrete mix for the detection of cracks and delamination. Furthermore, traditional strain gauges are susceptible to long-term signal drift; therefore, the signal can only be transmitted over short distances *[70]*.

The use of composite materials, such as FRP, in structural engineering applications, such as bridges and overpasses, is growing. In order to promote their applications, a new technology to monitor the performance of these composite materials and to detect their damages

effectively is in high demand.

Recent development of FOSs has provided an excellent choice to civil engineers because of their small dimensions, good resolution and accuracy, wide temperature operating range, and excellent ability to transmit signal over long distances *[71]*. They are immune to electromagnetic and radio frequency interference and may incorporate a series of interrogated sensors multiplexed along a single fiber. They are also suitable for internal strain measurements because they do not significantly affect the stress and strain states of the material in which they are embedded due to their small dimensions *[72]*.

The past two decades have witnessed an intensive international research in the field of fiber optical sensing. FOSs have been successfully applied to civil structures such as buildings, bridges, dams, etc. *[73], [74], [75]*. This study will focus on the review of recent development of FOSs and their applications in the field of civil engineering.

Fundamentals for FOSs

An optical fiber is a cylindrical dielectric waveguide made from silica glass or a polymer material. A schematic of a common form of commercial telecom fiber optic cable is shown in Figure 153. Both the core and the cladding are made from glass or plastic, and the surrounding coatings used to protect the optical fiber are made from acrylate or polyimide materials. Optical fibers come in two configurations: multi-mode (core size 50 ~ 100 μm) and single mode (core size <10μm).

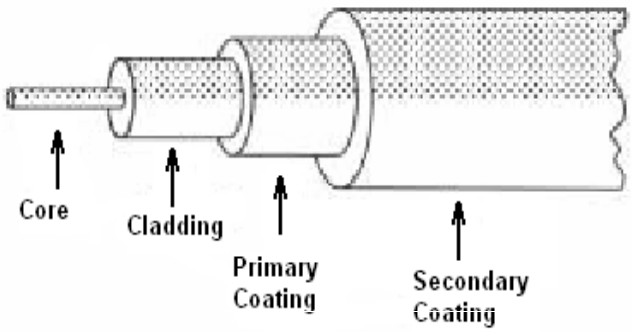

Figure 153
Structure of an optical fiber

FOSs embedded in or attached to structures expands or contracts by small amounts according to strains on the structure and temperature variations. When a portion of the light is sent down the fiber to the sensor, it is modulated according to the amount of the expansion or contraction (change in the length of the sensor). Then, the sensor reflects back an optical signal to an analytical device, which translates the reflected light into numerical measurements of the change in the sensor length. These measurements indicate the amounts of strains within the structure.

FOSs may be categorized according to various classification schemes. Based on one scheme, if the effect of the measurand on the light being transmitted takes place in the fiber, they are classified as intrinsic; however, if the fiber carries the light from the source and to the detector, but the modulation occurs outside the fiber, they are considered to be extrinsic. FOSs can also be divided according to whether sensing is localized (point), distributed, or multiplexed. A Localized or point sensor, as the name implies, detects measurant variation only in the vicinity of the sensor. If sensing is distributed along the length of the fiber, an OTDR is needed to determine the location of any variation in the measurand. Wavelength multiplexing can be achieved by fabricating gratings at slightly different frequencies within a broad-band source spectrum *[74]*. Two different types of FOSs are commonly used in civil applications: the Fabry-Pérot (FP) sensor (Figure 154) and the FBG sensor (Figure 155).

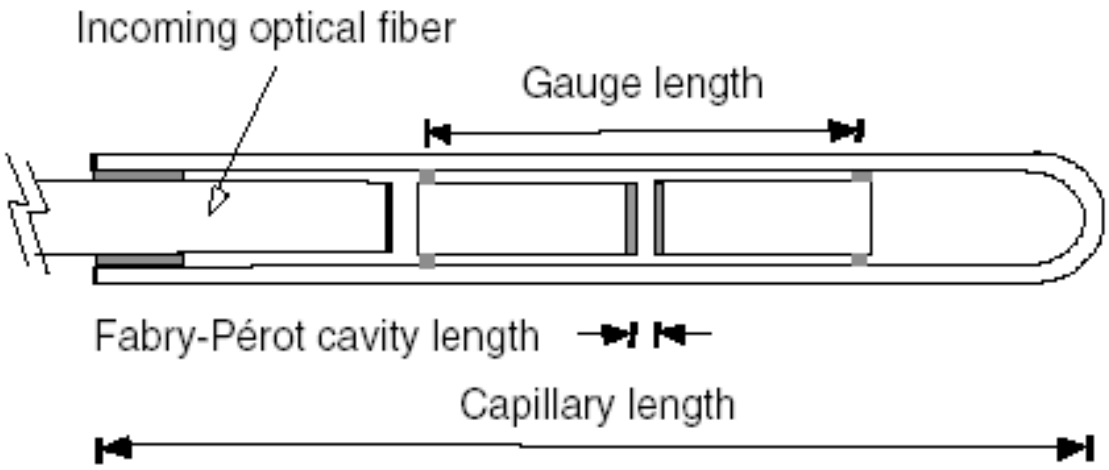

Figure 154
Schematic diagram of a FP sensor

An FP sensor consists of two semi-reflective mirrors facing each other, as indicated in Figure 155. The mirrors are placed on the tips of multimode optical fibers, which are spot-fused into a capillary. The air gap between the mirrors defines the FP cavity; the distance separating the

fuse spots is the gauge length. Any strain variation will change the length of the FP cavity, therefore inducing optical signals. To measure strains, a white-light is sent into one end of the fiber optic cable, and its reflected signal is received by a readout unit; then the strain in a FP sensor is measured using the following equation:

$$\varepsilon = \triangle L_{cavity}/L_{gauge} \tag{11}$$

where, $\triangle L_{cavity}$ is the change in the cavity length and L_{gauge} is the gauge length.

Taking the temperature effect into consideration, the real strain can be obtained using the following equation:

$$\varepsilon_r = \varepsilon - \beta \triangle T \tag{12}$$

where, ε is the total strain in a FP sensor obtained using equation (11), ε_r is the real strain of the structure, β is the thermal coefficient of structure, and $\triangle T$ is the temperature change relative to the temperature at installation.

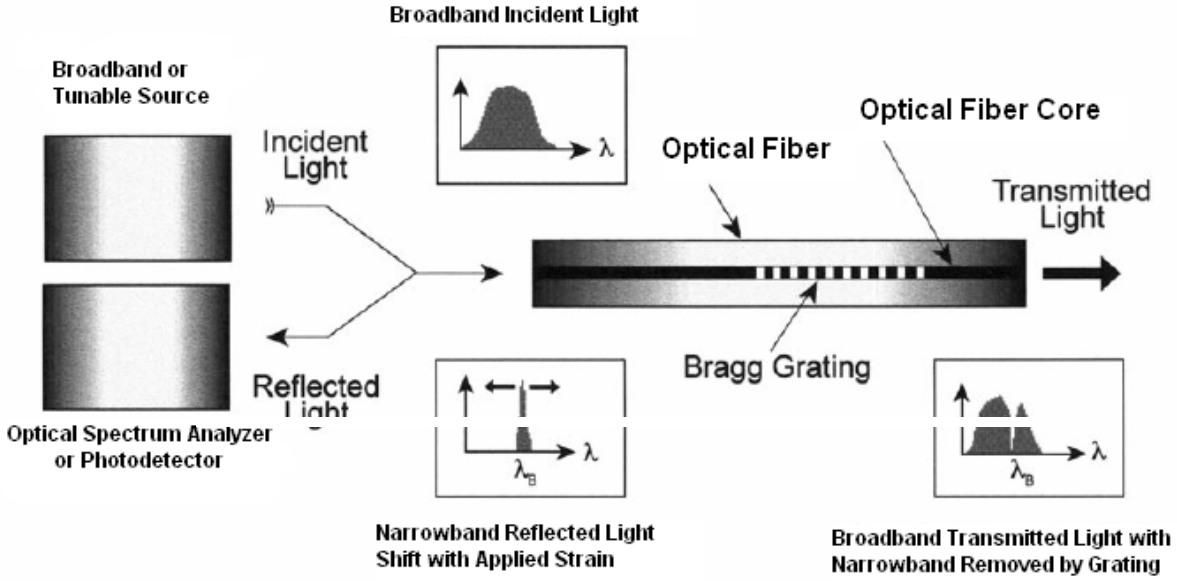

Figure 155
Fiber Bragg grating concept

An FBG sensor consists of a region of germanium-doped glass fiber core that has been exposed to ultraviolet radiation using a phase mask to fabricate a periodic "grating" of material with a modulated index of refraction. The precise spacing of the grating, called the "pitch," reflects the incident light with a narrow band centered about the "Bragg" wavelength, defined by:

$$\lambda_0 = 2n\Lambda \tag{13}$$

where, λ_0 is the Bragg wavelength, n is the average effective index of refraction of the grating, and Λ is the pitch spacing, as shown in Figure 154. The FBG also provides a linear response based on the measurement of wavelength shift ($\triangle\lambda$) due to the straining of the gauge. After taking into account temperature effects that will also cause a wavelength shift, measuring $\triangle\lambda$ provides a means of determining the strain according to the equation:

$$\triangle\lambda/\lambda_0 = (GF)\varepsilon + \beta\triangle T \tag{14}$$

where, $\triangle\lambda = \lambda - \lambda_0$, GF is the FBG gauge factor, typically about 0.75 – 0.82, ε is the strain, β is the thermal coefficient, and $\triangle T$ is the temperature change relative to the temperature at installation.

The sensed information of FP sensors is the FP cavity length, which is different from the sensed information of FBG sensors: the optic wavelength. However, both of them are absolute parameters. Therefore, the outputs of both sensors do not depend directly on the total light intensity levels and losses in the connecting fibers and couplers. While the FP technology can be very precise, with a maximum resolution of ±0.01με, the FBG technology is less precise, obtaining a resolution around ±10με with standard equipment. However, a new calibration is needed every time when the readings are stopped for a FP sensor, while a FBG sensor requires no calibration *[14]*.

A few kinds of FOSs specifically designed for monitoring parameters such as crack, strain, and corrosion have been developed. They are described in the following sections.

Typical FOSs

Crack sensors. The failure of concrete structures usually starts with cracks. The damage condition of a concrete structure can be assessed through the monitoring of cracks. Many non-destructive evaluation techniques, such as visual inspection, radiography, ultrasonics, and acoustic emission have been developed for damage detection; however, all of them have a common limitation that continuous assessment of cracks cannot be made in-situ during the service of structures. Fiber optic crack sensors developed recently have provided a good solution to this problem.

FOSs have been used for crack detection by a number of researchers. Wanser and Voss used multimode OTDR to measure both longitudinal and transverse crack growth and crack displacement such as longitudinal crack separation and transverse shear crack displacement,

respectively. Habel performed real-time crack detection and crack growth rate measurement by measuring the attenuation of light transmitted in the fiber optic crack sensors due to the surface crack growth. Liu and Yang used distributed FOSs to monitor concrete cracks based on the light loss due to the microbending of an optical fiber bridging cracks and with the use of OTDR. Lee et al. demonstrated the capability of intensity-based optical fiber sensors (IOFSs) to monitor the fatigue crack growth of steel structures by detecting the stiffness changes near the crack *[73], [76], [77], [78]* .

Although fiber optic crack sensors have been successfully applied in many cases, they suffer from some limitations. For example, conventional "point" sensors, which measure the strain at a local point, can detect and monitor the opening of a crack only if the cracking occurs in a small region that is known a priori, and thus can easily miss cracks *[79]*. Integrated sensors, which measure the displacement between two points separated by a relatively large distance, cannot distinguish the case of many fine cracks and the case of one widely open crack *[80]*.

To overcome these problems, Leung et al. developed a novel fiber optic "distributed" sensor that can (1) detect the formation of cracks without requiring a priori knowledge of the exact crack locations, (2) carry out continuous monitoring once the crack is formed, and (3) detect and monitor a large number of cracks with a very small number of fibers *[16]*.

The principle of the sensor is illustrated in Figure 156, which shows a "zigzag" sensor at the bottom of a bridge deck. Before the formation of cracks, the backscattered signal vs. time follows a relatively smooth curve (the upper line in Figure 156c). The signal loss in the straight portions of the fiber is probably due to the absorption of light by the cladding. In the curved portion, where the fiber changes in direction, some light energy will then move into the cladding and dissipate, causing bending loss, which depends on the radius of curvature. When a crack opens in the structure, a fiber intersecting the crack at an angle other than 90° has to bend to stay continuous (Figure 156). The sudden bending of an optical fiber at the crack results in a sharp drop in the optical signal (lower line, Figure 156c). From the time values on the OTDR record corresponding to the sharp signal drops, the location of cracks in the structure can be deduced. Also, from the magnitude of the drop, the crack opening can be obtained if a calibration relation is available.

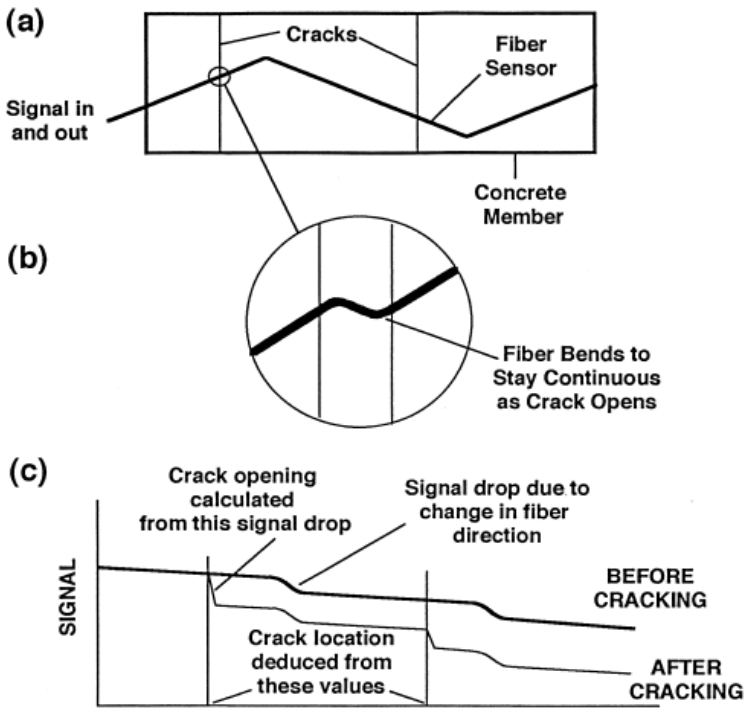

Figure 156
The novel crack sensing concept *[16]*

The proposed technique by Leung et al. does not require prior knowledge of the crack location, which is a significant advancement over existing crack monitoring techniques. However, for the sensor to work, the crack direction needs to be known. Also, to sense cracks effectively, several sensors should be employed because with a single fiber results will be difficult to interpret if a crack intersects the "zigzag" fiber at a location where the fiber direction changes *[16]*.

Strain Sensors. Due to their small size, FOSs can be either embedded into or surface-bonded onto different materials, such as concrete, steel rebars, steel plates, FRP strips, etc. There have been many reports on the application of FBG and FP sensors to structural performance monitoring in recent years, and many of them are based on the ability of FOSs to measure the internal strain of structures *[75]*.

Grossman and Huang used FP sensors for multidimensional strain measurement *[81]*. Bonfiglioli and Pascale carried out experiments using fiber optic strain sensors for internal measurements in concrete specimens. Their research showed the possibility of measuring the internal strain state without influencing the stress state of the specimen, owing to the small

dimensions of FOSs *[72]*. Kenel et al. used multiplexed FBG sensors to measure strains along 0.393 in. (10 mm) diameter reinforcing bars embedded in reinforced concrete beams subjected to bending. The authors found that the sensors were capable of measuring large strains and strain gradients with high precision, without significantly affecting the bond properties *[82]*.

In many cases, the health condition of a concrete structure depends on the strain condition of reinforcement bars. A lot of research has been conducted on the measurement of strains on reinforcement bars *[14]*. Figure 157 shows a FBG strain sensor bonded to a piece of rebar. The jacket of the fiber is only removed in the sensing zone, which is bonded to the polished surface of the rebar by means of cyanoacrylate. The sensing part is protected by several layers of rubber, and the input/output lead is protected by the fiber jackets.

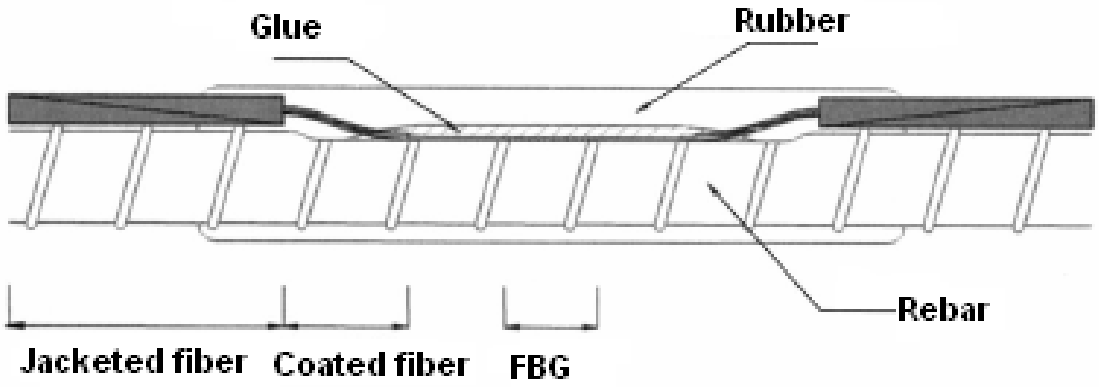

Figure 157
Scheme of the fiber Bragg grating strain sensor *[14]*

Recently, FRP sheets, laminates, and plates have been frequently employed in the rehabilitation of civil infrastructures strongly suffered from overload, aging, and chemical attack by deicing salts. The integration of FOSs with these advanced composite materials has been the subject of interest and intensive research in recent years. Gheorghiu et al. studied the performance of fiber optic strain sensors attached to the carbon fiber reinforced polymer (CFRP) plates used to strengthen concrete structures. Strain measurements from these FOSs were compared with those obtained by the collocated electrical strain gauges *[14]*.

Their experimental results showed that the FOSs were precisely measuring strains below 4000 με (the difference observed between FOSs and ESGs always remained lower than 5 percent), and that the load amplitude and the number of fatigue cycles had virtually no influence on the FOS readings for strains smaller than 3300 με. These results confirmed that FOSs were capable of measuring strains precisely for a variety of loading conditions, load

range, and number of fatigue cycles.

Corrosion Sensors. The corrosion of steel cables and reinforcing steel in concrete represents one of the leading causes of durability problems affecting civil infrastructures. As a result of the corrosion of reinforcing steel, a large radial pressure is exerted on the surrounding concrete, which may result in local radial cracks. These cracks in turn accelerate the corrosion process of the reinforcement. Finally, the reinforced member will experience a loss of strength. Detection of the corrosion of reinforcement bars has been one of the most challenging tasks in the health monitoring of civil infrastructures.

Using FOSs for corrosion detection is just somewhat recent research. Fuhr et al. installed all-fiber corrosion sensors on three bridges in Vermont *[83]*. Based on the absorption of light propagating in the evanescent wave by the steel reinforcement bar, the degree of corrosion can be measured. Fuhr and Huston studied the feasibility of using embedded FOSs for corrosion monitoring of reinforced concrete roadways and bridges. They proposed to use a warning alarm in which a predetermined threshold of "fiber events or faults" can be set when detecting the structure's internal damage *[84]*.

Casas and Frangopol proposed that the corrosion of a non-corrugated steel bar could be detected by using an FBG sensor placed around it in a circle perpendicular to its axis, by means of super glue. With this disposition, the sensor measures the angular strain produced around the bar. When the bar expands due to corrosion, the perimeter of its section increases and the FBG sensor is strained, which can be detected as a shift in the Bragg wavelength of the sensor *[85]*.

Similarly, Maalej et al. studied the feasibility of using fiber optic sensing technology for monitoring corrosion-induced damage in reinforced concrete beams through experiments *[70]*. However, the way in which the corrosion sensors were placed was different from that employed by Casas and Frangopol *[85]*. Figure 158 shows a photograph of the embedded FOSs used in their study. A concrete-embeddable fiber optic strain sensor based on the FP configuration was used to monitor the corrosion-induced tensile strain in the concrete perpendicular to the plane of the reinforcement steel bars where splitting cracks/delamination were likely to occur (Figure 159).

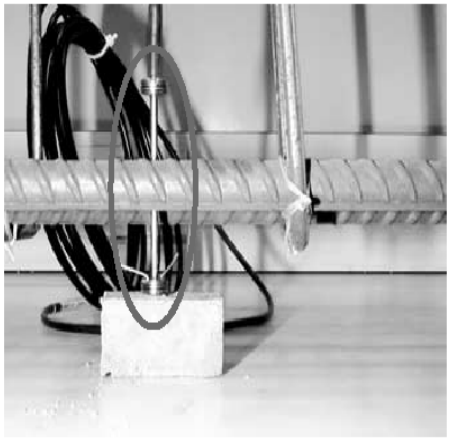

Figure 158
Location of fiber optic strain sensor *[70]*

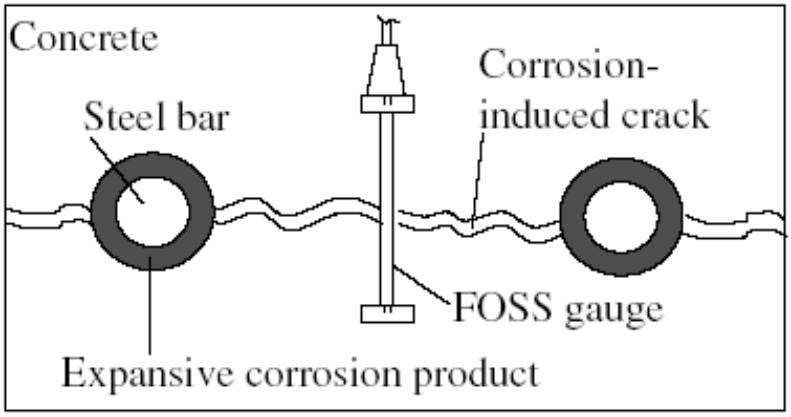

Figure 159
The concept of using FP sensor to detect corrosion-induced damage *[70]*

The research results in their study clearly demonstrated the feasibility of the proposed technique as an additional approach to monitoring corrosion-induced damage in reinforced concrete structures where visual inspection is not possible.

Applications of FOSs

Applications of FOSs in civil infrastructures have become very active in recent years. Successful applications of FOSs to health monitoring of civil infrastructure have demonstrated their advantages over traditional methods. In this section, recent applications

using FOSs in civil infrastructures are described.

Buildings

FOSs have been successfully used in measurement of parameters such as strain, temperature, displacement, and crack in buildings. Early in 1992, Fuhr et al. reported an embedded FOS network that was used for the monitoring of the Stafford Medical Building, a five-storey 65,000 ft^2 (6038.69 m^2) concrete structure at University of Vermont, Burlington. The sensors were instrumented in the way wind sensors were mounted to the external brick skin on the walls, and the other sensors were embedded into the floor, the load bearing support columns, and the ceiling by attaching to the rebars using tape. This sensor network allowed measurements of vibration, wind pressures, loading, creep, and parameters relating to building performance, such as crack development *[86]*.

Iwaki et al. developed a series of FBG sensor modules for a 12-floor steel frame building with damage tolerance construction techniques. A total of 64 FBG sensors were installed in this building. Utilizing the multiplexing capability of FBG sensors, six sensors were installed in a single optical fiber cable on average. Displacement, strain, and temperature of the building were measured. Their study showed that with the feature of multiplexing capability, FBG sensors are ideal for the performance monitoring of large structures *[87]*.

Apart from their applications in new buildings, the application of FOSs in the performance monitoring of historical buildings has also been subject to intensive research interests. In Italy, four long gauge FBG sensors were installed on the primary arch of the Cathedral of Como in Northern Italy, a significant cultural heritage built in 1936, to identify any significant structural deterioration *[88]*. These four sensors were installed across, above, and under the primary arch of this building, using surface mounting brackets. Each sensor has two serially connected Bragg gratings, with one measuring strain or displacement, while the other monitors temperature. The displacement resolution of 0.1 μm and temperature resolution of 0.1°C were achieved with the technique of an FP tunable filter demodulation system.

Palazzo Elmi-Pandolfi in Foligno, another historical building dating back to 1600 in Italy, has been repaired and retrofitted by CFRP with embedded fiber optic Brillouin sensors, which measure strains by using the Brillouin frequency shift. The low cost of the sensor made monitoring all the critical areas rather affordable, while the distributed sensing feature allowed detecting anomalies in load transfer between FRP and substrate and the location of eventual cracking patterns *[89]*.

Bridges

Among the applications of FOSs to all civil infrastructures, bridges are probably the most frequently reported ones. A state-of-the-art review of FOSs for bridge monitoring was reported by Casas and Cruz *[14]*.

In Germany, extrinsic Fabry-Pérot interferometer (EFPI) sensors were installed on a bridge in Berlin that had visible cracks *[90]*. The EFPI sensors were directly attached to the exposed steel reinforcement bars near a crack and measured both deformation and vibration due to a test load as well as normal traffic. Strains on the order of tens of microstrains with uncertainty of 1 microstrain were detected, which provided an accurate measurement.

In Switzerland, 58 long-gauge FOSs [between 9.8 ft. and 16.4 ft. (3 m and 5 m)] were embedded in pairs near the top and bottom surfaces of the concrete arch slab of the Siggenthal Bridge in order to measure the deformation of arch segments. From this measured deformation, the curvatures in the vertical plane and perpendicular displacements of the whole concrete arch during both the construction and in-service periods were determined. Preliminary monitoring results showed that the daily temperature fluctuation during summer had a particularly large influence on the arch and should be taken into consideration during the bridge design phase [*91]*.

Idriss et al. designed a multiplexed Bragg grating optical fiber monitoring system for a 40-ft. (12.192-m) span non-composite steel girder concrete deck bridge, with a strain resolution of 0.95 microstrain. Sensors were bonded to the tension steel in the slab and attached to the bottom flange of the girders to measure the strains throughout the bridge. Several levels of damage in the form of torch cuts in one of the girders were introduced with the final cut resulting in a half depth fracture of the girder. The monitoring system recorded a definite change in the structure's response. From the time when the change in condition was recorded, the time when the damage occurred was determined. The location of the crack was also obtained from the change in the response of the slab and a loss in load observed on one girder *[92]*.

In Canada, the application of FOSs to the health monitoring of bridges is very active. An overview of the development and application of FOSs for monitoring bridges in Canada was given by Tennyson et al. *[75]*.

The Beddington Trail Bridge in Alberta is the first bridge instrumented with FOSs in Canada and the first bridge known to contain pre-stressed carbon fiber composite cables with FBG sensors embedded in the concrete girders supporting the bridge. A total of 20 FBG sensors were installed by Electro-Photonics Corporation (EPC) of Canada in 1993 with pre-testing of

the composites and sensors performed at the University of Manitoba. The network of FBG sensors was connected to a junction box that provides onsite monitoring. To check the integrity of the carbon fiber cables and the FBG sensors, measurements were made in November 1998, and 18 of the sensors were still operative. No structural problems were detected at that time *[75]*.

The Taylor Bridge in Manitoba (Canada) is the world's largest span bridge that uses FRP for shear reinforcement and a FOS system for remote monitoring. This 541.33 ft. (165 m) long bridge consists of 40 pre-stressed concrete AASHTO-type girders, which are standard girders defined by AASHTO.

Monitoring technology for the Taylor Bridge is shown schematically in Figure 160. FBG sensors were used to monitor the strains in the CFRP reinforcement of the girders, the deck slab of the Taylor Bridge, and the GFRP reinforcement of the barrier wall. The FBG sensors used in the Taylor Bridge were fabricated by Electro-Photonics Corporation and have a full range of 10,000 microstrains.

A total of 65 FOSs were installed on the reinforcements of the structural members. Out of the 65 sensors, 63 were single FBG sensors and the remaining were multiplexed FBG sensors. As shown in Figure 159, these 65 sensors were installed on the following bridge components: the girders reinforced with CFRP, selected girders reinforced with steel, the deck slab reinforced with CFRP, and the barrier wall reinforced with GFRP. In addition, 20 thermocouples were used at different locations on the bridge in order to compensate for temperature effects. A 32-channel fiber optic grating indicator, the FLS3500R, was used to take strain measurements.

FOS technology has recently been used in China's fast growing infrastructure. Ou et al. reported an application of FBG sensors in the health monitoring of the 984.25 ft. (300 m) span Binzhou Yellow River Highway Bridge, the first cable stayed bridge with three towers along the Yellow River, the second longest river in China. In order to monitor the strain and temperature of the steel cable and reinforced concrete beam and to evaluate the health condition of the bridge, one sensing network consisting of about 130 FBG sensors mounted in 31 monitoring sections had been built. One four-channel FBG interrogator was used to read the wavelengths from all the sensors, associated with four computer-controlled optic switches connected to each channel. Both the interrogator and the optic switches were controlled by a written computer program simultaneously. Data obtained since the bridge's opening to traffic during the load test showed that the strain and temperature status of elements as well as the bridge were in good condition *[93]*.

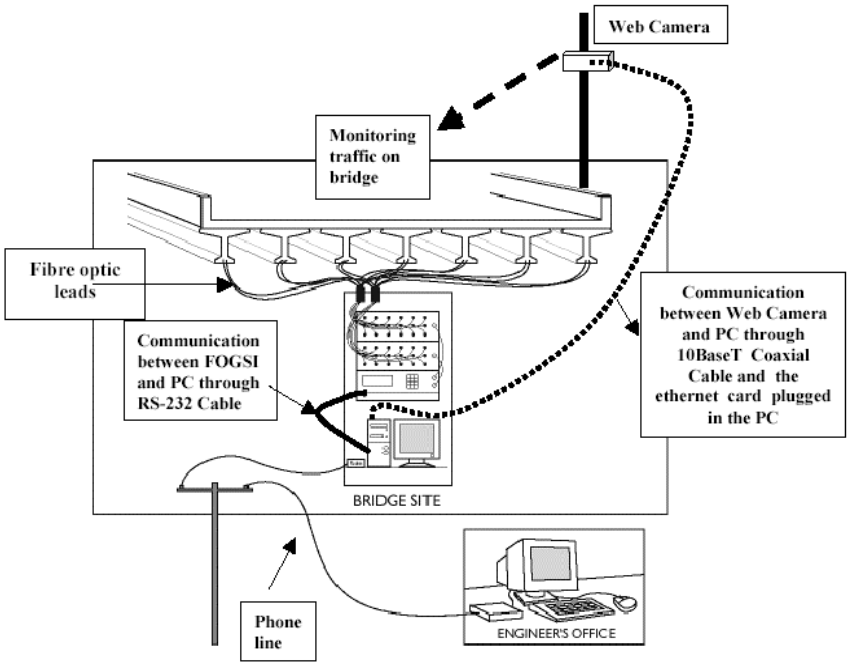

Figure 160
Monitoring technology for the Taylor Bridge *[75]*

Wang et al. reported another application of FOSs on the construction control of mass concrete of Nanjing 3rd Yangtze Bridge in China. A total of 237 FRP-packaged FBG temperature and strain sensors have been used to monitor the temperature and strain condition of mass concrete structures of the bridge. Their research results have shown that the FRP-packaged FBG sensors are proper for construction control of mass concrete structures *[94]*.

Pavements

FOTSs have been designed to embed into road surface of flexible pavement to detect traffic flow. FOTS technology was developed using the fiber optic microbending theory. When an external force or pressure is applied on an optical fiber, the fiber bends over the small radii mesh strands, and thus the light focused into the fiber's inner core is refracted out of the core into the fiber's protective buffer layers, causing a decrease in light intensity *[95]*. Early in 1993, Body et al. used FOSs embedded in road surface to detect vehicle weight *[96]*.

Eckroth suggested two methods in which an FOTS can be embedded into the road surface (Figure 161) *[97]*. In one method, an FOTS was horizontally embedded into the asphalt concrete, and in the other, an FOTS was vertically embedded.

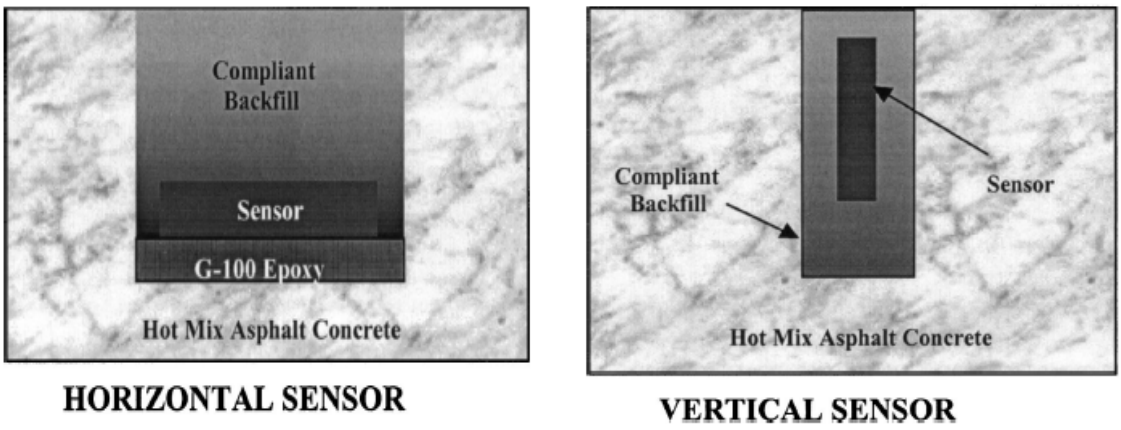

Figure 161
FOTS placement options *[97]*

Cosentino et al. studied how the sensor functioned when placed in narrow vertical grooves, and they concluded that compared with horizontally installed sensors, vertically installed sensors can avoid stress concentrations caused by vehicle tires, and display longer lives. When FOTSs are placed in narrow vertical grooves, the signal or light intensity losses are a result of the groove becoming narrower as tires load the surrounding pavement. The associated groove movements are sufficient to cause a light loss that can be recorded using existing roadside computer and data acquisition systems for either traffic classification or vehicle weighing for traffic moving at slow speeds *[98]*.

Cosentino et al. also suggested that vertically installed sensors should be placed near the pavement surface in a groove approximately 0.126 in. (3.2 mm) wide. Although the exact groove depth for optimizing the sensitivity was not determined, the groove theoretically moved more and would cause additional light to be refracted out of the microbending sensors as this depth increases. Finally, they suggested that a depth of approximately 0.75 in. (19 mm) would be acceptable, and claimed that depths in excess of this amount may cause premature structural damage to the pavement *[98]*.

Bergmeister and Santa installed an FOS in the neighborhood of the Colle Isarco viaduct to acquire traffic loads. The FOS installed (Figure 162) was double refractive, uncovered, and embedded between two metal strips that were welded together. The FOS system in their study has shown to be reliable for several years *[99]*.

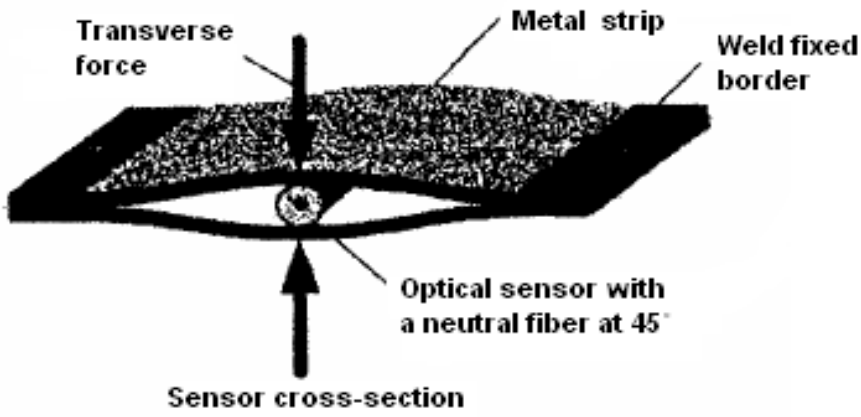

Figure 162
Fiber optic weight-in-motion sensor *[99]*

Udd et al. installed 28 specially designed FBG traffic sensors in surface-cut slots of the Horsetail Falls Bridge in the Colombia River Gorge National Science Area of the United States and tested the monitoring system by running vehicles of different weights at a speed of 10-18 kilometers per hour. They also installed five long gauge FBG sensors in the I-84 freeway to test the ability of these sensors to classify and counter vehicles. The sensing system they developed could achieve a resolution of less than 0.1 micro-strain with a dynamic range of 400 micro-strain at a 10kHz sampling rate, which can satisfy the traffic monitoring requirement and was able to discriminate tractor-trailer and buses and even the traffic in adjacent lanes in some cases since the amplitude of the signal appears to be closely proportional to the vehicle weight and the speed of the vehicle. The driving direction can also be determined by the separation of peaks and their order of appearance in adjacent FBG sensors. The test results obviously demonstrated the advantages of FBG sensors over traditional vehicle monitoring devices *[100]*.

Other Applications. Fuhr and Huston reported the application of FOSs to the Winooski One hydroelectric dam in Vermont *[101]*. Multi-functional fibers capable of simultaneously sensing vibrations and pressures were developed and embedded to measure and monitor the water pressure exerted on the upstream face of the dam's spillway and the vibration frequencies and amplitudes induced into the powerhouse section of the dam as the electrical and water loads vary. Vibration frequencies obtained from the embedded sensors showed good agreements with the induced frequencies with an average full scale error level of 0.77 percent and a peak error of 2.03 percent. The fiber sensors helped resolve a problem during the start-up of the hydroelectric plant when the expected generator efficiency was not achieved *[102]*.

In Switzerland, FOSs were applied for long term surveillance of a tunnel near Sargans. The sensors were made of glass fiber reinforced polymers (GFRP) with embedded FBG sensors and were used to measure distributed strain fields and temperature *[103]*.

In Italy, the San Giorgio Harbor pier was equipped with an array of more than 60 FOSs for continuous monitoring *[104]*. These sensors allowed continuous measurement of the pier displacements during the dredging works and ship docking. The sensors measured the curvature changes in the horizontal and vertical planes and allowed a localization of settlements with a spatial resolution of 32.808 ft. (10 m) over a total length of 1312.33 ft. (400 m). The system has been in operation since fall 1999, and data have been collected automatically and continuously since then.

In health monitoring of long pipelines, FOSs have demonstrated their great potential since it is difficult to detect damages in pipelines with conventional methods. In Indonesia, a 360892.4 ft. (110 km) pipeline was equipped with a vibration sensor to monitor its integrity and to alert ongoing damages caused by excavation equipment, theft, landslide, or earth movement *[105]*. The location of anomaly could be determined by detecting the changes of backscattered light characteristics caused by disturbances of fiber compression, elongation, or twist. In October 1998, the system successfully detected damage to the pipeline at a precise position, caused by a landslide.

Tennyson et al. investigated the application of "long gauge" FOSs to monitor the behavior and integrity of pipelines. Tests were conducted on pipe sections under a variety of load conditions, including internal pressure, axial compression, bending, and local buckling, and test data were monitored remotely through internet access. Results obtained showed that the FOSs could track changes in loads, detect pre-buckling deformations, and measure post-buckling plastic strains. Using analytical models in combination with real-time measurements of the pipe's response, predictions of the operational lifetime for the pipe were made *[106]*.

Glisic et al. monitored the average strains of two sets of piles under axial compression, pullout, and flexure tests using long gauge FOSs. The sensors used in their study gave rich information concerning the piles behavior and soil properties. The Young's modulus of the piles, the occurrence of cracks, the normal force distributions, and the ultimate load capacity in the case of axial compression and pullout tests as well as the curvature distribution, horizontal displacement, deformed shape, and damage localization in the case of the flexure tests were determined. Moreover, through the tests, the pile-soil friction distributions, the quality of soil, and the pile tip force were estimated *[107]*.

Lee et al. also performed a series of laboratory and field tests to evaluate the applicability of an FOS system in the instrumentation of piles. The authors found that the distributions of the axial load in three model piles and a field test pile evaluated from the strains measured by FBG sensors were comparable, in terms of both magnitude and trend, with those obtained from conventional strain gauges. Based on the successful application in the analysis of the axial load transfer in piles, the authors suggested that the use of these sensors in drilled shafts and other types of cast-in-situ concrete piles is feasible *[108]*.

Existing Problems with FOSs

Although FOSs have been successfully applied to many civil engineering structures to monitor displacements, strains, cracks, etc. and have demonstrated their advantages over traditional monitoring devices and technologies, some issues with the application of FOSs still need further investigation. The existing problems with FOSs will be described in the following sections.

Strain and Temperature Discrimination

One of the main drawbacks of FBG sensors is their dual sensitivity to temperature and strain. Therefore, in order to obtain accurate strain, the contributions to the wavelength shift caused by strain and temperature have to be separated. There are two approaches to address this problem. The first approach is called reference fiber method, which uses a reference Bragg grating subjected to the same thermal environment but free from mechanical load. Compensation can then be achieved by subtracting the wavelength shift of the reference grating from the wavelength shift of the sensing grating. The second approach is to obtain a temperature-wavelength shift curve to subtract the temperature effect. In this way, by measuring the temperature at the same point where the sensor is located, it is possible to correct the measured wavelength shift *[14]*. Currently, the research on simultaneous measurements of strain and temperature using FBG strain sensors is still very active *[15]*.

Effects of Coating Materials on Strain Measurement

Glass core of optical fibers is usually coated with low modulus softer protective coatings. Ansari and Yuan argued that the mechanical properties of the protective coatings employed in conjunction with optical fibers altered the strain transduction capabilities of the sensor. They pointed out that a portion of the strain was absorbed by the protective coating of the optical fibers and, hence, only a segment of structural strain was sensed *[109]*. Based on a few realistic assumptions and their experimental results, they found that the strain-transfer characteristics of optical fibers depended on the mechanical properties of the glass core, the protective coating, and the gauge length of the optical fiber. They finally developed a mathematic expression to represent the linear relationship between the strains measured by

the strain gauge, ε_g, and the corresponding strain ε_{sg} measured by the optical fiber over the gauge length 2L:

$$\varepsilon_g = \alpha(k, L)\, \varepsilon_{sg} \tag{15}$$

where, α is the constant of proportionality between the two measurements, and it is a function of the optical fiber gauge length, L, and its mechanical properties, k. The authors also stated that it was possible to achieve $\alpha = 1.0$ by using bare fibers.

However, Li et al. argued that while the assumption made by Ansari and Yuan was true for glass, it was not valid for some coating materials that undergo plastic deformation when subjected to strains beyond their elastic limits *[110]*. They argued that while the linear elastic model developed by Ansari and Yuan worked out in applications where the concrete deformations were small and within the linear range, in applications involving large deformations and when concrete cracking occurred, the fiber optic coating deformed in a plastic manner, and the linear elastic model did not adequately portray the concrete strains. They finally introduced an elasto-plastic model through which it was possible to interpret the actual level of structural strains from the values measured by an FOS. Their theoretical findings were verified by embedding interferometric sensors in mortar samples and then comparing the stress-strain response of the samples measured by extensometers and FOSs.

Bonfiglioli and Pascale did research on internal strain measurements in concrete elements with FOSs, and they suggested that, while the use of bare fibers should be the most suitable choice for the strain measurement, several factors should be taken into consideration. First, the small size could affect the reliability of the measurement because the gauge length could be too small compared to the aggregate size. Second, a particular procedure has to be developed and applied to hold in place and protect the fiber during casting so that only the sensitive part of the fiber comes in contact with the concrete, while the remaining part must be free of sliding to avoid damage due to concrete cracking. Moreover, the protruding part of the fiber has to be adequately protected and held in place to prevent breaking during casting, vibrating, handling, and testing of the specimen. Finally, the chemical compatibility between the optical fiber and the fresh concrete has to be evaluated *[72]*.

The Bonding of FOSs

There are many factors that can affect the performance of FOSs, such as installation procedure, poor choice of adhesive, insufficient anchorage or bond length of sensors, and the geometry and the mechanical properties of the capillary. To ensure accurate measurements, effective bonding between FOSs and the host materials is particularly important. A sufficient bond surface is always needed to achieve this. Experience with recent applications showed

that polyimide coated fibers and epoxy glues were possible to obtain an excellent mechanical coupling between the fiber and the anchorage in concrete structures *[105]*. In addition, some properties of adhesive, especially the thermal coefficient, should be approximately equal to that of the host material to avoid slippage between the interfaces.

Lee et al. observed some deviation of the IOFS's signal from the strain gauge signal, when using IOFSs to monitor the fatigue crack growth in steel structures. The authors argued that the delay of the IOFS signal may be due to the incomplete cure of the epoxy adhesive caused by the unbalanced and improper mixing. The authors also suggested that the sensor construction should be improved by using optimal bonding methods or fusion splicing *[111]*.

Gheorghiu et al. also observed a drop in the reading of FOS during their experiments. Figure 163 shows the comparison of the reading obtained from both FOS and ESG. They argued that this drop was probably due to the degradation of the bond between the FOS and the CFRP. The authors also argued that other factors such as the FOS installation procedure, and the geometry and the mechanical properties of the capillary could alter the performance of the sensor *[112]*.

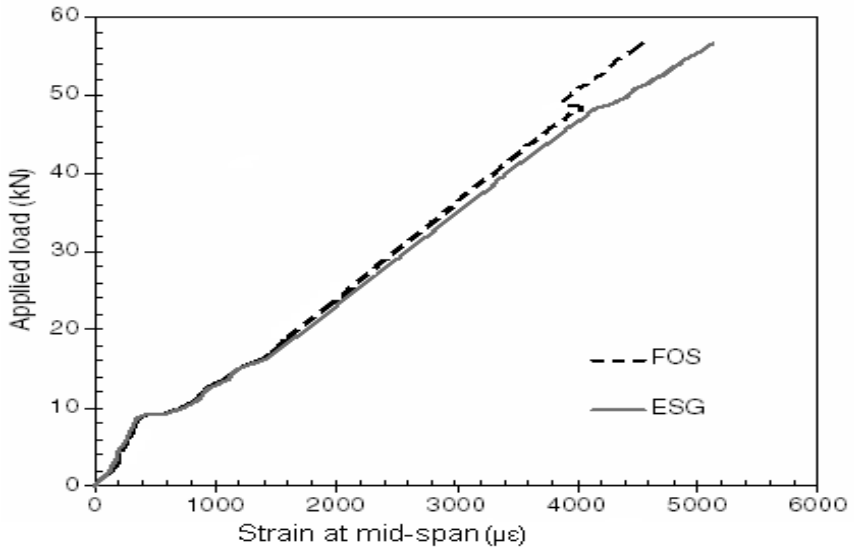

Figure 163
FRP strain at midspan (με) *[112]*

Effect of Embedded Optical Fibers on Properties of the Host Material

With the increasing applications of FOSs to structural health monitoring, the degradation of embedded sensors on the properties of host structures and materials have raised considerable concern. A state-of-the-art review on the effect of embedded optical fibers on mechanical properties of the host materials was given by Kuang and Cantwell *[113]*. They pointed out

that since the physical size of conventional optical fiber sensors (typically ranging from 100-300 μm in diameter) is at least an order of magnitude larger than the reinforcing fibers, they could be expected to compromise the mechanical properties of the host structure.

Roberts and Davidson performed a detailed study to evaluate the influence of different diameters of optical fibers and their coating types on the tensile and compressive strength of laminate in which the optical fibers were embedded *[114]*. Holl and Boyd studied the effects of embedded optical fibers on the mechanical properties of a graphite/epoxy composite host material. The static performance of the host material in which optic fibers with diameters of 125 μm and 240 μm were embedded was evaluated, and the research results showed little influence of the optical fibers on crack initiation or propagation as well as on failure strength *[115]*. Mall et al. studied the effect of embedded optical fibers on the compressive strength as well as the stiffness of a graphite-epoxy composite. They found that all specimens where the optical fibers were placed parallel to reinforcing fibers resulted in no degradation of the compressive strength. Also, no change in modulus was observed due to the presence of optical fibers in any group of specimens *[116]*. Previous research showed that FOSs have little effect on the host material if their size is small enough compared with that of the host material.

Table 13
A comparison of properties between FBG and FP sensors

	Characteristic	Sensed Information	Precision	Need for calibration	Temperature Sensitivity	Multiplexing ability
FBG	Intrinsic	Optic wavelength	Low	No	High	Yes
FP	Extrinsic	FP cavity length	High	Yes	Low	No

Through a thorough review of the recent research of FOSs and their applications to the structural monitoring of civil infrastructures FBG sensors and FP sensors were identified among the most common types used. The sensors can be used to measure strains and detect cracks as well as corrosions. A comparison of their properties is summarized in Table 13. In reality, FBG sensors are preferred in applications of large structures, such as buildings and bridges, since they can be multiplexed along a single fiber. Another advantage as shown in the table is that the FBG requires no calibration. However, FP has higher precision and lower temperature sensitivity. OTDR has also been used in crack detection. With the great

advantages over traditional sensors, FOSs are expected to play a more important role in the real-time structural performance monitoring of structures as well as in smart structures and intelligent systems in the future.